The effect of high-mass stars on low-mass star formation

Monica Pozzo

Submitted in partial fulfilment of the requirements of the degree of

Doctor of Philosophy

Department of Physics, University of Keele.

July 2001

Declaration

I certify that this thesis submitted for the degree of Doctor of Philosophy is the result of my own research, except where otherwise acknowledged, and that this thesis (or any part of the same) has not been submitted for a higher degree to any other university or institution.

Signed: ....
(Monica Pozzo)

Date: ....

Abstract

The effect that high-mass stars may have on the formation of their lower-mass siblings is crucial. The difficulty in finding faint low-mass stars in very large regions on the sky such as those covered by OB associations, can be overcome with joint optical, X-ray and spectroscopic surveys. This investigation method was proven to be extremely successful for the targets observed and discussed in this thesis.

We have discovered a low-mass pre-main sequence (PMS) stellar association in Cep OB3b. Isochrone fitting to the PMS objects reveals an apparent age spread of about 10 Myr, which cannot be explained only by means of unresolved binaries, photometric errors, spread in distance, or possible changing in reddening. Such a spread may have occurred before the birthline, due to different collapse timescales, and is suggesting star formation possibly triggered by a supernova explosion. The spectroscopic follow-up of the optically selected PMS sample has confirmed 14 association members (from Li I 6708 Å and Hα equivalent widths and radial velocities), giving 5 CTTS and 5 WTTS. Not all of the PMS stars are X-ray sources, suggesting the presence of an X-ray quiet population. We cross-correlated the optically selected PMS sample with NIR sources from the Second Incremental Release Point Source Catalogue: 4 objects show a NIR excess suggesting the presence of a circumstellar disc. The WTTS/CTTS ratio is only 1, despite the presence of OB type members: stellar winds and ionizing radiation from the high-mass members were possibly less effective in eroding the circumstellar discs.

We then present the serendipitous discovery of a low-mass PMS sequence stellar population around the Wolf-Rayet/O8 binary system γ^2 Velorum and the Vela OB2 association, thanks to photometric and ROSAT X-ray observations. High-resolution fibre spectroscopy of an optically selected PMS sample has confirmed the PMS nature of 23 stars, about half of them with an X-ray conterpart. 22 (or perhaps all) of them are WTTS, giving a WTTS/CTTS ratio of > 20. This suggests that the stellar winds and UV radiation from γ^2 Vel did not halt low-mass star formation, but that they may be responsible for the circumstellar disc erosion and subsequent evaporation.

Acknowledgments

The research presented in this thesis made use of *ROSAT* data obtained from the Leicester Database Archive Service at the Department of Physics and Astronomy, Leicester University, UK; of the SIMBAD database operated by the Centre de Données Astronomiques (Strasbourg, France); and of the US Naval Observatory A2.0 catalogue (Monet 1998).

Optical photometry observations of Cep OB3b were obtained by Tim Naylor at the Isaac Newton Telescope, Spanish Observatorio del Roque des los Muchachos of the Instituto de Astrophysica de Canarias, La Palma, Canary Islands, Spain, which is operated by the Royal Greenwich Observatory.

Optical photometry observations around γ^2 Velorum were obtained by Ed Totten at the Cerro Tololo Interamerican Observatory, Chile, which is operated by the Association of Universities for Research in Astronomy, Inc., under contract to the US National Science Foundation.

Optical spectra in the Cep OB3b subgroup were obtained by Rob Jeffries and myself with the Wide Field Fibre Optic Spectrograph at the William Herschel Telescope, La Palma, Canary Island.

Optical spectra in the region surrounding γ^2 Velorum were obtained by Fred Walter on the Hydra Spectrograph of the 4m Blanco telescope (Cerro Tololo Interamerican Observatory, Chile).

Near-infrared data for Cep OB3b were obtained from the Two Micron All Sky Survey, which is a joint project of the University of Massachusetts and the Infrared Processing and Analysis Center/California Institute of Technology, funded by the National Aeronautics and Space Administration and the National Science Foundation.

Computational work for this thesis was performed on the Keele node of the Starlink network funded by the Particle Physics and Astronomy Research Council.

Contents

List of Figures

List of Tables

1 Introduction

I know the stars
are wild as dust
and wait for no man's discipline
but as they wheel
from sky to sky they rake
our lives with pins of light

Leonard Cohen:"Another Night With Telescope"

One of the most intriguing problems in modern astrophysics is understanding the physical processes which govern star formation and evolution, a goal which will finally describe the birth, life and death of our own as well as other galaxies in the universe.

For this ambitious purpose to be achieved, as little as 15 years ago all attention was focused on gravitationally unbound objects known as OB associations and T associations, consisting respectively of early-type stars (with spectral types from O to B6), and very young, low-mass stars (T Tauri stars). It was believed that high-mass stars formed mainly in OB associations, whereas low-mass stars formed mainly in T associations (i.e., a bimodal star formation; see Larson 1986).

In the last few years it has become increasingly recognized that the majority of low-mass stars in the solar neighborhood are likely to have formed in OB associations. As pointed out by Walter et al. (2000), if we assume a Miller-Scalo mass function (Miller & Scalo 1979) in close OB associations and count the stars in T associations, then more than 90% of low-mass stars with ages less than 10 Myr are likely to have formed in OB associations. From extinct radionuclide abundances, it also seems plausible that our Sun was born close to an OB association (see Harper 1996, and references therein).

The main reason for this shift in paradigm is the discovery of numerous low-mass pre-main sequence (PMS) stars in young OB associations by virtue of their high levels of X-ray activity (see for example Walter et al. 1994, 2000; Naylor & Fabian 1999, Preibisch & Zinnecker 1999 and references therein). Recently, some evidence has been found that these X-ray selected groups can be quite small, concentrated around just one or two high mass stars, which are themselves part of larger associations. Examples include β Cru (Feigelson & Lawson 1997), σ Ori (Walter, Wolk & Sherry 1998) and η Cha (Mamajek, Lawson & Feigelson 1999).

The investigation of these low-mass PMS stars is of prime importance in establishing the form of the *initial* mass function (IMF). The mass function in OB associations may match the log-normal parameterizations of the general field population such as those proposed by Miller & Scalo (1979), with many low-mass stars formed for every O/B star. Although OB associations are by definition unbound, they are young enough that dynamical effects such as mass segregation and preferential evaporation (de la Fuente 1995) will not have occurred; and they are usually free of the heavy, variable extinction that plagues observations of active star forming regions. If the majority of low-mass stars are born in OB associations it is crucial to establish the influence that high-mass neighbors have on the formation and evolution of their lower mass siblings. The winds and ionizing radiation of hot stars could influence the mass function and circumstellar disc lifetimes of the lower mass stars, with implications for angular momentum evolution and planet formation. These ideas have gained currency with the discovery of evaporating discs around PMS stars in the Orion nebula (McCaughrean & O'Dell 1996) and theoretical studies showing that discs could be ionized and evaporated by the UV radiation fields of O stars (Johnstone, Hollenbach & Bally 1998).

It is well known that stars form thanks to the gravitational collapse of molecular clouds, rich in gas and dust, but the problem of what gives the impetus to start the contraction remains. Among proposed explanations are: density waves in the Galaxy (star formation preferentially occurs along spiral arms); shock waves caused by nearby supernova (SN) explosions; the ionizing radiation from early-type stars or high pressures from HII regions (see Lada, Elmegreen & Blitz 1978; Elmegreen & Elmegreen 1986; Shu, Adams & Lizano 1987 for a review of the possible triggering mechanisms).

Density waves may explain the spiral structure of star forming regions in other galaxies. Nevertheless, smaller-scale processes are claimed to explain irregular patterns in spiral galaxies, a clear example being offered by many nearby associations containing different subgroups with age differences of $10^6 - 10^7$ yr, a period of time which is shorter than that required by a density wave to occur twice (i.e., at most 10^9 yr; see Wielen 1974 and references therein). On the other hand, the main imprints of SN explosions, such as radio or optical remnants, do not survive until star formation: they disappear before newly born stars appear. But one may look for HI expanding shells, i.e., hot cavities of low-density gas surrounded by a dense expanding shell of cool gas (which can trigger star formation), which can live longer than 10^6 yr (McCray & Kafatos 1987). In more extreme circumstances, nearby SN explosions are invoked both as a means of terminating low-mass star formation (Walter et al.

1994) or triggering it (Preibisch & Zinnecker 1999). SN explosions are also claimed to explain the presence of newly synthesized elements responsible of starting star formation. Isotopic anomalies in meteorites were detected by Lee, Papanastassiou & Wasserburg (1977), and explained as the result of SN induced star formation (see for example Cameron & Truran 1977).

Once the collapse has started, the gas cloud condenses into protostars (determining the IMF) which, in turn, begin to contract individually along the Hayashi (1965) track in the Hertzsprung-Russell (H-R) diagram, until the core reaches temperatures high enough to start hydrogen nuclear reactions. A disc of gas and dust often surrounds these young stars, from which they accrete more mass. The IMF determined during star formation may be affected by mass loss and mass transfer processes involving the stars. Whereas high-mass stars evolve fast and can be observed when they have already started their main-sequence path, low-mass stars in OB associations are still PMS stars and are observed during the contraction when they are still embedded in gas and dust (which is gradually swept off by the ionizing radiation of OB stars, or perhaps impulsively dispersed by supernovae explosions).

Therefore, to understand star formation processes, the investigation of star forming regions must involve the identification of both high- and low-mass stars, and the determination of their age and of their mass function. This should allow us to answer some crucial points, such as the existence or not of a universal IMF; what is the influence of stellar winds and ionizing UV radiation from high-mass stars on low-mass star formation; what are the consequences for circumstellar disc lifetimes and hence what are the implications for protoplanetary disc timescales.

The fact that the majority of low-mass stars are likely to form in high-mass OB associations did not inspire observational projects, as one should have been expected, mainly due to the difficulty in finding low-mass stars: they are very faint objects to deal with. For this purpose, we have done both optical, X-ray and spectroscopic surveys to find these stars, in order to study the relationship between high-mass and low-mass star formation.

We have investigated the younger subgroup of the Cep OB3 association, Cep OB3b, discovering a low-mass population co-existing with the high-mass population present in the region (including not only an O7n star, but also several B-type stars). Spectroscopic analysis of the PMS stars has revealed that there are weak-line T Tauri stars (WTTS), mixed with classical T Tauri stars (CTTS). A cross-correlation with near-infrared data from the Two Micron All Sky Survey (2MASS) has revealed 4 objects showing near-infrared excess, attributable to an accretion disc.

We have also discovered a very rich, low-mass stellar association around the ultra-massive Wolf-Rayet star γ^2 Velorum. The presence of a low-mass stellar association in the extreme environment around γ^2 Velorum offers an excellent empirical test of the possible influence of winds and ionizing radiation on low-mass stars and their discs. Spectroscopic analysis has revealed the weak-line nature of these PMS objects, with no TTS having retained their discs.

Our observations contradict suggestions that low-mass star formation is halted by the presence of high-mass stars: low-mass stars can indeed form in such apparently hostile environments. The presence of CTTS in the Cep OB3b subgroup but not around the Wolf-Rayet star is striking: this suggests that indeed stellar winds and UV radiation by hot ultra-massive stars do make a difference to low-mass star formation, not halting it, but determining the nature of newly born stars. The fact that we find CTTS in Cep OB3 despite the presence of OB type members seems to suggest that stellar winds and ionizing radiation from the high-mass members of the association were possibly less effective in eroding and subsequently evaporating the circumstellar discs around the low-mass members. The importance of the environment is fundamental: it may influence the protoplanetary history, confining planetary formation to scales shorter than the disc evaporation time-scale. Observations at longer wavelengths are required to look for the presence of circumstellar material.

The rest of the thesis is organized as follows. Chapter 2 is mainly devoted to low-mass stars, the discovery of T Tauri stars and their subdivision into different subclasses. In Chapter 3 the discovery of a low-mass pre-main sequence cluster in Cep0B3b is presented, supported by photometric and X-ray investigations. Chapter 4 is devoted to the spectroscopic survey of pre-main sequence candidates in the Cep OB3b subgroup, and Chapter 5 to the near-infrared cross-correlations with data in the 2MASS survey. Chapter 6 presents the discovery a low-mass stellar association around the Wolf-Rayet star γ^2 Velorum, thanks to an X-ray investigation and the subsequent photometric follow-up of an optically selected pre-main sequence sample. Chapter 7 discusses the spectroscopic follow-up of the pre-main sequence objects around the Wolf-Rayet star. Concluding remarks are made in Chapter 8.

2 Finding low-mass stars in OB associations

In this Chapter we start by discussing the importance of studying OB associations to understand star-formation processes and the two widely used methods to date the age of the stellar subgroups. The remaining Sections are mainly devoted to the discovery of low-mass stars, their subdivision into different subclasses, how to find bona-fide pre-main sequence stars and how to classify them. Finally, we will discuss the different methods used to detect the presence of circumstellar discs; summarise what it is currently known about their dissipation timescales and the consequences for the formation of planetary systems.

2.1 The importance of OB associations

The term 'association' was introduced by Ambartsumian (1947), to indicate groups of OB stars. OB associations must be young, ~ 10 Myr (Ambartsumian 1949), since they have a stellar mass density less than $0.1 M_{\odot}$ per cubic parsec, which makes them unstable against Galactic tidal forces (Bok 1934; Mineur 1939).

OB associations are now defined as sparsely populated groups of very young stars (early-type stars, with spectral types from O to B6), whose spectral type, luminosities and positions imply a common origin. They are well known as the natural tracers of recent or current star formation (Blaauw 1991).

Unlike a globular cluster, which is gravitationally bound and consists of hundreds of thousands of coeval stars concentrated in a few parsecs, an OB association has in general too low a star density for it to be gravitationally bound and exhibits a greater diameter of several tens of parsecs: therefore, it can be observed only because it is young and its stars have not had time to disperse completely. When they become older than 25 Myr their spatial extent is considerable, some 10-50 pc, which makes them hard to recognise from the stellar background. This is why they are usually defined as transient objects having a short lifetime (since massive stars evolve fast) and are observed near their birthplaces, which, in several cases, are still involved in star formation. It has been demonstrated (Morgan, Whitford & Code 1953) that OB associations are also good tracers of galactic structure, and spiral structure in particular. Thanks to CO surveys of the galactic plane, in the first and second quadrant, Cohen et al. (1980) gave evidence that molecular clouds are also an excellent tracer of galactic spiral structure.

Newly formed stars are frequently found in OB associations related to dense molecular clouds, that is, embedded in rich interstellar gas and dust (for example: Orion OB1, Sco OB2, Cepheus OB3, etc.). The mass of the associations is a few $10^3\ M_\odot$ in contrast to $10^4 - 10^5\ M_\odot$ of the associated molecular cloud. In the hypothesis that molecular clouds collapse gravitationally to form stars, there would be many more stars than those actually observed (Zuckerman & Palmer 1974), therefore it is important to understand how stars form in the cloud, the relationship between an association and its molecular cloud, and what happens then to the cloud itself. Important issues immediately follow: what is the star formation rate and efficiency? How does star formation propagate through the molecular cloud? How is angular momentum (the angular momentum of the formed stars is less than that of the molecular cloud from which they were born) redistributed? What is the influence of newly-born high-mass stars (through their ionizing radiation, stellar winds, possible explosion as supernovae) on the interstellar medium and on subsequent star formation? In order to study the evolution of the cloud one has to look for an association with a considerable amount of interstellar material since the quantity of interstellar matter is inversely proportional (see Leisawitz, Bash & Thaddeus 1989) to the age of the association [= (expansion age)$^{-1}$; see Section 2.2].

The study of the properties of OB associations in our Galaxy (Blaauw, 1964), within 1 kpc from the Sun, has revealed that they have diameters of about $2 - 200$ pc, contain about $1 - 60$ OB2 stars and have an average age of about 8 Myr estimated from their expansion in galactic longitude. Many of them are composed of different subgroups, at different evolutionary phases and different ages, each containing $10 - 20$ OB stars (see Blaauw 1964).

A list of OB associations within 1.5 kpc was compiled by Ruprecht (1966). Garmany & Stencel (1992) reviewed the literature for OB associations between galactic longitude 55^o and 150^o, recomputing distances to all of them by main-sequence fitting of the B type stars (see also the review of Garmany 1994).

In the past, astrometric membership studies for nearby OB associations were very difficult because the association members may be spread over up to 100 square degrees on the sky. The larger the association dimension, the more difficult it was to distinguish the very faint low-mass members from field stars, even if accompanied by spectral classification, radial velocities and proper motion information. The reason was that both photoelectric and photometric instruments could only cover fields of a few arcminutes, so to have a general picture it would have been a huge effort to cover a large portion on the sky combining many fields. Similarly, spectroscopic observations were limited to single objects, with obvious consequences for a proper sample of radial velocities. Proper motion studies were confined to small samples of bright stars than about 6 mag. Therefore, previous studies in the literature limited themselves to the investigation of the central part of the associations. Recently, the use of wide field CCD detectors has allowed us to perform photometric studies on a considerable region of the sky (up to more than 20 arcminutes in a mosaic of CCDs), helping to identify the faintest association members. With the advent of multifiber spectrographs it is also now possible to do spectroscopy of 100-400 targets at once, in about $1-2$ degrees fields. Objective prism Hα surveys have been also performed, revealing the existence of young low-mass pre-main sequence stars (classical T Tauri stars; see Section 2.4). With the launch of EINSTEIN and ROSAT satellites, X-rays surveys became available, mainly revealing the presence of a large number of young weak-line emitting low-mass stars (weak-line T Tauri stars; see Section 2.5) in OB associations. Finally, with the Hipparcos satellite, new astrometric data became available: a census of the nearby OB associations within 1 kpc from the Sun, based on these new astrometric positions, proper motions, and parallaxes, was recently presented by de Zeeuw et al. (1999).

2.2 Determining the ages of the subgroups

The age of different subgroups of an association can be estimated by isochrone fitting in the H-R diagram, or by means of the kinematics of the members.

2.2.1 The isochrone fitting

Isochrones are essentially lines connecting points of equal age in the H-R diagram (the time the stars took to reach their current evolutionary state), determined according to the predictions of theoretical evolutionary models. A subgroup may be formed by stars at about the same age but with different masses. For high-mass stars (see Section 2.6 for low-mass stars) one has to look for the turn-off point from an isochrone, which gives their nuclear age: the early-type members have completed their

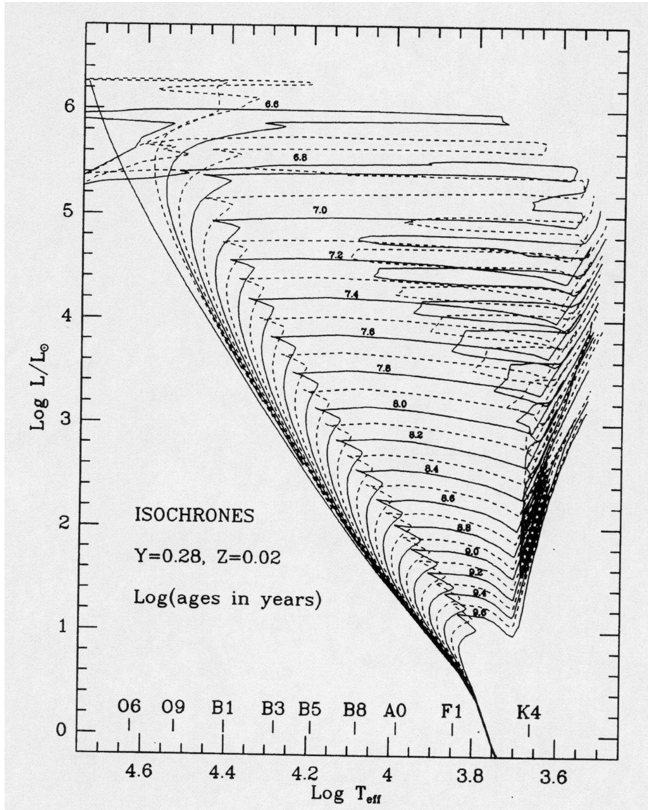

Figure 2.1: Isochrones for different stellar ages (between ~ 3 Myr and ~ 4 Gyr), in the mass range $120 < M/M_{\odot} < 0.85$, from Figure 2 of Maeder & Meynet (1991).

main-sequence life-time and are entering a more evolved phase by moving towards the red-giant region (there is no detectable pre-main sequence phase for massive stars, since they collapse quickly due to gravitational free-fall; see also Section 2.3).

The different phases in the lifetime of a star are represented by evolutionary tracks in the H-R diagram. The shape of both the evolutionary tracks and of the isochrones changes according to different models, which depend on the description of the microphysics and macrophysics adopted, with a consequent difference in the age estimates (see for example Figure 2.1). Regarding the microphysics, it depends: on the equation of state, which must take into account of all the nuclear reactions (such as H, He and C burning), the abundances of heavy elements plus their ionisation, and possible recombination processes (for example, for H, He, C, O and Ne); and on the opacities adopted (different opacities give rise to changes in surface parameters, such as the luminosity, the effective temperature and the structure of the envelope). Regarding the macrophysics, it depends: on the convection treatment (for turbulent fluids, a moderate overshooting distance is required for mixing processes); in this way it is possible to reproduce the main-sequence for stars with masses larger than 1.6 $M_{\odot}$; see Maeder & Meynet 1991); on mass-loss rates (which depend on metallicity); and on rotation (which affects transport and diffusion of the chemical elements on the stellar surface; see Maeder & Meynet 2000).

Ages are estimated with isochrone fitting, by looking for the star with the lower mass which has terminated its main-sequence path and has just moved off it, to the right of the H-R diagram. Note that turn-off ages estimated in this way are reliable for older clusters. In the case of young OB associations (for example, some $\sim$ 5 Myr old), there are not so many stars (sometimes just a few, or even one) which have a sufficiently high mass to be already evolved off the main-sequence, probably giving an underestimated age for the association. Therefore, ages derived from isochrone fitting must be treated with caution in young OB associations: a better way is to look for low-mass stars which are still contracting towards the main-sequence (turn-on the isochrone; see Section 2.6).

2.2.2 The kinematic method

Alternatively, one can determine the kinematic age of the association. There are two classical ways to do this. One method traces back in time the motions (by reversing the proper motions of the known members; see Blaauw 1983, 1991) until the smallest configuration in the past is found (this is the minimum possible configuration, but it does not mean it corresponds to the real initial one). The other method considers the linear expansion (see Blaauw 1964; Lesh 1968, 1969; Garmany 1973): the proper motion of the stars in a certain galactic coordinate (l or b) are plotted versus the coordinate itself, and then corrected for the motion relative to the solar system and the apparent expansion caused by the projected radial motion of the association. A least squared fit is performed, from which the slope gives the linear expansion coefficient and the reciprocal of the slope gives the kinematic age.

2.2.3 Disagreement in the age determination

A longstanding problem in determining the ages of OB associations, was that the two methods, i.e., isochrone fitting and kinematic methods, do not agree. More precisely, the kinematic ages are always much less than the nuclear ages given by isochrone fitting. The debate was to find out if one of the two was wrong, namely: the kinematic method may give unreliable age estimates from inprecise proper motion data and the isochrone fitting may give unreliable nuclear ages if incorrect input physics is used in the evolutionary models.

A simple model of linear expansion (like a growing spherical bubble) was initially adopted (Blaauw 1964) for the kinematic method, since OB associations are unbound and continue to expand freely during their lifetime. But, as Blaauw (1983) pointed out subsequently, the expansion could in fact be non-linear: what if the initial configuration for the subgroups was cigar shaped instead of spherical?

The kinematic ages of OB associations were recently discussed in detail by Brown, Dekker & de Zeeuw (1997). By using simple N-body simulations, they generated synthetic OB associations satisfying the constraint of unbound stellar groups. According to them, both classical ways used in the kinematic method to determine the ages give false results. The first way in deriving the kinematic ages (i.e., reversing of proper motions) always gives overestimated initial sizes for OB associations and underestimated ages: any change which causes a non-linear expansion can occur at any time (N-body interactions between members, and with the molecular cloud, the effect of Galactic tidal forces). Therefore, by tracing back the motions, the initial configuration is found well before the real one is reached, with the consequence that the deduced initial size of the association is larger, and its age younger, than they really are. The second way (i.e., the determination of the linear expansion coefficient) always gives an underestimated/overestimated age, if the proper motions are plotted versus the Galactic longitude/latitude (l/b), due to the effects of virtual expansion caused by radial motion.

Therefore they concluded that the discrepancy between kinematic and nuclear ages has to be ascribed to an underestimate of the kinematic age. This points in favour of the isochrone fitting, as the one which gives the most reliable age estimates (under conditions discussed in Subsection 2.2.1).

2.3 Finding young stars

How and where are stars born? The stellar nurseries are molecular clouds, where stars are born, accrete in mass and move towards a more evolved phase. Molecular clouds are composed mainly of hydrogen in molecular form, mixed with cosmic dust; however, they were discovered thanks to the radio emission of a minor component, the carbon monoxide CO molecule (H_2 is not usually detected because it has no net dipole moment due to its symmetry). The dense molecular cores condense to give protostars: they are immersed in cold envelopes which are their primary source of mass through accretion discs. The main accretion phase ceases once the envelopes disappear, but the newly born stars are still surrounded by interstellar material.

Radio and infrared wavelengths are then necessary to detect protostars and newly born stars still deeply embedded in dust, which can completely absorb visible and near infrared radiation and re-radiate in far infrared. Only when the interstellar material is cleared out (in most cases by bipolar jets and outflows; Reipurth & Bertout 1997), do systems of stars and discs become optically visible.

The youngest optically visible objects (see Herbig 1960) are the Herbig Be-Ae stars and T Tauri stars (TTS). Herbig Be/Ae stars are B/A pre-main sequence (PMS) and ZAMS stars, mainly showing Balmer emission lines caused by a remnant protostellar accretion disc, and with masses in the range 2-10 $M_\odot$. Their youth is suggested by disc (envelope) signatures through infrared (IR) spectrophotometric studies (see Hillenbrand et al. 1992). TTS are variable lower-mass PMS stars characterized by strong Balmer emission lines, and UV and IR excesses suggesting the presence of warm dust and active accretion, i.e., a circumstellar accretion disc (see for example Beckwith et al. 1990).

Herbig Be/Ae stars and TTS are respectively the progenitors of intermediate-mass stars and low-mass stars (LMS). High-mass stars (HMS) are not observable in their youngest phase (see below). Herbig Be-Ae stars are therefore considered the transition between early-type HMS and late-type LMS. The arbitrary separation is dictated by an initial mass of less than 2 $M_\odot$ for LMS (see also the next Section), between about $2-10$ $M_\odot$ for intermediate-mass stars, and up to 120 $M_\odot$ for HMS.

HMS reach the main-sequence first, as they collapse quickly by gravitational free-fall, reaching temperatures high enough to start hydrogen burning. LMS can instead be subject to a very slow phase of ambipolar diffusion, by acquiring magnetic flux and angular momentum from the dense cores of the molecular cloud (see for example Palla & Galli 1997). They remain in the protostellar phase, surrounded by a nebular disc and characterised by Deuterium burning, until an external trigger obliges them to cross the birthline (see below): they then start to contract along fully-convective Hayashi tracks. Among the proposed triggers (see Chapter 1), the main one invoked to start star formation in molecular clouds is ascribed to shocks caused by supernovae explosions, whose effect is enhanced by a favorable geometry of the ambient magnetic field, i.e., parallel to the direction of the shock front velocity (see Vrba 1977, and references therein; also Shu et al. 1987). Subsequent bursts of star formation may be caused by the ionising radiation of the early-type members, as well as new episodes of supernovae explosions. The birthline was defined by Stahler (1983) as the locus in the H-R diagram along which newly born stars make their first appearance as optically visible objects, at ages of about 10^5 yr. It intersects the main-sequence at about 8 $M_{\odot}$, therefore we cannot detect a PMS phase for stars with masses greater than this (see Palla & Stahler 1990, 1993).

Once LMS start to be optically visible, with strong T Tauri winds along the rotational axis (bipolar outflows) which contribute to sweeping away gas and dust grains which were shielding them, their isochronal clock is set to zero. Note that the "true" stellar age would be the sum of three different epochs in the stellar lifetime: i.e, its gravitational collapse time, plus the time it spent burning Deuterium on the birthline, plus its isochronal age.

It has been pointed out that a prolonged disc accretion phase would have the effect of holding the newly born stars on the birthline, delaying their contraction along the convective track, with the consequence that their ages would be underestimated (Hartmann et al. 1991; Hartmann, Cassen & Kenyon 1997; Siess, Forestini & Bertout 1997). Similarly, the arrival of low-mass stars on the birthline may be delayed by the presence of magnetic fields embedded in the molecular cloud. They oppose the gravitational collapse by keeping the circumstellar material bent along the magnetic field lines, and, at the same time, allow the contraction thanks to material accumulated by ambipolar diffusion across the magnetic field lines (see for example Palla & Galli 1997). At an isochronal age of about 1 Myr they are visible as T Tauri stars (TTS): approximately half of which are still surrounded by accretion discs (Strom, Strom & Merrill 1993; see Edwards 1993 and references therein; see also Section 2.13) which can survive as long as 10 Myr (see Strom et al. 1989a; Skrutskie et al. 1990; Beckwith et al. 1990) or even longer (see also Section 2.14). They continue to contract towards the main-sequence on the Henyey radiative tracks (Henyey, Lelevier & Levée 1955). Once hydrostatic equilibrium is achieved, LMS stop contracting: they are now on the zero-age main-sequence (ZAMS) and have core temperatures suitable to start the hydrogen nuclear reactions (H nuclei start to be converted into He nuclei at temperatures of about 15×10^6 K).

2.4 The discovery of T Tauri stars

TTS were first discovered by Joy (1945) with spectrographic observations of 11 irregular variable stars in or near Milky Way dark clouds. They were immediately recognized as emission-line variable stars belonging to a distinct class (named after the brightest member, T Tauri) thanks to their distinctive characteristics: irregular light variations of ~ 3 mag; spectral type F5-G5 with emission lines resembling the solar chromosphere; low luminosity; association with dark or bright nebulosity (see also Joy 1949). TTS radial velocities were found to be consistent with those of the associated molecular clouds (see, for example, Herbig 1977), and they were frequently found clustering together in the so-called T-associations. Proper-motion studies (see, for example, Jones & Herbig 1979) also confirmed their association with dark clouds. They were suggested to be young low-mass PMS objects (Ambartsumian 1947), because, when placed in an H-R diagram ($logL/L_{\odot}$ versus $logT_{eff}$), they appear well above the ZAMS. Their membership of the T-Tauri class is dictated by the spectroscopic characteristics reviewed by Herbig (1962; see the typical optical spectroscopic lines listed below). Bastian et al. (1983) added the conditions that they must be associated with a dark region, show strong Hα emission, and have a spectral type later than F. An extended overview was subsequently given by Bertout (1989) and by Appenzeller & Mundt (1989). TTS are optically irregular variables (with typical amplitudes of few magnitudes; see Herbig & Rao 1972; Mundt & Giampapa 1982; Herbst et al. 1994). Their emission line spectra are similar to those present in the solar chromosphere, but in a more extreme way, since the emission lines have considerably larger intensities and widths. The irregularity in the light variation is thought to be the result of an active chromosphere (mass loss through stellar winds, starspots, flares, etc.); as well as a variable obscuration caused by clumps of matter accreted from the parental molecular cloud, or by concentrations of dust levitated from the circumstellar disc through strong magnetic fields (see Herbst et al. 1994, and references therein).

The up-to-date definition of TTS is that they are: very young (from 10^5 yr to generally less than 10 Myr old; see Rydgren, Strom & Strom 1976; Kohen & Kuhi 1979; Appenzeller & Mundt 1989; Alcalá et al. 1996, 1997; Covino et al. 1997) low-mass PMS stars of late-type, with an initial mass smaller than 2 $M_{\odot}$, and spectral type from K0 to M6 (see Martín 1997). The cut-off at K spectral type is dictated by an observational fact: at present, the fraction of T Tauri objects of late-F and G spectral types is only a few per cent, and therefore it was suggested the denomination "PMS F-type stars" by Thé, de Winter & Pérez (1994), and a general "PMS Fe/Ge" by Martín (1997), putting them in an intermediate class between TTS and Herbig Be-Ae stars. Recently Neuhäuser et al. (2000) discovered new TTS in and around the Corona Australis molecular cloud with spectral types in the range F7 to M6.

TTS were discovered mainly through Hα objective-prism-surveys, close to regions of ongoing or recent star formation in nearby molecular clouds, clustering along dark filaments (see for example Gomez et al. 1993). These are referred to as classic TTS, CTTS, which optical spectrum is typically characterized by the following lines. In emission: strong (with equivalent widths, EW, up to more than 100 Å) hydrogen Balmer lines (6563 Å to 3970 Å; i.e., from Hα to Hϵ), strong Ca II H & K ($\lambda\lambda$3968, 3933), fluorescent Fe I lines ($\lambda\lambda$4063, 4132) probably excited by Ca II H or Hϵ (see Willson 1975), He I ($\lambda\lambda$5875, 6678), sometimes forbidden lines mainly from [O I] ($\lambda\lambda$6300, 6363) and [S II] ($\lambda\lambda$4068, 4076, 6717, 6731), originating from emission nebulae around the TTS. In absorption: strong Li I (λ6707.8), Ca I (λ6717.7), and Fe I ($\lambda\lambda$6495, 6546, 6663, 6678). Herbig & Soderblom (1980) showed that NIR spectra of TTS are characterized by Ca II triplet ($\lambda\lambda$8498, 8542, 8662) in emission, O I (λ8446) in emission, O I triplet ($\lambda\lambda$7771, 7774, 7775) in absorption or emission, weak Fe I ($\lambda\lambda$8387, 8514) in emission and Mg II ($\lambda\lambda$7877, 7896) in emission. They also found that the equivalent width of the triplet Ca II is comparable in intensity with that of Li I: they concluded that the Ca II triplet could be a powerful tool for discovering TTS which are heavily reddened, or in bright HII regions.

The spectrum of many TTS is "veiled" in the UV and blue part because of the presence of a continuous emission (Joy 1949), and sometimes it is so strong that it completely hides the photospheric absorption lines. As a consequence, the spectral type determined from the blue part of the spectrum can appear up to three subclasses earlier than that found from the red part of the spectrum (see for example Bouvier & Appenzeller 1992, and references therein).

The strongest lines in the spectra may also present P Cygni and inverse P Cygni profiles: the former are due to strong mass motions in the atmosphere, evidence for an outflowing T Tauri solar wind (Herbig 1962; Kuhi 1964); the latter are due to mass infall from circumstellar accretion discs (Walker 1972). P Cygni profiles can turn into inverse P Cygni profiles on timescales of a few days, and sometimes both may be present (see Krautter & Bastian 1980).

Large Hα emission is indicative of chromospheric activity (as well as other H Balmer lines, Ca II H & K), whereas even stronger emission is attributable to a star-disc interaction, possibly through a magnetic accretion column (Basri & Bertout 1989; Hartmann, Hewett & Calvet 1994). Furthermore, the presence of strong Balmer emission lines and forbidden lines is indicative of expanding envelopes, i.e., strong winds (Mundt 1984; Appenzeller, Jankovics & Östreicher 1984). Early-type (earlier than G8) PMS stars have Hα filled-in or in absorption, intermediate to mid-K have complex Hα emission, whereas PMS stars later than K5 will always display at least chromospheric Hα emission (Walter et al. 1988; Covino et al. 1997; Alcalá et al. 2000). TiO bands become evident for stars mid-to-late K and M stars (Walter et al. 1994).

TTS can display a variety of Hα line profiles. According to the classification given by Reipurth, Pedrosa & Lago (1996), Hα line profiles may be: symmetric, with no or weak absorption features (type I); double peaked, with the secondary peak more, or less, than half the primary peak (respectively type II, and type III); P Cygni or inverse P Cygni (type IV). Additional subtypes R and B are given for the secondary peak located redwards or bluewards of the primary peak. Covino et al. (1997) proposed a classification according to: Hα in absorption; Hα filled-in with emission; narrow and symmetric Hα emission (typically chromospheric); complex Hα line profile (such as double peaks, asymmetry, etc.) suggesting the presence of a residual circumstellar accretion disc.

TTS also show strong (see Section 2.13) IR and UV continuum excesses (Mendoza 1968; Rydgren et al. 1976; Rydgren, Schmelz & Vrba 1982; Rucinski 1985; Herbig & Goodrich 1986; Bertout 1987); and blueshifted forbidden emission lines (Edwards et al. 1987; Hartmann & Raymond 1989). All these observational properties can be explained by the presence of circumstellar discs. Circumstellar dust grains may absorb the visual radiation emitted by the central star and re-emit it in the IR (see Cohen & Kuhi 1979; Adams, Lada & Shu 1987, 1988; Kenyon & Hartmann 1987), whereas the UV excess is generated in the boundary layer between the disc and the star (see Bertout, Basri & Bouvier 1988). The heating of circustellar gas and dust due to accretion along magnetic field lines at close to free-fall velocities may produce the observed IR and UV excesses as well (Kenyon & Hartmann 1996; Gómez & Fernández 1996).

2.5 A new spectroscopic class: the weak-line T Tauri stars

TTS are strong and variable X-ray emitters: this can be explained as the result of a high magnetic activity (Feigelson & DeCampli 1981; Walter et al. 1988; Strom et al. 1990; Neuhäuser et al. 1995a;

Wichmann et al. 1997), such as flares, resulting from a solar-like chromosphere and corona. Flares similar to those seen on the Sun have been observed in TTS, with magnetic loops often deduced to be of huge sizes (often $\sim$ few stellar radii). X-ray emission is due to thermal bremsstrahlung of hot plasma channelled and heated along the magnetic field lines (see Montmerle 1999).

X-ray emission is a function of the stellar rotation: the X-ray luminosity, L_x, in TTS was found to be anti-correlated with their rotation period, i.e., correlated with their rotational velocity (see Bouvier 1986). In fact, a faster rotation seems to increase the number of particles which are channelled into the magnetic field lines and are accelerated to high energy. The produced X-rays can have strong irradiation effects on gas and dust (Casanova et al. 1995), particularly on the cloud cores, contributing in turn to star formation (see for example Silk 1995).

X-ray luminosity for TTS ranges from about 10^{28} up to 10^{32} erg/sec (0.4 to 2.5 keV), up to 10^5 times the X-ray luminosity of old m-s stars of the same spectral type (see for example Montmerle 1996; Feigelson & Montmerle 1999). For example, ordinary m-s stars emit in X-ray with L_x about $10^{31}-10^{34}$ erg/sec for O- and B-type, up to 10^{30} erg/sec for G-type, up to 10^{29} erg/sec for K- and M-type (Vaiana et al. 1981; Topka 1980). Therefore, X-ray surveys, such as Einstein Observatory (EO), ROSAT, and ROSAT All Sky Survey (RASS), turned out to be a convenient way in detecting low-mass PMS stars. The main difference in these surveys is that EO and ROSAT pointed observations are spatially biased towards specific interesting regions (where the so-called classic TTS, or CTTS, are already known to exist), whereas RASS is spatially un-biased, but of course flux-limited.

X-ray luminosity is not only a function of rotation: it was found to be correlated with stellar mass, bolometric luminosity, effective temperature and stellar age (see Neuhäuser et al. 1995a, and references therein). In particular, there is evidence for a strong correlation in TTS between L_x and the bolometric luminosity L_{bol} (see Strom & Strom 1994; Casanova et al. 1995; Montmerle 1996; Preibisch, Zinnecker & Herbig 1996; Wichmann et al. 1997), with typical values of $L_x \sim 10^{-4}$ L_{bol} in different star-forming regions (for a comparison, old late-type field stars show a ratio of ~ -6 , see Pallavicini 1989; and early-type stars of ~ -7, see Preibisch et al. 1996). As an example, a mean value of -3.6 for RASS selected TTS in Taurus-Auriga is reported by Neuhäuser et al. (1995a), with extremes of -4.06 for G-type TTS and -3.56 for M-type TTS; and $-3.5 < \log(L_x/L_{bol}) < -2.5$ for RASS and EO selected PMS stars in Upper Scorpius by Preibisch and Zinnecker (1999).

X-ray surveys (see for example Walter et al. 1988; Krautter 1996; and references therein) revealed TTS with spectroscopic features not matching those previously found in CTTS: their spectra were characterized by weak emission lines and lacking of UV and near-infrared continuum excesses, although sharing the same locus in the H-R diagram of CTTS. The new class was named naked-TTS (NTTS), to indicate stars which have lost their circumstellar material (see Walter 1986; Walter et al. 1988; and Herbig & Bell 1988, for a compendium of 742 PMS stars in various star-forming regions, including many TTS).

Note that there is some confusion in the literature, since T Tauri stars with weak Hα emission line are commonly referred to as weak TTS (WTTS), a definition which includes the NTTS as well. The main distinction is that some WTTS can still have NIR excesses, suggesting the presence of the circumstellar disc, whereas the NTTS do not have this feature and are therefore "naked", (i.e., WTTS can be defined from optical spectroscopy alone, but one needs IR data to confirm if they are naked). Therefore, all NTTS are WTTS, but the opposite is not true (see Walter et al. 2000). This is rather confusing, so, in the following, we will always adopt the WTTS name, meaning stars without an accretion disc (although some circumstellar material could be still detected for some of them at IR wavelengths).

The active stellar coronae of WTTS have thermal plasma emission with a temperature of $T = 10^7$ K $\equiv$ 1 keV (Feigelson & DeCampli 1981; Montmerle 1996; Preibisch et al. 1996), well matched by X-ray surveys (e.g., ROSAT have an energy range of 0.1-2.4 keV). According to Neuhäuser et al. (1995a; see also Montmerle 1996), WTTS are stronger X-ray emitters than CTTS because of their faster rotation (see Bouvier et al. 1993, 1995; Wichmann et al. 1998), or because a large fraction of X-ray flux is likely to be absorbed by the optically thick circumstellar material around CTTS (see Gahm 1981; Walter & Kuhi 1981). Flux-limited X-ray surveys are therefore biased against CTTS.

It follows that CTTS are the best objects in which to study the physics of the accretion process and the interaction of a young star with close environs, whereas WTTS offer the opportunity to determine the characteristics and evolution of LMS free from confusing disc signatures. It is not clear yet if WTTS evolve from CTTS after having dispersed their discs, or if they belong to two completely different families: some WTTS do appear to be very young, and located in the same region as the CTTS in the H-R diagram (see Bertout 1989; Neuhäuser et al. 1995b).

Following the evolutionary process (Lada 1987; Walter et al. 1988), we start with a CTTS having a spectrum dominated by non-stellar sources. When the circumstellar environment starts clearing out, the star becomes visible: this is the state shared by most of the CTTS, where both stellar and non-stellar spectra are present. It is thought that the CTTS angular velocity is fixed by the star-accretion disc magnetic coupling (Bouvier et al. 1993; Edwards et al. 1993; Bouvier 1994). The spinning up of the star, due to both its contraction and to accretion of high angular momentum material from the disc, is prevented and counterbalanced by the spinning down caused by magnetized winds and the interaction between the stellar magnetic field and the disc. As a consequence of this regulation mechanism, the star rotates at a roughly constant angular velocity. Once the circumstellar material is completely dissipated, the regulation mechanism is no longer valid, and the star is free to conserve its angular momentum: its contraction towards the ZAMS implies its consequent spinning up (lower momentum of inertia, thus higher rotational velocity). The spectrum is then dominated by stellar photosphere: the TTS appear more like WTTS.

The typical rotational velocity ($V sini$) value for TTS is in the range 10-30 km/s (Vogel & Kuhi 1981; Hartmann et al. 1986), less than 15% of the breakup velocity ($\sim$ 200 km/s; see for example Bertout 1989; Hartmann & Stauffer 1989). CTTS generally rotate at less than 20 km/s (see Bouvier et al. 1986; Hartmann & Stauffer 1989). WTTS rotate with velocities in the range 5-30 km/s, sometimes reaching even up to 60 km/s (faster rotators; see for example Bouvier et al. 1993, 1995; Choi & Herbst 1996). They appear, on average, to rotate faster than CTTS since they are free to spin-up after the circumstellar disc clearing (a prediction of the disc-regulated angular momentum paradigm; see Edwards et al. 1993; Bouvier, Forestini & Allain 1997). After arrival on the ZAMS (with a $V sini \sim 100 - 200$ km/s), the star slows down again due to magnetized stellar winds: this explanation, first introduced by Schatzman (1962), was observationally supported by Kraft (1967), from a sample of more than one hundred field stars. Such fast ZAMS rotators are seen in young clusters such as the Pleiades (Soderblom et al. 1993) and αPer (Balachandran, Lambert & Stauffer 1988),

Recently Stassun et al. (1999) studied the rotation period of more than 200 stars in the Orion Nebula, which were showing strong Hα emission attributable to material accreted onto the stellar surface from a circumstellar accretion disc. They found that that the characteristic features of active accretion from a circumstellar disc, i.e., NIR (I-K) excesses, are not confined to particular periods (i.e., not for slow rotators only) and that there is no trend among stellar ages and rotation periods; in particular, there are stars of about 1 Myr old which are already rotating at breakup velocity, well before their arrival on the ZAMS. This is in disagreement with the bimodal distribution of rotation periods proposed in the past, i.e., that rapid rotators come from slow rotators after having depleted their circumstellar discs.

WTTS appear more widely distributed than CTTS, i.e., not only inside star forming regions (SFR), but also far beyond the limits of the star-forming molecular clouds. Examples include stars in Taurus-Auriga (Walter et al. 1988; Magazzú et al. 1997), in Orion (Sterzik et al. 1995), in Chamaeleon (Covino et al. 1997; Alcalá et al. 1997), in Lupus (Wichmann et al. 1997; Krautter et al. 1997), in Upper-Scorpius (Preibisch et al. 1998), and in the Tucanae association (Stelzer & Neuhäuser 2000). An exception is represented by the CTTS TW Hydrae (see Rucinski & Krautter 1983) which, together with its association of WTTS (Sterzik et al. 1999; Zuckerman et al. 2001), is far from any molecular cloud. The small velocity dispersion within an association, typically of about 1-2 km/s (Herbig 1977; Jones & Herbig 1979; Hartmann et al. 1986; Lada, Bally & Stark 1991; see also Frink et al. 1997), cannot explain their position so far away from the nearest molecular clouds. At present, there are two mechanism claimed to explain the existence of very young objects outside SFR. In the first one, these objects are thought to be runaway TTS (RATTS; see Sterzik at al. 1995; Neuhäuser et al. 1995b, 1995c; Alcalá 1995) which are ejected by three body encounters in multiple protostellar systems (Sterzik & Durisen 1995; Kroupa 1998), or from the cloud in gravitational encounters (Gorti & Bhatt 1996). The second mechanism suggests that TTS can form in small, high velocity cloudlets (which have dissipated) within and around turbulent giant molecular cloud complexes with velocity dispersions of ± 5 up to ± 10 km/s (see Feigelson 1996; Mizuno et al. 1998). These may not be the only explanations for the existence of TTS far away from molecular clouds: this is at present a very controversial topic. A large fraction of the "dispersed" WTTS may in fact just be young ZAMS stars, from which X-ray selected objects cannot be distinguished (Briceño et al. 1997; see also Sections 2.8.2 and 2.11). Or, as suggested by Martín (1998), they may be post T Tauri stars (see Section 2.7) which are older than TTS, and which have had more time to disperse.

2.6 Low-mass stars isochrone fitting

For low-mass stars one has to look for the turn-on point to an isochrone, which gives their contraction age: the late-type members are approaching the main-sequence, after having passed from the protostellar phase to a slow contraction phase. Low-mass protostars in their early stages are thought to follow the Hayashi (1965) tracks, i.e., almost vertical evolutionary paths, at a given mass, in the H-R diagram (logL/L$_\odot$ versus logT$_{eff}$, with T_{eff} the effective temperature at the surface of the star), constructed according to a fully convective model. A star of a given mass descends its Hayashi track as its age increases. In this early phase, it has not contracted enough to reach core temperatures suitable to start hydrogen nuclear reactions. However, it can burn light elements, such as Deuterium, ^{6}Li, ^{7}Li, and ^{9}Be when the core reaches a temperature of about 2, 3 and 3.5×10^6 K respectively (see D'Antona & Mazzitelli 1994). As it contracts further, the protostar releases gravitational potential energy following the radiative track until when the hydrostatic equilibrium (i.e., no mass loss and no mass accretion) is achieved (at core temperatures of about 10^7 K) and the contraction phase stops. It has now reached the main-sequence, where it finally starts hydrogen burning. The theoretical evolutionary tracks in the H-R diagram can also be represented as isochrones.

The age given by isochrone fitting can vary from one model to the other, but the relative ages, i.e., of stars clustering along different isochrones in the same model, are considered accurate, since every evolutionary model is internally consistent. Theoretical evolutionary models differ in the abundances of heavy elements considered, in the opacities used at various temperatures and chemical compositions and in the turbulent convection treatment adopted. All of these different settings produce evolutionary tracks in the H-R diagram that differ both in position and in shape. Hayashi (1965) was the first to take into account the convective envelopes in low-mass stars of different masses (in the range $3.0M_\odot < M < 0.4M_\odot$), using mixing-length theory (MLT). Subsequent models used the MLT convection model, suitable for extremely viscous fluids, or the full-spectrum of turbulence (FST) convection model, suitable for low viscosity fluids such as those in the external layers of the envelopes of pre-main sequence stars (see for example Burrows, Hubbard & Lunine 1989; Schaller et al. 1992; Bertelli et al. 1994; D'Antona & Mazzitelli 1994, 1997; Baraffe et al. 1997, 1998). Recently, Palla & Stahler (1999) presented a new set of theoretical pre-main sequence tracks (in the mass range $0.1M_\odot < M < 6.0M_\odot$), starting from the stellar birthline (see Section 2.3) and ending along the zero-age-main sequence (ZAMS). The choice of one convection model or the other is crucial in determining the T_{eff} location of the evolutionary tracks in the H-R diagram. For example, the non-grey atmosphere models of Baraffe et al. (1998; for $0.075M_\odot < M < 1.0M_\odot$) are those which best reproduce the main-sequence location of very low-mass stars (see for example Hodgkin et al. 1999; they found a very

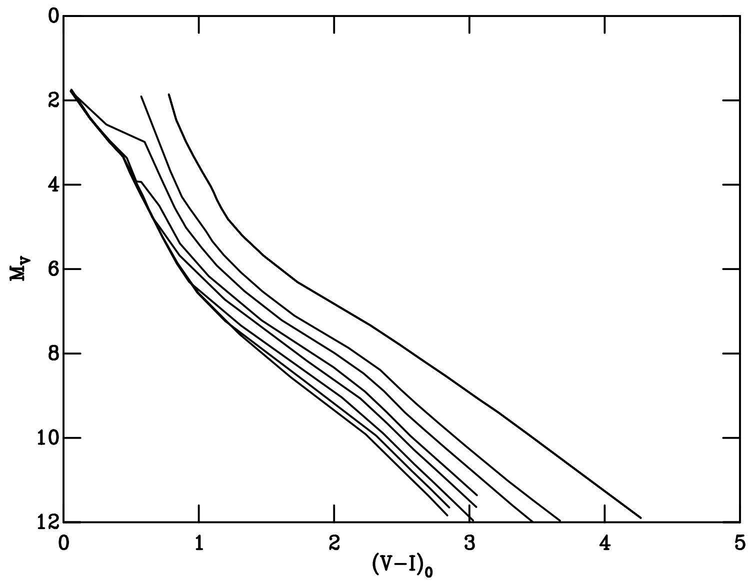

Figure 2.2: Isochrones, from right to left, at 1, 5, 10, 20, 30, 50, 70 and 100 Myr (D'Antona & Mazzitelli 1997).

good agreement with the infrared photometric data for low and very-low mass stars in the Praesepe cluster).

In what follows in the thesis we will adopt isochrones determined from the evolutionary models of low-mass stars by D'Antona & Mazzitelli (1997). The isochrones in this model are computed for stars with masses in the range $3.0M_{\odot} < M < 0.02M_{\odot}$ and younger than about 500 Myr, using updated turbulent fluxes by Canuto, Goldman & Mazzitelli (1996), for a helium and metal mass fraction of Y=0.28 and Z=0.02 respectively, and for three different Deuterium abundances ($X_D = 1,\ 2,\ 4 \times 10^{-5}$; for our isochrones $X_D = 2 \times 10^{-5}$ was adopted). We refer to D'Antona & Mazzitelli (1997) regarding the details of the different opacities and equation of state chosen at different temperatures. In Figure 2.2, we show some observational isochrones at different ages generated from the D'Antona & Mazzitelli (1997) models, by tuning the (V-I) - T_{eff} relation to match the Pleiades data at an age of 120 Myr, over the range $0.4 < (V-I) < 4.2$ (see Jeffries & Tolley 1998).

2.7 An additional class: the post T Tauri stars

As pointed out in the previous Sections, TTS are very young PMS stars contracting along convective Hayashi tracks, and subsequently approaching the ZAMS along mostly radiative tracks. The intermediate phase between the T Tauri phase and the ZAMS is thought (see Herbig 1978; Walter et al. 1988) to be filled by the post TTS (PTTS) phase, i.e., by older TTS ($> 5 - 10$ Myr) having lost their circumstellar material and evolving towards the ZAMS (on which solar-type stars arrive at an age of about 50 Myr; see Bouvier 1994). PTTS have spectral types in the range late F to M6. They should not show strong emission lines, and reduced or undetectable UV and IR excesses; they are in the process of Li depletion (see Section 3.1.7) but still showing Li I in absorption, strong Ca II in emission, weak Hα (in emission or absorption).

Herbig (1978) estimated that the T Tauri phase of a 1 $M_\odot$ star takes into account of just $\sim 5 - 10\%$ of its PMS lifetime. Hence, one would expect to find 10 times as many PTTS as TTS (i.e., CTTS and WTTS) in a star-forming region. This is contradicted by observations (Herbig 1978 himself found just a few of them) and has been referred to as the PTTS problem. As an example, Martín (1998) found 20 TTS and just 10 PTTS in Scorpius-Centaurus, but argued that the TTS/PTTS ratio may be of order of unity if we take into account that PTTS are in general fainter and harder to identify; Martín et al. (1998) found 53 TTS and just 6 PTTS in ρ Ophiuci; Martín & Magazzú (1999) found 11 TTS and 8 PTTS in Taurus-Auriga (see also Bouvier et al. 1997; Zickgraf et al. 1998). TTS in the Orion star-forming region not related to molecular clouds were detected by Sterzik et al. (1995) and suggested as possible older objects (> 10 Myr), i.e., PTTS. Mamajek, Lawson & Feigelson (1999) found that some of the X-ray detected WTTS around η Cha may be young PTTS (< 20 Myr). More recently, Neuhäuser et al. (2000) found new WTTS in the Corona Australis association: some of them could be classified as PTTS; and Torres et al. (2000) discovered 10 TTS in the Horologium association (at just ~ 60 pc from the Sun), the majority of which are bona-fide PTTS.

Overall, the number of detected PTTS is less than one third the known number of TTS. However, these PTTS are expected to be found in a region only if star formation has been ongoing for about 10 Myr (the typical sound-crossing timescale of a molecular cloud engaged in star formation). The lack of PTTS could be explained by observational limitations, since they do not show strong Hα emission and IR excess, and are therefore difficult to detect by conventional optical methods; or by the fact that they may have been confused with WTTS and ZAMS stars, due to their similar levels of chromospheric activity (see Martín, Magazzú & Rebolo 1992; Pallavicini, Pasquini & Randich 1992). However, recently Palla & Galli (1997) concluded that the PTTS problem is basically a false problem, because the rate at which molecular clouds form stars is not constant with time, but an increasing function of it. In weakly ionized media (such as those of the cloud cores) the timescale leading to gravitational collapse and star formation is determined by ambipolar diffusion. This timescale is similar to the ~ 10 Myr lifetime estimated for molecular clouds, and therefore reduces the probability of finding a large number of older stars in a star-forming region. According to Wichmann et al. (1998), this point of view could lose some validity in the case of low-mass star-forming regions, devoid of OB type members which contribute to their fast disruption through stellar winds and supernovae explosions. The lifetimes for such regions are very uncertain, and could be much larger than the assumed 10 Myr (see Elmegreen 1985), raising the probability of finding a large range of stellar ages.

Whereas CTTS tend to concentrate in groups (Gomez et al. 1993), WTTS and PTTS appear more spread (see Walter at al. 1988; and references given in the previous Section). This is probably due to the fact that PTTS are older and have had time to move away from their parent molecular clouds.

From recent studies of rotational periods, PTTS were found to rotate faster (less than a few days; see for example Wichmann et al. 1998; Bouvier et al. 1997) than WTTS (up to less than two weeks; see Bouvier et al. 1993), confirming the spin-up of the stars approaching the ZAMS predicted by theoretical models. However, as pointed out by Wichmann et al. (1998), this should be treated with caution, since the rotational periods of these PTTS were determined from a spectroscopic follow-up of X-ray sources. Therefore, the results may be biased towards the most X-ray active PTTS, i.e., towards those which are rapid rotators.

2.8 The Lithium criterion

Li I 6707.8 is a strong resonance line (doublet at 6707.76 Å and 6707.91 Å; see Grevesse 1968 and references therein). For Li I, the most abundant isotope ^{7}Li is meant; ^{6}Li is rarer, because it burns at lower temperature and has a shorter lifetime in stellar interiors (see Hayashi 1965).

The initial Li abundance in a star is set to the observed cosmic value (i.e., the value present in pre-stellar material) of logN(Li) $\approx$ 3.3 (on the standard scale where logN(H)=12) found in the interstellar medium (gas and dust; see Hobbs & Pilachowski 1988), in meteorites (Nichiporuk & Moore 1974; Anders & Grevesse 1989; Michaud & Charbonneau 1991), and for Pop I stars (i.e., stars in young open clusters, such as αPer and the Pleiades; see Duncan 1981; Boesgaard & Steigman 1985; Boesgaard 1990). No Li production is expected either during the PMS phase of gravitational contraction, or during the main-sequence phase (although Li is produced in the stellar interiors by $p-p$ chain reactions of H burning, the temperature where it forms is so high that it is immediately recombined with protons, never reaching the stellar surface).

The solar Li abundance is logN= 1.1 ± 0.1 (Grevesse & Sauval 1998), much smaller than the cosmic value, implying that Li was depleted during the Sun's lifetime. The problem is to find out if it was depleted in the PMS phase only, or if the process took place during the main-sequence phase too.

Lithium abundances are high in TTS (see for example Bonsack 1961; Basri, Martín & Bertout 1991; Martín et al. 1994), and similar to the undepleted initial value. Li I is so universally present in young PMS stars that it was chosen as one of the primary criteria for T Tauri identification (see Herbig 1962, 1965; Bodenheimer 1965; D'Antona & Mazzitelli 1984; also Walter et al. 1988; Strom et al. 1989b; Pallavicini et al. 1992).

According to theoretical results based on model atmospheres of Pavlenko et al. (1995), prominent Li I 6707.8 resonance lines are formed in the outer layers of G-M dwarfs at effective temperatures of 5500-3500 K; extending their model to extremely cool stellar photospheres, they found that such lines may even form down to temperatures of 3000-2000 K (at 2000 K most of the Li is present in molecular form).

2.8.1 Li depletion in low-mass stars

The PMS phase in low-mass stars is fully convective (see also Section 2.6). As the star contracts, the radius decreases, the temperature at the center of the star increases (at about 2.5×10^6 K, Bodenheimer 1965) igniting Li burning, according to thermonuclear reactions (^{7}Li,α)^{4}He (i.e., ^{7}Li + ^{1}H $\rightarrow$ 2^{4}He). At the beginning Li is depleted only in the core, because the convective envelope is deeper for cooler stars, so that the temperature at the bottom of the convection zone is not high enough to have a significant amount of Li depletion on the stellar surface. As the temperature increases due to further contraction, mixing processes in the convective envelope (Herbig 1965; Bodenheimer 1965), drive Li from the stellar surface to the interior, and there burnt, causing a surface depletion observationally detectable.

At first Li was thought to be an excellent tracer of the stellar age for all stars, independent of their spectral type, since surface lithium abundance is a decreasing function of the stellar age: it decreases with time as convection dredges Li-depleted material into the lower convection zone where the temperature is hot enough to destroy it. When the temperature at the bottom of the convection zone is $> 3 \times 10^6$ K, ^{9}Be burning starts too. Skumanich (1972) suggested a $t^{-1/2}$ dependence for Li depletion.

However, from observational results, it appears that Li depletion is not only an increasing function of the stellar age, but also a decreasing function of the stellar mass (Wallerstein, Herbig & Conti 1965; Zappala 1972). In other words, Li is more depleted in older and lower-mass stars (see Duncan 1981; Soderblom et al. 1995; Randich et al. 1997).

Some authors suggest that Li depletion may also depend on stellar rotation (see Vauclair et al. 1978; Pinsonneault, Deliyannis & Demarque 1992). This was confirmed observationally by faster rotators showing higher Li abundances, such as those in αPer (Balachandran, Lambert & Stauffer 1988), in the Pleiades (Soderblom et al. 1993) and in the Hyades binaries (Barrado y Navascues & Stauffer 1996). García López, Rebolo & Martín (1994) found that the Li-rotation connection is satisfied in the Pleiades by late-G and early-K stars, but not by late-K and early-M stars. Martín & Claret (1996) showed that the effect of rotation is to lower the temperature at the base of the convection zone, and hence to reduce the efficiency at which Li is depleted in the PMS phase. However, the opposite results were found from theoretical rotating models, predicting more Li depletion with respect to non-rotating models (see Pinsonneault et al. 1990; Sanctos Mendes, D'Antona & Mazzitelli 1997; D'Antona & Mazzitelli 1997). Recently, Ventura et al. (1998) suggested that the presence of a magnetic field might have the effect of decreasing Li depletion too. Therefore it was clear that Li cannot be indiscriminately used as an age indicator. Let us analyse what the situation is at different masses, and for different timescales.

There is little Li depletion in the PMS phase of stars with masses > 1 $M_\odot$ (mid-G stars and earlier; see D'Antona & Mazzitelli 1994; Martín et al. 1994; Martín & Montes 1997; and references therein) because the convection zone is not deep enough (and hence the temperature at the base of the convection zone is not high enough; see Baker 1967). From stellar evolution codes, Pinsonneault et al. (1989) predicted about 0.2 dex of Li depletion during the first 10 Myr for 1.2 $M_\odot$ stars, and Proffitt & Michaud 1989 less than 0.2 dex for stars with masses between 1-2 $M_\odot$. As an example, there are earlier than mid-F main-sequence stars ($M \simeq 1.4$ $M_\odot$) in the Pleiades cluster (some 120 Myr old) showing high Li abundances, logN(Li) ~ 3.2, similar to the primordial value known for Population I (see Soderblom et al. 1993). And no Li depletion was observed in nearby solar-like stars earlier than G5 at different ages by Pasquini, Liu & Pallavicini (1994), and by Favata, Micela & Sciortino (1996).

Conversely, Li burning is expected for stars of lower masses, $M < 1$ $M_\odot$ (later than G4), with more depletion towards later-type stars. In particular, M-type stars burn all their Li before reaching the main-sequence (see Pinsonneault, Kawaler & Demarque 1990; Martín & Montes 1997; Zapatero-Osorio et al. 1996). Li depletion is more effective in LMS, because the convection zone is deeper and mixing processes can drive Li down to the inner layers where the temperature is hot enough to destroy it (see the discussion below about the depletion timescales).

The situation is then reversed again, i.e., no Li depletion, for stars in the brown-dwarf mass range (< 0.065 $M_\odot$; see D'Antona & Mazzitelli 1994; Rebolo, Martín & Magazzú 1992; Magazzú, Martín & Rebolo 1993), because stellar contraction is not able to increase the temperature enough to allow nuclear reactions.

Let us concentrate then on low-mass stars with masses in the range $1.0 < M/M_\odot < 0.065$ (K-type to early-M type), for which Li is depleted in the PMS phase and therefore can be used as an age indicator. From evolutionary tracks of PMS stars, D'Antona & Mazzitelli (1994) showed that PMS Li depletion in stars with masses in the range 0.7-0.2 $M_\odot$ (corresponding to spectral types K0-M5) does not start until an age of 5-10 Myr (with higher ages for the lowest mass stars, because the temperature of the core is not high enough); and that Li is depleted by no more than a factor of 2 by 10 Myr.

2.8.2 A spectroscopic working criterion: the EW(Li)-T_{eff} diagram

A spectroscopic working criterion was dictated by the necessity to find a distance and reddening independent method to define bona-fide PMS stars, instead of deriving ages from theoretical isochrones (which are strongly model dependent; i.e., on the equation of state, opacities and convection models

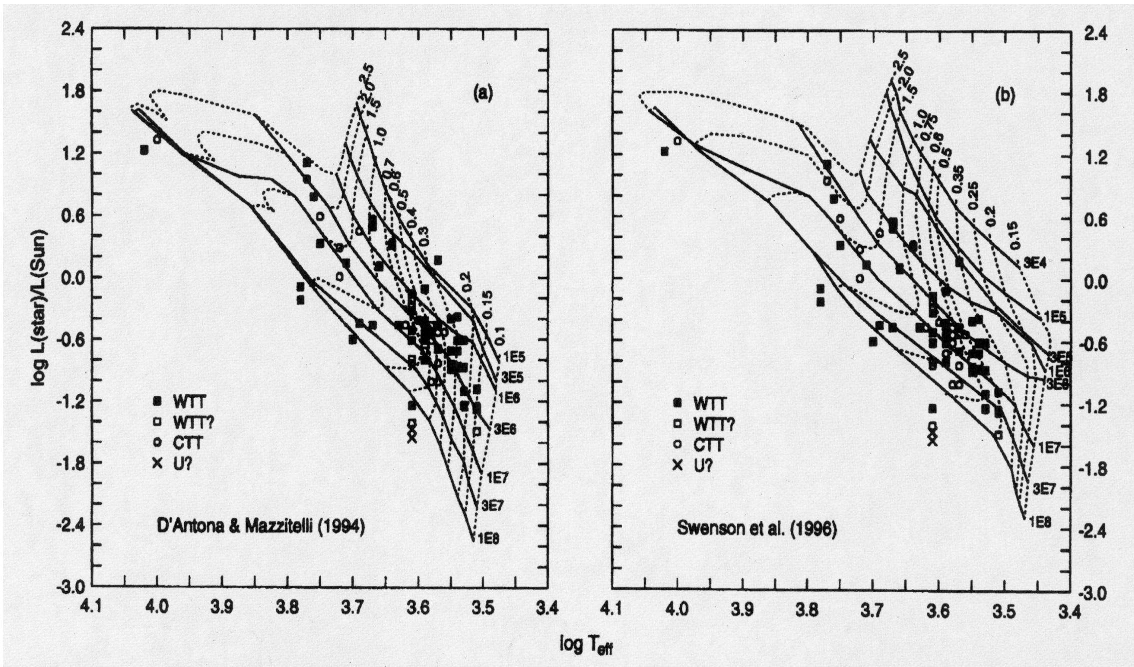

Figure 2.3: Colour-magnitude diagram of the Chamaeleon I stars (from Figure 6 of Lawson, Feigelson & Huenemoerder 1996), with evolutionary tracks and isochrones of (a) D'Antona & Mazzitelli (1994) and (b) Rogers, Swenson & Iglesias (1996; see also references therein). Isochrones (with ages expressed in yr) are shown as solid lines; evolutionary tracks at constant mass (given in solar masses) are shown as dotted lines. The ages inferred by the Rogers, Swenson & Iglesias (1996) are systematically greater by about a factor of two.

adopted; see Section 2.6) plotted on the H-R diagram to assess the youth of the observed objects. As an example, Figure 2.3 shows how different PMS evolutionary tracks may lead to different age estimations.

Bona-fide low-mass PMS can be found by plotting them in an EW(Li) versus T_{eff} diagram (see Figure 2.4): they must fall above the upper envelope for young open clusters (see Martín 1997 and references therein). In other words, they must show Li in excess of that found in the stars of young open clusters having the same spectral type (i.e., effective temperature).

Note that there is some possibility of confusion for stars hotter than about 5250 K, since for these stars Li is not depleted in the PMS phase. Therefore, stars of spectral type F or G and with EW(Li) $>$ 100 mÅ could be ZAMS stars or PMS stars. Wichmann et al. (1996) used a Li equivalent

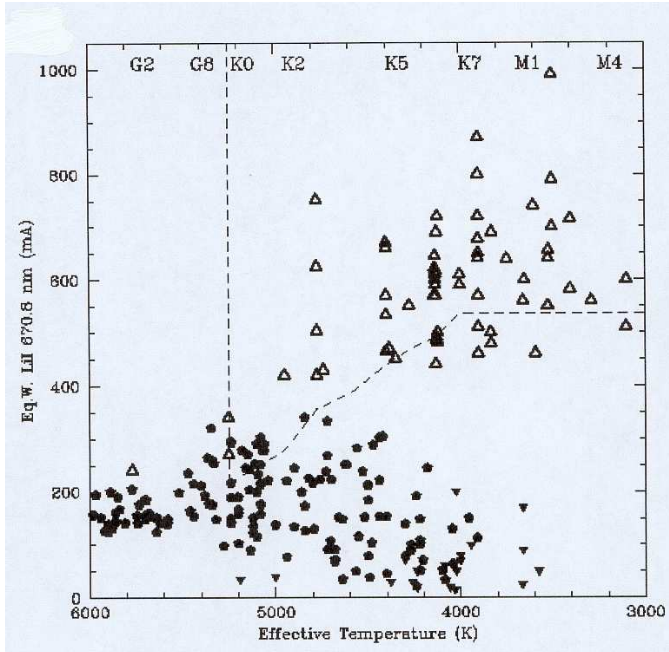

Figure 2.4: The EW(Li I)-T_{eff} diagram proposed by Martín (1997), from his Figure 1. The vertical dashed line represents the temperature limit cutoff of 5250 K for TTS, whereas the diagonal dashed line represents the proposed minimum Li I abundance for TTS for logN(Li)= 2.8. TTS are represented as triangles; as filled triangles if just upper limits for EW(Li) were derived. The pentagons represent the low-mass members of young open clusters some 30-100 Myr old (see references in Martín 1997). The empty region between TTS and the cluster stars (for T_{eff} < 4800 K) is the so-called post T Tauri (PTT) gap.

width limit > 100 mÅ, but, as pointed out by Martín (1997), the same line strength is also shown by PTTS and LMS in young open clusters, some 30-200 Myr old (see also Preibisch & Zinnecker 1999: they suggested 200 < EW(Li)< 350 mÅ). As an example, EWs(Li)∼ 300 mÅ have been measured in some stars belonging to the Pleiades cluster (Soderblom et al. 1993; García López et al. 1994), at 120 Myr old, and therefore much older than TTS; whereas EW(Li)< 100 mÅ in stars of the ∼ 600 Myr old Hyades cluster (Thorburn et al. 1993). In other words, Li can identify PMS K and M type stars, but only young ($< 100 - 200$ Myr) G and F stars.

From recent PMS evolutionary tracks (see for example D'Antona & Mazzitelli 1994; Martín & Claret 1996), the convenient upper limit to T_{eff} of a TTS is put to 5250 K, corresponding to spectral type K0 (see Martín 1997). This is the limit beyond which we have hotter stars, which do not deplete

Li I in an efficient way during their PMS evolutionary phase, so that the Li criterion cannot be applied to discriminate PMS objects, unless additional membership criteria are also satisfied.

In the literature there are different T_{eff}-spectral type calibration scales (Cohen & Kuhi 1979; Bessell 1979; de Jager & Nieuwenhuijzen 1987; Bessell 1991), with temperatures which may differ by several hundreds of Kelvin in certain spectral ranges (see discussion in Martín et al. 1994). For example, the T_{eff}-spectral type scale adopted by Cohen & Kuhi (1979) was found by Walter et al. (1994) to give temperatures up to $200 - 400$ K systematically hotter for G and K (V) stars. They found that the temperatures derived from intrinsic colours of G and K stars are in agreement with those of subgiants (IV), whereas those of M stars with those of dwarfs (V), a behavior already noted by Herbig (1977). Similarly, the Bessell (1979) scale has been demonstrated by Stauffer, Hartmann & Barrado y Navascues (1995) to underestimate the ages and masses of M stars in the H-R diagram determined from isochrones (D'Antona & Mazzitelli 1994) overplotted. The same problem is found with the de Jager & Nieuwenhuijzen (1987) scale, because it is similar to the Bessell scale. Martín (1997) takes the highest T_{eff} value for each spectral type among all those available from literature (see Table 6 in Martín et al. 1994). Note that the classification scheme proposed by Martín (1997) is distance and reddening independent, since it is based on the measurement of three spectroscopic observables: spectral type, EW(Li I), and EW(Hα) (the latter is used to distinguish CTTS, see Section 2.9).

The minimum Li I EW values plotted in Figure 2.4 depend on the effective temperature, and proposed values are 215 mÅ for K0-type stars, 280 mÅ for K2, 440 mÅ for K5, 490 mÅ for K7, and a constant value of 540 mÅ for stars with spectral types later than K7 (see Martín 1998). This last minimum value is assumed constant for stars with $T_{eff} < 4000$ K because TiO absorption bands depress the continuum at cooler temperatures, with the consequence that the curve of growth becomes unreliable.

The minimum values of the Li I 6708 Å EW correspond roughly to the Li isoabundance line of logN(Li)=2.8, adopting the non-LTE curves of growth of Martín et al. (1994). All PMS stars younger than 5 Myr (D'Antona & Mazzitelli 1994) are expected to have depleted Li by no more than a factor of 2 from an initial value of logN(Li)=3.1.

Note that measurement of the Li I 6708 line is difficult if low- to mid-resolution spectra are used, because the EW can be overestimated and erroneously lead to a PMS classification, where actually the stars are: PTTS, showing EW(Li) with values intermediate between those seen in WTTS and stars in young open clusters (and falling in the so-called post T Tauri gap of Martín 1997; see Figure 2.4 and Section 2.9); or very young active foreground LMS, some 100 Myr old (i.e., older ZAMS stars, belonging to open clusters similar to the Pleiades). According to Briceño et al. (1997), if star formation in the solar neighborhood proceeded at an about constant rate in the last 100 Myr, X-ray surveys would account for many ZAMS stars, which might be erroneously classified as WTTS if EW(Li) were not measured with high-resolution spectroscopy. A resolution of ≤ 1 Å is necessary to have reliable equivalent widths measurements (see Neuhäuser et al. 1997).

The problem of the Li I line strength overestimation arises from blending with nearby Fe I lines (at $\lambda\lambda$ 6703, 6705, 6707, 6710 and 6713). This effect is more pronounced for spectral types earlier than K6, where the strength of Fe lines starts to increase towards earlier spectral types and instead tend to decrease towards late K-type stars; M type stars are not affected (Walter et al. 1988; Covino et al. 1997; Zickgraf et al. 1998; Alcalá et al. 2000).

2.9 How to distinguish among CTTS, WTTS and PTTS

CTTS can be distinguished from WTTS by means of the different spectroscopic properties observed (see also Sections 2.4 and 2.5). CTTS have a composite spectrum: a part due to non-stellar sources (the dominant one) characterized by non-photospheric UV and IR continuum excesses, and forbidden emission lines; and a part due to the stellar photosphere. WTTS have instead "normal" photospheres and atmospheres: their spectrum is dominated by the stellar photosphere, whereas the contribution from non-stellar sources is negligible.

CTTS have a strong Hα line in emission, so strong that it cannot be explained by means of stellar chromospheric activity (as in WTTS; see Houdebine & Stempels 1997): it is explained by means of T Tauri winds, active accretion discs (Appenzeller & Mundt 1989), or magnetic accretion columns (Hartmann, Hewett & Calvet 1994). The Li I line (obviously in absorption) instead can have an equivalent width apparently smaller, because of optical veiling (Basri, Martín & Bertout 1991; Magazzú et al. 1992) by a strong blue continuum (the absorption lines are weaker than those of m-s stars of the same spectral-type). This blue veiling was originally explained as an emission component from the boundary layers between the accretion disc and the star (see Lynden-Bell & Pringle 1974;

Kenyon & Hartmann 1987; Bertout et al. 1988), or due to an active chromosphere filling-in the absorption lines produced in the photosphere (Calvet, Basri & Kuhi 1984). In the past few years emission from accretion columns confined by magnetic field lines (magnetically channeled material) has been offered as a more likely explanation (Hartmann et al. 1994; Calvet & Gullbring 1998).

Therefore, CTTS are immediately identified by means of their very broad and strong Hα emission, with an equivalent width larger than a certain minimum value which was initially defined at 5 Å (Herbig 1962; Bastian et al. 1983; Herbig & Bell 1988) by observational results, in order to exclude dMe stars. Other authors used 10 Å (Appenzeller & Mundt 1989; Strom et al. 1989a) or 15 Å (Neuhäuser et al. 1995a). The classification is therefore arbitrary. From recent studies, it resulted that Hα emission above the photospheric continuum depends on spectral type, binarity, flare activity, etc.

Conservative values proposed by Martín (1997; see also references therein) to classify a TTS as CTTS, instead of a WTTS, are

* EW(Hα) $>$ 5 Å for K-type stars (chromospherically active single and binary stars do not show higher values)

* EW(Hα) $\geq$ 10 Å for early-M (M0-M2) type stars (M stars in young open clusters and field stars can show values of 5-10 Å, so the limit needed to be increased)

* EW(Hα) $\geq$ 20 Å for late-M type stars

Because these are conservative values, it is possible that some CTTS with very low-mass accretion rates will be classified as WTTS: Muzerolle, Calvet & Hartmann (2001) have recently shown that there is a small or negligible emission in the cases with low accretion rates, i.e., less than about 10^{-8} $M_\odot$ yr^{-1}.

WTTS and PTTS must pass the lithium test first, in order to be confirmed as truly young, PMS objects. Then they can be distinguished spectroscopically in the EW(Li) versus T_{eff} diagram of Figure 2.4: they both lie above the upper envelope for young open clusters, but occupy different regions, with the PTTS falling in the PTT gap. Note that PTTS can be distinguished from the WTTS in an unambiguous way if and only if they have temperatures cooler than 4800 K (i.e., spectral type later than about K2), where the so-called PTT gap is well defined - at hotter T_{eff} they can be confused as both WTTS and ZAMS stars.

2.10 Testing the form of the IMF

One of the major issues in star formation studies is to understand how stars form, and if low-mass stars follow the mass function for the field stars (see Miller & Scalo 1979). The number of low-mass stars may be predicted from the number of high-mass stars assuming a universal initial mass function (IMF). To test the form of the IMF (and hence its universal validity), it is important to compare the predicted number of low-mass stars with the number estimated from observations.

Miller & Scalo (1979) defined the field star IMF (ξ (logM)), as the total number of field stars that have ever formed, per square pc and unit logarithmic mass. The IMF is valid for stellar masses at birth, since it is strongly affected by mass transfer and mass loss during stellar evolution. It is well approximated by a half-Gaussian distribution in log M (i.e., lognormal distribution), and its slope is defined by $\Gamma = dlog\,\xi(logM)/dlogM = -(1 + logM)$.

If the IMF has the same form in different star-forming regions, one may conclude that there is a unique process which is responsible for the fragmentation of the molecular cloud which always happen in the same way.

The IMF of an association is well defined for HMS (upper-end IMF), but not so well for LMS (lower-end IMF) because of observational problems (LMS are difficult to detect and to separate from the field stars). Under the assumption of a universal IMF, the number of LMS with masses in the range $(m_1 - m_2)$ (with $m_2 > m_1$), N$(m_1 - m_2)$, may then be predicted from the known number of HMS with masses larger than M_{min}, N$(> M_{min})$, using the field star IMF; i.e, from the relation

$$N(m_1 - m_2) = N(> M_{min}) \frac{F(> m_1) - F(> m_2)}{F(> M_{min})} \tag{2.1}$$

where F is the fraction of stars with a mass larger than the mass specified. F has the form $F(> M) = N(> M)/N(> 0.1)$, where N(> 0.1) gives the total number of stars in the IMF per square pc, since 0.1 $M_\odot$ is the minimum mass of main-sequence stars used in the Miller & Scalo (1979) investigation; F values are listed in their Table 9.

The difference between the predicted number and the observed number of LMS, may tell us how complete is the census of the low-mass stellar population in the studied star-forming region, under the assumption of a universal (log-normal) IMF. On the other hand, agreement between the two suggests a universal form for the IMF.

Miller & Scalo (1979) showed that the IMF of the Orion OB1 association is in agreement with the field star IMF for masses larger than 2.5 $M_{\odot}$. Under the assumption that the IMF in OB associations is similar to the Miller-Scalo (1979) IMF, the majority of low-mass stars in the solar neighborhood are thought to have formed in OB associations, rather than T associations (see discussion in Chapter 1). Indeed recent observational results seem to be in favour of a universal IMF, both in OB associations and in T associations. In particular, Walter et al. (1994) showed that LMS in the Upper Scorpius OB association form in number similar to that predicted from the field stars IMF (for masses > 0.3 $M_{\odot}$); this was later confirmed by Preibisch & Zinnecker (1999), and recently by Preibisch, Guenther & Zinnecker (2001). The same conclusion was found by Hillenbrand (1997) for stars in the Orion OB association, although there appear to be some differences for stars around 1 $M_{\odot}$. Naylor & Fabian (1999) showed that the IMF in the Cep OB3 association is consistent with that of the field stars for masses in the range 0.3 $M_{\odot} < M < 3$ $M_{\odot}$. Walter & Boyd (1991) studied star formation in the Taurus-Auriga T association and concluded that there is no compelling evidence for the IMF to be different from the field IMF (for masses > 0.2 $M_{\odot}$). The mass distribution for the Chamaeleon T association was found by Alcalá et al. (1997) to be consistent with the field IMF (for masses in the range 0.5 $M_{\odot} < M < 2.5$ $M_{\odot}$). Recently, Dolan & Mathieu (2001) found that the IMF in λ-Ori varies across the star-forming region, but globally it may match the field IMF. Note, however that the majority of these studies were performed on X-ray selected PMS samples (EO, ROSAT and RASS) and biased towards specific regions or flux-limited (see Section 2.5), except from the study of Hillenbrand (1997) which is based on an optical database, and that of Walter & Boyd (1991) which is based on kinematic data (radial velocities and proper motions) and spectroscopic parallaxes.

2.11 How to find low-mass PMS stars in OB associations

In the past, spectroscopic surveys and objective-prism Hα surveys were the tool to identify young low-mass PMS stars in OB associations; these surveys were then followed by X-ray surveys (see Section 2.5). Whereas Hα surveys are sensitive to CTTS, which show the highest Hα emission, X-ray surveys are mostly sensitive to WTTS, which are stronger X-ray emitters than CTTS (see discussion in Section 2.5). X-ray surveys are coupled with an optical and spectroscopic follow-up to confirm the PMS nature of the objects (PMS stars classified by spectroscopic study of Li I lines lie well above the main-sequence in a colour-magnitude diagram; see for example Preibisch & Zinnecker 1999).

Walter et al. (2000) proposed 3 different stages to have a complete sample of low-mass PMS stars. These are: an X-ray survey (LMS have an X-ray luminosity which can be up to 10^5 times the X-ray luminosity of old m-s stars of the same spectral type); then spectroscopy (Li I is un-depleted in young objects); and finally a wide field imaging photometry to extend the PMS locus, in the V versus (V-I) colour-magnitude diagram, to fainter objects than those actually identifiable by X-ray selection.

However, although X-ray surveys have proven to be a convenient method to find LMS in associations, caution must be taken in deducing conclusions about the properties of an X-ray selected sample because of incompleteness. Wolk (1996) found X-ray selected PMS stars sharing the same position in the CMD of non X-ray selected stars, and therefore demonstrated the presence of less magnetically active PMS stars. This implies that an X-ray PMS sample can be incomplete and lead to unrepresentative conclusions about the number and average level of X-ray emission from PMS stars, the rotation rates, the IMF, the WTTS/CTTS ratio and the circumstellar disc lifetime (see the following Sections). Furthermore, X-ray selected PMS stars are biased against CTTS, or WTTS that retained discs for a long time (see Section 2.5); and cannot necessarily be distinguished from ZAMS stars - which are also X-ray active (Briceño et al. 1997; see also Section 2.8.2). This may partly explain the widely spread WTTS population claimed to be found around some star forming regions (see Section 2.5 and reference therein). Finally, since X-ray emission is thought to be a decreasing function of the stellar age, an X-ray selected sample may be biased towards younger stars ($L_x \sim t^{-0.6}$; see Feigelson & Kriss 1989).

Bona-fide PMS stars must pass kinematic criteria first, to unambiguously assess membership, the radial velocity dispersion in an association being of order 1-2 km/s (see Section 2.5). Objects which are members of the same stellar cluster must show the same radial velocity (within the errors), with respect to the mean radial velocity of known members of the star-forming region studied, and to that of the associated molecular cloud (see Herbig 1977). This build up a compelling evidence that the objects are kinematic members of the same stellar cluster and kinematically associated with the molecular cloud.

We therefore propose the following strategy (which was adopted in this thesis and proven to be very successful) to select bona-fide PMS stars and confirm their nature.

1) CCD optical photometry of the interesting region in (U)BVI colours, and subsequent optical selection in the V versus (V-I) colour-magnitude diagram of PMS candidates for a spectroscopic follow-up.

2) Determination of the radial velocity for the objects in the optically selected PMS sample in order to find association members.

3) Confirmation of PMS status (where possible) thanks to Li I EW measurements (Li test) or large Hα emission in order to classify these objects as WTTS and CTTS.

Optical selection in this manner ensures that the resulting samples are free from the biases present in X-ray selected samples.

2.12 On the fraction of WTTS/CTTS

The value for the WTTS/CTTS ratio presented in the literature changes significantly in the different star-forming regions studied. In T associations it is in the range 1-13. In particular, WTTS/CTTS values from 1 (central region) to > 8 (wider region), 2-8, 4 and 13 were found respectively in Taurus-Auriga (Neuhäuser et al. 1995b; Hartmann et al. 1991), Chamaeleon (Feigelson et al. 1993; Alcalá et al. 1995), ρ Ophiuci (Martín et al. 1998) and Lupus (Krautter et al. 1997). All these studies are based on an optical spectroscopic follow-up of X-ray selected samples (which are biased against CTTS), in order to classify the PMS objects on the basis of the strength of their Hα emission lines, except for the study of Hartmann et al. (1991) which is based on a proper motion selected sample. A bias against CTTS implies that the WTTS/CTTS is an upper limit only.

There are not so many examples regarding the ratio of TTS in OB associations. To our knowledge, the only two for which the fraction of CTTS on WTTS has been determined (on the basis of the strength of their Hα emission lines) are the Orion and Upper-Scorpius OB associations. In these regions, the low-mass PMS populations have about the same age ($\sim 6-7$ Myr and $\sim 5 Myr$ respectively). From an optically selected sample followed by optical spectroscopy, Dolan & Mathieu (1999)

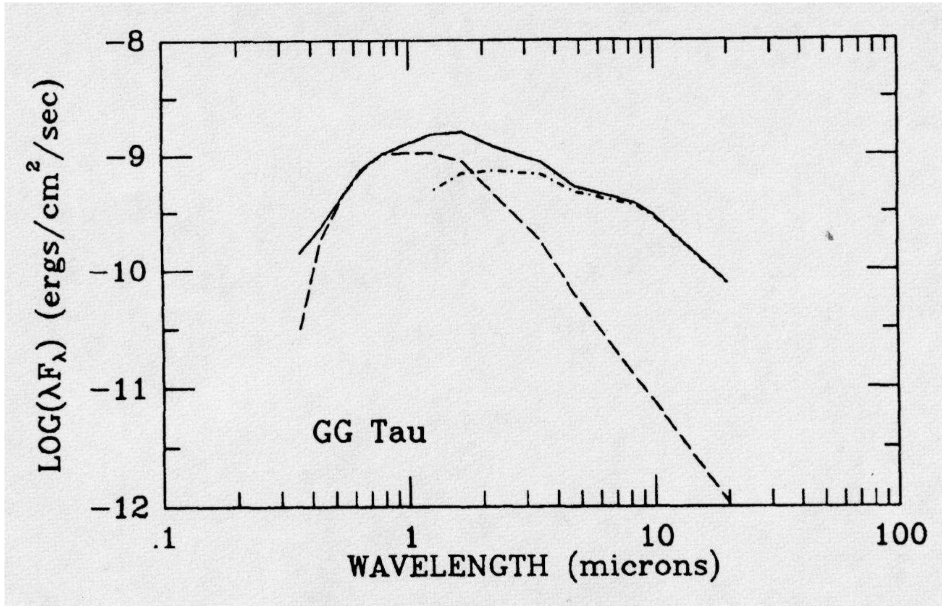

Figure 2.5: Broad-band spectral energy distribution (solid line) observed for the TTS GG Tau, corrected for interstellar extinction (from Figure 1 of Rydgren & Zak 1987). The dashed line represents the fitted photospheric spectral energy distribution (black body; i.e., that expected for a star without a disc), whereas the dot-dashed line is the IR excess component which must be added to the fit so to find the observed energy distribution.

found a value of 17 in λ-Ori. Recently, Dolan & Mathieu (2001) found a value of 35 in the central region of λ-Ori, from an optical photometric survey followed up by multiobject spectroscopy. In Upp-Sco, Walter et al. (1994) found a WTTS/CTTS ratio of 14 from an X-ray selected (EO) sample of PMS stars, together with optical spectroscopic and optical and NIR photometric follow-up. Preibisch & Zinnecker (1999) found a value of 24 (just 4 CTTS retaining their discs on 94 WTTS) from an X-ray selected sample (RASS and EO) of stars in the same region, followed by optical spectroscopy and photometry; a 2dF optical spectroscopic follow-up has recently revealed 98 new low-mass PMS stars in a 6 square degree field in the association, with a WTTS/CTTS of 9 (Preibisch et al. 2001). Note however that X-ray selected samples are incomplete, for the reasons given in Section 2.11, and biased against CTTS.

It is important to get the numbers of WTTS and CTTS right, since from isochronal ages derived for the PMS objects we then have an idea of the dissipation timescales of circumstellar discs. If the CTTS/WTTS ratio is different for associations of similar age, then we might conclude that the local environment has affected low-mass star formation, possibly through stellar winds and ionizing radiation from the high-mass members of the association, or previous episodes of supernovae explosions which may have truncated mass accretion and cleared the discs.

2.13 Disc diagnostics

The presence of circumstellar accretion discs can be revealed by the detection of strong Balmer emission lines, causing the so-called optical veiling (masking out the absorption lines). This is produced in the hot boundary layer between the accretion disc and the star, and it is found to be correlated especially to Hα emission (see Hartigan et al. 1990). In other words, strong Hα emission is associated with circumstellar material accreted from the disc to the stellar surface (see Muzerolle, Calvet & Hartmann 1998; Muzerolle, Hartmann & Calvet 1998). However, the determination of Hα EW may yield complicated results for stars in regions of high sky Hα nebulosity. Its mere detection is not considered an unambiguous method to identify discs, since Hα emission is not always indicative of PMS objects: not all PMS stars show Hα in emission (see for example Walter et al. 1988); and, by contrast, dKe and dMe stars (active main-sequence stars) may show an Hα EW up to 5 Å (see Stauffer & Hartmann 1986). Conservative values according to different spectral types have been then proposed by Martín (1997) (see Section 2.9): those PMS stars satisfying these conditions can be considered objects surrounded by an accretion disc. However, although subject to these requirements, the frequency of Hα emitting objects cannot be compared reliably with other disc frequencies in the literature for which other indicators were used.

The presence of circumstellar gas and/or dust discs can be also revealed through spectral energy distributions (see for example Adams & Shu 1986; Lada et al. 1987; Bertout et al. 1988; Beckwith et al. 1990). One of the distinctive features indicative of the presence of an optically thick circumstellar disc around PMS stars is a NIR (2.2 μm) excess (see Figure 2.5). This is explained as the result of thermal emission of circumstellar dust grains (see Kenyon & Hartmann 1987; Bertout et al. 1988) close to the surface of the star (r$<$ 0.1 AU). The NIR excess is of order few tenths of a magnitude. From a sample of eight TTS and one Herbig Be star, Rydgren & Zak (1987) estimated the average excess emission to be about 40-80% of the total, a contribution too large to be explained solely by

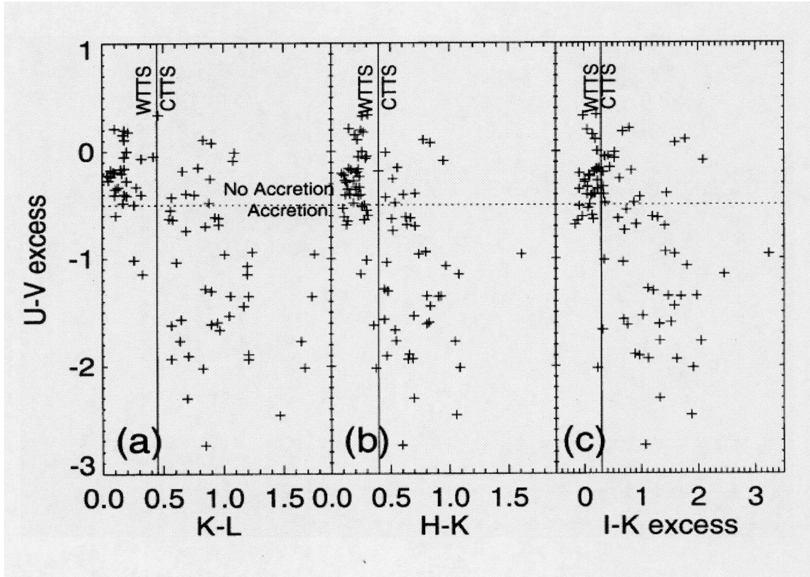

Figure 2.6: Comparison of IR and UV excesses (disc indicators) from Figure 25 of Rebull et al. (2000), based on optical and IR data from Taurus-Auriga found by Kenyon & Hartmann (1995). The dashed horizontal line at -0.5 is the UV excess limit, and separates the locii where non accreting and accreting stars tend to fall. WTTS and CTTS occupy two different locii, separated by the vertical vertical line, showing that stars with IR excess greater than 0.3 (a), 0.2 (b) and 0.3 (c) respectively in (K-L), (H-K) and (I-K) are good disc candidates.

means of reprocessed stellar light in a thin disc ($\sim$ 25 %; see Adams & Shu 1986) or a Keplerian accretion disc (see Lynden-Bell & Pringle 1974), suggesting instead an accretion disc with an intrinsic luminosity.

Strom et al. (1989a) studied a sample of 83 solar-type PMS stars in the Taurus-Auriga association and found that the $\sim$ 83% of the CTTS and $\sim$ 28% of the WTTS in the sample show a K excess larger than 0.1 mag, and suggesting the presence of heated dust in the inner regions (r$<$ 0.1 AU) of a disc. However, the WTTS are not accreting material from the disc, at least above a few times 10^{-9} $M_{\odot}$ yr^{-1} (see Bertout 1989), because no spectroscopic evidence of Balmer emission lines was found (see Basri & Bertout 1989). Hence the small infrared excess observed can be explained purely by means of reprocessed stellar light (with IR continuum data alone, mass accretion rates smaller than few times 10^{-8} $M_{\odot}$ yr^{-1} cannot be detected). This is not a problem in high-mass stars, where the effect of a cold disc can be disentangled from that of a hot photosphere; but IR excess can be ambiguous for low-mass stars (low contrast between the disc and the cold photosphere), since it is not always clear how to distinguish an excess due to an accretion disc from that produced by a purely reprocessing disc which absorbs the stellar light and re-emits it at IR wavelengths. Therefore, as suggested by Basri & Bertout (1989), one ideally looks for both IR and UV (see below) excesses. Furthermore, small NIR excesses (less than 0.1 mag in K) are not expected from an optically thick material, but they could be due to an optically thin circumstellar disc, as well as to starspots or the presence of a cool companion (see for example Wolk & Walter 1996).

UV continuum excess is interpreted as the result of interaction between an active accretion disc and its slowly (i.e., less than the breakup velocity) rotating star (see Kenyon & Hartmann 1987; Basri & Bertout 1989). It is defined as the difference between the de-reddened (U-V) colours and the expected values according to their spectral types.

Rebull et al. (2000) have compared two disc indicators, plotting the UV excess versus the IR excess for about 80 stars (with spectral type K0-M4) in the Taurus-Auriga star-forming region, for which optical UVI and IR HKL colours were known from Kenyon & Hartmann (1995). They show that stars undergoing active mass accretion are characterized by both excesses, with WTTS and CTTS occupying two different locii, separated by a vertical line (see Figure 2.6). The dashed horizontal line at -0.5 (UV excess limit) separates the locii where non accreting and accreting stars tend to fall. All the stars with IR excess greater than ~ 0.3 mag are good disc candidates.

Finally, further evidence for the presence of circumstellar discs may be provided by optical polarization studies (see for example Elsasser & Staude 1978), mapping in CO lines (Sargent & Beckwith 1987), direct millimetre emission with radio interferometers (Dutrey, Guilloteau & Simon 1994), optical emission with the Hubble Space Telescope (HST; see for example Burrows et al. 1996 and references in Section 2.14), near-IR adaptive optics imaging (Stapelfeldt et al. 1998), mid-IR imaging (Grasdalen et al. 1984; Beckwith et al. 1989), and interferometric observations at submillimetre wavelengths (to detect circumstellar discs around protostellar objects; Ward-Thompson, André & Lay 2000).

2.14 Disc survival times and the formation of planetary systems

After having analysed how circumstellar discs can be found by means of different techniques, some questions immediately arise regarding: what are the causes of disc loss; how long do discs survive before being cleared; what is the disc frequency as a function of age; and is there a unique circumstellar disc lifetime; if not, what conditions influence disc lifetimes.

There are several possibilities to explain the loss of a circumstellar disc (see Walter et al. 1988). A CTTS can lose its disc if it is lead out the natal cloud by a peculiar velocity (RATTS, runaway TTS); if it formed on the periphery of a cloud which then collapsed gravitationally; if it is a close binary and therefore orbital shrinkage causes the ejection of the disc; or if there are strong winds or molecular outflows, or the growing in size of disc grains. But the most exciting possibility is that disc loss is due to planetary formation, since planets are likely to accrete out of the circumstellar material. Therefore planets should form from CTTS (Lin & Papaloizou 1985; Hayashi, Nakazawa and Nakagawa 1985) and the disc time scale should be the time for the optically thick disc to evolve to an optically thin one, followed by a complete evaporation.

Johnstone et al. (1998) proposed a model of photoevaporation of circumstellar discs by an external source of UV radiation produced by nearby (less than 1pc) hot stars (O, B, and Wolf-Rayet stars for example): UV photons heat the surfaces of the LMS circumstellar discs, producing thermal winds and material loss. They show that this process is very quick for the Orion proplyds (i.e., externally ionized protoplanetary discs; see O'Dell, Wen & Hu 1993), the disc destruction time scale being of about 10^6 yr. This value is in agreement with the $10^5 - 10^6$ evaporation timescale recently proposed from theoretical models by Störzer & Hollenbach (1999), applied to discs detected by the HST in the Orion Nebula (see also O'Dell & Wen 1994; McCaughrean & O'Dell 1996; O'Dell & Wong 1996; Bally et al. 1998). The flattened distributions of dust and ionized envelopes are seen silhouetted against the background nebular emission, or detected thanks to radiation emitted in the outer disc regions which are exposed directly to the ionizing radiation of the neighboring OB stars. From a mid-IR imaging survey in the region, Robberto, Beckwith & Herbst (1999) found that $\sim 3/4$ of the Orion members (see Hillenbrand 1997) have thermal emission well above the photospheric flux, indicative of discs. However, just 2 out of 47 sources were found to have an active disc, i.e., a circumstellar accretion disc, very likely the direct consequence of the hostile environment in the Orion Nebula. This has the important implication that planets can form around low-mass stars (CTTS) in an hostile environment such as that characterized by high-mass stars, only if they can accumulate on time scales shorter than the evaporation timescale.

Recently, Dolan & Mathieu (2001) found 266 PMS stars in 8 deg^2 in λ-Ori: the stellar density is larger in the center of the star-forming region, where the OB stars are concentrated, but it is present up to about 20 pc away. There are just 2 CTTS out of 72 PMS stars in the central region, whereas the majority of Hα emitting objects appear at a radius of $\sim 2.4^{\circ}$ from λ-Ori (at the estimated distance of 450 pc, this corresponds to about 20 pc). Since stellar age cannot explain this difference, they attribute the paucity of accretion discs in the central region to photoevaporation from the OB stars (and perhaps to a supernova explosion).

From IR (2.2 and 10 μm) excess radiation, Skrutskie et al. (1990) found that about 50% of the low-mass stars in Taurus-Auriga retain their discs up to 3 Myr, but that less than 10% retain a disc by $\sim$ 10 Myr.

Strom et al. (1989a) studied a sample of 83 solar-type PMS stars in the Taurus-Auriga region, comprising 36 optically selected TTS with strong Hα emission (EW$>$ 10 Å) and 47 WTTS (EW$<$ 10 Å). They found that 30/36 CTTS and 13/47 WTTS show significant NIR excesses attributable to circumstellar discs. Furthermore, $\sim$ 60% of the PMS stars showed evidence of a disc at ages less than 3 Myr, whereas just 10% possessed discs at ages larger than 10 Myr. Under the assumption that all solar-type PMS stars are initially surrounded by discs, this would give a range for the circumstellar disc lifetimes of about $t \leq 3 - 10$ Myr, constraining the time available for the formation of planets.

Walter et al. (1994) found a value of less than 2 Myr for the disc lifetimes of stars in Upper-Scorpius, from an optical spectroscopic plus optical and NIR photometric follow-up of an X-ray selected sample (which is biased against CTTS, and may be incomplete, leading to unrepresentative results; see Section 2.11). Walter at al. (1988) derived a similar value from optical spectra plus optical and NIR colours in the Taurus-Auriga association.

Accretion disc survival times of 3 Myr or more are required by theoretical rotational models (Bouvier, Forestini & Allain 1997). However, some WTTS have been found to be younger than some CTTS, with ages in the range 0.3×10^{6} yr up to few 10^{8} yr (see Walter et al. 1988; Bertout 1989; Appenzeller & Mundt 1989; Lawson et al. 1996); and CTTS with ages in the range $\sim 10^{5}$ yr (see Basri & Bertout 1989; Andrè & Montmerle 1994; Wolk & Walter 1996) up to about 30 Myr (Lawson et al. 1996). This suggests that some TTS have lost their discs well before the typical deduced values of few Myr, and that others may retain discs up to $\sim$ 30 Myr (see also below, and Figure 2.7).

Preibisch & Zinnecker (1999) found that just less than 10% of the PMS population in Upper Scorpius have discs at an age of about 5 Myr, whereas in other star forming regions is more than

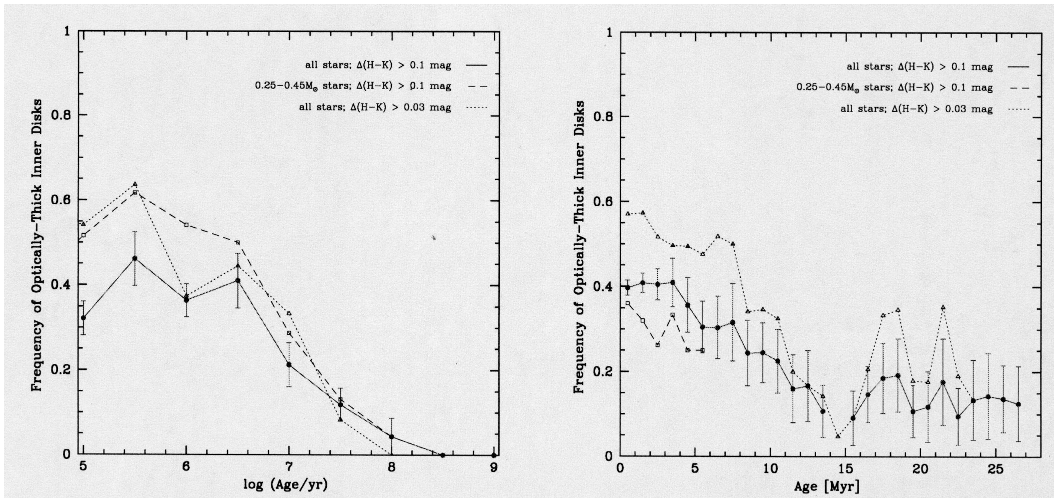

Figure 2.7: Inner disc frequency versus stellar age for $\sim$ 2550 stars in nearby star-forming regions, for which the IR excess (H-K) is known (from Figure 2 of Hillenbrand & Meyer 1999).

three times higher (see Section 2.12). Therefore the authors suggest as a possible explanation the faster dissipation of circumstellar discs caused by strong winds and ionizing radiation generated by the early-type stars in the OB association. This picture was previously suggested by Walter et al. (1994), who hypothesised that the environment may affect the circumstellar disc timescale of low-mass PMS stars. And proposed by Dolan & Mathieu (1999) for PMS stars around the O-star, λ-Ori.

Figure 2.7 shows the disc frequency as a function of age for more than 2500 low-mass stars in nearby star-forming regions, with optical and NIR photometric and spectroscopic data (from Figure 2 of Hillenbrand & Meyer 1999). It shows that there is a large dispersion in accretion disc lifetimes, with very young (< 1 Myr) stars which have already lost their discs, and older (> 10 My) stars still retaining their inner accretion disc. However, there is a general trend of a decreasing number of stars with disc towards larger ages, with a minimum at about 15 Myr (although there are few older objects still showing discs).

Note that dust discs do not contain gas, and dust particles survive for less than 1 Myr (Habing et al. 1999): the smaller ones are blown out of the system by radiation pressure, while the larger ones lose orbital momentum as effect of interaction with stellar radiation, spiralling along lower orbits and eventually being vaporised (Poynting-Robertson effect). But there are discs detected by the Infrared Space Observatory around main-sequence stars some 400 Myr old: there must be a mechanism for a continuous supply of dust.

Recently Haisch, Lada & Lada (2001) presented a JHKL study of young stars in the IC 348 cluster, some 2-3 Myr old, a relatively low-mass start forming region, in which the highest mass star is of spectral type B5 V. They find that JHK colours give a lower disc fraction than JHKL. From L-band images they determine that the disc fraction ($\sim$ 60%) of objects in the cluster is the same (within the errors) of that for objects in Taurus of similar ages, suggesting that in clusters devoid of O type stars the disc lifetime is independent of the environment. Surprisingly, 59% of their WTTS do appear to have discs, therefore confirming that WTTS are not necessarily disc-less (see Brandner et al. 2000). On the other hand, they find that the circumstellar disc fraction is dependent on spectral type: PMS stars earlier than G do not have discs, whereas the highest percentage is found in M stars. Therefore they suggest that the circumstellar disc timescale is not only a function of the time but also of the mass: discs around massive stars dissipate quicker.

Haisch, Lada & Lada (2001b) reported the results of the L-band survey of the clusters NGC 2264, NGC 2362 and NGC 1960 (of intermediate age, 2.5-30 Myr), using JHKL colours to obtain a census of the cluster objects with a circumstellar disc. They found disc fractions of 52 %, 12 % and 3 % respectively. Coupled with previous studies on other clusters, i.e, NGC 2024 (Haisch et al. 2001), Trapezium (Lada et al. 2000) and IC 348 (Haisch, Lada & Lada 2001), the results suggest that the disc fraction in a cluster is initially very high ($>$ 80 %), and rapidly decreases as the cluster age increases; that about half the stars in the cluster lose their discs in less than about 3 Myr; and finally that all the cluster members lose their discs in about 6 Myr.

3 The discovery of a low-mass PMS cluster in Cep OB3b

3.1 Introduction

3.1.1 Distance to Cep OB3

Cepheus OB3 is a very young association at about 800 pc from the Sun (Garrison 1970; Moreno-Corral et al. 1993), with galactic coordinates l^{II} = 109.3° - 111.7° and b^{II} = 2.4° - 3.7° (Blaauw 1964). It covers a region on the sky from 22^h46^m to 23^h10^m in right ascension, and from +61° to +64° in declination. Its first distance estimate of 730 pc was given by Johnson (1957), who also presented a colour-magnitude diagram (CMD) for 45 possible members of the association from unpublished data. Table 3.1 lists distance estimates to the association presented in the literature, derived according to different methods: i.e., by main sequence fitting in intrinsic colour-magnitudes diagrams (msfCMD), or in Hertzsprung-Russell diagrams (msfHR); and by averaging the distance modulus value found to individual members of the association (av). We refer to Table 3.7 in Section 3.1.4 about our adopted mean distance value.

distance (pc)	references	method used
725 – 730	Johnson (1957); Blaauw, Hiltner & Johnson (1959); Garmany & Stencel (1992)	msfCMD
740 ± 170	Crawford & Barnes (1970)	av, (a)
770 ± 50	Clausen & Gimenéz (1991)	(b)
800	Garrison (1970)	msfHR
850 ± 60	Moreno-Corral et al. (1993)	av

Table 3.1: Distance estimates to the Cepheus OB3 association, derived: with main-sequence fitting in intrinsic colour-magnitude diagrams (msfCMD) or in Hertzsprung-Russell diagrams (msfHR); averaging the distance moduli found to individual members (av). (a) determined without BHJ 11, (b) determined for BHJ 69br.

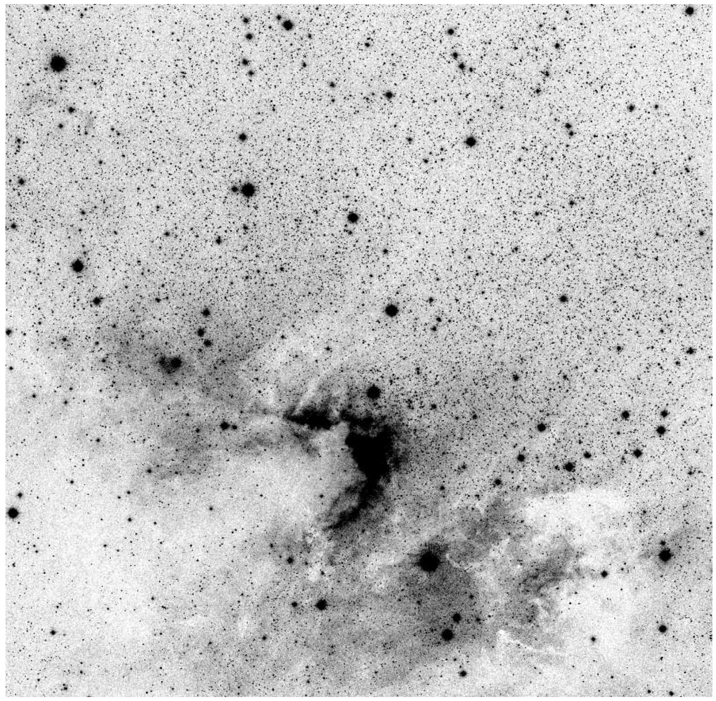

Figure 3.1: The Palomar Sky Survey image ($\sim 1.7^\circ \times 1.7^\circ$) of the region surrounding the Cep OB3b subgroup.

3.1.2 Membership of Cep OB3

Cepheus OB3 is one of the smaller associations in the Cygnus-Orion arm, between the Sagittarius-Carina Arm and the Perseus arm (Georgelin & Georgelin 1976), but it is of great interest since it contains three late O-type and several early B-type stars. Blaauw, Hiltner & Johnson (1959, and *erratum* in 1960; hereafter BHJ) defined 40 members in total, with V from 7.41 mag up to 13.95 mag, derived from a starting list of 91 OB stars chosen from the Hiltner (1956), Münch (1954a,b) and Brodskaja (1955) lists. The association members were selected from their position in the CMD, their interstellar absorption (A_V), and their position on the sky. BHJ calculated the association dimensions to be about 50×30 pc in diameter respectively in the direction of galactic longitude and latitude. In a study of OB associations in the solar neighborhood (within 1 Kpc), Blaauw (1964) found that, in general, the older the subgroup, the more it is dispersed, and the less it is associated with the molecular cloud. In particular, he found that Cepheus OB3 is composed of two main subgroups at different evolutionary phases: the older, Cep OB3a, whose largest projected dimension is of 17 pc; and the younger, Cep OB3b (shown in the Palomar Sky Survey image in Figure 3.1), more compact and close to the molecular cloud, whose largest projected dimension is 10 pc.

Membership of 26 BHJ stars was confirmed by Crawford & Barnes (1970), in an *ubvy* and Hβ study: the determined colour excess E(b-y) for the members (from measured b-y colours and known spectral types) is higher than that of the non-members, suggesting the foreground nature of the latter; members and non-members appear well separated in a diagram in β (Hβ index, well correlated with luminosity) versus c_0 (dereddened Balmer-discontinuity parameter, well correlated with temperature for B stars, derived from the measured c_1 parameter and colour excess); members and non-members appear to be well separated in a E(b-y) versus c_0 plot as well; the members are well fitted by a line whose slope fits the calibration of Crawford (1970) at the true distance modulus of the association in an intrinsic V versus β plot ($V_0 = V - 4.3E(b-y)$, with V from BHJ, $E(b-y) = 0.70E(B-V)$, and $R(b-y) = 4.3$ which is equivalent to the usual $R(B-V) = 3.0$), whereas the non-members appear well above the line and are clearly foreground stars.

Garrison (1970) determined the total to selective absorption ($R = A_V/E(B-V)$) across the association, and defined the spectral types for 71 BHJ stars on the MK system, noting that a reflection nebula surrounds BHJ 15br (spectral type B2 IV-Vne), and that “curiously, the O-type stars do not seem to be connected with much nebulosity”. From different determinations of R, we derive a value of 3.18 ± 0.04 as appropriate for the members of the Cepheus OB3 association (see Johnson 1957; Crawford & Barnes 1970; Garrison 1970; Moreno-Corral et al. 1983; Cardelli, Clayton & Mathis 1989; Clausen & Giménez 1991).

Garmany (1972) defined 7 BHJ stars as spectroscopic binaries, which were added to those proposed by Heard (1967) (see also Table 3.2). The relative proper motions of 77 BHJ stars were derived by Garmany (1973) (from two plates observed 47 years apart), and radial velocities were determined for 37 of them. The astrometric results confirmed membership for 27 BHJ stars, showing an average velocity of -22.5 ± 1.5 km/s. Both the old and the young subgroups were found to be expanding from each other in the galactic longitude direction, with a velocity difference of about 4 km/s, and with a bigger expansion in the galactic latitude direction (space velocities of -30 km/s and $+3$ km/s in l and b respectively). From the position above the lower end of the Cepheus OB3 main-sequence (m-s), interstellar absorption and proper motion, 3 BHJ stars were then proposed as possible pre-main-sequence (PMS) stars: BHJ 9, 42 and 45 (which BHJ considered non-members). Another 3 (all known members) were proposed as possible PMS stars by Sargent (1979): BHJ 37 and BHJ 44 (from traces of PMS circumstellar shells in their spectra), and BHJ 50 (from UV photometry).

Table 3.2 lists the BHJ stars which are members of Cep OB3a and Cep OB3b respectively. The binary status of some of them is noted, as well as possible PMS stars which are known members. Note that the 3 possible PMS stars proposed by Garmany (1973) are not listed, since they were considered non-members by BHJ. A comment is added for those stars whose membership is controversial. Spectral types are from Garrison (1970) (but see also Table 3.3). BHJ 11 (considered a member by BHJ) is the reddest star in the association, together with BHJ 3 (considered a non-member by BHJ and therefore not listed in Table 3.2): their membership is uncertain according to Garrison (1970).

Table 3.3 shows the different spectral type classifications for some of the BHJ stars presented in the literature. Furthermore, notice that BHJ 44 could be a peculiar star: BHJ and Garrison (1970) classified it as B3 V (from it visual spectrum), whereas Massa & Savage (1984) are in favour of B2 V (from UV extinction parameters), in agreement with Crawford & Barnes (1970).

Recently, Jordi et al. (1992) presented Strömgren *uvby*-β photometry for 45 stars in the association, claiming to have found 5 new possible members. One of them is BHJ 54, already known as a member; and a second one, BHJ 61, was previously classified as a non member by BHJ. Anyway, there are three new possible members, two belonging to the older subgroup ($+64^o1714$, $+64^o1717$) and one to the younger subgroup ($+62^o2114$), which could extend the association dimensions. Making use of UBV photoelectric data by Särg & Wramdemark (1970) (containing 16 BHJ stars), Jordi et al. (1992) also proposed another 28 possible members (see their Table 3) using the Q-method (Johnson & Morgan, 1953). Trullols et al. (1997) performed a kinematic analysis of Cepheus OB3, using Hipparcos astrometric data: they confirmed 23 members and found the membership of BHJ 2 doubtful. A search for faint members was performed in UBVRI-CCD photometry by Jordi et al. (1995, 1996; hereafter J95, and J96), in 18 randomly selected fields in Cepheus OB3 (7 fields in Cep OB3a and 11 fields in Cep OB3b, with a field of view of only $3.0' \times 4.4'$ each), including 22 BHJ stars. They proposed 8 new association members: 6 belonging to Cep OB3a and 2 belonging to Cep OB3b, all of them of spectral type B.

BHJ	Sp.	binarity	comments
Cep OB3a			
BHJ 14	B1.5 V		
BHJ 18	B2 IV-V		
BHJ 19	B7 V		
BHJ 23	B5 V		
BHJ 37	B6 V nnp		possible PMS star (9)
BHJ 44	B3 V	sb (6)	possible PMS star (9)
BHJ 46	B0.5 V	sb (4)	
BHJ 47	B1.5 V	cd: (2)	
BHJ 50	B3 V	sb: (5),(6)	possible PMS star (9)
BHJ 54	B1.5 Vn	sb: (5),(8)	
BHJ 56	B1 V		
BHJ 59	B2 IV	cd: (2); sb (8)	
BHJ 66	B0.5 IIIn	sb (5),(6),(8)	
BHJ 68	B1 V	sb (5),(8)	
BHJ 69	B1.5 Vn	eb (1); sb (4),(6)	
BHJ 70	B1 V		
BHJ 75	B0 III		dbm(9)
BHJ 76	B0 IV	sb (5),(8)	
BHJ 77	B2 V		
Cep OB3b			
BHJ 2	B1 V		dbm (12)
BHJ 8	B2 V		
BHJ 10	O8 V		
BHJ 11	B1 V		extremely dbm (9),(10); nm (11)
BHJ 15	B2 IV-Vne	eb: (3); *	
BHJ 16	B0.5 V		
BHJ 17	B1.5 V		
BHJ 20	B1 V	sb (5),(8)	
BHJ 22	B1 V		
BHJ 24	B1 V		
BHJ 25	B5 Vn		
BHJ 26	B2.5 V		
BHJ 31	O8.5 V		
BHJ 33	B5 V		
BHJ 39	B0.5 Vn	sb: (7)	
BHJ 40	B1 Vn	sb (5),(8)	
BHJ 41	O7n		

Table 3.2: The list of BHJ stars in the older and younger subgroups. Note that 3 possible PMS stars (BHJ 9, 42, 45; Garmany 1973) are not listed since they were considered non-members by BHJ. Spectral types are from Garrison (1970), referring to the brightest component when the star is signed as binary. In column 3, sb stands for spectroscopic binary, eb for eclipsing binary, cd for close double, with : for suspected; * spectroscopic binarity for BHJ 15 was excluded by Garmany (1972). In column 4, dbm stands for doubtful membership, nm for non member. References are as follows: (1) Gaposhkin (1949), (2) BHJ, (3) Hill (1967), (4) Heard (1967), (5) Doremus (1970), (6) Garrison (1970), (7) Walborn (1971), (8) Garmany (1972), (9) Sargent (1979), (10) Crawford & Barnes (1970), (11) Jordi, Trullols & Galadì-Enrìquez (1996), (12) Trullols, Jordi, Galadí-Enríquez (1997).

BHJ	Garrison (1970)	Crawford & Barnes (1970)	Walborn (1971)	Conti & Leep (1974)
BHJ 10	O8 V	O9 V	O8.5 V	O9.5 V
BHJ 19	B7 V	B3 V		
BHJ 31	O8.5 V	O9 V	O9 IV	O9 V
BHJ 39	B0.5 Vn	O9 V	B0 IV	
BHJ 41	07 Vn	O9 V	O7 Vn	O6.5:
BHJ 75	B0 III	B0 V	B0.2 IV	

Table 3.3: Different spectral classification for some BHJ stars.

3.1.3 Age of Cep OB3

The ages of Cep OB3a and Cep OB3b were estimated from CMDs (by isochrone fitting to the upper main-sequence stars) to be 8 Myr and 4 Myr respectively (Blaauw 1964), and subsequently 10 Myr and 7 Myr (Blaauw 1991). Clausen & Gimenéz (1991) found an age of 10 ± 1 Myr for CW Cep (BHJ 69br; this is the bright component of the binary system) belonging to the older subgroup, and 10 Myr for the older subgroup itself (by fitting isochrones from Claret & Giménez, 1989), in agreement with previous estimates. They also noted a very large spread around the 10 Myr isochrone, which could be explained by errors in observations, or by dereddening or calibration errors, but could also be a real age spread.

Table 3.4 is a summary of the ages present in literature, for the older and the younger subgroup, or for the entire association, by means of the nuclear age (isochrone fitting) or the expansion age (kinematic method). The latter gives a much lower age (see Subsection 2.2.3 in Chapter 1 for a discussion of the possible causes), and is determined by reversing proper motions of the association members and tracing them back in time until the smallest configuration is found.

Note that the ages of the two subgroups derived by J96, from evolutionary models by Schaller et al. (1992), are based on a quite poor statistics for the turn-off point, therefore they do not offer a reliable improvement on previous estimates. Furthermore, as pointed out by Garmany (1994), “the concept of a turn-off age from the most massive evolved stars is meaningless in OB associations”, since low-mass stars may continue to form after the high-mass stars have formed (i.e., they are not

age Cep OB3a (Myr)	age Cep OB3b (Myr)	age Cep OB3 (Myr)	method	references
8	4		1	Blaauw (1964)
		1.6	2	De Vegt (1966)
0.48		0.72	2	Garmany (1973)
	0.3		2	Assousa, Herbst & Turner (1977)
0.5-0.7	0.1-0.3		2	Sargent (1979)
8-12	5-9		1	de Zeeuw & Brand (1985)
10			1	Clausen & Giménez (1991)
10	7		1	Blaauw (1991)
7.5	5.5		1	J96
0.8	0.4		2	Trullols et al. (1997)

Table 3.4: (1) nuclear age (isochrone fitting), (2) expansion age (kinematic method). The latter always underestimates the age for several reasons, as discussed in Section 2.2.3 (see Chapter 1).

necessarily co-eval populations). We therefore conclude that the age ranges for the two subgroups given by de Zeeuw & Brand (1985) are the more realistic, i.e., an age of 7 ± 2 Myr and 10 ± 2 Myr respectively for the younger and the older subgroups.

3.1.4 Extinction

The brightest stars of the association (BHJ 10, BHJ 31, BHJ 41 and BHJ 54) were observed with the International Ultraviolet Explorer (IUE) satellite by Barsella, Panagia & Perinotto (1982): they determined the UV extinction in front of them, separating the contribution of foreground dust from that due to the dust in the association. The dust in Cepheus OB3 appears to be composed primarily of graphite grains with sizes considerably smaller than those belonging to the interstellar medium. Wesselius et al. (1982) compiled an UV photometric catalogue from data obtained with the Astronomical Netherlands Satellite (ANS). Massa & Savage (1984) obtained IUE data to study the UV extinction of OB stars situated north of the association molecular cloud ($l^{II} = 109°$ to $113°$, and $b^{II} = 2°$ to $4°$). The UV extinction is strongly dependent on the size distribution and composition of dust grains: it turned out that grain sizes diminish with increasing distance from the cloud suggesting grain destruction or mantle modifications after they emerge from the molecular cloud. The opposite

$E(B-V)$ (Cep OB3)	$E(B-V)$ (a)	$E(B-V)$ (b)	references
0.82 ± 0.03	0.73 ± 0.02	0.92 ± 0.04	BHJ (1959)
0.83 ± 0.04			Crawford & Barnes (1970), (1)
0.80 ± 0.03			Garrison (1970), (2)
0.84 ± 0.04	0.72 ± 0.03	0.95 ± 0.04	Moreno-Corral et al. (1993)

Table 3.5: Colour excess $E(B-V)$ for the Cepheus OB3 association and for its subgroups, old (a) and young (b) respectively. (1) mean value determined from the relation $< E(b-y) >= 0.70* < E(B-V) >$. (2) mean value from the colour excesses obtained from the spectral types.

A_V (Cep OB3)	A_V (a)	A_V (b)	references
2.47 ± 0.08	2.76 ± 0.11	2.21 ± 0.08	BHJ
2.48 ± 0.12	2.05 ± 0.09	2.91 ± 0.14	Moreno-Corral et al. (1993)
	2.28 ± 0.34	2.59 ± 0.48	J96 (*)

Table 3.6: Interstellar reddening to the Cepheus OB3 association and/or its subgroups. (*) values obtained omitting BHJ 11 and including 8 new members (6 belonging to the old, and 2 belonging to the young subgroup).

process, i.e., growing of small grains as they approach the molecular cloud from outside to inside, is unlikely, since it would contrast with the motion of the expanding HI shell which surrounds the association (see Section 3.1.5). Data from high-resolution CO and ^{13}CO emission line observations of the interface Cep B/S155 HII region (Minchin, Ward-Thompson & White 1992) are in favour of a continuous grain size distribution encompassing polycyclic aromatic hydrocarbons to large silicate grains.

We searched in the literature for extinction or reddening values for the Cep OB3 association and/or for its older and younger subgroups. Measured colour excesses and interstellar reddenings are summarized in Tables 3.5 and 3.6 respectively.

Moreno-Corral et al. (1993) presented values of $E(B-V)$, A_V, R_V, and distance modulus to the

$E(B-V)$	A_V	R_V	dm
0.91 ± 0.02	2.81 ± 0.10	3.08 ± 0.09	9.65 ± 0.20

Table 3.7: Adopted reddening values and distance modulus (plus associated 1σ errors) to the Cep OB3b subgroup. From this we derive also $E(V-I) = 1.18$ mag, from the relation $E_{V-I} = 1.3 * E_{B-V}$, with 1.3 from the reddening relationship of Winkler (1997).

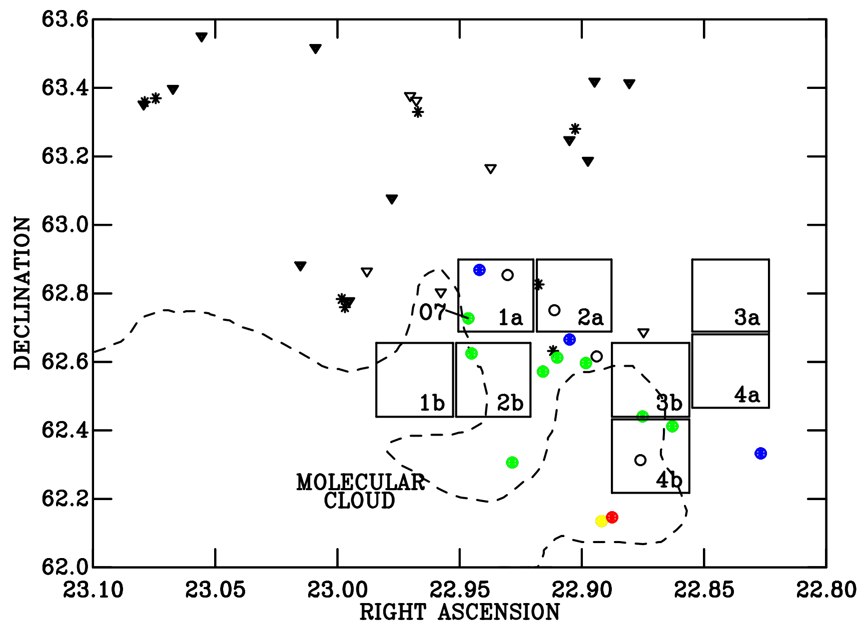

Figure 3.2: Distribution of reddening for the members observed by Moreno-Corral et al. (1993). Stars with A_V less than 2.45 mag are shown as blue filled circles; those with A_V values within the ranges 2.45-3.17 mag and 3.17-3.53 mag as green and yellow filled circles respectively; those with A_V larger than 3.53 mag as red filled circles (see also text). The superimposed boxes are our survey CCD fields (see Section 3.2). Members (according to BHJ) of the Cep OB3a are shown as filled triangles, those of Cep OB3b as open circles; possible PMS stars from Garmany (1973) and Sargent (1977) are shown as open triangles; new possible members (J96) as asterisks; the lowest CO contour of the molecular cloud (Sargent 1977) is defined by dashes.

individual members of both the older and the younger subgroup, giving the corresponding mean values for the entire association. Note that the authors do not supply the errors: the individual extinction values were found by extrapolating the colour excess $E(V-\lambda)$ (with $\lambda = J, H, K, L', M$) of the early-type members and using the mean extinction law for OB stars determined by Leitherer & Wolf (1984). In so doing, they also included BHJ 11, whose membership to Cep OB3b is considered very doubtful (see Table 3.2). For a correct determination of the mean $E(B-V)$, A_V, R_V, and distance modulus values for the Cep OB3b subgroup, we therefore preferred to take the individual values to its members from their Table 2, but omitting BHJ 11 from the calculations. The resulting mean values and associated errors (from 13 members) which were adopted in this thesis are reported in Table 3.7. In the past it was generally assumed that the distribution in reddening is fairly constant throughout the association, the high-mass members suffering small extinction. In Figure 3.2 we plot the individual reddening values of the Cep OB3b members across the subgroup according to Moreno-Corral et al. (1993). We adopted a colour scale according to: A_V values which are more than 1σ smaller than our adopted value (i.e., $A_V < 2.45$ mag) are shown as blue filled circles; A_V values within $\pm 1\sigma$ range from the adopted value (i.e., $2.45 < A_V < 3.17$ mag) are shown as green filled circles; A_V values between 1σ and 2σ larger than the adopted value (i.e., $3.17 < A_V < 3.53$ mag) are shown as yellow filled circles; and finally A_V values which are larger than 2σ from the adopted value (i.e., $A_V > 3.53$) are shown as red filled circles. The only star with an interstellar reddening considerably larger than the adopted value for the Cep OB3b subgroup is the one which is more on-cloud, for which one should expect a larger A_V. The general picture is therefore confirming a quite smooth distribution, with no apparent trend moving across the subgroup, from west to east. But we can notice that the reddening seems to be decreasing with distance to the CO contour, whereas stars which appear on-cloud are suffering a higher extinction.

3.1.5 Radio, X-ray, and IR observations

Cepheus OB3 represents an ideal target in which to study the relationship between an OB association and its molecular cloud. It is a region of recent star formation but contains stars old enough to give an idea of the evolution of the molecular cloud. A mapping in ^{12}CO lines (Sargent 1977) revealed the considerable dimensions of the the molecular cloud (20×60 pc), which is elongated parallel to the galactic plane and has a mass of $5\times10^3 M_\odot$ (Sargent 1979). This mass value could be an underestimate, since it does seem to be of order $10^4 M_\odot$ from ^{13}CO measurements (Carr 1987). The mapping made by Sargent (1977) revealed the presence of several components, whose emission velocities agree with the values known for the association members and with those of the HII region Sh 2-155 (from the Sharpless (1959) catalogue of Hα nebulosities; hereafter the S155 HII region). The HII region is about 35 pc in size (Heyer, Carpenter & Ladd 1996), and is created by the ionizing radiation of the OB stars (in the vicinity of the O7n star BHJ 41). It is in physical contact with the molecular cloud, which is retreating with a contraction velocity of about 2.5 km/s (Panagia & Thum 1981). A bright arc of nebulosity defines the interface between the S155 HII region and the molecular cloud (see Figure 3.1), already noted by Garrison (1970). The presence of an HII region and of a reflection nebula, i.e. the signs of the interaction between the molecular cloud and the OB stars previously formed, confirm that recent star formation has taken place in the region (Mezger et al. 1967 were the first to recognize that HII regions are signatures of recently formed O and B stars).

Sargent (1977, 1979) divided the molecular cloud into different regions, about 1-2 pc in dimensions (see Figure 3.3, a scan of Figure 4 given by Sargent 1977): Cep A ($M \simeq 500 M_\odot$), a site of continuing star formation and birth site for a new subgroup in the association; Cep B ($M \simeq 100 M_\odot$), having the highest CO peak antenna temperature, but which clearly cannot be considered the formation site of a new subgroup (there is no sign of density enhancement); Cep C ($M \simeq 300 M_\odot$), a site of future star formation; Cep D and Cep E not considered potentially active regions; and, finally, Cep F. New far-infrared sources in Cep F, close to BHJ 10 and BHJ 11, and BHJ 15 and BHJ 16 respectively, were subsequently found by Sargent et al. (1983). A mapping in ^{13}CO of the eastern part of the molecular cloud, diametrically opposite with respect to Cep F (and about 15-35 pc from the association members) revealed the presence of 45 individual clouds (or clumps), about 3 pc or less in size, and with masses from 3 to 300 $M_\odot$: anyway, none of them appears to be involved in past or recent massive star formation (Carr 1987).

From 21-cm radio line observations, Simonson & van Someren Greve (1976) found an HI concentration around Cepheus OB3, centered at $l \sim 111°$ and $b \sim +3°$. The HI shell is 8° in diameter, with a mass of $5.3 \times 10^4 M_\odot$ and expanding at 10 km/s. The existence of the HI expanding shell was confirmed by Assousa, Herbst and Turner (1977), and its location centered on the older subgroup Cep OB3a. The expansion velocity was corrected to 35 km/s and the radius calculated to be 53 pc:

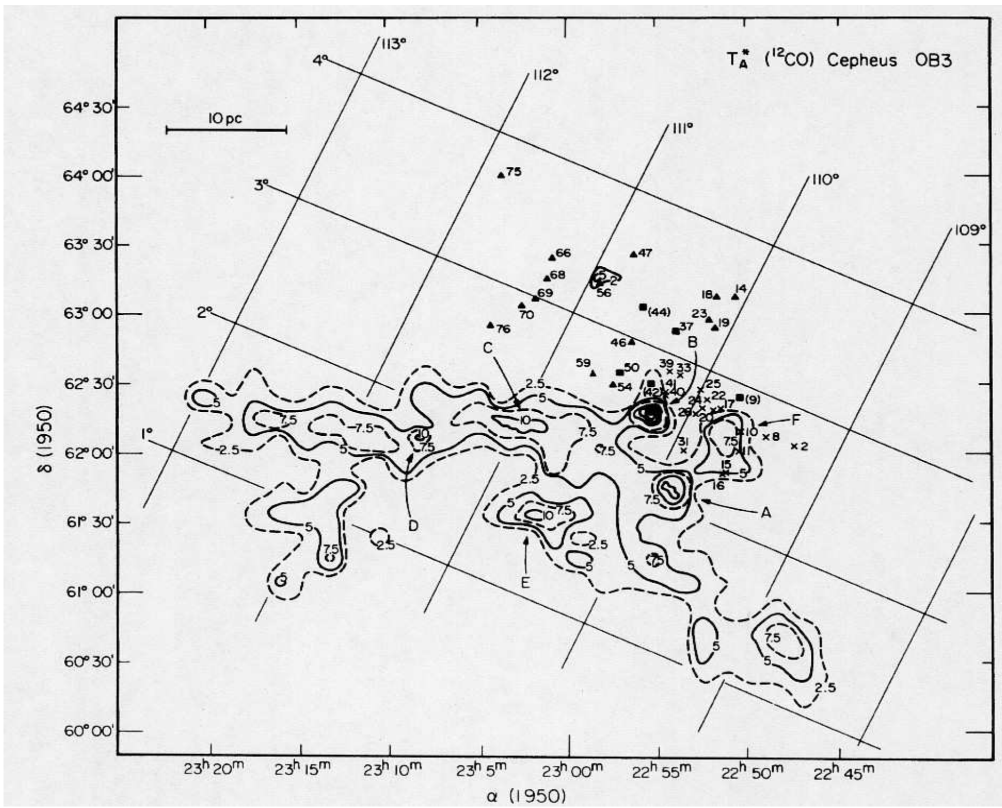

Figure 3.3: The Cep OB3 association and ^{12}CO contours of peak antenna temperatures for the associated molecular cloud, from Figure 4 of Sargent (1979). Members of Cep OB3a and Cep OB3b are represented as filled triangles and crosses respectively. Also shown the possible PMS stars (filled squares). The numbering system is from BHJ.

the shell was identified with a supernova (SN) remnant (type II), 4.3×10^5 years old. The pulsar PSR 2223+65, 1.14×10^6 years old, was suggested as a possible stellar remnant of the SN event. In this scenario, the authors proposed a SN-induced star formation process for the younger subgroup of the association, which was estimated to be $\sim 3 \times 10^5$ years old by kinematic method. However, this method is known to underestimate the likely true age (i.e., the nuclear age; see Section 2.2 in Chapter 1), and we know that the younger subgroup is instead a few Myr old, therefore the proposed pulsar is too young to be the remnant of the SN which may have triggered star formation in this subgroup. Therefore another pulsar quoted by these authors, PSR 2324+60, some 10 Myr old, seems to us a better candidate.

Surveys in X-ray (Fabian & Stewart 1983), in radio (Felli et al. 1978) and infrared wavelengths (Evans et al. 1981), showed that the emission peaks lie at the interface of the S155 HII region and the molecular cloud, with a minimum in the N-W direction, where no cloud material is detected. The X-ray emission is extended, and was at first interpreted as a hot bubble of gas created by the stellar winds of the early-type association members. This interpretation turned out to be wrong as shown by Naylor & Fabian (1999; hereafter NF99), since the X-ray emission comes from a group of T Tauri stars clustering close to the interface. Cep B was recently surveyed in CO lines by Beuther et al. (2000), revealing that there are different kinetic temperatures along the line-of-sight, strongly indicating a temperature gradient larger than 50 °K between the surface (close to the S155 HII region) of the molecular cloud and its cooler inner parts in the S-E direction.

Panagia & Thum (1981) showed that the clumps in Cep B are about 30 times denser than the surrounding media, suggesting the presence of stars in the early stages of formation. Furthermore, from NIR observations, Moreno-Corral et al.(1993) identified a PMS cluster in Cep B, in the area defined by BHJ 40, BHJ 41, and the S155 HII region. They found 50 low-brightness sources, about 60% of which are in or close to Cep B, suggesting the formation of a large number of low-mass stars. BVRI-Hα photometry gave more than 100 objects, most of which fall above and to the right of the m-s in the CMD, suggesting their PMS nature. From photometry, the authors found that 23% of these stars are apparent double or multiple systems (from a fitting of the stellar profiles), a value very close to that (25%) found by Garrison (1970) for the early-OB type association members.

Testi et al. (1995) performed a survey in the radio and NIR of the Hα knot at the interface between the Cep B and S155 HII regions. Radio results (see their Figure 1a and 1b) showed that the source no. 9 of Felli et al. (1978) is a complex of four different sources: a ridge, tracing an ionizing front to the north of the knot, an HII region (radio source A), and two non-thermal sources (source B and C). NIR results revealed the presence of a cluster of young stars embedded in Cep B: all but three (A-NIR, B-NIR and C-NIR; see their Figure 2) were already pointed out by Moreno-Corral et al. (1993). A-NIR is explained by a highly reddened m-s star of spectral type B1, in agreement with the star suggested by Minchin et al. (1992), which is also responsible for heating the cloud (see also Olmi & Felli, 1998). B-NIR and C-NIR are close to radio sources B and C respectively, and are likely to be PMS objects. The age of the cluster of newly-born stars is in the range 10^4-10^5 years (from the dynamical time scale of radio source A and the ionizing-shock crossing time; see also Moreno-Corral et al. 1993). This cluster of PMS stars could represent the third generation of early-type stars in the association.

Cep B seems to be already evolved to a phase in which the typical signs of youth, such as H_2O masers (Wouterloot & Walmsley 1986), OH masers (Braz et al. 1990), CO outflows (see Lada 1985) and ammonia cores (Wouterloot, Walmsley & Henkel 1988) are not present anymore. In particular, H_2O maser emission is normally indicative of an HII region or a protostar (see Codella et al. 1994). Recently, a double outflow from a deeply embedded source was instead found in Cep E (Ladd & Hodapp 1997), suggesting that the region is involved in the early-stages of star formation.

3.1.6 Sources of heating and ionization

A question immediately arises: what is heating Cep B and Cep F? Felli et al. (1978) (along with Panagia & Thum 1981) suggested that the main ionizing source of Cep B was the O7n BHJ 41 star (HD 217086), followed, to a lesser extent, by the O8.5 BHJ 31 star (HD 216898) and the B1 star BHJ 40 (HD 217061) (see Table 3.2, and Figure 3.3 for their location with respect to the edge of the CO contour). Sargent (1979) showed that Cep B has the highest peak of ^{12}CO antenna temperatures, possibly because of a newly born star in the younger subgroup, behind the cloud or embedded in it. Possible candidates are the AFGL 3000 infrared source of Price & Walker (1976), close to its center, or the thermal source no. 9 found by Felli et al. (1978). Evans et al. (1981) showed that Cep B is heated from outside the cloud, by stars belonging to Cep OB3b, and perhaps by the star which is ionizing the source no. 9 of Felli et al. (1978), which is close to the edge of the molecular cloud (the strongest FIR emission, in fact, comes from the interface between the molecular cloud and the HII region). From observations of continuum IR emission in the Cep B dust cloud, Gordon (1990) found a NIR excess in the region (characteristic of some reflection nebulae; Sellgren et al. 1985) suggesting external heating. The excess could be due to a small dust component at high temperature embedded in Cep B. Testi et al. (1995) suggested BHJ 40, BHJ 41, and an embedded star (B1 or earlier) as mainly responsible for the heating of Cep B, in agreement with Minchin et al. (1992). Moreno-Corral et al. (1993) suggested four stars as exciting and heating the S155 HII region and Cep B. The first is BHJ 41 (located 4-6 pc behind and to the west of the centre of the molecular cloud), which has a large NIR excess caused by a dense stellar wind. The second is BHJ 40, responsible for the bright rim seen at the interface Cep B/S155 HII region. The third is a B0 star, probably exciting the infrared source AFGL 3000 (Price & Walker 1976), which is a bright extended NIR source associated with the cloud, and at least partially embedded in it. Finally, a B1.5 star is associated with a newly discovered infrared source, and may also be contributing to the heating. Recently, Beuther et al. (2000) claimed that the main sources of UV radiation close to Cep B are BHJ 40 and BHJ 41, with other B star members clustered at the north-eastern part only weakly contributing to it. They also pointed out that Cep B is highly clumped, with volume filling factors of only 2% to 4% of the whole cloud. They estimated the average clump diameter to be of just 0.02 pc, implying that the UV radiation can reach further into the cloud than would be allowed for a homogeneous cloud. They also suggested additional heating by internal sources and/or heating by shocks, to possibly explain the very high ratio in ^{12}CO transitions they found for Cep B.

Regarding Cep F, Sargent et al. (1983) claim the heating may be caused by the O8 BHJ 10 star; whereas Felli et al. (1978) claim that the O8.5 BHJ 31 star is mainly responsible (see Table 3.2, and Figure 3.3).

3.1.7 How star formation is proceeding in Cep OB3

The members of the younger subgroup of the Cepheus OB3 association lie between the older subgroup and the molecular cloud. On the cloud, $A_V = 46^m$ (Felli et al. 1978), and so any optical detection of embedded stars is impossible. This strengthened the hypothesis of the sequential model for star formation (Sargent 1979) suggested by Elmegreen & Lada (1977). According to this model, the ionizing radiation of early-type stars is responsible for the propagation of a shock wave front through the cloud, making the material gravitationally unstable and causing its condensation into new massive stars. In other words, once a subgroup is formed, another one grows thanks to the radiation generated by the previous one. The predictions of such a model would be that: bursts of star formation would occur every few Myr, about 10-50 pc apart; there would be a substantial amount of gas near the younger subgroup, but none (or very little) in the older subgroup; the velocity difference between the two subgroups (or gas velocity, or both) would be in the range $5-10$ km/s. This is effectively what is occurring in Cepheus OB3, with: a temporal separation between the older and the younger subgroup of about 4 Myr and a spatial separation of about 13 pc; the younger subgroup is closer to the molecular cloud; and a velocity difference of about 4 km/s. As remarked by Baade (1963), "when star formation is going on in an area it spreads in some way like a disease".

Although the star formation process in Cepheus OB3 appears to occur sequentially, Sargent (1979) left open the possibility of star formation triggered from the passage of the galactic density wave (Woodward 1976) for the initial subgroup (i.e., the older) of the association. According to the author, there is no evidence for its star formation started by a SN explosion, since the age of the stellar remnant proposed by Simonson & van Someren Greve (1976), and by Assousa et al. (1977), is too young to have initiated star formation in Cep OB3. However, as we discussed in Section 3.1.5, another stellar remnant, some 10 Myr old, may have indeed triggered star formation in the association.

New far-infrared sources were discovered by Sargent et al. (1983) in Cep F, close to BHJ 10 and BHJ 11, and BHJ 15 and BHJ 16 respectively . These sources could be embedded protostars, or the result of dust heating caused by members of the younger subgroup. In addition, the discovery of a compact HII region at S-E of Cep F (Harten, Thum & Felli 1981), suggests that it may be an area of active star formation. Its CO antenna temperature peak is comparable to that found in Cep B, and the presence of the BHJ 10 star (spectral type O8) close to it suggests that radiation-driven implosions (Sandford, Whitaker & Klein 1982) could be the trigger for this active star forming region (Sargent 1983).

In the past it was generally assumed that high-mass stars formed after low-mass stars (Iben & Talbot 1966; Herbst & Miller 1982), and that a significant number of massive stars in a region signalled the end of all future star formation because their ionizing radiation would blow away the gas and dust and raise the temperature of the cloud (Herbig 1962; Larson 1986; Garmany 1994).

But recently, NF99 have discovered more than 50 X-ray sources in Cep OB3b thanks to ROSAT observations. These sources are probably low-mass T Tauri stars (TTS, see Chapter 2), concentrated close to the molecular cloud, just between the OB stars and the cloud itself. They are likely to be young low-mass PMS stars, from their strong Li I 6707.8 absorption (see Section in Chapter 2) and the ratio of X-ray to optical luminosity of about $10^{-1.5}$, which is typical of very active stars (see Stocke et al. 1983). This is against the general assumption which rules out low-mass star formation in the presence of early-type stars.

Despite the fact that the Cepheus OB3 association has been studied for more than 40 years, it is clear that the problem of how star formation is taking place in the younger subgroup of the association, and in particular, the relationship between low and high mass stars, is not yet completely understood. In the rest of this Chapter we discuss a UBVI CCD photometric study of Cep OB3b, surveying the region from Cep B toward Cep F, and covering an area on the sky of about 1300 arcmin^2.

3.2 Photometric observations and data reduction

The UBVI CCD images were taken on August 10/11 and 11/12 1997, with the 2.5m Isaac Newton Telescope (INT), La Palma, Canary Islands, Spain, equipped with the Wide Field Camera (WFC), an array of 4 Loral CCDs, and the filters B (Harris), V (Harris), I (RGO INT-WFC), and U (RGO).

Even though the WFC was composed of four Loral CCDs, unfortunately only data from CCD2 and CCD4 were reduced: CCD1 was dead, while CCD3 had a sensitivity problem and a non-uniform response. Images were 2076×2076 pixels in size, with an active area of 2034×2019 pixels and 2043×2040 pixels, for CCD2 and CCD4 respectively. They each cover approximately 12×12 arcmin^2 (one pixel is equivalent to about 0.37" on the sky).

Figure 3.2 shows the surveyed region. Members belonging to the older and younger subgroups are represented respectively with filled triangles and open circles (according to BHJ). The O7n star (BHJ 41) is marked. Possible PMS stars are defined with open triangles (from Garmany 1973, and Sargent 1979); the new members recently proposed by J96 are represented with asterisks. The superimposed boxes are our WFC fields for CCD2 (fields a) and CCD4 (fields b); the dashes represent the lowest ^{12}CO contour of peak antenna temperatures for the molecular cloud (taken from Sargent 1977; see Figure 3.3).

CCD fields	centre (RA, dec) (J2000)		Exposure times (sec) in (U,B,V,I) (long; short)
1a	22 56 06.78	+62 47 31.67	100, 40, 20, 10; 10, 4, 1, 1
1b	22 58 05.34	+62 32 41.21	100, 40, 20, 10; 10, 4, 1, 1
2a	22 54 11.77	+62 47 42.84	100, 40, 20, 10; 10, 4, 2, 1
2b	22 56 10.43	+62 32 52.44	100, 40, 20, 10; 10, 4, 2, 1
3a	22 50 21.14	+62 47 44.88	100, 40, 20, 10; 10, 4, 2, 1
3b	22 52 19.63	+62 32 53.92	100, 40, 20, 10; 10, 4, 2, 1
4a	22 50 21.78	+62 34 22.50	100, 40, 20, 10; 10, 4, 1, 1
4b	22 52 18.97	+62 19 32.20	100, 40, 20, 10; 10, 4, 1, 1

Table 3.8: CCD fields surveyed in the Cep OB3 region. Fields a correspond to CCD2, fields b to CCD4 (see Figure 3.2).

Three Landolt standard fields were observed to determine the colour correction coefficients and the atmospheric extinction. One field in the older subgroup (termed the local field) was observed 4 times to choose the best aperture size and test the colour transformation equations, and four fields (8 target CCD frames) in the younger subgroup moving from Cep B toward Cep F to test possible age variations. All the observations were made with short and long exposures in all of the UBVI filters (see Table 3.8). The average seeing was $1.3''$ during the first night of observation, and $1.1''$ in the second night. Both nights were photometric. The field centers of each CCD and exposure times through each filter are listed in Table 3.8.

The first step in the data reduction process was bias subtraction for all the raw images (standard, local and target frames). The bias frames for CCD4 did not exhibit structure and therefore the raw images were de-biased by subtracting the bias level found from their under-scan region (this region was defined from the sky-flat image with the highest counts number).

CCD2 had problems, since it suffered from vertical streaking (across the whole y dimension, from a minimum of four stripes to more than ten displayed mainly along one half of the x dimension). The stripes were found to be varying in position and intensity from one image to another, with a maximum streaking at dusk (a cut across the two halves of bias frames revealed a difference of about 140 counts), diminishing through the night, and disappearing at dawn. This was interpreted as probably due to problems in the electronics. The bias frames of CCD2, therefore, displayed vertical stripes across the whole CCD, changing from bias frame to bias frame: in this case the bias level was removed by subtracting by hand, from each raw image, that bias frame which was able to delete completely the vertical stripes giving a clean image, i.e., exactly that bias frame displaying the same sequence of vertical stripes. Subsequently, the bias subtraction process was completed by subtracting the median of the over-scan region. The de-biased images were then flat-field corrected using sky-flat frames (sky images taken at dawn).

Different aperture radii, r, were selected for aperture photometry, in order to find the aperture giving a good signal-to-noise without being badly affected by seeing changes. Fixing $r = 50$ pixels as the aperture giving 100% of the photon flux arriving from the star (and containing the noise from many sky pixels), the aperture has subsequently been reduced in order to obtain a flux ratio $[C(r)/C(r = 50)]$ of 98%. A larger aperture radius in fact contains the noise from an increased number of sky pixels and other negative contributions such as bad pixels and cosmic rays (see Stetson 1987). The best aperture size is that which includes 98% of the photon flux in order to obtain 1% photometry even with small changes in the seeing during the observing run. This was fixed at $r = 15$ pixels (equivalent to $5.6''$).

The colour calibration was performed by fitting the instrumental colours, obtained from photometry, to the standard colours derived by Landolt (1992) in the Johnson-Kron-Cousins system. A total of 48 standard stars were observed over both nights for both CCDs, in the standard fields SA107, PG1633+099, and SA110. The colour transformation equations used are of the form

$$V = \psi_v * (B - V) + v + \xi_v - k_v * X, \tag{3.1}$$

$$(B - V) = \psi_{bv} * (b - v) + \xi_{bv} - k_{bv} * X, \tag{3.2}$$

$$(V - I) = \psi_{vi} * (v - i) + \xi_{vi} - k_{vi} * X, \tag{3.3}$$

$$(U - B) = \psi_{ub} * (u - b) + \xi_{ub} - k_{ub} * X. \tag{3.4}$$

The parameters to be determined are ψ, ξ and k, respectively the colour correction term, the zero point (that magnitude which would give 1 C/s, practically the difference between the true magnitude and the instrumental magnitude in each filter-band), and the atmospheric extinction coefficients

	CCD2 (1)	CCD4 (1)	CCD2 (2)	CCD4 (2)
ψ_v	-0.004	0.000	-0.004	0.000
ξ_v	25.307	25.526	25.357	25.595
k_v	0.146	0.146	0.174	0.174
ψ_{bv}	1.049	1.064	1.049	1.064
ξ_{bv}	0.249	0.226	0.139	0.100
k_{bv}	0.217	0.217	0.133	0.133
ψ_{vi}	0.945	0.954	0.945	0.954
ξ_{vi}	0.649	0.621	0.743	0.738
k_{vi}	0.028	0.028	0.105	0.105
ψ_{ub}	1.038	1.042	1.038	1.042
ξ_{ub}	-1.593	-1.753	-1.629	-1.817
k_{ub}	0.163	0.163	0.130	0.130

Table 3.9: Colour transformation coefficients for CCD2 and CCD4 in the first (1) and second (2) night of observations.

(taking into account atmospheric absorption). X is the average airmass for the different filters. k also varies with filter, since the atmospheric extinction is wavelength dependent.

We expected about the same colour correction term for both CCDs (close to 1, since instrumental magnitudes should be close to the Landolt values; close to 0 in the eq. 3.1), and zero points showing small changes from night to night for both CCDs. The colour terms were assumed to be different for the two CCDs, but constant in time. The extinction coefficient was assumed the same for both CCDs, but different on each night. The zero points were assumed different for the two CCDs and from night to night. This required a fit to 8 parameters, (i.e., 2 colour terms, 4 zero points and 2 extinction coefficients), for each colour transformation equation. The fit is based on a weighted least-squares method, the total χ^2 to be minimized is then given by the sum of the χ^2 for both devices on both nights. A systematic error was added in quadrature to the total error in order to find a reduced χ^2 equal to 1. The added systematic error was about 1% for (V-I), (B-V) and V calibrations, whereas it was about 2.7% for (U-B), as we expected, since the U-band is always more problematic for CCD observations. Table 3.9 lists the parameters values obtained respectively in the first and second night of observations.

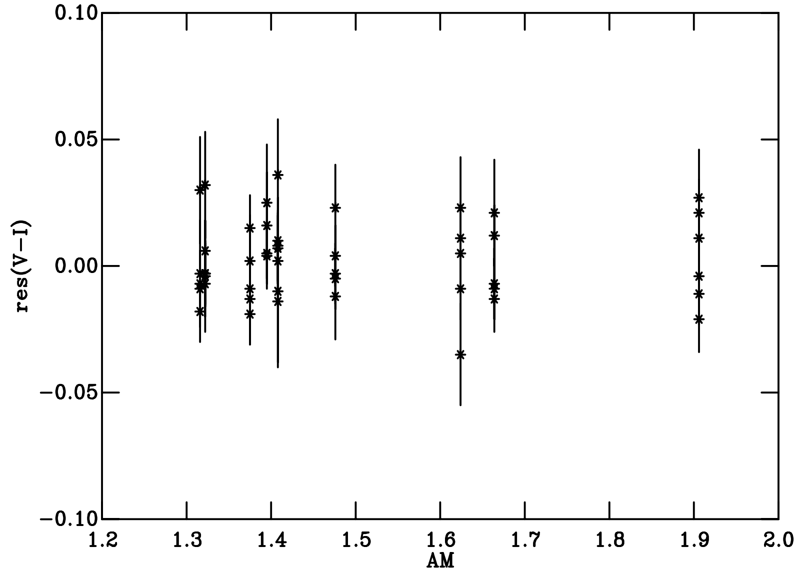

Figure 3.4: Residuals in (V-I) against the airmass, as a result of the fit for both CCDs in both nights.

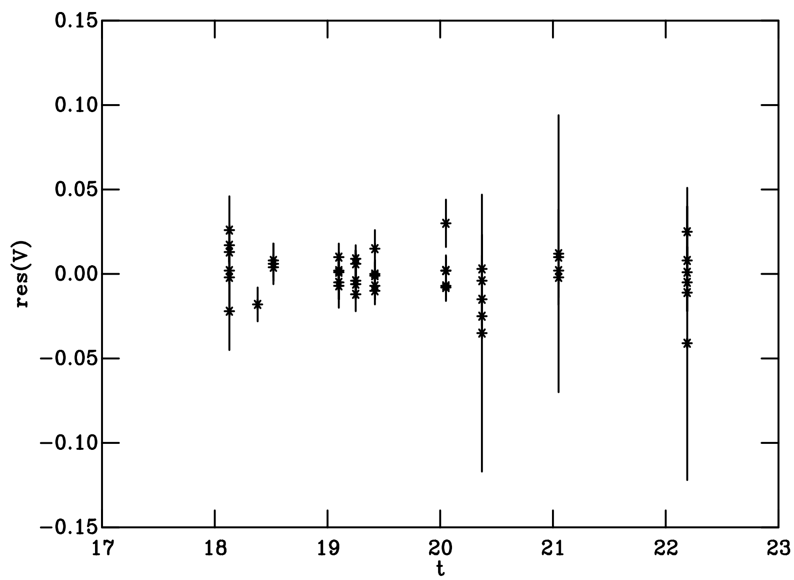

Figure 3.5: Residuals in V against the time t, as a result of the fit for both CCDs in both nights.

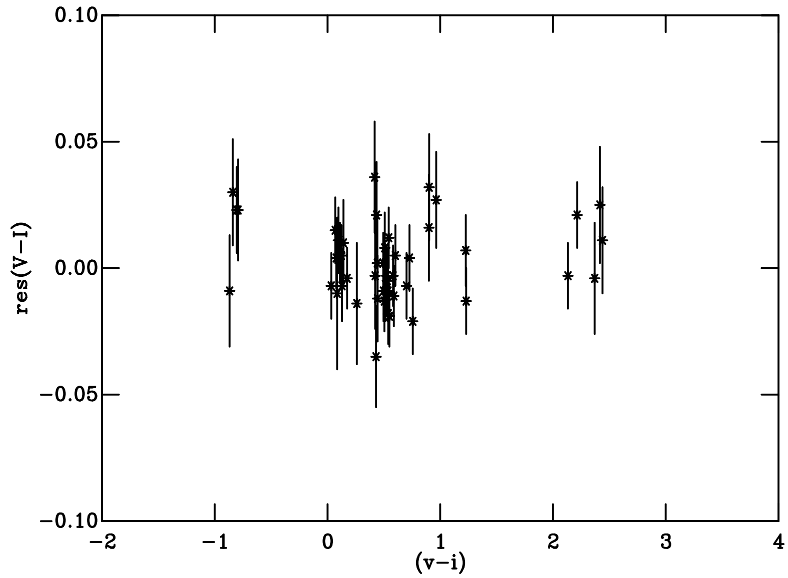

Figure 3.6: Residuals in (V-I) against the instrumental colour (v-i), as a result of the fit for both CCDs in both nights.

As an example, Figures 3.4 and 3.5 are given, where we plot the residuals in $(V-I)$ (i.e., Landolt colours minus our obtained colours) against the airmass, and the residuals of the visual magnitude V against time, for both CCDs on both nights, showing a homogeneous scatter around the zero. Analogous plots were made (but not shown) for (B-V) and (U-B) colours too. The residuals are always less than about 0.05, and show no systematic trends.

Finally, Figure 3.6 shows the residuals in (V-I) against (v-i), obtained by fitting both CCDs in both nights. Again, similar plots can be found for the other colours against the corresponding instrumental colours, showing maximum discrepancies around 0.05.

The target fields were observed in a small range of airmasses of about 0.1, between 1.2 and 1.3. Standard stars were observed up to an airmass of 1.9.

Multiple observations of the local field allowed us to test our final field-to-field internal precision, which was about 0.02 mag.

3.3 Optical Photometry Data Reduction

To create a stellar catalogue of all the objects appearing on the images, with associated UBVI colours, errors, flags, and astrometric positions, use was made of various ARK programs, as pre-steps before running the master program CLUSTER. This program is the final result of work done in collaboration, the majority of which was written by Ed Totten and Tim Naylor. It was first fully tested and, as a result, substantially improved by the present author's testing of the code on the Cep OB3 data presented here, and on the Gamma Velorum data presented in Chapter 6. As a result, the author had significant input into the design and coding, especially regarding the profile correction technique and through the verification of reasonable answers. The problem of determining profile corrections in the case of a PSF varying with position was addressed and tested by Tina Devey. We give a general description below.

3.3.1 ARK_KEY and DEGLITCH

First of all, the ARK program ARK_KEY was run. The user is asked for the x and y dimensions of the frames (i.e., the active area), the saturation, and the gain, which are then written into the headers of the images, to be used by subsequent reduction steps. ARK_KEY is especially useful when dealing with images of different dimensions, since they carry this basic information directly stored in their headers. In our case, the images of each CCD were of the same size (see Section 3.2). The gain was $g = 1.2$ photons/ADU, determined by subtracting two sky-flat images properly normalized, making a histogram of the resulting number of pixels with a given number of counts, and fitting it with a Gaussian (with its σ representing the total noise, i.e., photon noise and read-out noise). A saturation limit of 20000 counts was adopted for both CCDs. Note that the term saturation here, means the limit of linearity. Each pixel can accumulate only a certain amount of electronic charge, after which there is a non-linear response with respect to the number of photons detected. If this limit is exceeded, the electrons escape from the potential wells and are free to contaminate nearby pixels on one or more columns and get a blooming effect, i.e., the star is saturated and characterized by very bright spikes. This is why it is necessary to mask all the images before running any algorithm to find the number of stars on a frame. Cosmetic defects, such as saturated pixels (i.e., brighter than the local sky, displaced in one or more columns, or rows), must be removed, to decrease the number of false events detected (and also save computational time). The same masking process was applied to pixels which were significantly darker than the local sky. We used the ARK program DEGLITCH to do that. The program reads a list of bad pixel positions provided by the user, and replaces the corresponding pixels on the image with the median of the surrounding pixels. The same list is used subsequently by the program OPPHOT (see Subsection 3.3.4) to flag properly any star with a bad pixel in its mask, since the photometry would be unreliable.

3.3.2 MAPCCD

The second step was to run the ARK program MAPCCD. The user is asked for: the approximate full-width at half-maximum (FWHM) for the stellar profile; what sigma events above the sky to search for; if there might be a rotation between the frames; and a list of images, input in such a way that the first image given is taken as the reference frame from which to calculate the offsets of the other images (in our case the V band long exposure frame). MAPCCD then: finds all the objects on the reference image that are the specified sigma above the sky; decides which of them are stars; fits the star having the brightest (unsaturated) pixel with a point spread function (Gaussian) to determine the shape (i.e., FWHM and orientation) of the PSF (a 2-D brightness distribution of the source); uses the parameters found for the PSF to determine the positions of the other stars in the reference frame; and finally it repeats the same procedure for all the other available frames, trying to match the pattern of the stars found in the reference frame. The output file, ”offsets.dat”, contains the image names, followed by their corresponding offsets in x and y, the mean sky counts, the rotation (in degrees) between the frames (if there was one), the number of stars whose positions were matched between the frames, and the FWHM found with the fit in each frame.

3.3.3 FLAMSTEED

The star-finding program FLAMSTEED creates two files, “stars.pos” and “psf.pos”, containing a list of stellar objects with their x and y coordinates, the seeing (FWHM), and a flag indicating if they are stellar or non-stellar objects (in the first file only). The former file contains all the detected sources, without discrimination, with stellar and non-stellar objects flagged with 0 and 1 respectively. The latter file has a list of just the stellar objects, which will be the starting list from which to search for good PSF stars in the program OPPHOT (see the next Subsection).

The user is asked for the approximate seeing; what sigma events to search for (in our case, 5σ, so to have a S/N= 5 in the search algorithm and to ensure we are complete to a S/N$\sim$ 10 in the final catalogue: the S/N given by the sliding cell algorithm is always somewhat worse that that of the final catalogue because it works by adding the signal in a 3×3 pixels box only, to gain speed); the order of the PSF polynomial which will be subsequently used for the profile correction (see Section 3.3.5.1), assuming that the PSF is varying (in our case, 2, in both x and y); the long and short exposure images of the chosen reference frame (in our case, the V-band frames).

First, the program deals with the long exposure. For blocks of 50 by 50 pixels it determines the sky and the noise, by fitting a skewed Gaussian. It then interpolates these sky values on a pixel-by-pixel basis to determine a significance map, i.e., (data-sky)/noise. The images are then smoothed by a filter, with a width in pixels comparable to the number of pixels defining the seeing. Starting from a very high σ level (typically of about 100 σ, just below the saturation level), it performs a series of sigma cuts, detecting all the sources from the highest to the lowest one (corresponding to the one asked for at the beginning of the run and provided by the user), therefore filtering out all the events which are less than the supplied sigma above the sky. Starting from the top cut level, it finds the islands with high σ events and labels them as stars. It does the same in the subsequent lower cut level, and goes on until the bottom one. If any lower σ level island has the peak equivalent with that of one of the higher σ level islands, the program assumes that the lowest island is indeed part of the highest island, i.e., they are the same source. The detected sources are sorted in order of peak flux, and the fainter objects of double stars (i.e., close pairs within 2*FWHM from each other) are removed, since these would give duplicates in the list and therefore a mismatching problem in further analysis.

The program then determines the flux in a large and a small aperture, i.e., within a radius respectively equal to that used for the optimal extraction (see Subsection 3.3.4 for its definition), and to the FWHM seeing. If the ratio of the flux in the large aperture to the flux in the small aperture is within 3σ of the median, the objects are flagged as stellar, otherwise they are flagged as non-stellar, i.e., not point-like sources (such as saturated stars with blooming; or with funny shapes). Note that in the case of a PSF varying with position over the CCD field, this ratio is first fitted with a polynomial (of the given order) as a function of position.

Stars which are close to saturated stars with blooming (sometimes spread over more than one pixel column) and which passed the non-stellar check, are rejected on the basis of a background skewed gradient (for these stars, the sky would be ill-determined, and their consequent photometric colours poor in any case).

What is left is then a starting list of stars which is passed to the short exposure analysis, by correcting it with the proper offsets, and by repeating analogous steps to those explained above. If a star is saturated in the long exposure, its position and flag are taken from the short exposure.

3.3.4 OPPHOT

The subsequent step was to run the OPPHOT program, which performs optimally weighted photometry on the stars in the supplied list (see Naylor 1998 for details). Contrary to the aperture photometry method, which calculates the flux from a star by measuring the counts in the given aperture radius, and sky-subtracting the counts measured in a larger size sky box, in the optimal extraction procedure the measurement is subject to a weighting discrimination, pixel by pixel. More precisely, those pixels falling within the clipping radius (a small aperture, representing the core of the star; see below for its exact definition) are given a weight according to their signal-to-noise, those outside are given zero weight.

The input files for OPPHOT are: the two output files from FLAMSTEED, i.e., stars.pos (a list of all the stars in the image) and psf.pos (stars suitable for use as PSF stars); an offsets.dat file (containing the list of input images to be read, i.e., the short and long frames in all the requested filter-bands, with associated offsets with respect to the reference frame); and a data file containing a list with the positions of defective pixels. It also requires the radius for clipping the weight map (in FWHM) in the optimal extraction procedure. OPPHOT will use the list of bad pixels to check if they are in the mask of any star, and assign to the latter a bad pixel flag if required. OPPHOT was run so as to optimise the extraction for stars with sky background limited signal-to-noise.

OPPHOT chooses the first 49 brightest, unsaturated, and isolated stars from the list of possible PSF stars in the psf.pos file, and fits them with an elliptical 2-D Gaussian, giving parameters which define the PSF shape (i.e., the major and minor axes, $FWHM_1$ and $FWHM_2$, and rotation θ of the ellipse) from the star with the median FWHM. This is done in each of the input frames. Fixing

flag no.	meaning
0	ok
-1	non-stellar object
-2	object too near to CCD edges
-3	failed to fit the sky
-4	saturated star
-5	ill-determined sky

Table 3.10: Meaning of the flags values assigned by OPPHOT in the .opt files.

these parameters, it then fits all the stars in the list supplied in the stars.pos file, giving fluxes and coordinates (with associated errors) for each star in the frame. The clipping radius for the optimal extraction is set to be a multiple of the FWHM of the PSF star chosen in each frame, i.e., $2*(FWHM_1*FWHM_2)^{1/2}$. In this way, the clipping radius is adjusting to the seeing in each frame.

The output files are ".opt" files (one for each input image), containing a list of stars with x and y coordinates and associated errors, counts with errors, and flags. The flags indicate the stars with good photometry, and give a clear explanation of why for the other stars, bad photometry was found. The flags range from 0 to -5, and the corresponding meaning is summarized in Table 3.10. Flag -1 is given when FLAMSTEED marked the star as "non-stellar", such as extra-galactic sources or close double stars. Flag -2 is assigned when the star is too close to CCD edges to find its position and to do photometry. Flag -3 is given when the sky cannot be fitted, because of a sky gradient across the sky box, caused by a neighboring very bright saturated star. Flag -4 is given when the star is saturated (i.e., above the linearity limit), whereas flag -5 is given if the sky was fitted, but still had a large gradient or higher order slope (the algorithm assumes a flat sky: if it is not, it will work only in the case of a linear slope).

3.3.5 CLUSTER

The program CLUSTER, originally designed for open clusters, is here applied to an OB association (in Chapter 6 it will be applied to a star forming region as well). It is a very structured program, and several separate subroutines are called in a complete run. Here we limit ourselves to the presentation of the main processing steps.

In summary CLUSTER: calculates the profile correction (see below) for all the stars listed in the .opt files; performs optical photometry by finding instrumental magnitudes and colours, and transforming them into the standard system; calculates astrometric positions and sort the objects in the final catalogue by increasing right ascension. Let us comment briefly on each of the steps.

3.3.5.1 Profile correction

The profile correction is a mandatory step. We have to correct OPPHOT measured fluxes for the fact that the true profile of a star is not exactly an elliptical Gaussian such as that assumed for the extraction mask. Were the true profile and the fitted profile perfectly matching, the profile corrections would be zero. Obviously, this is not the case: deviations from the adopted profile do occur, and give non-zero corrections.

The profile corrections are obtained by selecting a maximum of 80 good candidates in each CCD frame, which are the brightest, isolated, and unsaturated stars with a sufficient S/N (> 10). To find these, the following steps are repeated in each CCD frame. The FWHM and rotation are measured for all the selected stars for which the sky-fitting does not fail (otherwise they are discarded). We stress that this is a very conservative way of rejecting possible good candidate stars, since the sky fitting procedure uses a much larger (square) sky box (a function of the standard aperture radius, see Naylor 1998 for its definition) than the standard aperture size. Such a large size box is chosen in order to have good photometry for the stars, since the resulting measured sky error is small with respect to the errors in star measurements. But, obviously, in so doing, there is a big chance that the sky box contains some sky gradients, leading to the rejection of the star from the list of PSF candidates.

Subsequently, those stars having a discrepant FWHM with respect to the mean value are rejected (the mean should be close to the value found for the PSF star chosen by OPPHOT, and written in the header of the .opt file). This is done by a sigma-clipping method, i.e., stars more than 2σ from the mean value are rejected. The values found for the mean FWHM are in the range $2.9 - 4.8$ pixels, equivalent to 1.1-1.8 arcsec, for all the fields.

The local sky for all of the surviving stars is subtracted so that for each star, a sky-subtracted image (35×35 pixels in size and centered on the star in question) can be created, representing the star plus noise. Each of these images is then normalised so that the optimally extracted flux is the same for each star (i.e., scaled to the same total counts).

A median stack plus sigma-clipping procedure is then performed. Starting from the image centered on the brightest star, a reference image is created, taking the core (corresponding to twice the clipping radius used for optimal extraction) of the star as representative of the PSF, and the median of the pixels of all the remaining original images for the pixels outside the core. Aperture photometry is then performed on these stars, using the same aperture radius as that used for the standard star calibration. A comparison with the optimally extracted flux gives a list of profile corrections, which should be consistent, although their scatter gives an idea of the true error in the correction. The median value of profile corrections is subsequently determined and the list of reference stars is subject to a sigma-clipping procedure until just one half of them survive. The final profile correction is found by doing a weighted mean of the corrections found for the brightest few stars (a sixth of the surviving stars). Note that before creating the median image, the stars put in the centre of each 35x35 image must be resampled. Taking as reference the grid of the brightest star in the sample, a smoothing procedure is then performed in order to place their centre as close as possible to that of the reference star, so as to avoid any error in the optimal flux determination (the optimal mask being strongly weighted toward the centre of the star). We point out that this centering error affects the flux at the 1% error only when it is about a tenth of a FWHM, and that it does not contribute significantly to the signal-to-noise for objects with $S/N > 1$.

If the PSF is thought to be varying with position on the CCD, because of known distortion over the field of view, the profile corrections must then be given as a function of position too. This time the user is asked for the fraction of the X and Y dimensions to be used to select the stars for the profile correction in the central region of the CCD, and the order of the polynomial to use to represent the profile corrections over the whole CCD. The stars in the central region of the CCD are first used, and the weighted mean of their profile corrections gives the profile correction for the centre of the field. Then 80 stars in the entire CCD field are used, i.e., at different positions with respect to the centre of the field. Their profile corrections are fitted with a 2-D polynomial function, whose order is chosen by the user at the beginning of the run, and with the zeroth-order term fixed to the value of the profile correction determined in the centre of the field. These varying profile corrections are

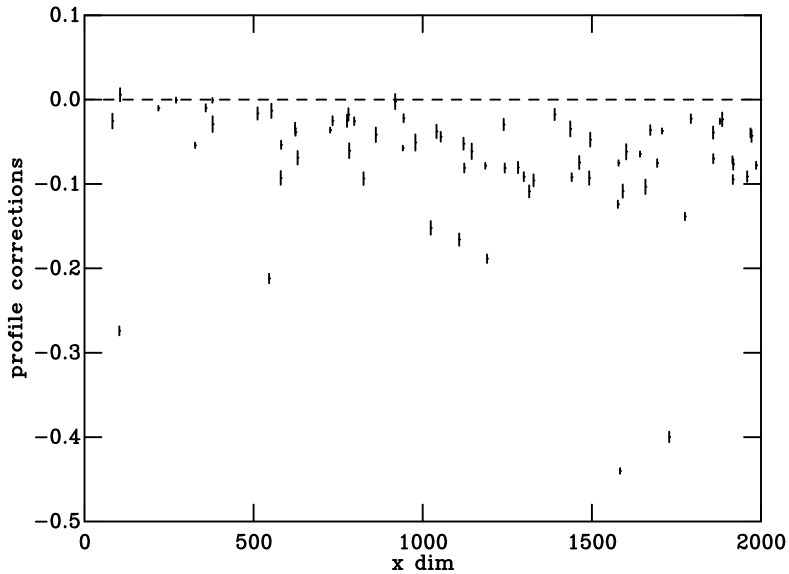

Figure 3.7: Typical (raw) profile corrections found as a function of the x position, with error bars overplotted.

then sigma clipped so to remove all the objects with a star falling in the large aperture, and which would give discrepant corrections. As a result of this varying PSF option, additional data files are output: one containing profile corrections as a function of x and y position, and one with the residuals of the polynomial fit for the profile corrections found in the two different dimensions. The order of the polynomial must be chosen so that the residuals are scattered around zero over the whole CCD.

We used this second procedure, allowing for spatially varying profile corrections to be fitted with a second order polynomial function. We found values varying from just a few 10^{-2} mag up to 0.3 mag.

Figure 3.7 shows an example of the profile corrections found as a function of the x position, and Figure 3.8 the corresponding residuals from the polynomial fit (points far away are due to stars having other stars in the aperture radius, and are rejected from the fit by σ clipping).

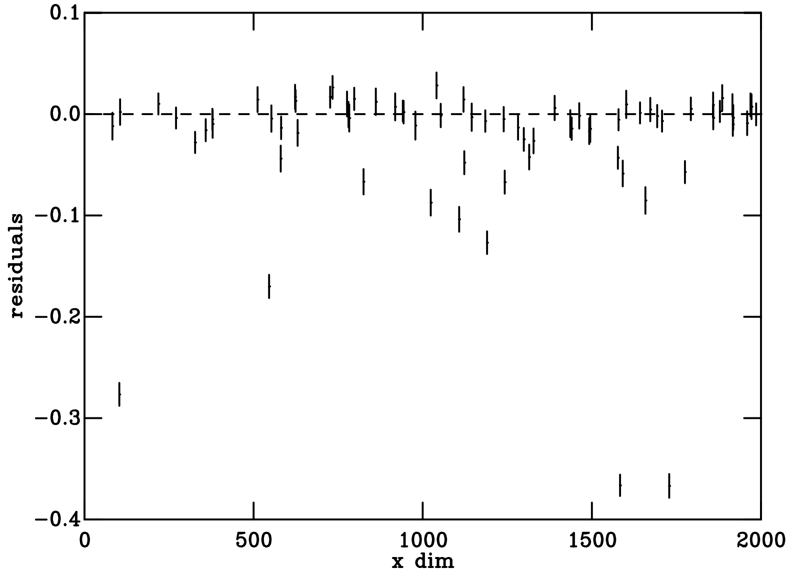

Figure 3.8: The residuals from the second order polynomial fit of the profile corrections of Fig. 3.7. A systematic error of 0.01 has been added in quadrature to the profile correction errors to take into account of errors other than the statistical ones.

3.3.5.2 Optical Photometry

In this stage, all the measured counts (C) and associated errors (ΔC) in the .opt files are converted into instrumental magnitudes (m) and associated errors (Δm) according to the equations

$$m = -2.5 * log_{10}\left(\frac{C}{T_{exp}}\right), \tag{3.5}$$

$$\Delta m = \frac{1}{2}\left[2.5 * log_{10}\left(\frac{C+\Delta C}{T_{exp}}\right) - 2.5 * log_{10}\left(\frac{C-\Delta C}{T_{exp}}\right)\right], \tag{3.6}$$

with T_{exp} the corresponding exposure time, and preserving the flags which were assigned by OPPHOT. These magnitudes are then profile corrected (by adding the proper profile correction). The magnitudes are then corrected to a common average air mass among those measured for all the exposures of a given field in all the filter-bands. The "relative" transparency corrections are then determined by means of a weighted mean of magnitude differences (in each filter-band). This is done by matching stars between the long and short exposures in each filter, rejecting stars with low S/N (< 10), saturated stars, and all the other stars flagged as bad. The matching stars left in the list are ordered by decreasing magnitude (from the long exposure). An iterative procedure then clips these until all the points included in the fit between frames are within 2σ of each other. These corrections are then applied both to the short (subtract half the difference) and long exposures (add half the difference). They should be small, and give an indication of the stability of the profile corrections and the photometric stability. We found corrections as small as 4×10^{-5} up to $\sim 10^{-2}$ mag.

Instrumental magnitudes of stars from long and short exposures in each filter-band are then averaged with a weighted mean (i.e., the values are weighted inversely by the square of their corresponding errors). The same is then done for different filter-band magnitudes, giving instrumental colours. To have apparent magnitudes and colours, the photometric results are then converted onto the same photometric system in which the standard calibration was done, using the colour transformation equations given in Section 3.2, with the coefficients presented in Table 3.9 (provided by the user in a separate file).

3.3.5.3 Astrometry

This stage finds the astrometric positions of the stars for which we have optical photometry. The astrometric positions are found by matching the positions of reference stars found on the CCD frames, which are in the USNO-A2.0 Catalogue (typical astrometric errors of 0.25"; Monet 1998), using a 6-coefficient transformation between pixels and celestial coordinates. The useful region in the USNO Catalogue is automatically selected once the user has provided a file with the field number, its centre and its dimensions in arcminutes.

In our case, since we have a mosaic of 4 CCDs, the centre of the telescope field is not the centre of any of the CCDs. It was estimated by calculating the mean distance between the centers of the 2 CCDs we have used (see Table 3.8). Furthermore, in the header of the file there must be a line describing the projected geometry, because the telescope suffers from astrometric distortion with respect to tangent-plane geometry. The distortion is due to aberration of the optics, which causes a nonuniform magnification from the centre toward the edges of the image: this can be smaller (barrel distortion) or larger (pincushion distortion) toward the edges. For the INT prime focus we used GENE 220, i.e., generalized pincushion distortion; 220 (determined from the optics of the INT) is a numeric coefficient, q, which enters into a multiplying factor $(1+q(\xi^2+\eta^2))$ of each of the tangential coordinates

ξ, η. The coordinates of the telescope centre must then be followed by the field dimensions, i.e., in our case, to cover both CCDs.

A file with 3 reference stars in the field is also needed, containing the field number, their x and y positions, and their approximate RA and Dec found by identifying the same stars in the corresponding Digitized Sky Survey image plotted with SAOIMAGE.

With this information, CLUSTER identifies which of the 10 USNO CDroms contains the target area, and the user is asked to mount it. The program extracts all the stars falling on the specified region. It then reads the file with the 3 reference stars in the region, and performs a transformation between (x,y) and (RA, Dec). The same astrometric transformation is used to calculate (x,y) from (RA, Dec) for the USNO selected stars. In so doing, the selected USNO stars become the new reference stars and are then fed to a subroutine based on the STARLINK "astrom" package (see Wallace 1998). An iterative fitting routine is then performed, between the photometric positions in the optical catalogue and the USNO reference stars, which retains only good reference stars (i.e., rejects all the reference stars with a bad fit). At this point we have the best possible fit. RMS errors in the fits were up to 0.56", from a minimum of about 70 stars up to more than 600 stars, depending on the stellar density of the field, with the majority giving an rms of about 0.4". The transformation coefficients are then applied to the positions in the optical catalogue to find the corresponding astrometric positions. Astrometric and photometric results are then combined to give a catalogue containing a running number for the stars in a particular field, their associated RA, Dec, (x,y) CCD positions, V magnitudes and colours with corresponding errors and associated flags.

The star catalogues written for each field, can then be combined to give a file containing all the stars from all the observed fields. The objects in the file are then sorted in increasing RA. This is the final catalogue.

A posteriori, we checked for systematics in the astrometric residuals as a function of positions in the field, by plotting them for two different CCD fields, field 1a (covered by CCD2) and field 1b (covered by CCD4), either side of the rotator centre of the telescope. Although there appears to be no trend with respect to the rotator centre, (see Figures 3.9 and 3.11), there does appear to be a systematic with respect to the centre of each CCD in the y dimension (see Figures 3.10 and 3.12). These systematic residuals at the 0.4 arcsec level are possibly due to distortions in the CCD structure, but no subsequent correction was attempted for the coordinates reported in the catalogue, because

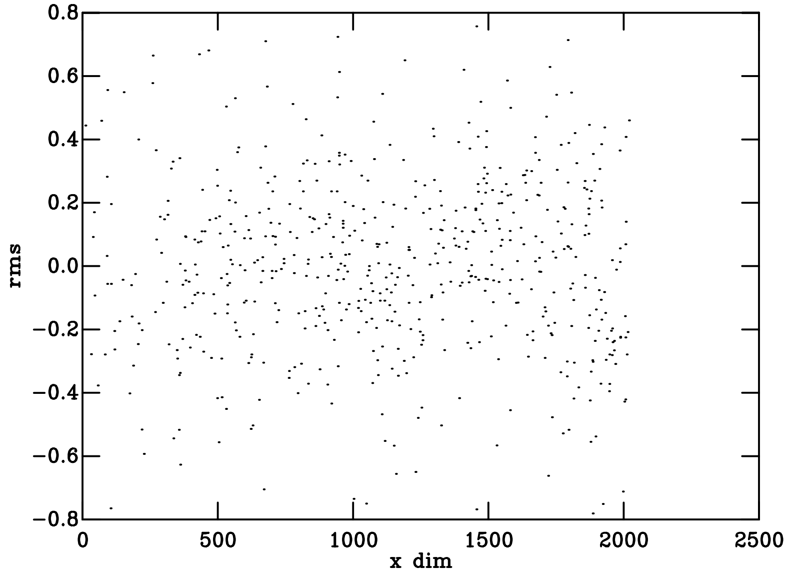

Figure 3.9: Astrometric residuals as a function of x dimension in CCD2, for a total of 590 reference stars in field 1a. No systematic trend is visible.

they are accurate enough for the purposes of this thesis.

3.4 The optical catalogue

UBVI photometry of Cep OB3b was performed by running the CLUSTER program presented in the previous Section. A global astrometric catalogue of 13657 objects was found, containing all the possible sources (i.e., both unflagged and flagged stars). This will be referred to as the global catalogue.

If we remove from the global catalogue flagged stars (i.e., stars with flags different from 0), and stars for which no colour or magnitude is determined to better than 0.1 mag for the purposes of further analysis, it then contains 7600 objects, with visual magnitudes in the range $V = 12.05 - 21.04$ mag: this will be the only catalogue used in the subsequent analysis, unless otherwise specified. Photometry is good to better than 0.1 mag in all the UBVI colours for 1241 objects, with visual magnitudes in the range $V = 12.32 - 19.88$ mag.

An extract of the global catalogue of stars in the Cep OB3b subgroup is shown in Table 3.11.

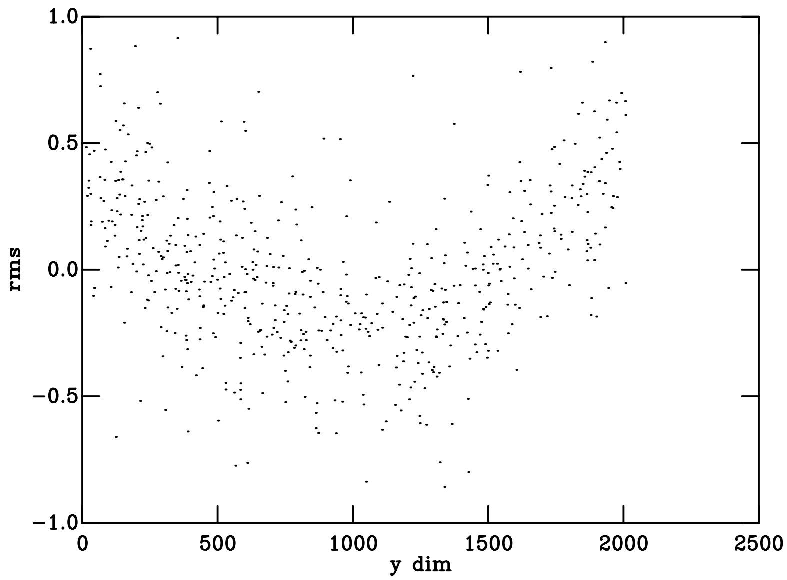

Figure 3.10: Same as Figure 3.9, but with astrometric residuals plotted as a function of y dimension. It clearly shows a systematic trend.

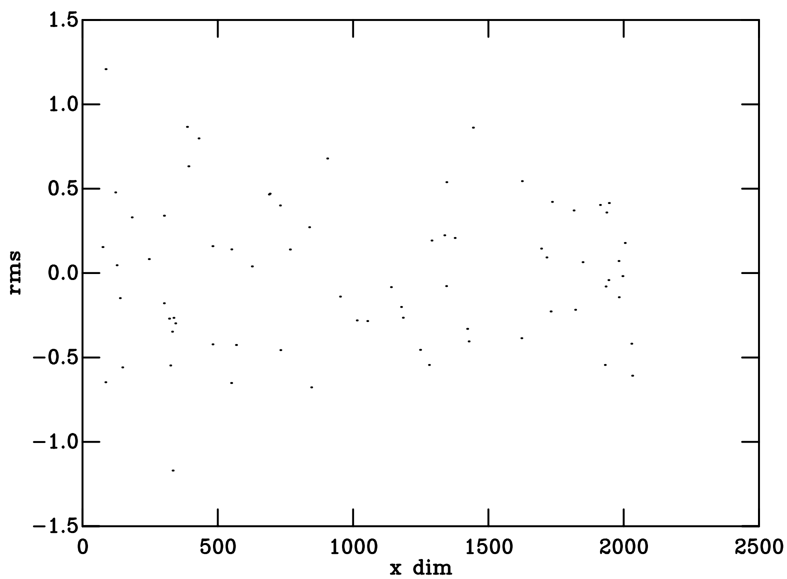

Figure 3.11: Astrometric residuals as a function of x dimension in CCD4, for a total of 71 reference stars in field 1b, showing no trend.

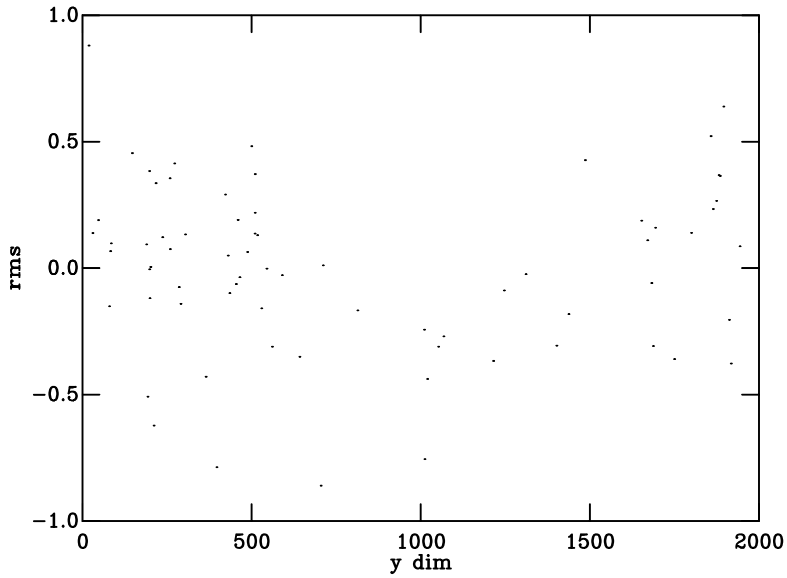

Figure 3.12: Same as Figure 3.11, but with astrometric residuals plotted as a function of y dimension. Again, a systematics with respect to the central part of the CCD is found, as in Fig. 3.10, suggesting that there must be a distortion in the CCDs structure.

Only a few entries are shown to illustrate the catalogue content. Column 1 shows the field number the star belongs to; column 2 has the running star number in the catalogue; columns 3 and 4 give the corresponding RA and Dec, in (h,m,s) and (deg,min,sec) respectively (Equinox J2000.0); columns 5 and 6 give the x and y coordinates on the CCD chip; columns 7 to 9 report the visual magnitude with associated error and flag; columns 10 to 18 give the (B-V), (V-I), (U-B) colours with associated errors and flags. The errors in the colours are those due to statistical errors only.

The flags consist of two digits, referring to the first and second filter band necessary to determine the colour. For V, the flag refers to the B and V filters, since V was computed from (B-V) colour (see eq. 3.1): note that if one or both filters are flagged as bad, V is computed in any case but flagged accordingly; if the B filter is absent, the (B-V) colour and associated error are set equal to 0.0, so in computing V it is set to 0.0 too and flagged accordingly. Each digit can run from 0 to 9, and they have the same meaning as the flags given by the OPPHOT program, (although with the sign reversed), plus another three summarized in Table 3.12.

Field	id	RA	Dec	x	y	V	errV	F(V)	
	(B-V)	err(B-V)	F(B-V)	(V-I)	err(V-I)	F(V-I)	(U-B)	err(U-B)	F(U-B)
1a	1688	22 55 55.79	62 50 09.13	1233.605	1431.522	19.216	0.398	00	
	1.497	0.678	00	1.171	0.377	00	2.650	1.038	00
1a	2230	22 55 55.79	62 41 39.94	1195.889	44.920	20.574	0.078	90	
	4.645	0.082	90	-0.733	0.627	00	-4.873	0.816	09
2b	281	22 55 55.79	62 35 05.12	1307.986	1366.221	18.549	0.015	00	
	2.085	0.046	00	2.614	0.016	00	1.756	0.439	00
2b	106	22 55 55.81	62 31 09.06	1282.586	728.333	18.309	0.073	11	
	1.867	0.222	11	2.313	0.076	11	0.709	1.265	11
1a	112	22 55 55.83	62 51 31.64	1239.344	1657.158	16.168	0.004	00	
	1.191	0.007	00	1.336	0.006	00	0.665	0.013	00
2b	960	22 55 55.83	62 31 15.84	1282.813	746.710	20.750	0.087	00	
	2.082	0.314	00	2.536	0.088	00	-0.088	0.740	00
1a	2944	22 55 55.85	62 53 31.17	1248.567	1984.728	25.071	0.000	99	
	0.031	0.000	99	3.870	0.339	90	-2.989	0.329	09
2b	1183	22 55 55.86	62 34 12.16	1301.187	1223.330	21.033	0.104	00	
	1.515	0.265	00	2.437	0.107	00	0.123	0.690	00
2b	1148	22 55 55.88	62 35 16.63	1307.572	1397.362	20.909	0.096	00	
	3.145	1.039	00	3.600	0.093	00	-3.459	1.396	00
1a	5	22 55 55.91	62 53 12.55	1245.937	1933.660	10.826	0.002	44	
	0.681	0.002	44	0.556	0.002	44	-0.091	0.002	44
1a	2610	22 55 55.92	62 43 23.46	1200.844	326.349	21.391	0.149	00	
	1.684	0.385	00	2.004	0.161	00	0.653	2.527	00
1a	67	22 55 55.95	62 52 39.02	1242.553	1841.726	15.858	0.004	00	
	1.209	0.006	00	1.457	0.005	00	0.395	0.010	00
2b	644	22 55 55.96	62 34 54.31	1303.788	1337.192	19.754	0.037	00	
	1.783	0.102	00	2.144	0.040	00	0.940	0.523	00
2b	1651	22 55 56.02	62 27 38.11	1255.505	156.314	21.165	0.161	00	
	1.825	0.426	00	1.589	0.219	00	0.459	0.381	90
1a	2498	22 55 56.04	62 49 57.81	1228.171	1400.690	21.313	0.140	00	
	1.532	0.322	00	1.808	0.162	00	0.570	0.284	90
1a	2773	22 55 56.04	62 51 17.97	1234.381	1619.822	21.373	0.166	00	
	2.630	0.956	00	2.213	0.169	00	-1.356	1.038	00
1a	86	22 55 56.05	62 44 20.70	1202.511	482.071	17.806	0.010	00	
	1.227	0.018	00	1.466	0.013	00	0.435	0.032	00
1a	784	22 55 56.06	62 48 46.13	1222.237	1204.995	19.313	0.028	00	
	1.495	0.057	00	1.895	0.032	00	0.535	0.142	00
1a	360	22 55 56.08	62 50 16.51	1228.772	1451.792	17.950	0.124	00	
	1.359	0.192	00	1.599	0.117	00	0.194	0.144	00
1a	777	22 55 56.12	62 45 04.72	1204.550	601.839	19.270	0.027	00	
	1.356	0.051	00	1.782	0.031	00	0.721	0.140	00
2b	169	22 55 56.12	62 38 11.81	1321.526	1869.904	17.734	0.009	00	
	2.104	0.026	00	2.730	0.010	00	1.422	0.164	00
1a	141	22 55 56.14	62 43 15.66	1196.193	305.236	16.800	0.006	00	
	1.164	0.010	00	1.403	0.008	00	0.393	0.016	00

Table 3.11: A sample portion of the global optical catalogue.

flag no.	meaning
7	data unavailable for this filter band
8	bad pixel in mask
9	S/N < 5

Table 3.12: Meaning of the additional flag values (to those given in Table 3.10) in the optical catalogue presented in Table 3.11. In the catalogue, the flags are paired, one for each filter-band, and the minus signs are suppressed.

V	σ_V		$\sigma_{(B-V)}$		$\sigma_{(V-I)}$		$\sigma_{(U-B)}$	
< 13.0	0.003	(20)	0.004	(20)	0.004	(11)	0.006	(20)
13.0 – 13.5	0.004	(11)	0.006	(11)	0.006	(8)	0.007	(11)
13.5 – 14.0	0.005	(29)	0.007	(29)	0.007	(28)	0.007	(29)
14.0 – 14.5	0.007	(44)	0.009	(44)	0.008	(41)	0.009	(44)
14.5 – 15.0	0.003	(45)	0.005	(45)	0.006	(45)	0.008	(45)
15.0 – 15.5	0.003	(59)	0.005	(59)	0.006	(58)	0.015	(59)
15.5 – 16.0	0.004	(84)	0.007	(84)	0.005	(84)	0.020	(84)
16.0 – 16.5	0.005	(128)	0.009	(128)	0.006	(128)	0.032	(128)
16.5 – 17.0	0.007	(189)	0.014	(189)	0.008	(189)	0.059	(188)
17.0 – 17.5	0.009	(246)	0.018	(246)	0.010	(246)	0.086	(246)
17.5 – 18.0	0.012	(388)	0.026	(388)	0.013	(388)	0.125	(386)
18.0 – 18.5	0.016	(525)	0.037	(525)	0.018	(524)	0.193	(512)
18.5 – 19.0	0.022	(753)	0.055	(753)	0.025	(753)	0.269	(729)
19.0 – 19.5	0.037	(977)	0.096	(977)	0.041	(976)	0.414	(917)
19.5 – 20.0	0.054	(1351)	0.139	(1351)	0.058	(1346)	0.577	(1213)
20.0 – 20.5	0.082	(1777)	0.218	(1777)	0.087	(1764)	0.744	(1425)
20.5 – 21.0	0.109	(2251)	0.328	(2251)	0.117	(2240)	0.920	(1589)
≥ 21.0	0.160	(3069)	0.522	(3069)	0.173	(3052)	1.015	(1937)

Table 3.13: Mean photometric errors. In parenthesis the number of stars found in all the colours having a visual magnitude in the corresponding V range listed in column 1.

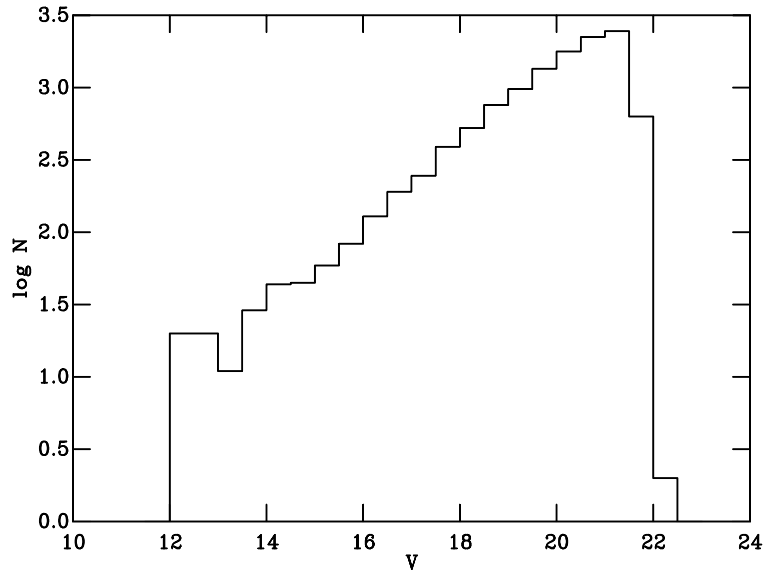

Figure 3.13: The frequency histogram of V magnitude, plotted in steps of 0.5 mag.

In Table 3.13, the mean (statistical) photometric errors at steps of 0.5 mag in V-band magnitude are reported. Here, we are still including all the stars with good flags but without any restriction on the photometric errors. We remind the reader that all the subsequent data analysis will be performed on unflagged stars with photometric errors less than 0.1 mag, which will be the only stars plotted in the colour-magnitude and colour-colour diagrams (see the next Section).

Finally, we have done a rough estimate of the completeness of our optical catalogue. The V magnitude distribution for (unflagged, but with no restriction on the photometric error) stars in the optical catalogue is presented in Figure 3.13, binned by 0.5 mag. After fitting a power law to the brighter part of the plot ($V = 14.75 - 18.25$ mag), we extended it to fainter magnitudes: incompleteness occurs where there is a significant drop in $logN$ below the power law. We therefore estimate that our optical catalogue is at least 85% complete for V magnitudes brighter than ~ 19 mag. Note that the catalogue is also slightly incomplete because of all the deglitched pixels, bad sky determinations, and whatever caused a star to be flagged as bad.

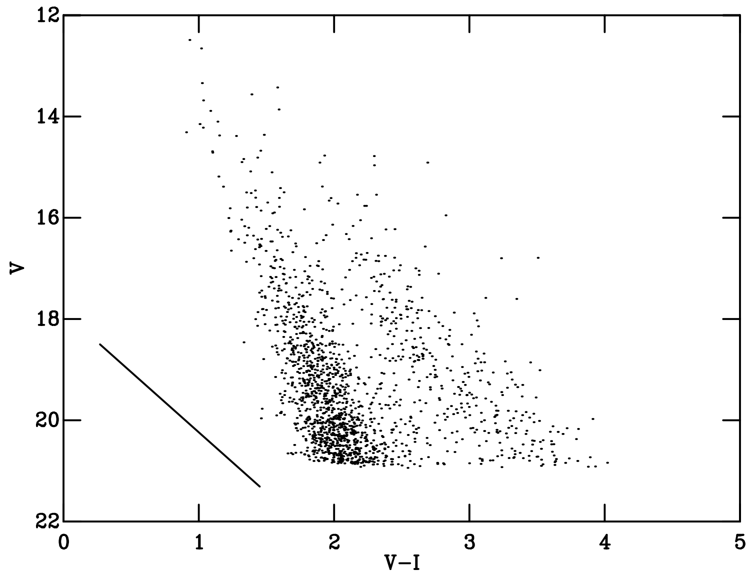

Figure 3.14: Colour-magnitude diagram in V versus (V-I) for the field 1a. The mean association reddening vector is shown, with $< A_V >= 2.81$ mag and $E(V-I) = 1.18$ mag (see Table 3.7 in Section 3.1.4).

3.5 Colour-magnitude and colour-colour diagrams

For each of the eight target fields, colour-magnitude and colour-colour plots in UBVI are available, as well as the plots showing the errors against visual magnitude. In Figures 3.14, 3.15, 3.16, 3.17, 3.18, 3.19, 3.20, and 3.21, the colour-magnitude diagrams in V versus (V-I) for all the CCD fields are shown.

As an example, we also give the plots of the statistical (as given by OPPHOT, see Section 3.2) errors against V for the field 1a in Figures 3.22, 3.23, 3.24 and 3.25 (similar plots are found for the other fields). As expected, the errors increase at fainter magnitudes (they are always less than 0.1 since we have filtered out all the stars with bigger errors, which will be not considered in the subsequent analysis). The (U-B) colours show greatest values for a corresponding visual magnitude, as expected.

Some error plots show two error curves. The one at brighter magnitudes represents errors calculated only from the short exposure, since the stars were saturated in the long exposure frame.

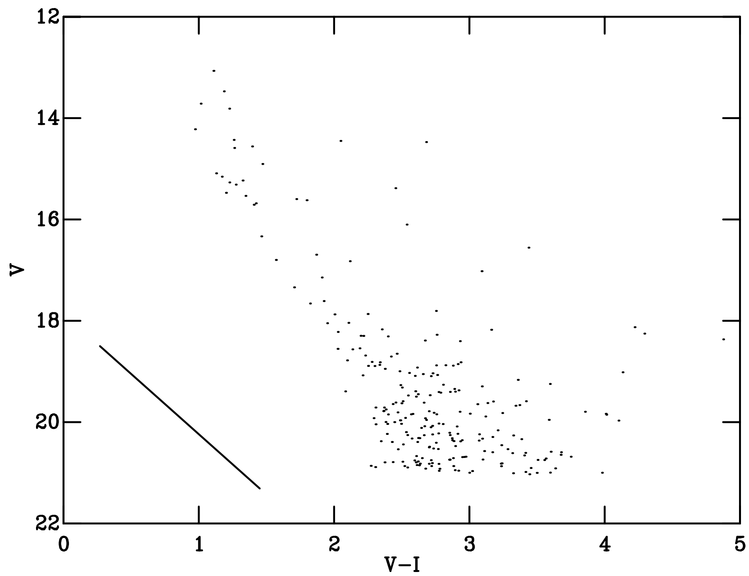

Figure 3.15: Colour-magnitude diagram in V versus (V-I) for the field 1b.

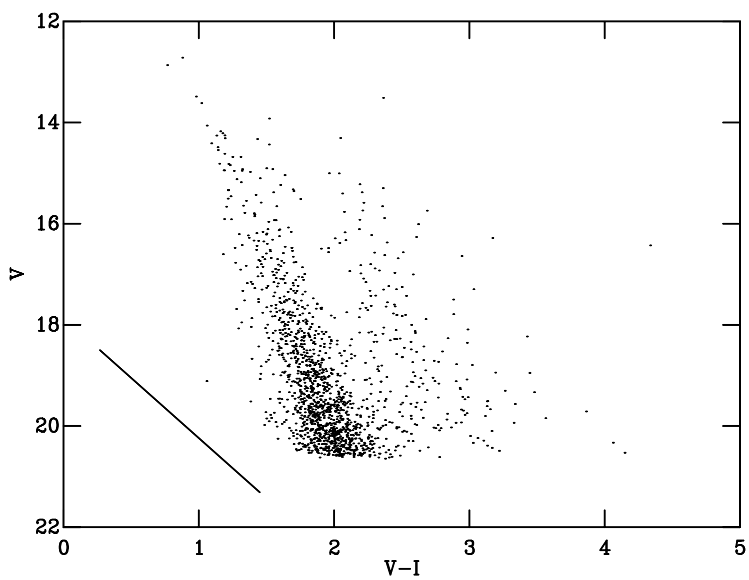

Figure 3.16: Colour-magnitude diagram in V versus (V-I) for the field 2a.

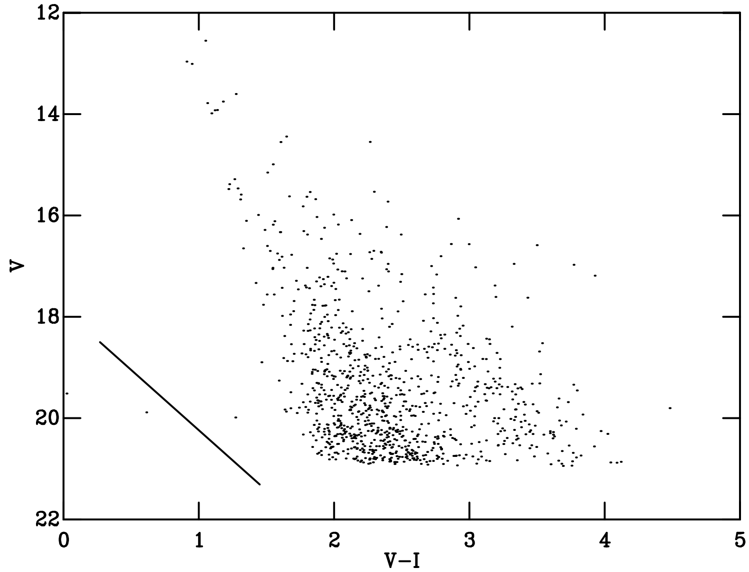

Figure 3.17: Colour-magnitude diagram in V versus (V-I) for the field 2b.

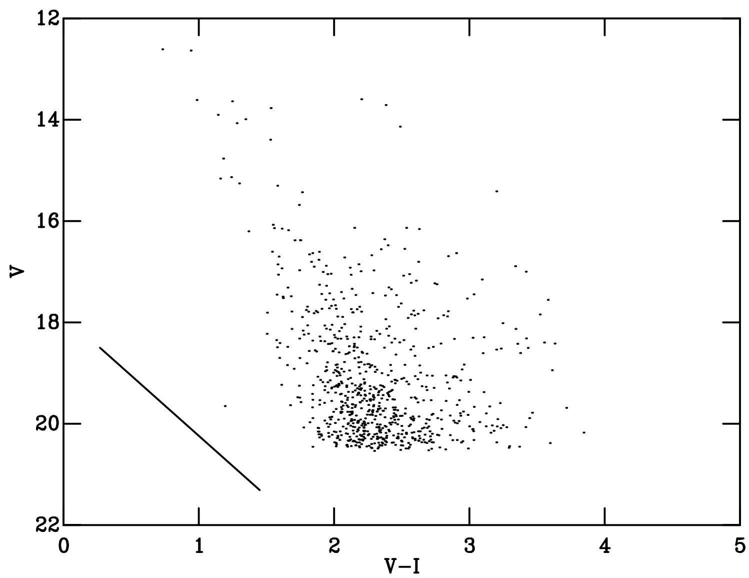

Figure 3.18: Colour-magnitude diagram in V versus (V-I) for the field 3a.

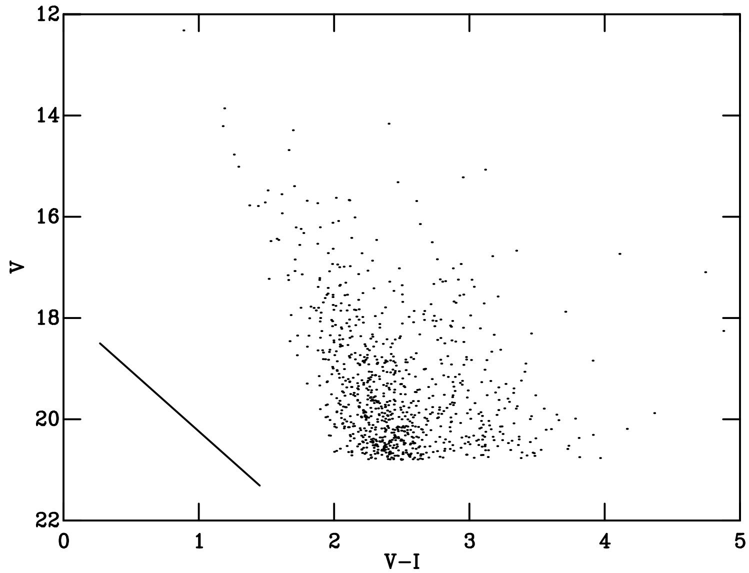

Figure 3.19: Colour-magnitude diagram in V versus (V-I) for the field 3b.

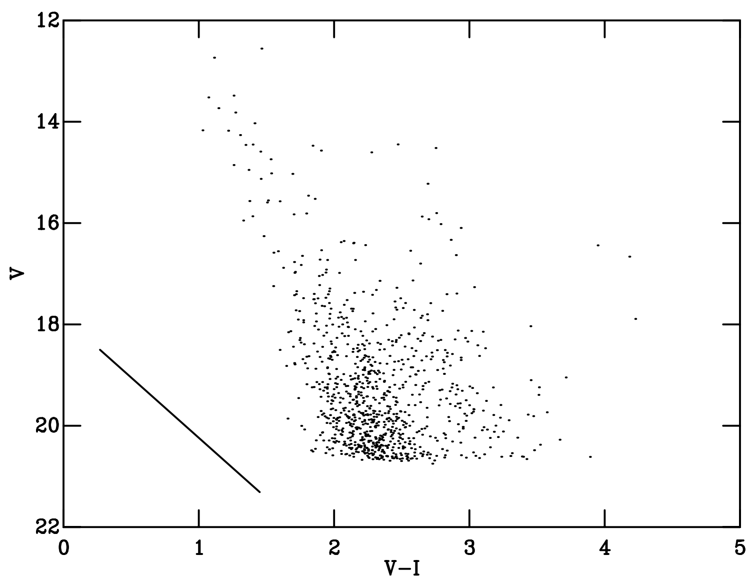

Figure 3.20: Colour-magnitude diagram in V versus (V-I) for the field 4a.

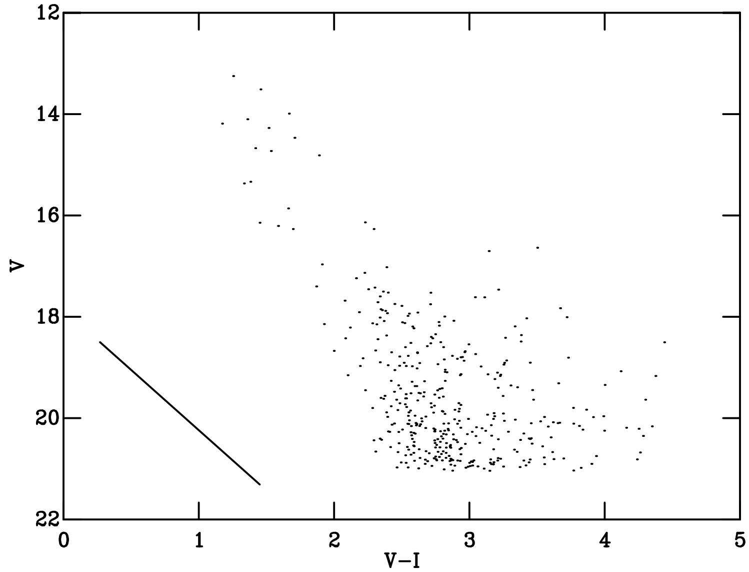

Figure 3.21: Colour-magnitude diagram in V versus (V-I) for the field 4b.

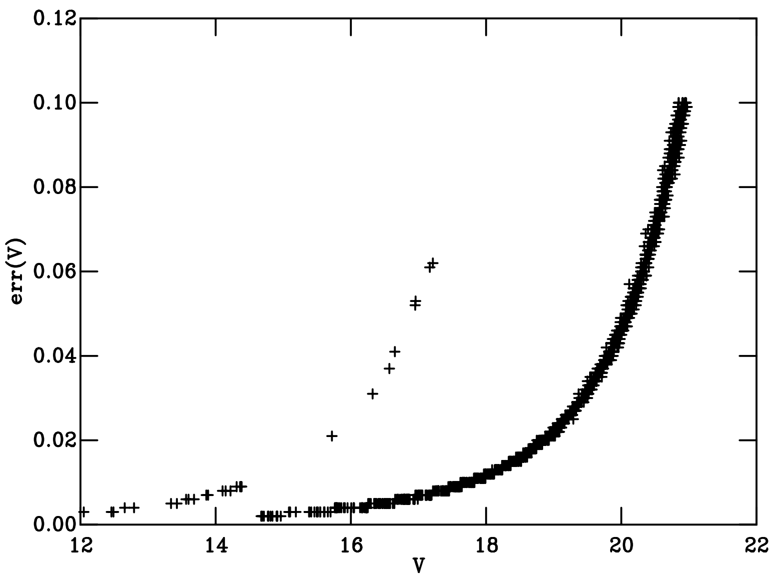

Figure 3.22: Errors in V versus the visual magnitude (field 1a).

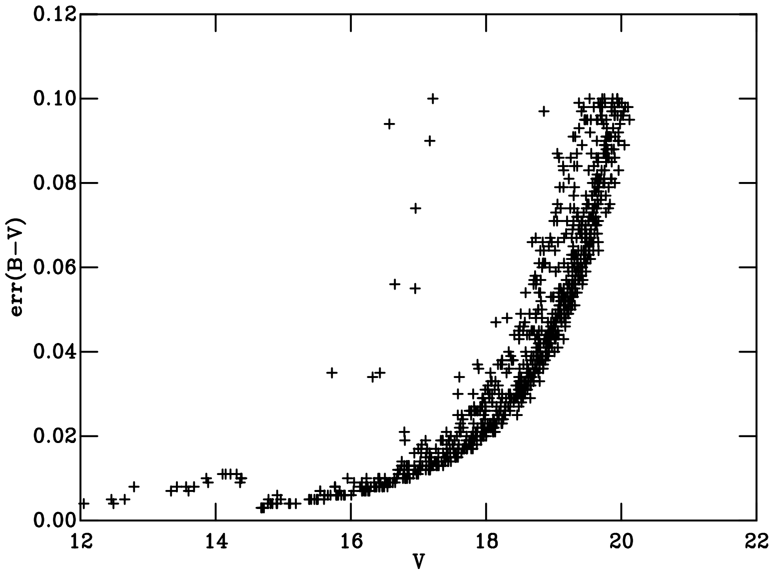

Figure 3.23: Errors in (B-V) versus the visual magnitude (field 1a).

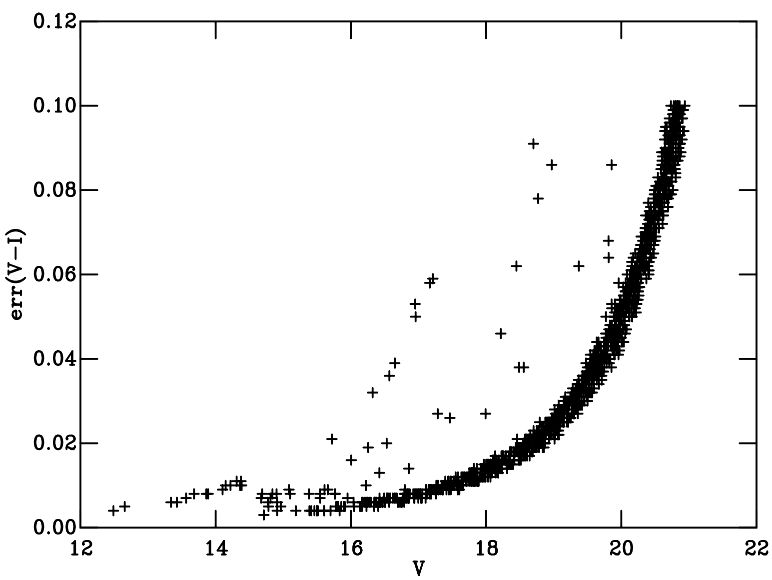

Figure 3.24: Errors in (V-I) versus the visual magnitude (field 1a).

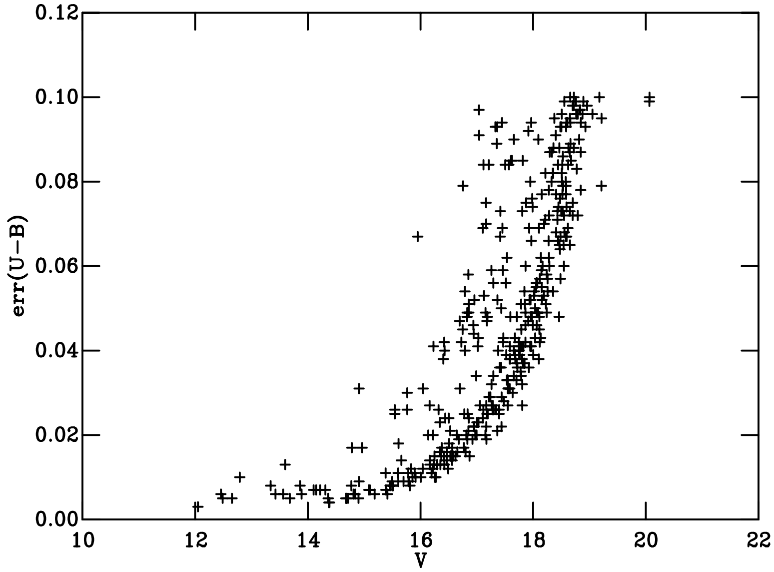

Figure 3.25: Errors in (U-B) versus the visual magnitude (field 1a).

Conversely, the curve at fainter magnitudes represents errors calculated from both short and long exposures. The upper curve at fainter magnitudes was investigated, and it was found that it is due to stars whose V was measured in the short exposure only. A further check on the images, revealed that these stars are stars close to saturated stars with blooming in the long frames, so that the CLUSTER program flagged them because of a possible gradient in the sky, and calculated their V using the short exposure only.

CMDs in V versus (B-V), (V-I) versus (B-V), and (U-B) versus (B-V) for field 1a are also given (see Figures 3.26, 3.27, and 3.28). Analogous plots are found for the other fields.

3.6 What are the stars in the CMDs?

Let us analyse first the CMD in V versus (V-I) for field 1a (see Figure 3.14). Two clear sequences appear in the plot, the obvious deduction is that they represent a general population of background stars and a possible pre-main sequence. But one could also perhaps argue that they are the result of

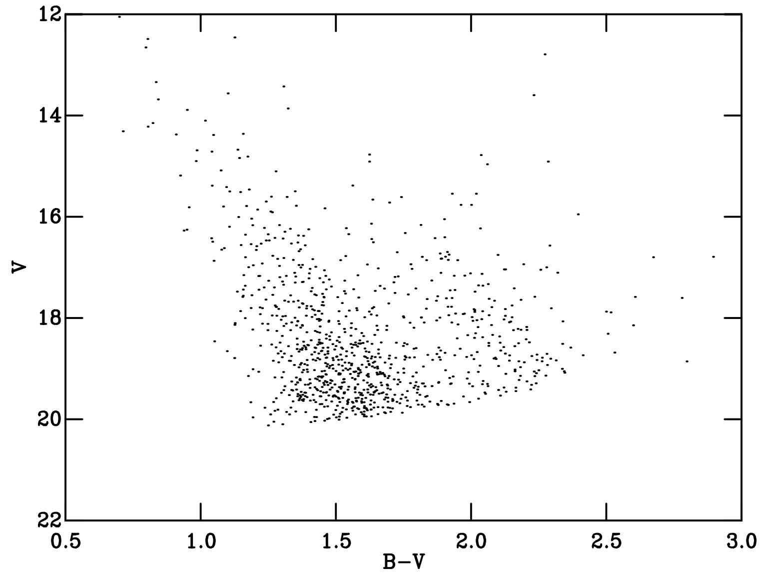

Figure 3.26: Colour-magnitude diagram in V versus (B-V) for the field 1a.

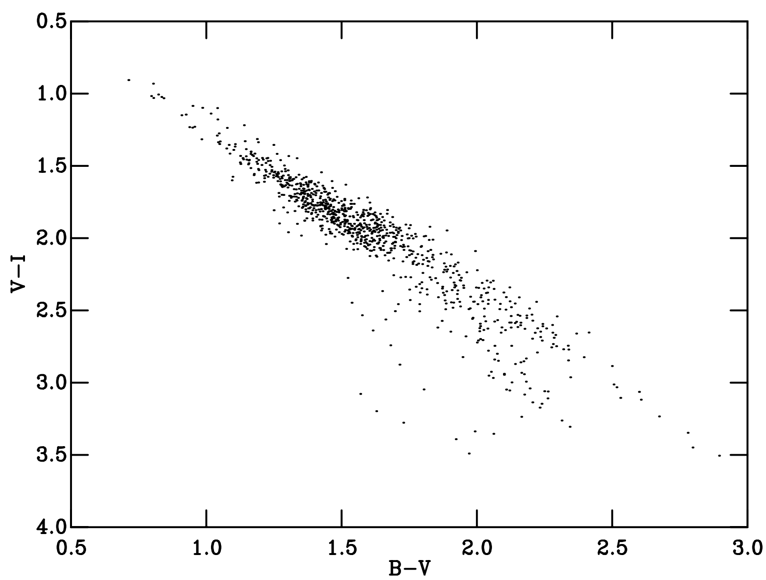

Figure 3.27: Colour-colour diagram in (V-I) versus (B-V) for the field 1a.

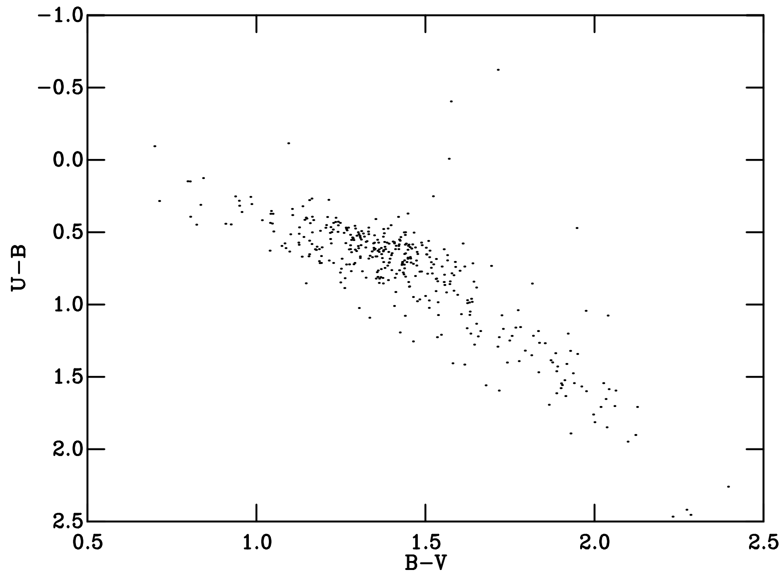

Figure 3.28: Colour-colour diagram in (U-B) versus (B-V) for the field 1a.

an enhancement of the reddening value for some objects with respect to the others, or of an accuracy effect of the data points. The first objection is unlikely to be the case, since the reddening vector is almost parallel to the PMS strip: not only it would be required an additional 3 mag in $< A_V >$ besides the adopted one of 2.81 mag (see Table 3.7) to move one sequence on top of the other in an intrinsic CMD, but this would have to occur on scales much smaller than the CCD size of ~ 12 arcmin, and to affect just the low-mass members, because the early-type members of the subgroup are suffering a spread in extinction of at most ~ 1 mag (see Section 3.1.4). Note that there is a clear space between the two sequences (at least in field 1a) so that a bimodal reddening distribution would be necessary to explain the splitting. Neither can the two sequences be reduced to a single location in the CMD by means of the accuracy of our photometric data, since the internal errors do not cover the separation at all, as can be seen from Figure 3.29.

Therefore, these two sequences are real. They are present in all the other fields (see Figures 3.14 - 3.21), with the exception of field 1b, which is on the cloud and gives an idea of the foreground contamination of stars at smaller distances, plus some possible contribution from PMS stars belonging

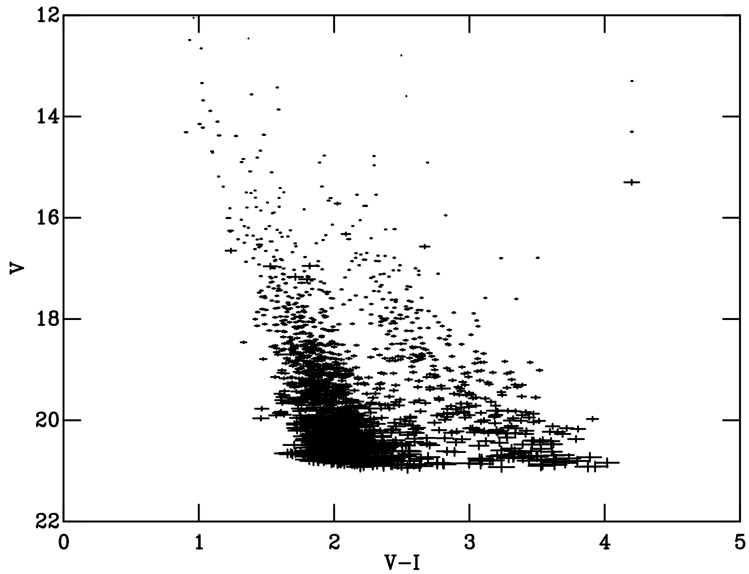

Figure 3.29: The error bars for field 1a data points; plotted also the error bars for V = 12, 17, 20 mag as reference.

to the subgroup but in front of the molecular cloud. In its colour-magnitude plot (see Figure 3.15) the lower part of the first sequence is missing, which therefore must represent a background population. What is left by comparing fields 1a and 1b, apart from background and foreground stars, are the possible association members.

What are the background objects in Figure 3.14, and how far away are they? A first guess could be made if we could plot the number of stars as a function of the apparent distance modulus, $dm + A_V = D$, where dm is the distance modulus, and D can be determined from the relation $D = V - M_V$. The Q-method (Johnson & Morgan, 1953) can uniquely find new possible main-sequence members earlier than A5 (with luminosity classes III and V), because for these stars there is a unique *reddening independent* parameter $Q = (U - B) - 0.72 * (B - V)$, which is smaller than 0.47 (down to negative values, for O and B type stars; a positive value suggesting instead stars later than A5). Q permits us to calculate the interstellar reddening (or colour excess) from the measured $(B-V)$ colour and the intrinsic $(B - V)_0$ colour, according to the relation $(B - V)_0 = -0.009 + 0.337 * Q$. From this, one can find the absolute visual magnitude M_V, and hence $D = V - M_V$, using a standard

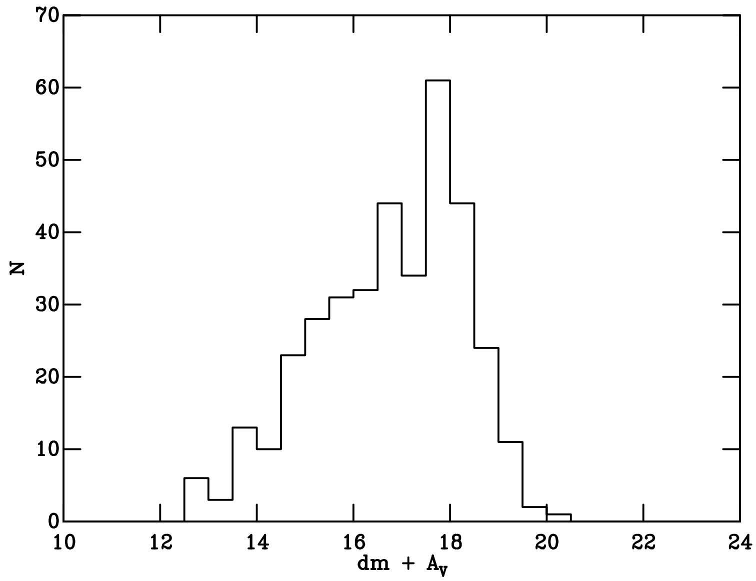

Figure 3.30: Number of stars per $dm + A_v$: the peak for Cep OB3b should be at 12.46. The peaks close to 18 suggest stars belonging to the Perseus and Perseus + I arm.

M_V-$(B-V)_0$ relation. We used the absolute-magnitude versus intrinsic $(B-V)_0$ calibration for the ZAMS stars given by Walker (1985). Only intrinsic $(B-V)_0$ values in the range -0.32 to 0.15 are retained (see also Fitzgerald 1970), and corresponding Q values < 0.47.

Furthermore, note that our catalogue contains stars in the range $V = 12.05 - 21.04$ mag, which, for CepOB3, corresponds to $M_V \sim -0.4$ to 8.5 mag: on the ZAMS, this is equivalent to stars with spectral types B7V to K7V. Therefore, we do not expect to find many objects in Cep OB3 from the Q-method. It should instead reveal the presence of background objects, mainly B stars (since A stars are more common but fainter), concentrated in spiral arms and less than 100 Myr old.

The result is given in Figure 3.30. Stars belonging to Cep OB3b should have $dm + A_V = 12.46$ mag ($dm = 9.65$ mag, $A_V = 2.81$ mag). As we can see from the plot, there is no such peak, suggesting that we are not dealing with stars earlier than A5, at least in the field under examination (i.e., 1a); or at least not A5 stars at the distance of Cep OB3b. But what is notable is the huge peak at about $dm + A_V = 18$ mag, suggesting stars which are much farther away. It is known that Cepheus OB3 is in the Cygnus-Orion arm, between the Sagittarius-Carina arm and the Perseus arm. According to

Georgelin & Georgelin (1976), the latter extends in distance from 2.5 to 5.0 kpc (corresponding to a distance modulus of about 12 to 13.5 mag), but it is at more negative latitudes than Cep OB3, suggesting that the stars in question should not belong to it. A careful search in literature has instead revealed that there are several strands of evidence for the existence of a second arm beyond the Perseus arm (see Kimeswenger & Weinberger 1989, and all the references therein; also Vallée 1995). More precisely, the Perseus arm extends from 1.5 to 2.5 kpc only, whereas the new arm, Perseus + I (according to the nomenclature adopted by Vallée 1995) extends from ~ 3 kpc outward. Noteworthy is that among the optical spiral arm tracers used by Kimeswenger & Weinberger (1989) to detect the distinct arms, there are young open clusters, OB associations and single OB stars which are located at positive latitudes, not only within few degrees of the galactic plane but also up to about $\sim 8°$. Verschuur (1973) postulated the existence of a new arm, named the α-arm, beyond the Perseus arm, extending from $b \sim 0°$ to $b \sim +10°$, which is indeed along the line of sight of Cep OB3b. He also pointed out that at latitudes close to the galactic plane the two arms appear blended one into the other in the latitude-velocity maps, but that "at $b \geq +3°$ the α-arm and the Perseus feature are well separated in velocity".

The main conclusion is therefore that the stars corresponding to the $dm + A_V = 18$ peak belong to the Perseus + I (or α-) arm. Assuming a distance of ~ 5 kpc corresponding to $dm \sim 13.5$ mag, then an A_V value of ~ 4.5 mag for the background stars would be required. This is a reasonable value, as it must be higher than that for Cep OB3b. Obviously one can trade-off the values for distance modulus and the interstellar absorption, but we believe we have proved that there are background stars along the line of sight belonging to the most distant arm in our Galaxy currently known. In the same way, from Figure 3.30, one can argue that stars to the right of the $dm + A_V = 18$ mag peak belong to the same arm as well, whereas those at left probably belong to the innermost Perseus arm.

At a $dm+A_V = 18$ mag, stars in our catalogue, with visual magnitudes in the approximate range $V = 12 - 19.5$ mag and corresponding (B-V) colours between $\sim 0.8 - 1.8$ mag (see Figure 3.26), would have absolute magnitudes between about -6 and 1.5 mag and intrinsic $(B-V)_0$ between -0.7 and 0.3 mag, for a distance modulus of ~ 13.5 mag and $E(B-V) = A_V/R = 1.5$ mag (assuming $A_V = 4.5$ mag and R=3.0). This would suggest that the background population is composed of early-type stars, apparently ruling out the presence of supergiants ($M_V \sim -4.5$ mag, but with $(B-V)_0 \sim 0.4 - 1.6$ mag) and giants ($M_V \sim 0.0 - 1.4$ mag, but with $(B-V)_0 \sim 1.5 - 0.5$ mag). Note, however, that with the Q-method we have discarded stars with $(B-V)_0$ outside the range -0.32 to 0.15 mag: in Figure 3.30 there are only plotted 368 stars out of 1462 for which we have (B-V) colours (see Table 3.18), and so just 25 % of the stars detected in field 1a. The other 75 % of background objects are most likely to be G and K dwarfs and giants, with $M_V \sim 1-6$ mag, distance moduli of 8-14 mag and extinction values ≤ 4 mag. These objects have $(B-V)_0$ too red for the Q-method to work.

3.7 Cross-correlation with data in literature

3.7.1 Cross-correlation with other optical photometric catalogues

The majority of the work in the literature on the Cep OB3 association, are studies of the BHJ stars classified by BHJ. Besides these, there are some authors who studied the Cep OB3 region from a general point of view. Särg & Wramdemark (1970) presented photoelectric photometry of early-type stars in a Milky Way field in Cepheus, and Jordi et al. (1992) performed Strömgren photometry for 45 stars in the association. We have not tried a cross-correlation with their catalogues, since all their observed stars are brighter than ours (respectively $V < 11.54$ mag and $V < 10.72$ mag, whereas we have stars with V> 12 mag).

We cross-correlated our optical catalogue with the catalogue of J95. They observed 1056 stars from 18 randomly selected fields in Cep OB3, 7 in the old and 11 in the young subgroup. Their catalogue contains 1056 stars with $V = 8-21$ mag, with complete photometry in all the colours down to $V = 15.5$ mag for just 130 stars.

In Figure 3.31, the V versus (V-I) colour-magnitude diagram derived from J95 is shown on the same scale as Figs. 3.14 to 3.21. By comparing it with the CMD we have for just the field 1a (see Figure 3.14), we can see that the pre-main sequence is less defined, almost imperceptible. This is a dilution effect, due to the fact that their total number of stars is less than half the number we have in just one field, and that the objects belong to fields scattered all over the Cep OB3 region, with a field of view of just $3.0' \times 4.4'$ each. Therefore, for the first time, thanks to a wide surveyed area and deep photometry, we have been able to unambiguously detect a low-mass pre-main sequence in the Cep OB3 association.

We cross-correlated our optical catalogue with the J95 catalogue searching for correlations within

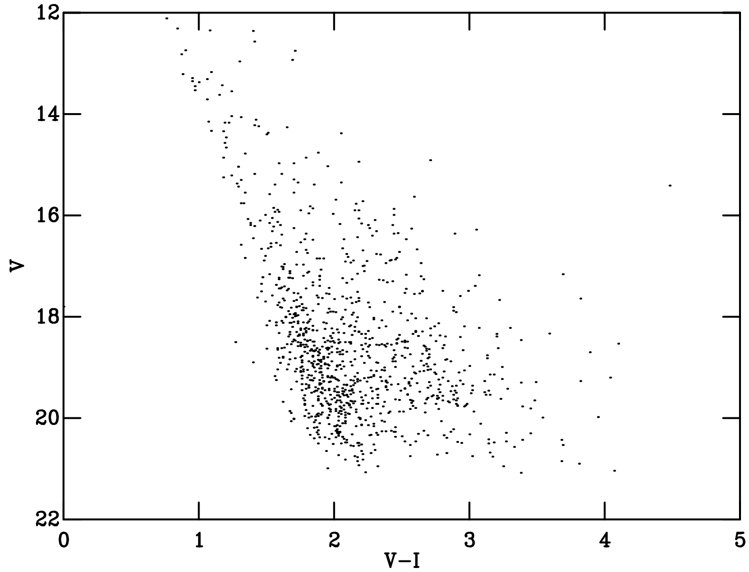

Figure 3.31: The V versus (V-I) colour-magnitude plot for data obtained by J95.

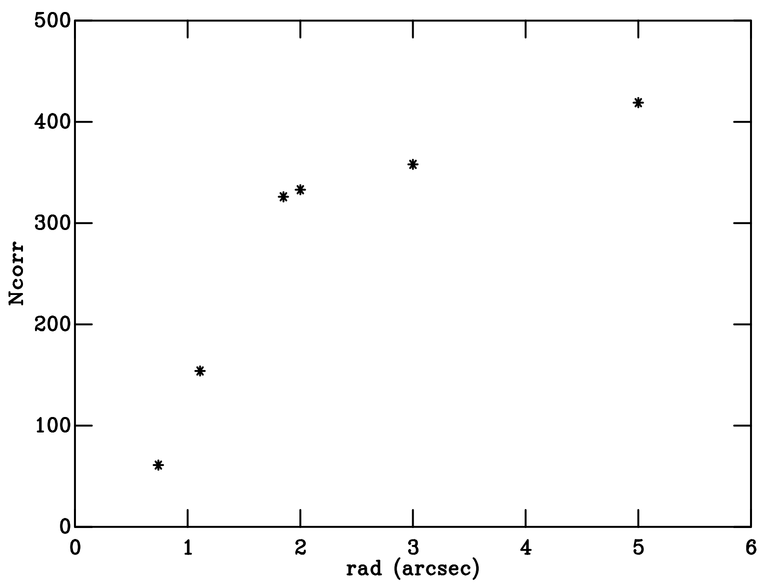

Figure 3.32: Cumulative distribution of the number of matches our optical catalogue - J95 catalogue as a function of the searching radius. The cross-correlation radius giving the maximum number of correlations without introducing too many spurious objects is found to be of 1.85”.

Error	this work	J95
V	0.02	0.06
(B-V)	0.05	0.15
(V-I)	0.02	0.06
(U-B)	0.02	0.12

Table 3.14: Comparison of photometric errors of this work and J95, for a visual magnitude of V=19 mag for BVI colours, and V=17 mag for (U-B) colour.

an increasing radius. We then plotted the cumulative distribution of the number of matches obtained at different radii (see Figure 3.32). The number of counterparts to the optical sources is obviously a function of the search radius, but should flatten towards larger values, once the majority of the counterparts have been found. The radius beyond which there is a further increase in the number of correlations can be taken as the correlation radius at which we have obtained the maximum number of counterparts before spurious correlations contribute significantly to the distribution. This was found to be 1.85 arcsec (corresponding to 5 pixels on the CCD frames). Such big differences in positions are probably due to J95 astrometric errors, because our mean astrometric accuracy is of about 0.4". J95 used reference stars from the Guide Star Catalogue (GSC; with astrometric precision of 0.25" (see Lasker et al. 1990), but they obtained an astrometric accuracy worse than 1" since the number of GSC reference stars falling on their fields is quite small. The limiting magnitude of the GSC in the Cep OB3 region is about V= 14 mag, therefore most of their fields contain just two reference stars.

We found 326 matches in total (within the correlation radius of 1.85"), for stars in fields 1a, 2a, 2b, and 4b. Tables A.1, A.2, A.3, and A.4 (see Appendix A) show just a few entries for matched stars in the different fields. All the information available (i.e., id number, astrometric coordinates, photometric colours, associated errors, and flags) is given for the matched stars from both catalogues.

In Figure 3.33 we compare our CCD measurements for V with the optical data given by J95 (both full catalogues, without restriction on the photometric errors), finding no systematic trend and a mean difference of about 0.04 mag. Analogously for (V-I), (B-V) and (U-B) colours, with mean differences of about 0.08, -0.04 and 0.06 mag respectively. The higher dispersion noticeable for fainter

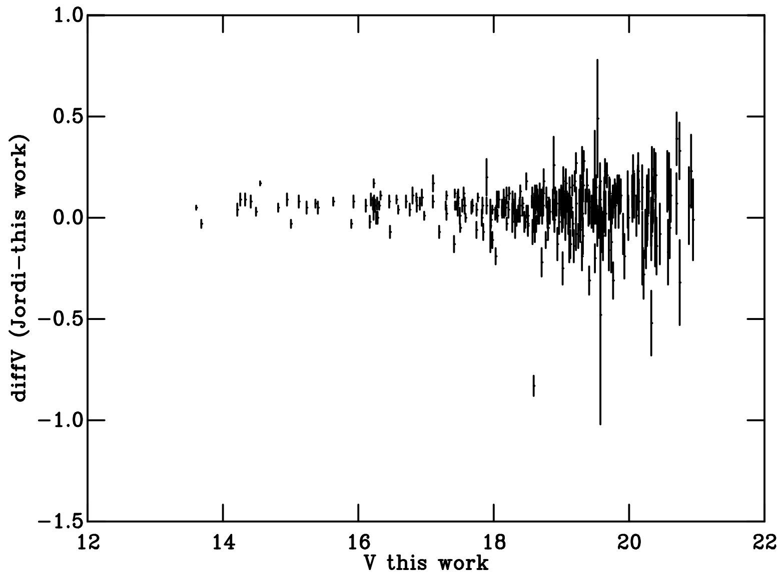

Figure 3.33: V magnitude differences J95 - this work versus visual magnitudes from this work.

stars is an effect due in part to larger errors in the J95 catalogue, in part to some faint stars in our catalogue which are affected by light from a close saturated star, and for which quite large errors were indicated by the OPPHOT program. However, note that we will perform our subsequent analysis on just good stars in our optical catalogue: for these, at a given magnitude, our colours have errors far smaller than those by J95. As an example, we report the error values for different colours at a given magnitude in Table 3.14.

3.7.2 Cross-correlation with X-ray sources

We also cross-correlated our optical catalogue with the (0.1-2.4 KeV) X-ray sources recently detected by NF99 with the Position Sensitive Proportional Counter (PSPC) and the High Resolution Imager (HRI) on board the ROSAT satellite. There are a total of 56 distinct X-ray sources, although some of them could be multiple. For 23 of them, NF99 found an optical counterpart in the magnitude range $7.6 < V < 16.8$, leaving 33 unidentified sources. The number of X-ray sources found by NF99 is well above the number of contaminating foreground and background objects (i.e., active field stars and

AGN), which they estimated to be just 4. The suggestion made by NF99 that these X-ray sources may be young T Tauri stars is strongly supported by both the ratio of X-ray to optical luminosity for the faintest objects, and by their X-ray variability, with values typical of other PMS associations (see Montmerle et al. 1993).

We then determined the separations between the X-ray sources and our possible optical counterparts, and accepted correlations within 15" of a PSPC position, and 7" of a HRI position because the HRI positions are more accurate (NF99). When more than one optical counterpart was found, the brightest was then chosen because X-ray luminosity is approximately proportional to the optical luminosity (see Feigelson et al. 1993).

We find a total of 10 counterparts to the NF99 X-ray sources with good photometry, as listed in Table 3.15.

For completeness, in Table 3.16 we list the number of optical counterparts not considered for further analysis: one is rejected (*) because it is too faint with respect to the visual magnitude reported by NF99 (the other two counterparts are even fainter); another one (+) because of photometric errors > 0.1 mag, and therefore not useful for the subsequent analysis; the remaining ones because of flagged colours. Note that stars which have been assigned the non-stellar flag (i.e., 1), could be double stars.

Figure 3.34 shows the location of the 10 optical counterparts (red crosses) to the X-ray sources of NF99 (black crosses) with respect to the CCD fields. The majority of them belong to field 1a, and seem to lie solely in the pre-main sequence part of the CMD (see Figure 3.35), as we might expect for young, active stars. Note that the two counterparts belonging to field 2b are embedded in the Hα nebulosity, on the edge of the molecular cloud, and might be expected to be suffering from higher reddening. In particular, source 48 (associated with our star at V=15.15 and V-I=1.51 mag) is considered to be a "heavily reddened early-type star emerging from the molecular cloud" by NF99. According to the results we have found in Chapter 4 (see object no. 9 in Table 4.4), its optical counterpart is not a member of the association.

Finally, we derived the number of random correlations to be expected among those found. For this purpose, we repeated the cross-correlation by shifting the X-ray positions of NF99 by 20" north, south, west and east, and retaining only acceptable correlations according the criteria used before. The probability of having a correlation with one of the shifted X-ray sources is reported in Table 3.17, for PSPC and HRI respectively. Also tabulated are the number of good correlations found with the

X-ray id.	V (NF99)	n.c.	sep.	Field	id.	RA (J2000)	dec (J2000)	V	V-I
14 (P)		6	8.4”	1a	176	22 55 30.10	+62 47 39.35	16.94	2.18
20 (P)		1	8.2”	1a	374	22 56 01.55	+62 47 46.84	17.94	2.74
24 (H)		7	3.5”	1a	420	22 56 18.34	+62 45 16.66	18.14	2.80
26 (P)		7	3.9”	1a	191	22 56 20.15	+62 52 23.30	16.79	2.44
27 (H)	15.3	10	5.6”	1a	57	22 56 26.39	+62 41 29.58	15.38	1.91
29 (P)	15.5	6	9.2”	1a	55	22 56 29.67	+62 45 28.52	15.66	1.96
34 (H)	14.2	5	2.5”	2b	22	22 56 38.75	+62 37 14.46	14.55	2.26 (**)
35 (H)	14.9	7	4.1”	1a	32	22 56 39.07	+62 45 09.28	14.91	1.89
44 (P)	13.5 (GSC)	3	6.8”	1a	23	22 56 56.47	+62 52 42.83	14.36	1.48 (*)
48 (P)		2	13.4”	2b	31	22 57 05.28	+62 38 39.01	15.15	1.51

Table 3.15: Optical counterparts to the X-ray sources of NF99. X-ray source number and visual magnitude from NF99 are given respectively in columns 1 and 2. (P) is for PSPC, (H) for HRI. The number of correlations found within a 1.85” radius is given in column 3. Column 4 refers to the separation to the brightest optical counterpart (see also the text) belonging to the field specified in column 5 (as given in Figure 3.2) and with id number reported in column 6. Columns 7 - 10 list the positions, visual magnitude and (V-I) colour of the optical counterpart. (*) this object is very close (8 pixels, corresponding to 2.96” on the sky) to another star not numbered in the catalogue: possible binary? (**) this object is cross-correlated with BHJ40-096 (J96), and is K type according to NF99.

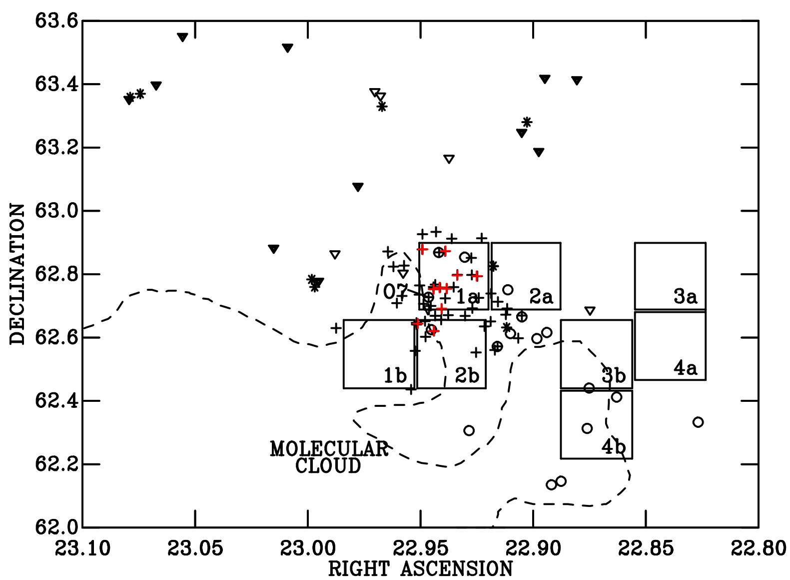

Figure 3.34: The location of the 10 optical counterparts (red crosses) to the X-ray sources of NF99 listed in Table 3.15. X-ray sources of NF99 for which we do not have an optical counterpart are shown as black crosses. Other symbols as in Figure 3.2.

X-ray id.	sp.type	V (NF99)	n.c.	sep.	Field	id.	V	V-I	comment
8 (H)	(late-B, early-A)	11.9 (BHJ)	3	6.4”	2a	4			F4,(c)
13 (H)	(late-K type)	15.3	6	3.9”	1a	29			F8
15 (P)		15.1	3	8.4”	2b	772	20.30	3.60	(*)
16 (P)		16.8	1	4.5”	1a	59			F2
18 (H)		12.1 (GSC)	5	6.4”	1a	9			F1,(a)
21 (H)	(early type)	12.1	10	3.9”	1a	8	12.05		F4 in I
32 (H)	(K type)	15.2	4	4.2”	1a	51			F1
37 (P)			3	14.2”	1a	17			F1
38 (P)			6	9.6”	1a	1264	21.20	1.46	(+)
39 (H)	(O7n type)	7.7 (BHJ)	1	0.0”	1a	1			F4,(b)
42 (H)		15.4	3	2.6”	1a	71			F1

Table 3.16: List of optical counterparts to the X-ray sources by NF99, falling on our CCD fields, but not considered for further analysis. (P) is for sources detected with PSPC, (H) for those detected with HRI. Spectral types and visual magnitudes in columns 2 and 3 are from NF99, unless otherwise specified. The number of optical counterparts found to the X-ray sources is given in column 4, the separation to the brightest one in column 5. Columns 6 - 9 give respectively the field (as in Figure 3.2) and id number, V and (V-I) colour (only if unflagged) of the optical counterpart. (*) this counterpart is considered unreliable because too faint with respect to the visual magnitude given by NF99. (+) this counterpart is rejected because of photometric errors > 0.1 mag. The other couterparts are rejected because of flagged colours, see last column (F is followed by the flag number according to Tables 3.10 and 3.12). (a), (b) and (c) are cross-correlated with BHJ34-011 (J96), BHJ 41, and BHJ 27.

range	Prob(PSPC)	Prob(HRI)	N(PSPC)	N(HRI)	N_r(PSPC)	N_r(HRI)
V < 15.15	0.02	0.02	1	2	0	0
V < 16.15	0.05	0.02	3	3	0	0
V < 17.15	0.06	0.04	5	3	0	0
V < 18.15	0.10	0.09	6	4	1	0

Table 3.17: Probability of finding a correlation (the brightest) with a shifted PSPC and HRI X-ray source respectively, the number of correlations with the original X-ray sources, and the number of random correlations expected in the V range shown.

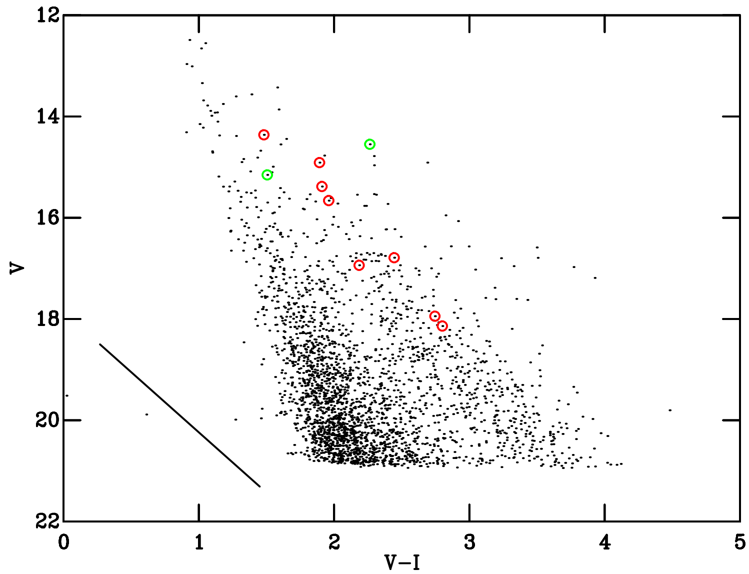

Figure 3.35: The colour-magnitude plot for fields 1a and 2b plotted altogether, with the 10 optical counterparts to the X-ray sources of NF99. The X-ray sources falling in the field 1a are shown as red circles, whereas the two on field 2b are shown as green circles. Also plotted the reddening vector, with $< A_V >= 2.81$ mag and $E(V-I) = 1.18$ mag (see Table 3.7 in Section 3.1.4). Note that the counterparts in field 2b are suspected to be heavily reddened (see text).

original X-ray sources in the corresponding V range, and the number of random correlations for PSPC and HRI respectively. We therefore expect at most one out of the 10 optical counterparts to be a random correlation. More precisely, one of the 6 which are correlated with a PSPC X-ray source.

3.8 Isochrone fitting

How old are the PMS objects? Is there an age gradient within the same field? Is there an age gradient across the Cep OB3b association?

To answer to these questions we have to compare the colour-magnitude plots in V versus (V-I) for different fields by means of isochrone fitting (see Chapter 1, Subsection 2.2.3).

If one can fit the PMS stars in one field with different isochrones, the most tempting conclusion would be a spread in ages. However, there are several factors which can contribute to cause such a spread: these are binarity, photometric errors, a spread in distance, and differential reddening.

About 50 % of low-mass PMS stars are multiple systems. As an example, Simon et al. (1992)

found 11 binaries and 2 triples out of 28 young stars in the Taurus star forming region, and Ghez et al. (1993) found 33 binaries in their sample of 69 TTS in the Taurus-Auriga and Ophiucus-Scorpius star forming regions. Unresolved binarity can produce objects that are brighter than single stars. The global effect gives stars scattered above the isochrone by up to 0.75 mag depending on the mass ratio (see Hurley & Tout 1998; see also Preibisch & Zinnecker 1999). The scatter caused by unresolved binaries has the effect of widening the isochrone to a band. If a star is an unresolved binary, it appears brighter, since two stars are really contributing to its visual magnitude, and its age is consequently underestimated because it is fitted by a younger isochrone (the maximum effect is given in the case of two identical components). Similarly, if the star is closer (or further away) than the mean adopted distance to the association, it is fitted by a younger (older) isochrone. Reddening values to the early-type members of the association are known (see Subsection 3.1.4). However, testing the case of differential reddening across the same CCD field is difficult, as one really needs spectroscopic observations in order to infer interstellar reddening from the derived spectral types and the measured colours. In the case that isochrones of different ages are required to fit the PMS in different fields, after having taken into account of the others factors discussed above, there could be a spread in ages across the association; but it would leave also open the possibility of a large-scale reddening variations within the region. We will analyse all these possibilities in detail in one field first, and then from one field to another.

Since the OB stars present in the association have not swept away completely the material (gas and dust) of the parental molecular cloud in the Cep OB3b subgroup (see also the Palomar Sky Survey image in Figure 3.1), we would perhaps expect some differential extinction and reddening across the region, with smaller values in regions close to the early-type members of the subgroup. In other words, we would expect a larger extinction for stars belonging to the westernmost fields with respect to field 1a, but, at the same time, a larger extinction for stars closer to the CO contour (see also Subsection 3.1.4).

Isochrones are taken from the evolutionary models of D'Antona & Mazzitelli (1997; DAM97), which make use of updated turbulent fluxes by Canuto, Goldman & Mazzitelli (1996) to describe the evolution of low-mass stars ($3.0M_{\odot} < M < 0.05M_{\odot}$). DAM97 isochrones are produced in $L_{bol} - T_{eff}$ coordinates, and were converted to absolute magnitudes M_V and intrinsic colours $(V-I)_0$ using empirical bolometric corrections of Bessell (1991; for T_{eff} < 4500 K) and Flower (1996; for hotter stars) and a (V-I,T_{eff}) relationship derived by forcing the low-mass stars in the Pleiades cluster to fit a 120 Myr isochrone (see Jeffries & Tolley 1998). These isochrones are valid for intrinsic $(V-I)_0$ in the range $0.0-4.2$ mag (the extent of the calibrating Pleiades data), and masses in the range $3M_\odot < M < 0.15M_\odot$. In the following Sections (see Figures 3.36 and 3.37) we plot isochrones corresponding to 1, 10, and 30 Myr, applying extinction ($A_V = 2.81$ mag), reddening ($E(B-V) = 0.91$ mag) and distance modulus ($dm = 9.65$) adopted for Cep OB3b (see Table 3.7).

Let us now analyse the different causes which may contribute to the observed spread.

3.8.1 Scatter within a CCD field

For field 1a (see Figure 3.36 [left]), one can see that the X-ray sources are likely to be 1-10 Myr old, in agreement with the age ($\sim$ 7 Myr) determined for the B-type members of the younger subgroup (see Table 3.4 and related discussion in the text). Note that there is a lack of stars between the 10 and 30 Myr isochrones: this clearly defines the PMS locus in the CMD - the bulk of which occupy the region between the 1 and 10 Myr isochrones with a few at even younger ages.

The vertical spread of the pre-main sequence objects around the isochrone is of about 3 mag. This is more than the spread expected as effect of unresolved binaries (0.75 mag) plus our photometric errors for V (less than a hundredth of a mag up to V= 17.5, and $\sim$ 0.05 mag up to V= 20.0 mag; see Table 3.13). Furthermore, also allowing for a spread in distance, which is at most 0.5 mag for the Cep OB3b members, we could explain a spread of about 1.3 mag at most, well below the observed value. Note that Preibisch & Zinnecker (1999) found a similar PMS CMD for stars in the Upper Sco OB association, finding a spread of about 1.2 mag, which they explained as the effect of unresolved binaries, photometric errors and spreads in distance. They concluded by saying that a small spread in ages cannot be excluded, but that it is probably not larger than about 2 Myr. Our spread is almost three times larger, and therefore binarity, photometric errors and spread in distance cannot be the sole cause of the spread.

The case of a spread caused by differential reddening within the same field is less likely, for several reasons. As one can see from Figure 3.36 (left): the background population appears to be tightened to a well defined sequence; the slope of the reddening vector is almost parallel to the pre-main sequence isochrone; a change in extinction of about 3 mag in A_V would be required to explain

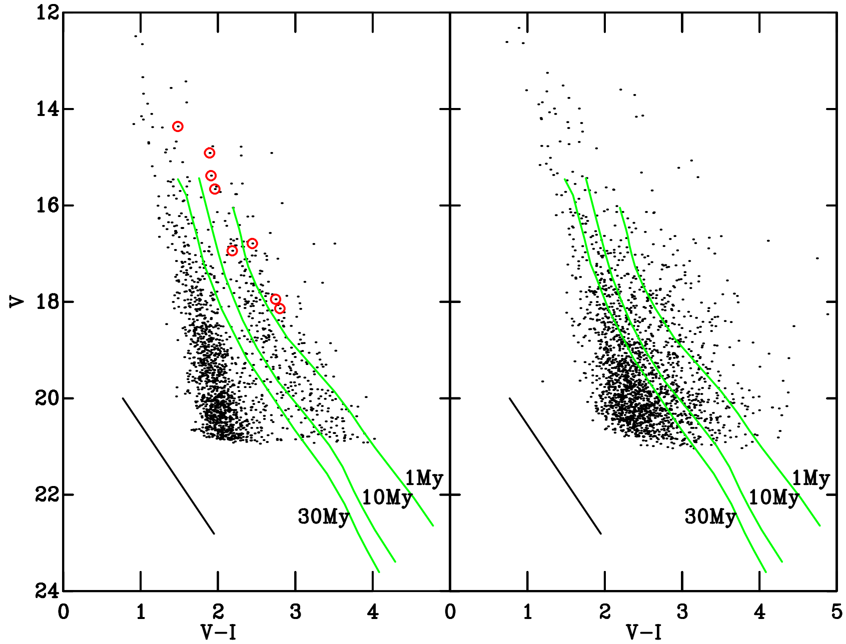

Figure 3.36: Isochrones for 1, 10, and 30 Myr (D'Antona & Mazzitelli 1997) for the field 1a (left), and fields 3a, 3b and 4b (right). The X-ray sources in field 1a are shown as red circles. Also is plotted the average reddening vector for Cep OB3b (see Table 3.7).

the spread around the isochrone; and it would have to occur on scales much smaller than about 12 arcmin (the size of a CCD field). Last, but not least, these changes in extinction should preferentially affect the low-mass stars: the OB-type members of the subgroup, in fact, are suffering a small scatter in extinction of at most 1.2 mag (see Table 3.7).

This leaves open the possibility of a real spread in ages across the field. It could be caused by mass accretion on the birthline or later (see also Section 2.3 in Chapter 2). Low-mass stars are not greatly affected by mass accretion, whereas high-mass stars are not affected at all. However, a 1 $M_\odot$ PMS star accreting at 10^{-7} $M_\odot$/yr (see Tout, Livio & Bonnell 1999) would *appear* to be $>$ 10 Myr when it is only 5 Myr old. Since our stars are in the mass range $1.9 - 0.6$ $M_\odot$, the age spread of a few Myr we are observing could be explained only in the presence of a high accretion rate: PMS stars would have to accrete a significant fraction of their mass after arriving on the birthline.

The more likely cause of the age spread, seems therefore to be ascribed to stars which start to collapse at different times (see Section 2.3 in Chapter 2). Low-mass stars can be subject to a very slow phase of ambipolar diffusion, which can last up to 10 Myr (see Palla & Galli 1997) and produce a scatter in ages which is a significant fraction of this time. Low-mass stars remain in the protostellar phase until an external trigger obliges them to cross the birthline through the collapse of the protostellar core and the dispersion of the protostellar envelope. At that time they become optically visible and then, and only then, their isochronal clock is set to 0. At an age of about 1 Myr they are visible as T Tauri stars: approximately half of them are still surrounded by accretion discs (Strom et al. 1993; Edwards 1993, and references therein) which can survive as long as 10 Myr (see Strom et al. 1989a; Skrutskie et al. 1990; Preibisch & Zinnecker 1999).

In conclusion, after taking into account of binarity, photometric errors, spread in distance and a small amount of differential reddening, we are still left with a vertical spread of about 0.5 mag in the CMD. This spread in magnitude corresponds to an apparent spread in ages of about ± 2.5 Myr (according to isochrones of D'Antona & Mazzitelli 1997), which can be explained as the result of stars starting collapse at different times being hold on the birthline due to a prolonged disc accretion phase or to ambipolar diffusion.

3.8.2 Scatter between different CCD fields

For a comparison among different fields, one has to keep in mind that the number of stars we have detected in each field varies with their position on the sky, with the consequence that the number of objects in the PMS strip varies too, biasing its appearance. We therefore derived the number of stars for which we have visual magnitude and (V-I) colour in each of them. The values are reported in Table 3.18, together with the number of stars in the other colours for completeness.

Field 1a has the highest stellar density, therefore, to have a comparison field with the same number of stars, we added altogether 3 fields in Cep F (i.e., 3a, 3b and 4b). The resulting colour-magnitude diagram in V versus (V-I) is given in Figure 3.36 (at right). It is clear from the plot that the isochrone fitting does not show a clear gap between 10 and 30 Myr anymore, and it seems that there are more objects younger than 1 Myr. It is also clear that the overall distribution of background sources is broader, strongly suggesting varying extinction across these fields. This is strongly suggesting that we are in the presence of fields more reddened than field 1a (see also Figures 3.14 to 3.21).

We tried to address this by asking what are the stars that fill the gap between the 10 and 30

Field	$N_{V,V-I}$	$N_{V,B-V}$	$N_{V-I,B-V}$	$N_{U-B,B-V}$
1a	2128	1462	1402	899
2a	1702	1138	1120	531
3a	848	434	418	203
4a	1073	635	607	315
1b	310	187	173	118
2b	1251	760	718	459
3b	1084	621	594	323
4b	499	279	257	164

Table 3.18: Number of stars plotted in the CMDs in V versus (V-I) for the different fields, after filtering out stars with bad flags and/or errors > 0.1 mag. Also given the number of stars available in the other colour-magnitude diagrams.

Myr isochrones in fields 3a, 3b and 4b? We found that it is possible to match by hand each of the three westernmost fields with field 1a, by superimposing one on top of the other and shifting them up and to the left (i.e., dereddening them), along the reddening vector, by a certain amount. Matching the position of their background sequences to that in field 1a, their PMS go to occupy almost the same locus of the PMS of field 1a. This means that the westernmost fields indeed appear to be more reddened than field 1a. As an example, we have found that dereddening field 4b by an $A_V = 1.4 \pm 0.2$ mag, produces a shift in the direction of the reddening vector which brings the background sequence into agreement with that in field 1a (see Figure 3.37). In other words, field 4b is suffering a total extinction of $A_V = 2.81 + 1.4 = 4.21$ mag and a global $E(V - I) = 1.18 + 0.6 = 1.78$ mag.

The same argument holds for the other CCD fields, and Table 3.19 gives the additional extinction derived with respect to field 1a (apart from field 1b, which is looking at the cloud and gives us the foreground contamination, therefore the comparison with the background sequence of field 1a was not possible). Therefore, the majority of the stars filling the gap between the 10 and 30 Myr isochrones in the westernmost fields are background stars which are shifted towards redder colours.

If we have a look at the position of field 4b in Figure 3.2, we can see that it is the field which is more on-cloud (besides field 1b, which is in front) with respect to the others. Furthermore, it contains two BHJ stars for which the reddening is known: BHJ 8 (at N-W) and BHJ 11 (a non-member, about

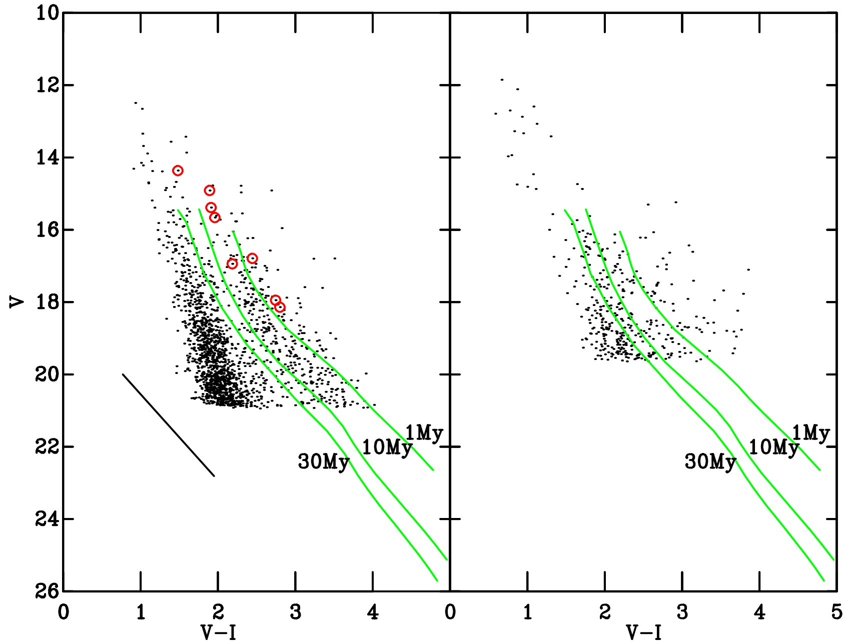

Figure 3.37: The colour-magnitude diagram in V versus (V-I) of field 4b (at right), dereddened of its additional extinction value (see Table 3.19) in order to be compared with that of field 1a (at left). The background sequences appear now to have about the same location in the diagram. The X-ray sources of NF99 are shown as red circles. Also plotted the mean reddening vector for Cep OB3b and isochrones for 1, 10, and 30 Myr (D'Antona & Mazzitelli, 1997).

ΔA_V(2a)	ΔA_V(3a)	ΔA_V(4a)	ΔA_V(2b)	ΔA_V(3b)	ΔA_V(4b)
0.15 ± 0.10	0.6 ± 0.2	0.5 ± 0.2	0.5 ± 0.1	0.8 ± 0.2	1.4 ± 0.2

Table 3.19: Additional extinction suffered by different fields with respect to the reference field 1a (it was not possible to derive a value for field 1b, since it is the one more on-cloud: it gives an idea of the foreground contamination and the background sequence is missing).

in the center), having respectively $A_V = 2.71$ and $A_V = 4.27$, from values given by Moreno-Corral et al. (1993). Two other stars, BHJ 15 and BHJ16, which are outside field 4b (at its S-E) have respectively $A_V = 3.54$ and $A_V = 3.19$. The total A_V we derive for field 4b in the hypothesis of a differential reddening is of 4.01 mag. What is responsible for this? Maybe an extra clump of molecular material and dust in between us and the stars detected in this field?

If we combine the information given in Table 3.19, about the additional extinction estimated to be suffered by the different fields, with the location of the fields on the sky (see Figure 3.2), we have an idea of the distribution of the reddening across the Cep OB3b subgroup. It appears that the reddening is decreasing as a function of distance from the CO contour, towards the older members. The extinction is higher for field 2b than for fields 1a and 2a; for field 3b than for fields 3a and 4a; or for field 4b, with respect to fields 3a and 4a. However, at the same time, from our results it is clear that fields 1a and 2a, which contain early-type members of the younger subgroup, are suffering a lower extinction, whereas, by contrast, fields 3a and 4a which not only do not contain, but are also farther away from other, early-type members are suffering a slightly higher extinction.

Therefore, after allowing for reddening in fields other than 1a, the background sequence and the PMS can be matched quite well on the corresponding sequences in field 1a: the spread of PMS objects around the isochrones appears to be almost the same as that found in field 1a. Taking into account additional reddening and recalling the same arguments to explain this possible spread as effect of binarity, photometric errors and spread in distance as discussed in Section 3.8.1, we deduce that there is a real spread in ages in all the fields. Note, however, that the westernmost fields do appear to contain both younger objects and objects more evolved towards the ZAMS than those in field 1a, giving an apparent larger spread in ages: we interpret this with the same arguments discussed in Section 3.8.1, i.e., stars collapsed at different time.

This is in disagreement with the sequential model of star formation, which would predict bursts of star formation every few Myr as the cloud retreats along a south-eastern direction (see Subsection 3.1.7). Since the velocity of the ionisation front is of about 2 km/s (see Subsection 3.1.5), it would have taken about 5 Myr to cover the distance of ~ 10 pc between the westernmost fields (3a and 4a) and the easternmost fields (1a and 2b). This would imply that stars in field 1a would have to be about 5 Myr younger that those in fields 3a-4a, and this is not what we actually see.

3.9 Summary and conclusions

Summarising the main issues discussed above, after having taken into account of all the possible causes which may contribute to the apparent vertical spread around an isochrone (i.e., unresolved binaries, photometric errors and spread in distance, as well as possible differential reddening within a CCD field; see Subsections 3.8.1 and 3.8.2), we can say that we do not see the required age gradients of about 1.2 Myr from field to field across the younger subgroup of the association, as one would have expected from the popular sequential scenario: this would have implied that newly born stars in the westernmost fields were about 5 Myr older that those of the easternmost fields, as they are unveiled by the retreating molecular cloud. Furthermore, after allowing for reddening across the subgroup (the westernmost fields appear to be more reddened that the easternmost ones), the background sequence and the PMS appear to occupy almost the same location in the CMD of each of the fields. We are therefore in favour of a "contemporaneous" model of star formation in the younger subgroup of the Cep OB3 association, i.e., of star formation possibly triggered by a supernova explosion.

The observed spread in ages in a single field, may be caused by mass accretion on the birthline or later only if the fraction involved is significant with respect to the stellar mass. Therefore, we are in favour of an age spread occurring before the birthline, possibly caused by different timescales in ambipolar diffusion: the collapse may start earlier for some stars with respect to others.

However, we must note that patchy differential reddening (of about 1.9 mag) could also be contributing to the age spread. This hypothesis, although less likely (for the reasons explained in Subsection 3.8.1, especially because of the lack of such a spread in the background population and no such spread in the early-type population), cannot be excluded a priori: it must be taken into consideration and tested.

A spectroscopic investigation of the PMS population is then demanded, to select true association members and restrict the possible age range. This will also allow us to investigate their nature giving a PMS classification, and testing the truthfulness of the reddening gradient hypothesis across the Cep OB3b subgroup. An initial spectroscopic survey is discussed in detail in the next Chapter.

4 Spectroscopic observations for PMS candidates in Cep OB3b

From the colour-magnitude diagrams obtained through an optical photometric survey of the younger subgroup of the Cep OB3 association (see Chapter 3), the presence of a PMS stellar association was inferred. Spectroscopic observations of these PMS objects are necessary to check their nature, i.e.: to test their kinematic membership to the association and confirm that they are truly young objects (see Section 2.11 in Chapter 2). The first objective is achieved with radial velocity measurements, and the second using equivalent width measurements of the Li I 6708 Å line, a youth discriminator for PMS stars (lithium criterion; see Section 3.1.7 in Chapter 2). Furthermore, the comparison of the spectral types derived from intrinsic colours with those determined from visual inspection of a library of stellar spectra, will allow us to test the hypothesis of a change in reddening across the association.

4.1 Selection of PMS candidates

The objects for the spectroscopic follow-up observations were selected from a "PMS strip" in a V versus (V-I) colour-magnitude diagram, after having added altogether fields 1a, 2a, 3a, 4a, 2b, and 3b. Fields 1b and 4b were left out because they are pointing at the molecular cloud, and are therefore most likely to contain only foreground objects. The PMS strip was defined within the ranges $12 < V < 19$ mag, with $0.4 < V - I < 2.3$ mag for $V = 12$ mag, and $2.2 < V - I < 4.2$ mag for $V = 19$ mag (see Figure 4.1), in such a way as to surround the optical counterparts to the X-ray sources of NF99 (see Chapter 3), and to allow a generous PMS sample in case of age spreads and differential reddening across the Cep OB3b subgroup (both responsible for a spread of the objects around the isochrones in the CMD; see Section 3.8 in Chapter 3). X-ray sources are likely to be young, since low-mass PMS stars are strong X-ray emitters (see Section 2.5 in Chapter 2).

All the catalogue stars with good flags and photometric errors less than 0.1 mag falling in the strip were retained. An exception was made for those flagged as non-stellar objects (flags 11), which were retained since they could be double stars. We did not select stars fainter than $V = 19$ mag, mainly because they would be too faint to do spectroscopy. The result of this selection is shown in

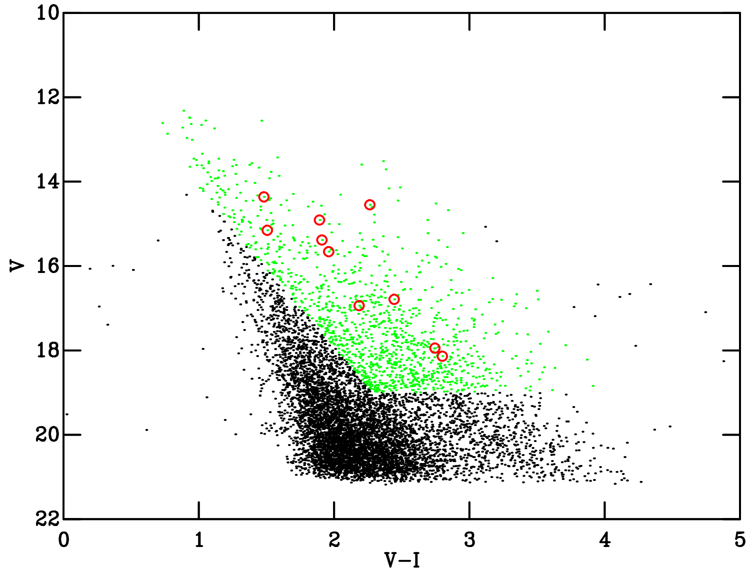

Figure 4.1: The PMS objects selected from the PMS strip (green dots), encompassing the optical counterparts to the X-ray sources of NF99 (red circles).

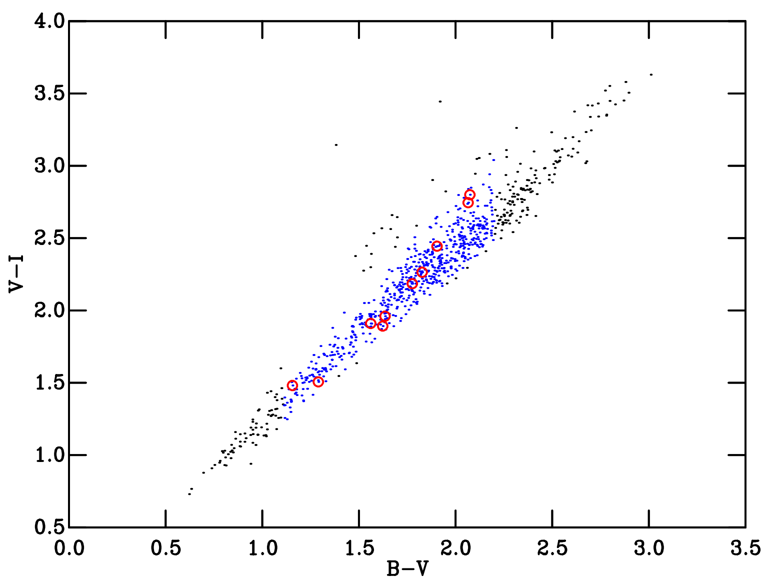

Figure 4.2: Additional selection from the possible PMS objects selected in the V versus (V-I) colour-magnitude diagram of Figure 4.1. The resulting objects are shown as blue dots, the optical counterparts of the X-ray sources of NF99 are circled in red.

Figure 4.1: selected objects are plotted in green dots, optical counterparts to the X-ray sources are circled in red. There are 1225 selected objects out of 7884.

We then performed a further selection in the PMS sample of 1225 objects, by choosing stars having an error less than 0.1 mag and a good flag in the (B-V) colour too, and picking up only those stars which were contained in a strip in the (B-V) versus (V-I) colour-colour diagram, again defined by the optical counterparts to the X-ray sources of NF99. The region was defined within the ranges $1.11 < B - V < 2.2$ mag, with $1.6 < V - I < 1.2$ mag for $B - V = 1.1$ mag, and $2.5 < V - I < 3.1$ mag for $B - V = 2.2$ mag (see Figure 4.2). The result of this additional selection left 616 possible PMS objects (out of 847), plotted in Figure 4.2.

These optically selected objects were the sample for the spectroscopic investigation to be carried out with the multifibre spectrograph WYFFOS.

4.2 WYFFOS/AF2

WYFFOS is the RGO Wide Field Fibre Optic Spectrograph, fed with fibres coming from the prime focus of the WHT. The selected fibres, in each configuration prepared in advance by the observer (see Section 4.3), are automatically placed by AF2, the WHT prime focus robotic fibre positioner. AF2 is working at present with the Large Fibre Module (126 OH silica glass fibres, with a diameter of 2.7 arcsec on the sky). It can position up to about 90 fibres (including fiducial and sky fibres), over a circular field of view of 1 degree diameter.

A configuration program, AF2_configure, helps to prepare in advance the configurations for the observational run, selecting from the sample the largest possible number of fibres which will be used according to the placement rules (fibres cannot be placed closer than $\sim 25''$ from each other, because of the size of the fibre buttons in AF2; and they cannot cross) and weighting constraints which will be described in detail in the next Section.

4.3 The configuration program: AF2_configure

Before running the configuration program AF2_configure, the user must download the most recent versions of the large_fibres.dat and wht_prime.dat files, which contain respectively the current status of the fibres (some fibres could be dead, i.e., with very low transmission, or disabled) and the distortion map of the field of the telescope.

A file ".fld" is required. Its header must specify the name of the field, the date of the observation, the equinox, the position angle of the spectrograph on the sky (in degrees), the name of the fibre bundle to be used (in our case, the large one), the coordinates of the centre of the field, and finally the hour angle of the observation. This last information is crucial for the correct calculation of a refraction correction (taking into account differential refraction through the Earth's atmosphere across the field of view).

The header is then followed by id number, RA, Dec, and visual magnitude for each of the possible target stars. Finally, a list of fiducial stars must be attached at the bottom of the file: these are the stars which help to acquire the field and to keep the telescope pointed correctly during the observation. The fiducial stars should not be too bright, since they may display blooming on the acquisition camera, or be nearby with high proper motions; and not too faint, since they would not be visible. We selected fiducial stars in the range $12.5 < V < 13.5$ mag, but, as further selection, we compared their positions with those given in the USNO-A2.0 catalogue (Monet 1998), and retained only those stars discrepant by less than 0.4" (our astrometric accuracy). This left us with a list of 14 possible fiducial stars which should have small proper motions.

Stars were identified as targets or fiducials by appending respectively a P or an F in the ".fld" file. Blank sky positions were also generated and labelled with an S. Weights were assigned to the program stars to increase the chance that a particular object will be allocated (values higher than zero mean higher weight). The configuration program then optimises the fibre placement choosing that combination which gives the highest total weight of allocated objects. We have assigned weights according to the visual magnitude, in order to ensure a roughly even spread of target magnitudes across the CMD. Their values are reported in Table 4.1, together with the number of targets to be selected from.

We ran the program in angle scanning mode, so to sample different values of the sky position angle (from 0 to 360, at steps of 90 degrees), with the fast algorithm, to see which object can be reached by which fibre (with the limitations of a minimum spacing of 25" between the fibres and their non-crossing). Once the best possible orientation was found, i.e., the one which gave us the maximum number of allocated objects, the final placement of the fibres was performed with the slow algorithm,

V	weight	N
< 13	0	2
13-14	0	7
14-15	15	33
15-16	6	73
16-17	4	138
17-18	3	183
18-19	3	180

Table 4.1: Weights assigned to the stars to be used by the configuration program for fibre placement.

Configuration	centre (RA, Dec)	SKYPA	HA	allocated fibres
1	22 54 19.11 +62 41 36.88	200.56	2.0	59P, 4F, 21S
2	22 52 25.01 +62 38 31.46	355.00	2.0	61P, 4F, 25S

Table 4.2: Information for the two configurations used. After observing, the analysis of the extracted spectra revealed that 1 sky fibre in each configuration had a faint star falling in.

so to maximise the total number of fibres placed and the total weight of the allocated objects. Then the configuration file was edited to move all possible unused fibres onto blank sky positions. More than 20 sky fibres were allocated to be used in the data reduction procedure to create a mean sky spectrum to be subtracted from each target spectrum (see Subsection 4.5.4). As a result of the configuration procedure, a configuration file, ".cfg", was created, which is read by the fibre positioning program (AFSETUP) during the observational run at the telescope.

We prepared two configurations. The configuration centre, position angle of the spectrograph on the sky, hour angle, number and type of fibres allocated in the first and second configuration respectively are reported in Table 4.2. Note that in preparing the second configuration, those stars which had a fibre allocated in the first configuration were assigned zero weight, so that fibres were placed on previously unselected stars.

The two configurations used at the telescope are shown in Figures 4.3 and 4.4. By comparing the stellar distribution with Figure 3.2 in Chapter 3, visualising the position of the stars in the different fields in Cep OB3b is straightforward (in the first configuration the fields appear upside down, since the overall field is rotated by 200 degrees). Each fibre has its corresponding fibre number. Target stars are shown as crosses. Blue fibres are the fibres pointing to fiducial stars, denoted as asterisks. Fibres which do not point to any object are the dedicated sky fibres. Red fibres outside the field are parked or disabled fibres.

4.4 Observations

Intermediate-resolution spectra of the optically selected possible PMS objects were obtained on December 11-12, 1999, with the WYFFOS/AF2 multifibre spectrograph at the WHT telescope, La Palma, Canary Islands, equipped with a CCD TEK 6 chip (type TK1024), the WYFFOS echelle grating (632 grating rulings/mm) and the echelle order-sorting filter number 4 (6625 Å) to cover the region occupied by the Hα (6563 Å) and Li I (6707.8 Å) lines.

We obtained a wavelength coverage of about 440 Å, in the approximate range 6380-6820 Å. The nominal dispersion is of 17.8 Å/mm (equivalent to 0.43 Å/pixel), with a spectral resolution (FWHM) of about 2 pixels, equivalent to about 1 Å, determined from arc lines, and a resolving power of about 7700. The CCD dimensions are 1024×1024 24μm pixels, with a gain of 1.7 e^{-}/ADU and a read-out noise of 5.6 e^{-}.

Note that the fibres ends were positioned in the slit assembly in groups of three by three parallel rows: as a consequence, the wavelength coverage is not exactly the same for each spectrum (the starting wavelength may be shifted by up to 30 Å, the amount of wavelength coverage does not change by more than 1 Å).

Each field was acquired through fiducial stars. First, a fiducial star close to the centre of the field was centered using x,y offsets; then it was the turn of a fiducial at the edge of the field using telescope rotation; and finally all the remaining ones. The subsequent centering during the observing run was guided by hand.

The careful selection of fiducial stars was extremely important: all the 4 fiducial stars in each configuration were acquired and well centered, giving us confidence in the placement of the other fibres.

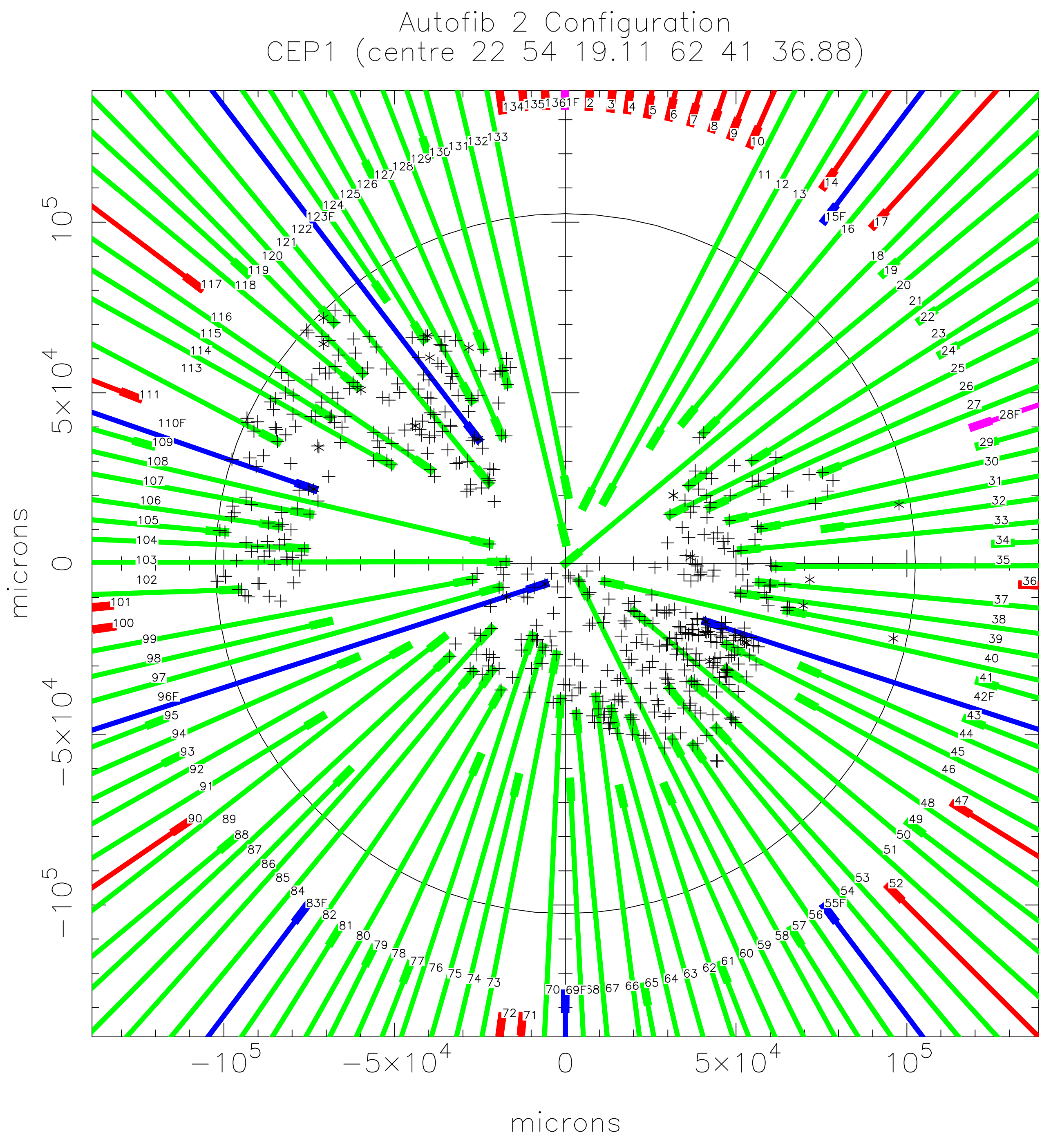

Figure 4.3: The first fibre configuration. The position angle is 200 degrees.

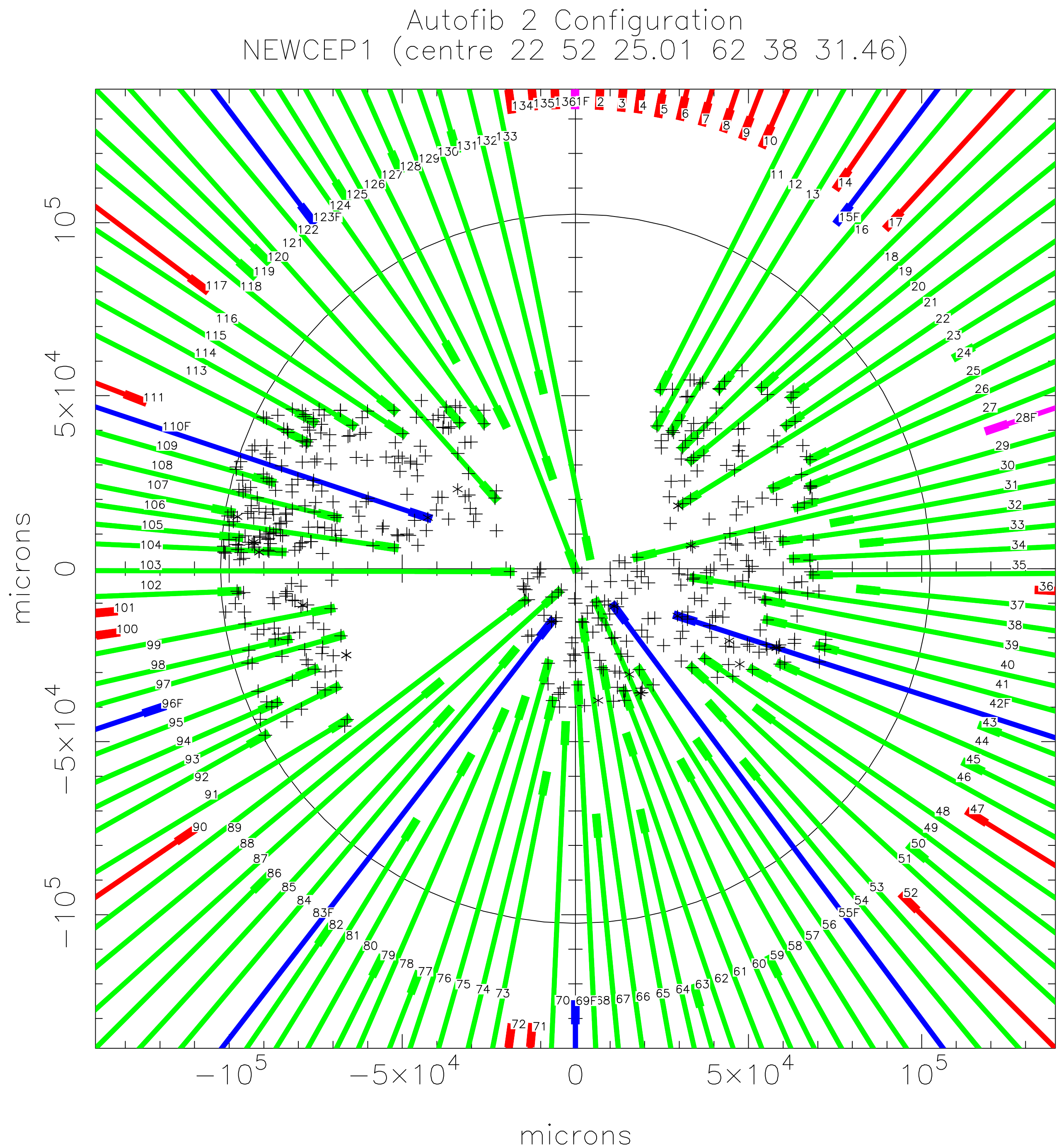

Figure 4.4: The second fibre configuration. The position angle is 355 degrees.

Target, bias, arc, flat and offset sky frames were taken. Target frames were observed for 3×1800s in the first configuration (first night), and for 3×1500s in the second configuration (second night). Zero second exposures (7 on the first, 3 on the second night) were taken for bias-subtraction. Flat frames (3 on the first, and 7 on the second night) of 1s exposure were taken with a Tungsten calibration lamp (with all available fibres in a circle of the smallest possible radius). These were used for flat fielding in the dispersion direction and for aperture identification.

Arc frames of 3s exposure were taken from a Neon lamp and used for the wavelength calibration of each spectrum in each configuration. Three offset sky frames (of 400s and 300s on the first and second nights respectively), were taken for each configuration by beam-switching the telescope to close sky (at 15 arcsec north, south and west of the target position). These are usually taken in order to normalise the fibre transmissions (throughput/vignetting correction), under the assumption that the night sky is the same brightness through each fibre. The dedicated sky fibres are used to create a mean sky spectrum; note that a mean offset sky frame could also be created and used to do sky subtraction directly (see Subsections 4.5.5 and 4.5.6). In addition, on the second night we measured some radial velocity and spectral type standard stars through a single fibre at the centre of the field.

4.5 Data Reduction: WYF_RED

The IRAF[1] wyf_red data reduction task was used to process the images and extract the multifibre spectra obtained with WYFFOS. The input frames for each run of wyf_red were: a target image, one arc, all available flat fields, one flat to be the reference frame for the aperture identification, and a mean offset sky frame which was created separately with the task IMCOMBINE (by median filtering the normalised sky frames). No bias frames were used, since after inspection (by displaying them in SAOIMAGE) they did not show any spatial structure: wyf_red determined the bias from the overscan region of each processed image. Furthermore, the parameter *w_interact=yes* was set, which allowed us to do some of the procedures interactively (i.e., the arc line identification in the arc spectrum, the fitting and smoothing of scattered light both for offset sky and target frames).

[1]IRAF (Image Reduction and Analysis Facility) is distributed by the National Optical Astronomy Observatory (NOAO), which is operated by the Association of Universities for Research in Astronomy (AURA), Inc. under cooperative agreement with the National Science Foundation.

4.5.1 Initial reduction

The first thing wyf_red does in a run is the CCD processing (using the IRAF CCDRED package), trimming each input image and bias subtracting it with the bias determined from the overscan section. A mean flat field is then created automatically, with the IRAF task IMCOMBINE, by averaging all the available flat fields, properly normalised, in order to correct for pixel to pixel sensitivity variations. The target frame is then paired with the mean offset sky frame.

From the Tungsten flat reference frame, wyf_red finds the apertures by locating each spectrum on the CCD image and tracing its spatial distortion. The aperture definition is a crucial step: the spectra have a shape which is not generally straight, but curved in the dispersion direction due to the spectrograph optics. For each spectrum it is therefore necessary to know its exact location on the CCD, the number of pixels it is spread over and its distortion as a function of position in the dispersion direction (this effect and can be large especially at the edges of the CCD).

The number of apertures is equal to the number of available fibres (at present there are 99 fibres, counting both the allocated fibres and the unused fibres which are parked or disabled). The user can edit the apertures to check if all of them were found by the algorithm, and manually add any that were missing. A table is created, which pairs each aperture number with: the information on the status of the fibre (flagged with 1 if it is pointing to a target star; 0 if it is placed on sky; -1 if it is parked or disabled); as well as the information on the star it is pointing to (i.e., RA, Dec, and visual magnitude as acquired from the configuration program; or just RA and Dec if it is pointing to the sky, or a comment if it is parked or disabled). Let us summarise the main reduction procedures.

4.5.2 Scattered light

Scattered light is fitted and subtracted from the mean offset sky frame. The light scattered in the spectrograph is proportional to the total incident light coming from different parts of the spectrograph, but there may be also a component caused by light from a bright object observed with a fibre and scattering into adjacent regions occupied by other fibres. The scattered light was modelled using pixels that were clearly between the fibre spectra on the CCD. A first order Chebyschev polynomial was fitted perpendicular to the dispersion direction, whilst a third order spline polynomial with eight knots was fitted in the dispersion direction. The program then uses the APSCATTER task to model the excess of light between spectra across the CCD, and subtracts it everywhere in the frame (i.e., including where the spectra are).

4.5.3 Wavelength calibration

In order to perform the wavelength calibration (or dispersion correction) of the target spectra, line identification is performed on a Copper-Neon arc frame. The arc reference image is extracted, and the arc lines are marked (giving the corresponding known tabulated wavelength values). The relation between pixel and wavelength is then fitted for each fibre with a third order polynomial resulting in a typical rms residual of 0.06 Å. Six well identified lines were used in all of the fits. The dispersion function defined in such a way can then be used to dispersion correct the target spectra.

4.5.4 Throughput correction and sky subtraction

After initial bias subtraction and scattered light subtraction, the target spectra are extracted with an optimal extraction procedure (more weight is given to pixels with higher S/N close to the centre of the spectrum, less to those with lower S/N close to the edge). Wavelength calibration is achieved using the dispersion relation determined from an adjacent (in time) arc exposure. Both target and offset sky spectra were extracted as target spectra without an automatic sky subtraction, since we preferred to do it ourselves. There are two obvious methods to choose for sky subtraction: using a mean sky determined from the dedicated sky fibres, properly throughput corrected (hereafter, method 1); or a mean offset sky frame (hereafter, method 2).

In the following we discuss what we have found for the first target frame in the first configuration. An analogous procedure was then repeated for the other two target frames of the same configuration, and for the three target frames of the second configuration as well.

4.5.5 Method 1

To test the 21 available sky fibres and to select just good sky fibres to be used in determining a mean sky, wyf_red was run with the automatic sky subtraction procedure. As a result, one sky fibre (fibre 89) was revealed as dead, and therefore its spectrum was not extracted. Another 4 sky fibres were rejected, because of a bad response, high residuals, or bad curvature (if the RMS at the red end of the spectrum was very different from that at the blue end). In particular, one of them yielded a stellar spectrum so was not a sky fibre at all! Finally, one sky fibre was discarded since it was pointing in a region with known sky Hα nebulosity, and had the highest peak in Hα counts. Its inclusion would have biased the mean towards higher values.

Therefore we identified 15 good sky fibres to be selected from both target and mean offset sky multispectra images. They were median combined with the task SCOMBINE to have a single output image (let us call them target15 and sky15 respectively, for a better comprehension of the subsequent steps).

4.5.5.1 Throughput correction

Analogously to pixel-to-pixel sensitivity variations in the CCD, we had to determine and properly take into account the fibre-to-fibre sensitivity. Knowledge of the throughput correction of the fibres is vital because of the need to do sky subtraction, and is nowhere near the same for all fibres. Fibre throughput may vary because of the slightly different fibre material composition, and of the type and order of the filter used during the observing run (for the echelle filter order number 4, fibres transmission is of about 90 %; see the AUTOFIB2/WYFFOS User Manual). Tests during manifacture suggested that no more than $\sim$ 10 % light losses would be expected in the fibres and fibre connectors (see the AUTOFIB2/WYFFOS User Manual). However, the fibres were subsequently cut to 26.5 m long during the installation of the Large-Fibre Module and light losses are expected to be larger than the quoted value.

To do the throughput correction of the fibres, we run wyf_red (again without sky subtraction) on each of the three offset sky frames separately, as if they were target frames, producing three offset sky multispectra images. The following steps were repeated for each offset sky multispectra image, to find the correct response, R, of each fibre.

For each placed fibre s in an offset sky frame, we determined its relative response by dividing its spectrum by that obtained combining the 15 sky fibres of the mean offset sky frame, i.e.,

$$(R_s)^{med} = \frac{\mathrm{offsetsky_s}}{\mathrm{sky15}} \tag{4.1}$$

where $(R_s)^{med}$ is the median of the values found in each of the 1024 pixels over which its spectrum is spread. Since the offsetsky fibre could have a lower transmission, or a star in it instead of blank sky, we then compared its $(R_s)^{med}$ value found in the three different offsetsky frames. We looked for that offset sky frame (let us call it the coherent frame) having not very discrepant $(R_s)_1^{med}$ values for the fibres. We then found the mean of these $(R_s)_1^{med}$ values and rejected those fibres having a value discrepant by more than 1 σ from this mean value. We then redetermined the mean, $< R_1 >$, from the remaining fibres. We worked accordingly in the other two offsetsky frames, i.e., rejecting those fibres having the same fibre number of those rejected in the coherent frame, and determining the corresponding $< R_2 >$ and $< R_3 >$ from the remaining $(R_s)_2^{med}$ and $(R_s)_3^{med}$ respectively.

It was then possible to do a comparison of R values, for each fibre in the three different frames. More precisely, between $(R_s)_1^{med}$ in the coherent frame and $(R_s)_2^{med}$ and $(R_s)_3^{med}$ properly normalised to it in the other two frames, i.e., $(R_s)_2^{med} * < R_1 > / < R_2 >$ and $(R_s)_3^{med} * < R_1 > / < R_3 >$. Finally, for each fibre: the mean of these three values was computed; those values discrepant for more than 3% from the mean were rejected; the final response R_s of the fibre was computed as the mean of the surviving values. In this way we determined the proper throughput correction for each placed fibre.

4.5.5.2 Sky subtraction

At this point, to obtain a sky subtracted target image, T_i^{skysub}, a mean sky image obtained from the selected sky fibres and properly scaled with the correct response, $R_i * < target15 >$, was subtracted from each single target image T_i, i.e.,

$$T_i^{skysub} = T_i - R_i * < target15 > \tag{4.2}$$

(with i equal to the number of the extracted target spectra).

The spectra extracted in this way may still suffer from contamination by nebular Hα emission lines, since the sky fibres are close to the target objects in a region characterized by inhomogeneous Hα nebulosity. Therefore, in target regions with high Hα nebulosity the average sky subtracted spectrum underestimates these lines; conversely, in target regions with low Hα nebulosity the sky subtracted overestimates them. A check of the Hα peak in the sky fibres revealed a higher value close to the CO

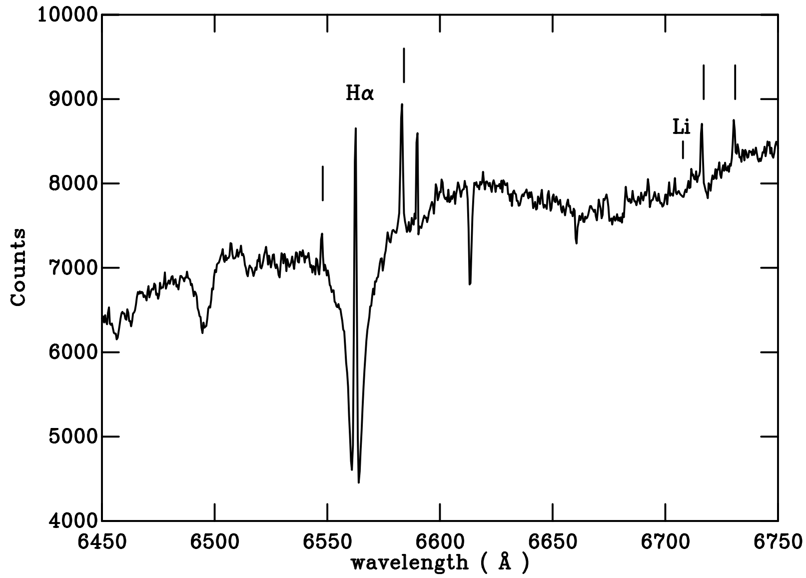

Figure 4.5: Typical spectrum extracted with a throughput correction and sky subtraction performed with method 1. This is a spectrum of a star in a field with Hα nebulosity present. The Hα line is in absorption, but it is contaminated by a strong sky Hα line in emission. Also present are the NII ($\lambda\lambda$ 6548, 6584) and SII ($\lambda\lambda$ 6717, 6731) nebular lines.

contour of the molecular cloud, as expected (see Figure 3.2), with the maximum occurring for a fibre on-cloud. Spectra like the one plotted in Figure 4.5 are the result of a throughput correction and sky subtraction obtained with method 1. This is the spectrum for a star in field 1a (fibre 48 in Figure 4.3; note that the fields are upside down in that configuration), which is partially on-cloud. There is a strong remaining nebular Hα emission line. Note that there are other nebular lines present in the spectrum, i.e., NII ($\lambda\lambda$ 6548, 6584) and SII ($\lambda\lambda$ 6717, 6731). There are no nebular lines close to the Li 6708 Å line.

4.5.6 Method 2

This method uses a mean offset sky frame (obtained from the three offset sky frames; see Sections 4.4 and 4.5) to do the sky subtraction of the target spectra. It allows determination of the sky contribution without contamination of nebular Hα lines from target regions of high nebulosity. To do this, the multispectra mean offset sky had to be scaled to the exposure of the target multispectra before subtraction.

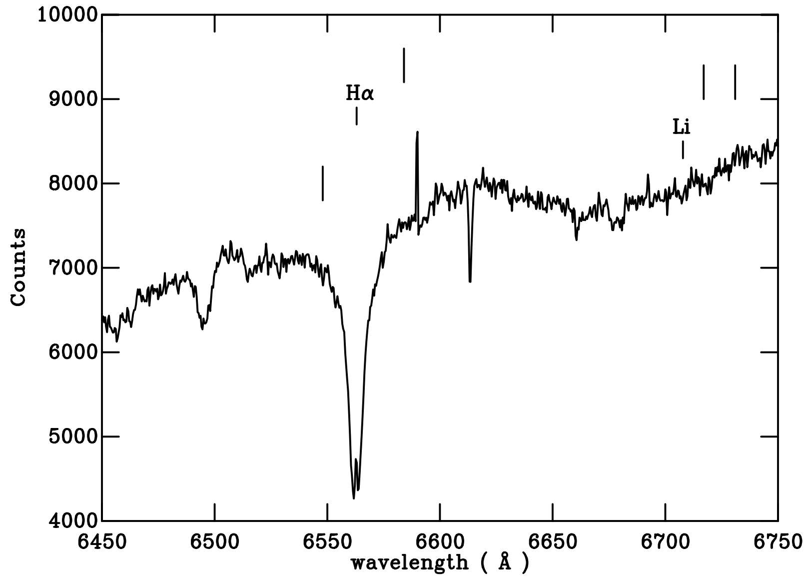

Figure 4.6: The same spectrum of Figure 4.5, extracted by subtracting a mean offset sky frame properly scaled to the exposure of the target frame (method 2). The Hα line contamination is now visibly reduced, and the spectrum is clean from the NII ($\lambda\lambda$ 6548, 6584) and SII ($\lambda\lambda$ 6717, 6731) nebular lines. The emission line still present at λ 6590 is a cosmic ray. Note though that the noise in the continuum has increased.

As a comparison, in Figure 4.6 we give the same spectrum of Figure 4.5 found by subtracting a mean offset sky frame. We can see that the sky Hα line contamination is much reduced, so that now the measurement of the line is more reliable. Furthermore, the nebular emission lines of NII and SII are now removed (the emission line right of Hα is a cosmic ray, because it is not present in the spectrum extracted in the other two target frames of the same configuration). However, overall, the spectra which are background subtracted in this way are noisier, because the offset sky exposures are shorter than the target exposures.

As a consequence, we decided we will have to adopt the following criterion for measuring the equivalent widths (EWs): EW(Li I) were measured in the spectra where the sky subtraction was done with method 1 (i.e., using a mean sky determined from the throughput-corrected sky fibres); whereas EW(Hα) were measured in target spectra extracted with method 2 (i.e., sky subtracted with a mean offset sky, properly scaled for their shorter exposure time).

We worked in the same way for the other two target frames of the first configuration. We extracted 53 spectra in total from each frame: 52 target spectra, plus 1 spectrum from a dedicated sky fibre in which a star fell in (some other fibres appeared to have almost zero response and were discarded). The spectra were combined with the ARK program ADD.

We repeated all the steps for each of the other three target frames of the second configuration (second night). Spectra were extracted in each target frame with the two different methods discussed above. The mean offset sky frame was obtained by median combining three separate offset sky frames, and the resulting multispectra image extracted was scaled by the proper factor and subtracted from the target frames. The throughput correction and sky subtraction were done as before, one spectrum after each other, by using 21 sky fibres. In total 57 spectra were extracted with both methods in each target frame of the second configuration: 56 target spectra, plus 1 spectrum from one dedicated sky fibre in which a star fell in (again some other fibres were discarded because of an almost zero response).

4.6 Results

4.6.1 Radial velocities

Radial velocity (RV) measurements were performed on all the spectra of both configurations extracted with method 1 (see Subsection 4.5.5), using the Starlink software package FIGARO. By visual inspection of the extracted spectra (see for example Figures 4.11 and 4.12) we derive a typical signal-to-noise of S/N> 10 for the majority of them. The spectrum of the IAU radial velocity standard star HD 213947 (spectral type K4 III) was extracted too. All the objects and standard spectra were rebinned to a logarithmic wavelength scale, giving constant velocity bins of 19.152 km/s. The targets were cross-correlated with the radial velocity standard star in the spectral range 6400-6550 Å (a region containing easily identifiable metallic lines), in order to determine the relative shifts, and calculate RVs. We tried the region 6650-6800 Å but the cross-correlation peak was weaker and did not improve the result. Note that possible cosmic rays and NII ($\lambda\lambda$ 6548) or SII ($\lambda\lambda$ 6717, 6731) nebular emission lines falling in the used region were masked before performing the cross-correlation.

The standard was cross-correlated with itself, giving a cross-correlation function with a peak of about 3 pixels FWHM. Some of the objects had cross-correlation functions showing peaks with a broader FWHM than that found for the standard ($FWHM_{st}$). Therefore the standard was blurred with a Gaussian of half width $0.5\sqrt{FWHM^2 - FWHM_{st}^2}$ pixels, and the cross-correlation was determined again. In the case of double peaks in the cross-correlation function, the cross-correlation was repeated in the region 6650-6800 Å: if both peaks were still separated (indicating a possible binary nature of the object), we fit a double Gaussian to find the shifts (and hence RVs) for both of them.

From repeat measurements of a number of targets taken for a different programme on the same observing run, we estimate an RV accuracy of $\pm 2 - 3$ km/s (Jeffries, private communication). The relative RVs were heliocentrically corrected. Results for objects in both configurations are shown in Table 4.3. For some of the objects we could not trust the RV measurement, because of a too noisy spectrum or because of a too weak cross-correlation peak (too few lines to be used for the cross-correlation procedure, due to an early spectral type), and these are flagged with a colon.

We found that objects nos. 3, 73, and 99 are possible double-line spectroscopic binaries (SB2), from their double-peaked cross-correlation functions (as shown in Figures 4.7 to 4.9).

The presence of broad lines in the spectrum is instead indicative of close binaries and/or fast rotation. Object 58 is a suspected triple. Objects no. 4, 7, 12, 19, 50, and 62 have broad lines, but have single-peaked cross-correlation functions, suggesting therefore that they may be fast rotators. This is likely to be the case especially for object no. 7 (see Figure 4.11).

Radial velocity measurements allow us to decide which objects are kinematic members of the Cep OB3 association, by comparing them with the mean value derived from already known members.

Figure 4.10 shows the radial velocity distribution of 74 (two of which are SB2) out of 110 spectroscopic objects (for the other 36 we have no radial velocity measurement). There is some evidence for a clustering around the mean heliocentric RV value of known members of the Cep OB3 association, i.e., around -22.5 ± 1.5 km/s (determined from values ranging from -39.4 km/s up to -5.7 km/s; see Garmany 1973). Objects with RV values within 2 sigma (= 6.0 km/s) of this mean value, i.e., in the range -28.5 km/s to -16.5 km/s, can be considered candidate kinematic members of the association.

We found 22 candidate kinematic members in total (53 are kinematic non-members), i.e., just the 30% of the spectroscopic objects observed.

#	RA (hhmmss)	Dec (ddmmss)	RV_{hel} (km/s)	V	(V-I)	$(V-I)_0$	T_{eff}	sp.type	Jac.
1	22 55 21.02	+62 26 58.8	:	17.103	2.056	0.876	5035	K1-K2	G
2	22 55 19.39	+62 34 31.1	-51.3	17.106	2.077	0.897	4986	K2-K3	G
3	22 55 45.11	+62 32 44.9	5.8, -72.7 (*), SB2	14.442	1.646	0.466	6540	F5-F6	K
4	22 56 25.75	+62 32 52.7	-46.1	16.918	2.344	1.164	4575	K4-K5	G
5	22 56 17.96	+62 35 12.9	:	16.030	1.870	0.690	5607	G4-G6	F
6	22 56 43.01	+62 35 31.9	:	16.308	1.773	0.593	6031	G0-F8	A
7	22 56 38.72	+62 37 14.4	-24.2	14.548	2.264	1.084	4690	K3-K4	K
8	22 56 28.95	+62 38 41.5	-20.2	16.733	2.347	1.167	4570	K4-K5	K
9	22 57 05.21	+62 38 38.6	-45.1	15.153	1.506	0.326	7258	F0-F2	F
10	22 54 51.61	+62 41 52.4	-25.7	15.004	1.962	0.782	5278	G8-K0	F
11	22 57 25.68	+62 45 22.1	:	(a)					A
12	22 56 39.09	+62 45 09.4	-20.3	14.910	1.892	0.712	5528	G4-G6	F
13	22 55 17.65	+62 43 23.4	-20.9	15.783	1.593	0.413	6784	F4-F5	K
14	22 56 18.49	+62 47 13.7	-31.9	15.545	2.310	1.130	4625	K3-K4	G
15	22 56 47.54	+62 50 08.5	-11.1	14.812	1.432	0.252	7706	A6-A8	A
16	22 56 05.06	+62 48 27.3	-25.2	15.912	1.543	0.363	7041	F2-F4	G
17	22 56 35.95	+62 52 13.3	-38.7	14.485	1.513	0.273	7217	F0-F2	F
18	22 56 20.13	+62 52 23.2	-22.3	16.789	2.444	1.264	4424	K4-K5	K
19	22 54 32.85	+62 42 32.0	-58.7	15.040	1.634	0.454	6595	F5-F6	F
20	22 55 45.40	+62 52 01.1	-30.7	16.565	1.717	0.537	6278	F6-F8	F
21	22 55 30.90	+62 52 06.0	-40.5	14.781	2.294	1.114	4649	K3-K4	K
22	22 55 15.80	+62 51 22.4	-82.5	16.857	2.132	0.952	4876	K2-K3	G
23	22 55 06.59	+62 53 19.8	-39.6	15.920	1.503	0.323	7276	F0-F2	F
24	22 54 51.41	+62 52 36.8	-84.6	16.925	2.332	1.152	4593	K3-K4	G
25	22 54 36.73	+62 49 12.3	-68.0	15.235	1.602	0.422	6740	F4-F5	F
26	22 54 25.09	+62 49 01.2	-11.6	14.975	1.378	0.198	8063	A5-A6	G
27	22 54 14.93	+62 48 25.1	-32.6	18.305	2.412	1.232	4473	K4-K5	K
28	22 54 00.08	+62 52 02.8	-80.0	14.921	1.544	0.364	7035	F2-F4	G
29	22 53 42.74	+62 53 04.1	-12.1	14.906	1.499	0.319	7300	F0-F2	F
30	22 53 22.12	+62 52 30.7	-39.4	17.261	2.293	1.113	4650	K3-K4	G
31	22 53 44.20	+62 49 04.4	-88.1	17.774	2.435	1.255	4438	K4-K5	G
32	22 54 07.29	+62 53 42.2	-27.1	16.939	2.113	0.933	4914	K2-K3	K
33	22 53 38.68	+62 45 31.0	:	17.251	2.500	1.320	4337	K5-K7	K
34	22 53 20.76	+62 42 18.8	-15.2	15.103	1.451	0.271	7587	A8-F0	F
35	22 50 29.47	+62 40 17.3	:	14.590	1.805	0.625	5875	G0-G2	A
36	22 51 52.23	+62 38 51.5	-19.5	15.670	2.108	0.928	4924	K2-K3	G
37	22 50 59.59	+62 36 43.6	-62.1	17.737	2.134	0.954	4872	K2-K3	G
38	22 52 20.51	+62 38 05.4	-27.0	14.770	1.259	0.079	8894	A2-A4	G
39	22 53 18.26	+62 45 40.9	-29.2	15.380	1.550	0.370	7000	F2-F4	F
40	22 50 52.51	+62 52 05.9	-23.7	16.920	2.116	0.936	4908	K2-K3	G
41	22 53 36.90	+62 43 15.0	-53.6	15.323	1.694	0.514	6360	F6-F8	F
42	22 51 13.83	+62 48 02.6	-37.1	17.059	2.123	0.943	4894	K2-K3	F
43	22 50 12.69	+62 48 58.6	:	17.693	2.473	1.293	4379	K5-K7	F
							...	continue	

... continued

44	22 50 50.81	+62 46 59.5	:	18.084	2.194	1.014	4780	K2-K3	G
45	22 51 08.84	+62 45 09.6	:	15.432	1.763	0.583	6077	F8-G0	A
46	22 51 06.18	+62 33 24.7	:	14.457	1.345	0.165	8363	A4-A5	A
47	22 51 12.75	+62 31 50.0	-68.2	15.128	1.458	0.278	7543	A8-F0	G
48	22 50 37.54	+62 28 17.4	:	14.741	1.531	0.351	7111	F0-F2	A
49	22 53 02.75	+62 37 06.5	-20.8	16.030	1.867	(b)			K
50	22 51 45.67	+62 27 32.9	-27.3	14.676	2.841	1.661	3982	K7-M0	F
51	22 52 30.92	+62 31 11.8	:	15.395	1.704	0.524	6325	F6-F8	G
52	22 52 27.22	+62 26 54.8	-16.4	15.583	2.502	1.322	4334	K5-K7	G
53	22 52 52.47	+62 29 00.1	:	14.682	1.664	0.484	6467	F6-F8	A
54	22 51 10.94	+62 52 54.5	-116.3	18.350	2.513	1.333	4318	K5-K7	G
55	22 51 15.64	+62 49 55.6	:	18.992	2.636	1.456	4152	K5-K7	noisy
56	22 51 04.77	+62 49 25.4	-20.9	16.853	2.180	1.000	4798	K2-K3	G
57	22 50 27.90	+62 52 30.1	:	16.607	1.888	0.708	5542	G4-G6	G
58	22 50 58.17	+62 47 53.9	:, T?	18.396	2.423	1.243	4456	K4-K5	K
59	22 49 57.22	+62 52 12.4	-63.8	16.991	2.196	1.016	4777	K2-K3	G
60	22 50 52.70	+62 46 46.0	:	14.394	1.528	0.348	7129	F0-F2	A
61	22 49 41.71	+62 48 49.6	-2.8	13.991	1.344	0.164	8372	A4-A5	K
62	22 51 01.73	+62 43 12.1	-0.7	16.974	2.291	1.111	4653	K3-K4	G
63	22 49 26.92	+62 45 47.8	:	16.557	2.345	1.165	4573	K4-K5	G
64	22 49 55.08	+62 43 45.9	:	16.676	2.275	1.095	4676	K3-K4	A
65	22 51 39.03	+62 39 01.6	:	18.577	2.415	1.235	4469	K4-K5	K
66	22 49 51.69	+62 39 11.9	-30.7	16.720	1.893	0.713	5524	G4-G6	G
67	22 49 45.56	+62 37 39.8	-51.7	14.604	2.275	1.095	4676	K3-K4	G
68	22 49 32.67	+62 36 08.6	:	14.950	1.368	0.188	8154	A5-A6	A
69	22 50 58.86	+62 36 50.6	-24.6	15.553	1.511	0.331	7229	F0-F2	K
70	22 50 08.27	+62 34 25.1	-53.5	14.590	1.455	0.275	7562	A8-F0	F
71	22 50 08.73	+62 32 44.2	-65.7	16.919	1.940	0.760	5357	G8-K0	G
72	22 49 33.70	+62 30 10.7	:	18.521	2.602	1.422	4188	K5-K7	K
73	22 50 02.70	+62 28 57.0	:, SB2	14.030	1.412	0.232	7831	A5-A6	M
74	22 50 22.94	+62 28 42.2	+32.9	16.727	1.949	0.769	5324	G8-K0	G
75	22 50 56.54	+62 29 58.5	-13.2	14.449	1.398	0.218	7918	A6-A8	G
76	22 50 22.26	+62 25 21.6	-24.1	(a)					G
77	22 51 06.43	+62 29 18.6	:	17.024	1.912	0.732	5457	G6-G8	G
78	22 51 44.86	+62 29 31.1	-13.6	15.554	1.611	0.431	6700	F4-F5	F
79	22 52 11.70	+62 35 32.7	:	17.362	2.038	0.858	5079	K1-K2	F
80	22 51 57.75	+62 27 50.9	:	15.732	1.876	0.696	5585	G4-G6	F
81	22 52 11.10	+62 29 46.7	-17.4	15.676	2.113	0.933	4914	K2-K3	K
82	22 52 23.14	+62 33 56.0	-78.9	18.362	2.487	1.307	4357	K5-K7	G
83	22 52 30.57	+62 28 41.9	:	16.417	2.127	0.947	4886	K2-K3	A
84	22 52 50.15	+62 27 33.8	:	15.626	2.013	0.833	5142	K0-K1	K
85	22 52 51.07	+62 30 43.9	+33.7	16.012	2.151	0.971	4838	K2-K3	M
86	22 52 39.06	+62 36 40.0	-16.4	16.996	2.038	0.858	5079	K1-K2	G
87	22 55 19.07	+62 27 30.1	:	18.837	2.569	1.389	4236	K5-K7	K
88	22 56 16.72	+62 26 49.0	:	16.697	2.290	1.110	4655	K3-K4	G

... continue

... continued

89	22 55 25.23	+62 30 15.7	:	16.762	2.118	0.938	4904	K2-K3	:
90	22 56 07.13	+62 29 24.9	:	16.725	2.260	1.080	4695	K3-K4	noisy
91	22 55 39.37	+62 31 54.3	:	18.556	2.546	1.366	4270	K5-K7	noisy
92	22 55 19.39	+62 34 31.1	:	17.106	2.077	0.897	4986	K2-K3	G
93	22 55 56.92	+62 34 33.6	+3.1	16.092	2.126	0.946	4888	K2-K3	K
94	22 55 15.64	+62 44 26.6	-39.9	16.047	2.192	1.012	4782	K2-K3	G
95	22 55 59.66	+62 47 45.1	-26.2	17.128	2.626	1.446	4160	K5-K7	K
96	22 55 32.47	+62 50 53.0	:	15.896	1.556	0.376	6970	F2-F4	G
97	22 55 26.45	+62 52 30.3	+12.2	15.700	1.506	0.326	7258	F0-F2	F
98	22 54 58.68	+62 52 02.1	-40.9	16.476	1.686	0.506	6389	F6-F8	F
99	22 54 23.05	+62 51 04.1	+71.0, -62.7 (*), SB2	15.512	1.750	0.570	6136	F8-G0	K
100	22 55 25.09	+62 36 51.3	-21.2	16.180	2.028	0.848	5104	K1-K2	K
101	22 56 29.79	+62 38 53.7	-17.1	15.727	2.395	1.215	4500	K4-K5	F
102	22 53 13.03	+62 38 44.5	-43.0	16.320	1.773	0.593	6031	F8-G0	G
103	22 55 56.44	+62 41 53.6	-12.9	15.102	1.538	0.358	7070	F0-F2	F
104	22 56 25.70	+62 43 19.9	-12.1	17.189	2.272	1.092	4680	K3-K4	M
105	22 54 36.28	+62 41 33.8	-47.8	16.108	2.184	1.004	4792	K2-K3	G
106	22 56 29.68	+62 45 28.7	-22.4	15.660	1.960	0.780	5285	G8-K0	K
107	22 54 27.86	+62 53 02.1	-105.0	16.886	2.300	1.120	4640	K3-K4	G
108	22 53 19.70	+62 45 04.0	-86.9	18.642	2.500	1.320	4337	K5-K7	K
109	22 53 40.85	+62 51 36.7	-90.0	17.679	2.189	1.009	4786	K2-K3	K
110	22 53 22.92	+62 51 22.8	:	18.133	2.274	1.094	4677	K3-K4	K

Table 4.3: Id number, astrometric positions, heliocentric radial velocities, visual magnitudes, measured and intrinsic (V-I) colours, T_{eff} and spectral types for the stars observed in the first (1-53) and second (54-110) configuration. In column 4: SB2 means double-line spectroscopic binary; a colon (:) indicates noisy spectrum or a cross-correlation peak too weak to trust the RV measurement (probable early-type star). Intrinsic colours in column 7 are determined from the measured colours of column 6 assuming a uniform reddening, i.e., using a colour excess of $E_{V-I} = 1.3 * E_{B-V} = 1.18$ mag, where $E_{B-V} = 0.91$ (see Table 3.7 in Chapter 3). Spectral types in column 9 are those derived from T_{eff} of column 8, according to the temperature scale of Table 4.5. Column 10 lists the spectral types derived from a comparison of the spectra with those in the Jacoby library. (a) star falling down a sky fibre, for which we do not have optical photometry. (b) object on a bad column, properly flagged by CLUSTER: we cannot trust its photometric colours to determine its associated T_{eff} from the intrinsic colour, and hence the spectral type. (*) this object has a double-peaked cross-correlation: the shifts for both peaks were determined by fitting a double Gaussian; it is not a member (see text). Note that we do not have RV measurements for object 84, but we assume it is an association member too, since it is a CTTS (see Section 4.7). Object 58 is probably a triple system (T?), but the peaks were too weak in both cross-correlation regions to try a Gaussian fit. No. 92 is the only star observed in the first configuration as well (= no. 2): unfortunately, its spectrum is very noisy (there are 300s less in exposure time in this specatrum with respect to that taken in the first configuration).

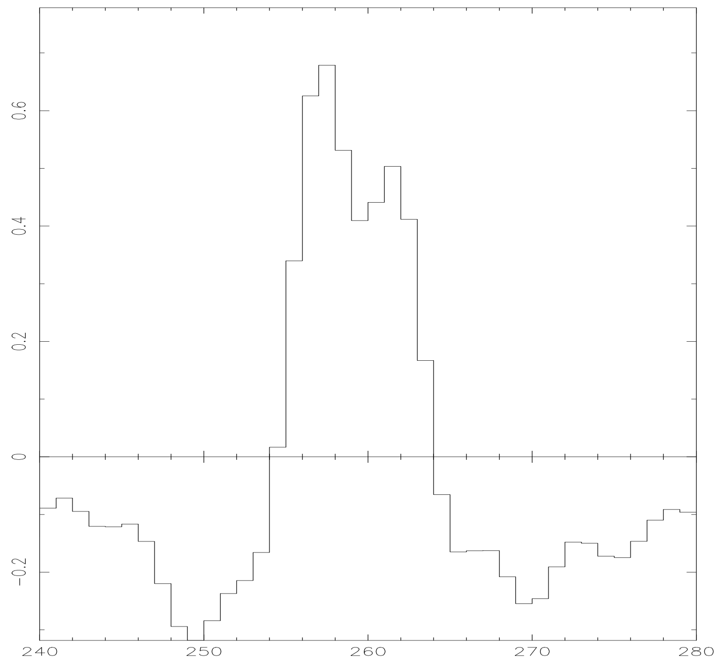

Figure 4.7: Cross-correlation function of object 3. The double peak suggesting its binarity nature is clearly visible.

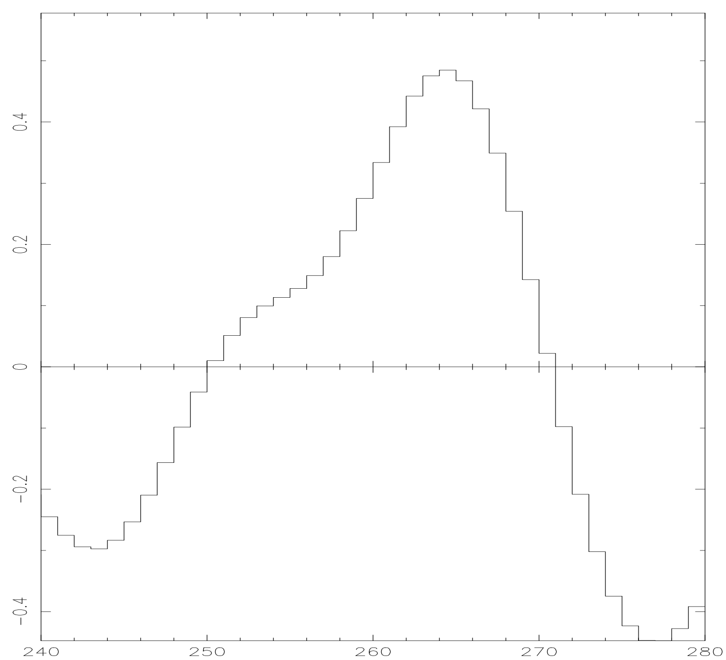

Figure 4.8: As in Figure 4.7, for object 73.

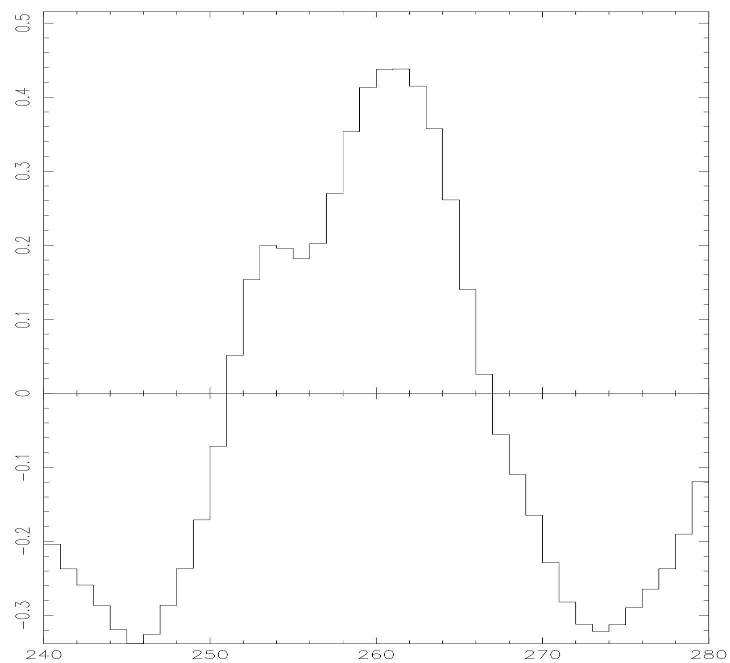

Figure 4.9: As in Figure 4.7, for object 99.

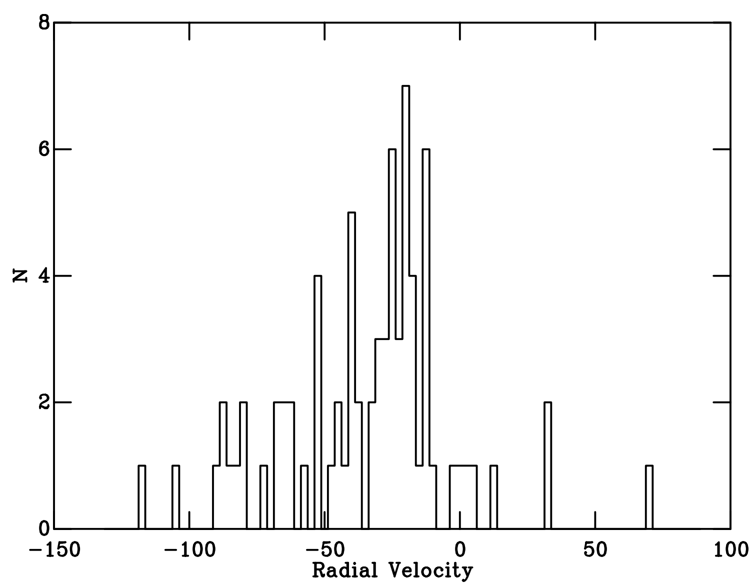

Figure 4.10: Radial velocity distribution of the PMS candidates for which we have a RV measurement.

Note that we also consider object 84 to be a kinematic member, even though we do not have its RV measurement: this object will be classified as CTTS in Section 4.7.

About 25% of the known OB members are double systems (Garrison 1970; see also Section 3.1.5 in Chapter 3), therefore there is the possibility that binary association members are missed through classification of the RV measurement alone. In the case of visible double-peaked cross-correlation functions, the kinematic membership of the possible spectroscopic binary (with equal mass components) is likely to be verified if they are symmetrically placed at left and right with respect of the cluster RV; otherwise the more massive component should be closer to the mean RV of the association. Objects no. 3 and 99 are spectroscopic binaries but likely to be kinematic non-members. Furthermore, to obtain RVs we cross-correlated with a K4 (III) radial velocity standard: some hotter stars could be association members as well, but for them we do not have proper RV measurements.

4.6.2 Li I and Hα equivalent widths

The Li I (λ6707.8) and Hα (λ6563) equivalent widths were measured using the Starlink DIPSO package. The EW is measured by integration below a linear continuum between the two extremes points of the specified line. Each EW was measured three times, and a mean value determined. The mean estimated errors are of about 20 mÅ and 0.2 Å respectively for Li I and Hα equivalent widths, as a result of uncertainty in the continuum location.

The results are summarised in Table 4.4 (the first 53 spectra are those extracted in the first configuration, the remaining ones are those extracted with the second configuration). Positive values are for a line in absorption, negative values for a line in emission. Objects for which a weak RV cross-correlation peak was found, have an uncertain rest wavelength calibration, and therefore the location of the Li I line cannot be determined: for these objects we cannot give an EW measurement, hence they are flagged with a colon. For almost all the spectra, however, the Hα line was always clearly identifiable, so that the corresponding EW measurement was possible (some of them were too noisy though).

#	fib.	(V-I)$_0$	sp.type	EW(Li I) (mÅ)	EW(Hα) (Å)	class	A_V^{ded}	comm.
1	18	0.876	G	:	0.9	:	$>$	
2	25	0.897	G	33	1.3	non-PMS	$>$	nm
3	26	0.466	K	324	0.4	non-PMS	$<$	nm
4	31	1.164	G	15	1.2	non-PMS	$>$	nm
5	33	0.690	F	:	3.2	:	$>$	
6	35	0.593	A	:	3.6	:	$>$	
7	37	1.084	K	493	1.1	WTTS	$=$	m, fr, X34
8	38	1.167	K	422	-5.9	CTTS	$=$	m
9	39	0.326	F	no	11.8	non-PMS	$<$	nm, X48
10	40	0.782	F	76	4.2	non-PMS	$>$	m, (**)
11	46	(a)	A	:	7.5	:		
12	48	0.712	F	no	3.6	non-PMS	$>$	m, X35, (**)
13	50	0.413	K	197	0.8	PMS?	$<$	m
14	51	1.130	G	46	1.2	non-PMS	$>$	nm
15	53	0.252	A	no	4.9	non-PMS	$=$	nm
16	54	0.363	G	138	2.4	PMS?	$<$	m
17	56	0.273	F	no	3.4	non-PMS	$<$	nm
18	58	1.264	K	480	-6.2	CTTS	$=$	m, X26
19	59	0.454	F	no	3.7	non-PMS	$=$	nm
20	61	0.537	F	no	2.7	non-PMS	$=$	nm
21	63	1.114	K	105	1.0	Y	$=$	nm
22	66	0.952	G	59	1.2	non-PMS	$>$	nm
23	67	0.323	F	88	2.6	non-PMS	$<$	nm, vb
24	70	1.152	G	76	1.4	non-PMS	$>$	nm
25	73	0.422	F	no	2.1	non-PMS	$=$	nm
26	75	0.198	G	15	1.6	non-PMS	$<$	nm
27	76	1.232	K	73	0.2	non-PMS	$=$	nm
28	82	0.364	G	no	2.0	non-PMS	$<$	nm
29	84	0.319	F	30	2.3	non-PMS	$<$	nm
30	87	1.113	G	no	1.3	non-PMS	$>$	nm, vb
31	85	1.255	G	no	1.8	non-PMS	$>$	nm
32	80	0.933	K	412	-0.9	WTTS	$=$	m
33	97	1.320	K	:	2.0	:	$=$	
34	108	0.271	F	10	3.0	non-PMS	$<$	nm
35	113	0.185	A	:	2.4	:	$>>$	(*)
36	114	0.928	G	185	1.4	PMS?	$>$	m
37	115	0.954	G	no	0.2	non-PMS	$>$	nm
38	116	0.079	G	no	1.3	non-PMS	$<$	m, (**)
39	99	0.370	F	no	3.0	non-PMS	$=$	nm
40	102	0.936	G	no	1.2	non-PMS	$>$	m, (**)
41	103	0.514	F	16	2.6	non-PMS	$=$	nm
42	104	0.441	F	30	1.2	non-PMS	$>>$	nm, (*)
43	105	0.441	F	:	1.2	:	$>>$	(*)

continue ...

... continued

44	106	1.014	G	:	2.9	:	>	
45	107	0.583	A	:	3.2	:	>	
46	118	0.165	A	:	6.7	:	=	
47	120	0.278	G	no	1.4	non-PMS	<	nm
48	121	0.351	A	:	4.4	:	=	
49	122	(b)	K	400	-27.3	CTTS		m
50	125	0.441	F	no	3.6	non-PMS	>>	m, vb, (*), (**)
51	127	0.524	G	:	4.0	:	<	
52	129	1.322	G	no	1.3	non-PMS	>	nm
53	131	0.484	A	:	5.1	:	>	
54	11	1.333	G	154	0.6	Y	>	nm
55	12	1.456	noisy	:	:	:		
56	13	1.000	G	12	2.3	non-PMS	>	m, (**)
57	16	0.708	G	:	3.4	:	=	
58	18	1.243	K	:	1.7	:	=	
59	19	1.016	G	92	2.0	non-PMS	>	nm
60	20	0.348	A	:	5.4	:	=	
61	22	0.164	K	26	1.2	non-PMS	<	nm
62	23	1.111	G	no	2.4	non-PMS	>	nm
63	25	1.165	G	:	1.9	:	>	
64	26	0.185	A	:	5.4	:	>>	(*)
65	30	1.235	K	:	0.3	:	=	
66	32	0.713	G	31	1.1	non-PMS	=	nm
67	34	1.095	G	13	2.1	non-PMS	>	nm
68	35	0.188	A	:	4.7	:	=	
69	38	0.331	K	47	1.0	non-PMS	<	m, (**)
70	39	0.275	F	8	3.1	non-PMS	<	nm
71	40	0.760	G	41	1.5	non-PMS	=	nm
72	41	1.422	K	:	1.3	:	=	
73	44	0.232	M	:	:	:	<	
74	46	0.769	G	no	1.8	non-PMS	=	nm
75	48	0.218	G	35	1.4	non-PMS	<	nm
76	49	(a)	G	no	1.7	non-PMS		m, (**)
77	51	0.732	G	:	3.7	:	=	
78	57	0.431	F	no	3.2	non-PMS	=	nm
79	60	0.441	F	:	4.2	:	>>	(*)
80	61	0.696	F	:	3.8	:	>	
81	65	0.933	K	309	0.5	WTTS	=	m
82	66	1.307	G	23	2.6	non-PMS	>	nm
83	68	0.185	A	:	4.6	:	>>	(*)
84	74	0.833	K	:	-13.4	CTTS	=	m, veiled
85	75	0.971	M	16	-2.3	non-PMS	<	nm
86	87	0.858	G	12	2.6	non-PMS	>	nm
87	91	1.389	K	:	:	:	=	
88	92	1.110	G	:	2.3	:	>	

continue ...

... continued

89	93	0.938	K	:	:	:	=	
90	94	1.080	noisy	:	:	:		
91	95	1.366	noisy	:	:	:		
92	97	0.897	G	:	4.5	:	>	
93	98	0.946	K	51	-1.6	non-PMS	=	nm
94	108	1.012	G	123	1.4	Y	>	nm
95	109	1.446	K	637	-28.4	CTTS	=	m, X20
96	113	0.376	G	:	2.6	:	<	
97	114	0.326	F	37	2.0	non-PMS	=	nm
98	115	0.506	F	88	0.3	non-PMS	=	nm
99	116	0.570	K	141	0.3	non-PMS	<	nm
100	99	0.848	K	365	0.3	WTTS	=	m
101	102	0.441	F	120	2.1	PMS?	>>	m, (*)
102	103	0.593	G	35	2.3	non-PMS	<	nm
103	104	0.358	F	66	2.4	non-PMS	=	nm
104	105	1.092	M	no	0.3	non-PMS	<	nm
105	106	1.004	G	17	1.6	non-PMS	>	nm
106	107	0.780	K	400	-0.8	WTTS	=	m, X29
107	118	1.120	G	32	0.1	non-PMS	>	nm
108	121	1.320	K	no	2.1	non-PMS	=	nm
109	122	1.009	K	132	0.3	Y	=	nm
110	124	1.094	K	:	:	:	=	

Table 4.4: Id number, fibre number, adopted intrinsic colour, adopted spectral type, Li I and Hα equivalent widths, classification, derived difference in extinction and membership for the objects observed with the two configurations (1-53, 54-110 respectively). Intrinsic colours in column 3 are those determined in Table 4.3 from measured colours, assuming a uniform reddening, for all the objects having a derived extinction (see column 8) consistent with the adopted value of $A_V = 2.81$ mag; except for those objects (*) with a very discrepant derived extinction value (see Section 4.8), for which there are reported the intrinsic colour values expected from the Jacoby spectral type (see the text). Column 4 lists the Jacoby spectral types. Columns 5 and 6 list the equivalent widths of the Li I 6708 Å and Hα lines: positive values are for lines in absorption, negative values for lines in emission; objects for which an equivalent width determination was not possible are labelled with a colon. Classification of the objects is given in column 7, on the basis of their RVs and Li I and Hα EWs (see Section 4.7). Uncertain classifications, due to uncertainties in the EW(Li I) measurements, are flagged with a colon. Symbols are as follows: classic TTS (CTTS), weak TTS (WTTS), possible pre-main sequence (PMS?), non pre-main sequence (non-PMS), young (Y), double-line spectroscopic binary (SB2). See the text why we distinguish between PMS? and Y. In column 8 we give the size of the interstellar reddening with respect to the adopted value of $A_V = 2.81$ mag (see Table 3.7 in Chapter 3): it is deduced by comparing the spectral types deduced from intrinsic colours and those from Jacoby (see Table 4.3). Symbols are as follows: objects with a reddening smaller (<), equal (=), larger (>) or considerably larger (>>) than the mean value adopted (see Section 4.8). In column 9 we add some comments: m indicates kinematic membership to the association, nm kinematic non membership; six objects are optical counterparts to the X-ray sources of NF99 (X plus X-ray id number); vb and fr mean respectively visual binary and fast rotator. (a) star falling down a sky fibre, for which we do not have optical photometry and hence we cannot deduce the change in reddening from a spectral type comparison (a search of its coordinates in the SIMBAD database revealed no known associated object); for it, we adopt the Jacoby spectral type. (b) this is a PMS object, but, unfortunately, it is on a bad column and is flagged by CLUSTER, therefore we cannot trust its photometric colours to determine its spectral type and hence its amount of reddening; for it, we adopt the Jacoby spectral type. (**) these objects probably have the correct RV by chance (see text).

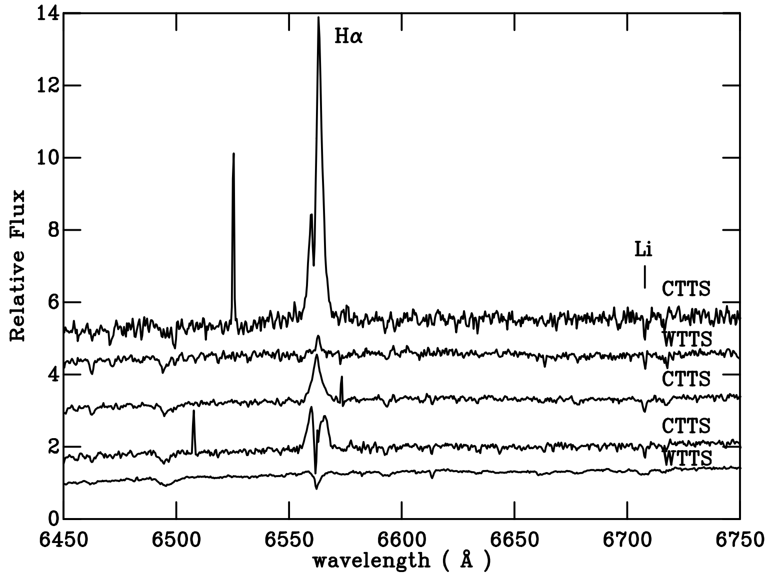

Figure 4.11: The spectra of the 5 TTS from the first configuration. From bottom to top, respectively: object 7 (fibre 37, field 2b), object 8 (fibre 38, field 2b), object 18 (fibre 58, field 1a), object 32 (fibre 80, field 2a), and object 49 (fibre 122, field 4b). They were extracted with method 2, used to measure the Hα line (although the continuum is noisier; see Subsection 4.5.6), normalised to 1 and then offset.

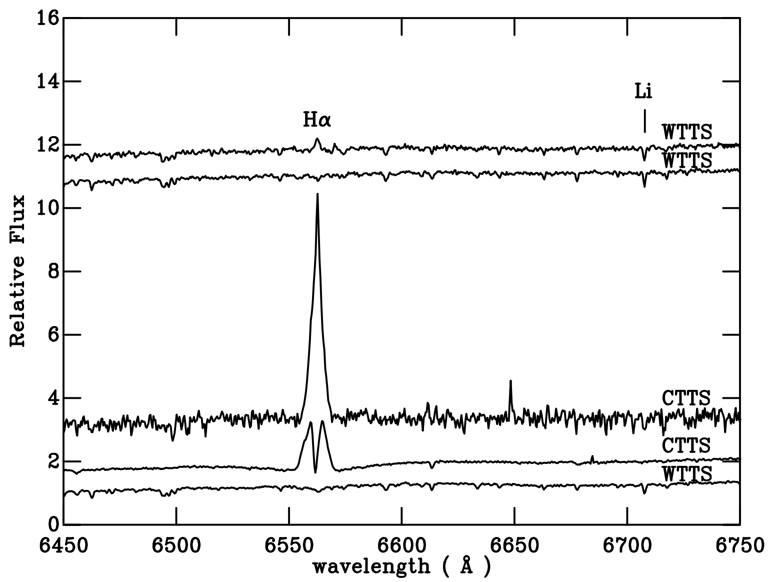

Figure 4.12: The spectra of the 5 TTS from the second configuration. From bottom to top, respectively: object 81 (fibre 65, field 4b), object 84 (fibre 74, field 4b), object 95 (fibre 109, field 1a), object 100 (fibre 99, field 2b), and object 106 (fibre 107, field 1a). They were extracted with method 2, used to measure the Hα line (although the continuum is noisier; see Subsection 4.5.6), normalised to 1 and then offset.

Note that at our resolution the Li I 6708 Å line cannot be separated from an Fe I line at 6707.4 Å, although strong Fe I lines at 6705 Å, and 6710 Å are clearly resolved. Note, however that the likely strength of the 6707.4 line for K type stars such as our TTS, would be $\leq$ 20 mÅ (its EW being estimated from the empirical relationship [20(B-V)$_0$ −3] mÅ given by Soderblom et al. 1993).

In Figures 4.11 and 4.12, a montage of some of the spectra extracted with method 2 (see Subsection 4.5.6) in the first and second configuration respectively are presented. The objects are all PMS stars according to our classification method (see Section 4.7). We call attention to object no. 7, since it is the optical counterpart to the X-ray source no. 34 of NF99, for which they give EW(Li I)= 380 mÅ, and EW(Hα)= 0.6 Å, whereas we find values about 30% and 80% larger.

4.6.3 Spectral types

Spectral types can be estimated using two methods: from the intrinsic (V-I)$_0$ colours of the target stars, or by comparison with a library of stellar spectra. The former applies when the stars in the sample are known to be at the same distance and suffering a certain amount of extinction. Obviously, in the case of a change in reddening, such as the one we suspect across the younger subgroup of the association (see 3.8.2 in Chapter 3), such a method is no longer valid. However, coupled with the latter method, allows one to test the hypothesis of a change in reddening with respect to the adopted one. It can be seen whether the spectral type derived from the intrinsic colour is different from the one derived from the corresponding spectrum.

From our measured (V-I) colours we can find the intrinsic colours $(V-I)_0$ by using a colour excess of $E(V-I) = 1.3{*}E(B-V) = 1.18$ mag, determined from the reddening relationship of Winkler (1997) and $E_{B-V} = 0.91$ (see Table 3.7 in Chapter 3). We can then find T_{eff} by interpolating the T_{eff}-$(V-I)_0$ scale given by Jeffries & Tolley (1998), and from it the expected spectral type according to Table 4.5. This Table is the combination of the sp.type-T_{eff} scales proposed by: Martín (1997), for stars cooler than 6000 K, where the maximum T_{eff} value from different scales available in literature is associated to each spectral type (see Table 6 of Martín et al. 1994; see also Subsection 2.8.2 in Chapter 2); and de Jager & Nieuwenhuijzen (1987), for hotter stars. Results of the T_{eff} interpolation and spectral types assigned are given in Table 4.3. Note that objects no. 4, 23, 30, 35, 50, and 52 are flagged as non-stellar objects in the optical photometric catalogue. A close examination of the CCD

Sp.T.	T_{eff} (K)	references	Sp.T.	T_{eff} (K)	references
A2	9016	(1a)	G8	5445	(3)
A4	8433	(1a)	K0	5236	(3)
A5	8185	(1a)	K1	5105	(3)
A6	7962	(1a)	K2	5000	(2)
A8	7603	(1a)	K3	4775	(3)
F0	7311	(1a)	K4	4581	(3)
F2	7047	(1a)	K5	4405	(1a)
F4	6792	(1a)	K7	4150	(1a)
F5	6653	(1a)	M0	3917	(3)
F6	6531	(1a)	M1	3681	(3)
F8	6252	(1a)	M2	3524	(1a)
G0	6000	(2)	M3	3404	(1a)
G2	5794	(1a)	M4	3288	(1a)
G4	5636	(1a)	M5	3221	(1b)
G6	5500	(2)			

Table 4.5: The spectral type - T_{eff} scale adopted. For stars hotter than 6000 K we have adopted the spectral type - T_{eff} scale of de Jager & Nieuwenhuijzen (1987) for class V (1a). For stars cooler than 6000 K, we have followed the scale proposed by Martín (1997), based on Table 6 of Martín et al. (1994); chosen values are the maximum T_{eff} values for a given spectral type among those available in literature, i.e., those of (1b) de Jager & Nieuwenhuijzen (1987) for class IV, (2) Bessel (1979), (3) Cohen & Kuhi (1979).

images revealed that no. 23, 30 and 50 are visual binaries (and flagged as vb in Table 4.4); no. 52 is extended but single peaked. No. 4 and 35 are not visual binaries and are single peaked. None of these objects is in the SIMBAD database.

We then checked the spectral types by comparing the spectra with the library of stellar spectra given by Jacoby, Hunter & Christian (1984). They have a resolution of 4.5 Å, so we smoothed our spectra (resolution $\sim$ 1Å) to make a comparison.

The presence of TiO features, identifiable by a continuum discontinuity, in the spectral range observed is indicative of late-K to M stars. In our spectral range ($\sim 6400 - 6800$ Å) TiO absorption molecular bands are expected in the region 6651-6852 Å (see for example Montes et al. 1997), and can be noticed although our spectra cover just a small spectral range and are not flux-calibrated, as can be seen in Figure 4.13. An Fe I blend ($\lambda6495$) is clearly seen in most of the spectra, together with other Fe I absorption lines ($\lambda\lambda6546, 6663, 6678$), and Ca I ($\lambda6718$).

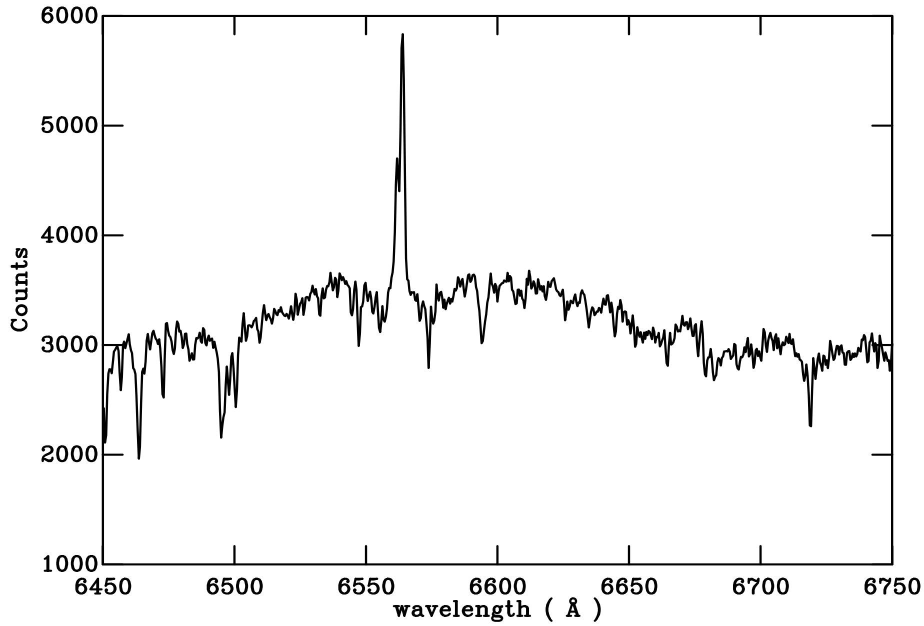

Figure 4.13: Spectrum of object no. 85, an M-type star. TiO absorption molecular bands start to be visible in the region 6650-6750 Å.

From our limited spectral range it is not possible to give a detailed spectral classification in subclasses, but this is enough to check if the spectral types (column 10 in Table 4.3) are consistent with those derived from the dereddened colours (column 9 in Table 4.3).

Some spectral types are in agreement with the spectral types estimated from (V-I) colours, but others are earlier or later. Stars with an earlier spectral type than that we derived from the colour have a higher temperature, smaller intrinsic $(V-I)_0$, and therefore A_V must be larger; conversely, stars with a later spectral type mean have lower temperatures, larger intrinsic colours, and hence lower reddening. For stars showing very large reddening changes (i.e., with spectral types different by 2 classes; objects no. 35, 42, 43, 50, 64, 70, 83 and 101), the resulting reddening vectors are not exactly parallel to the isochrones in the V vs (V-I) CMD: the majority of these stars cannot be considered objects still belonging to the PMS, as confirmed by their earlier spectral type (A, F) and small or no Li detected, suggesting their background nature. However, there is one object (no. 101) which has a large extinction and enough Li detected to be classified as a possible PMS member (although levels of Li of 120 mÅare seen in ZAMS F-stars; see also Section 4.7).

#	class	type	sp. type (Jacoby)	$V_{H\alpha}$ (km/s) (FWZH)
7	WTTS		K	460
8	CTTS	II-R	K	630
18	CTTS	I	K	630
32	WTTS	III-B	K	260
49	CTTS	III-B	K	620
81	WTTS		K	430
84	CTTS	II-B	K	830
95	CTTS	I	K	670
100	WTTS		K	410
106	WTTS	I	K	260

Table 4.6: The PMS objects found in the first and second configuration. For each class, column 3 gives the type according to the scheme by Reipurth et al. (1996): I for symmetric profiles with no or weak absorption features; II for double peak profiles, with the secondary peak more than half the strength of the primary one; III for double peak profiles with the secondary peak less than half the strength of the primary peak. B and R define the location of the secondary peak with respect to the primary (i.e., bluewards or redwards). The velocity widths of Hα lines (from the full-width at zero height) confirm that the EW measurements are not affected by possible residual Hα sky emission lines.

4.7 Membership criteria

The classification of the spectroscopic objects is based on their RVs and Hα and Li I EWs, and reported in Table 4.4. Stars for which we do not have a Li I EW measurement, because of a too noisy spectrum or because of a weak cross-correlation peak (with an uncertain rest wavelength calibration and the consequent uncertainty in the Li line location), are flagged with a colon.

4.7.1 Hα EWs

The EW of the Hα line can be used to classify an object as a possible classical TTS (CTTS) belonging to the association, providing it has the correct radial velocity. In fact, although its Li I EW can be small because of optical veiling (responsible for a masking of the absorption lines; see for example Basri, Martín & Bertout 1991), a CTTS can be immediately recognised thanks to a very wide and strong Hα emission line, not explicable by means of a stellar chromospheric activity such as that observed in weak TTS (WTTS). It must show Hα in emission larger than the conservative value for its spectral type (see columns 6 and 4 respectively in Table 4.4), i.e., a value larger than 5 Å for K-type stars, 10 Å for early M type stars, and 20 Å for late M type stars (see Section 2.9 in Chapter 2). There are 5 kinematic members which are strong Hα emitters (no. 8, 18, 49, 84, 95), and therefore likely CTTS in the association.

We checked the velocity width of the Hα emission lines in these objects (and also in those which will be classified as WTTS in Section 4.7.2), so to be sure that they were larger than any rotational broadening. From the strength of the line in each of the PMS objects (full-width at zero height) we can say that possible problems in the sky subtraction procedure are not going to change the results of our classification (any sky line contamination is unresolved at FWHM $\sim$ 50 km/s). Values are reported in Table 4.6.

RV values for the 5 CTTS are all within 2σ of the mean value known for the Cep OB3 members (see Subsection 4.6.1 in Section 4.6). From the strength of the Hα line and their RV, we therefore classified these 5 PMS candidates as CTTS (one of them is clearly veiled) members of the association (and flagged as m in Table 4.4). Their spectra are shown in Figures 4.11 and 4.12, together with those of the 5 WTTS which are classified in Section 4.7.2.

We call attention to object no. 84 in Figure 4.12: this is the veiled CTTS, and the extension of the wings on both sides of the Hα line suggests a strong T Tauri wind.

In general, the spectoscopic objects having Hα in emission show single-peaked as well as more complex profiles. The majority of the stars showed Hα in absorption. For the PMS objects, a classification in these terms is also given in Table 4.6, by using the scheme given by Reipurth et al. (1996), derived from an atlas of Hα emission line profiles in pre-main sequence stars.

4.7.2 Li I EWs

For all the other objects with measured RV, the classification is performed using an EW (Li I) versus intrinsic $(V-I)_0$ diagram, similar to that of Martín (1997; see also Subsection 2.8.2 in Chapter 2), as shown in Figure 4.14. The dashed line is analogous to the Li isoabundance line drawn in the EW(Li I) versus T_{eff} diagram of Martín (1997), derived for logN (Li) = 2.8, i.e., the minimum Li abundance

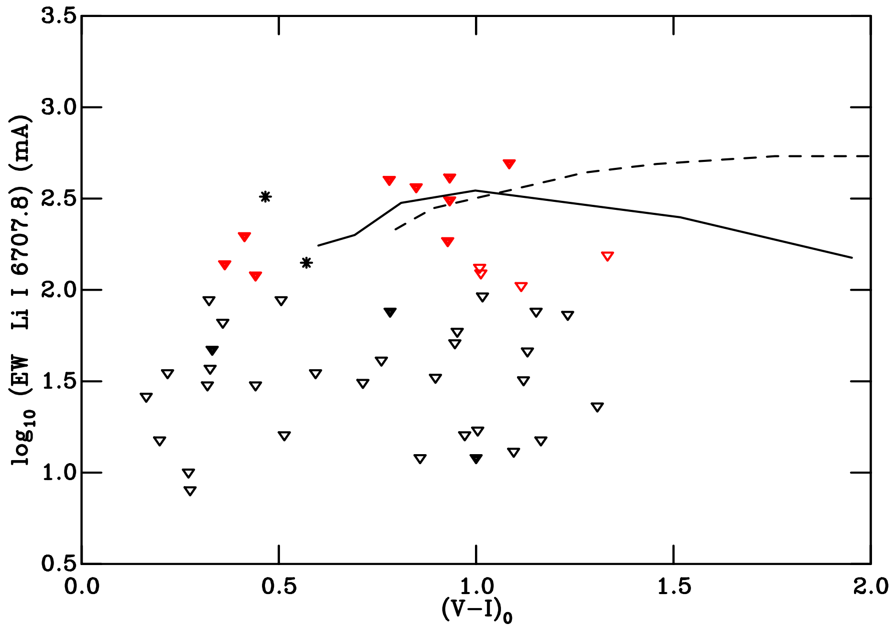

Figure 4.14: Li I 6707.8 EWs versus $(V-I)_0$ diagram for the objects with measured RV. The dashed line is the Li isoabundance ($\log N(Li) \simeq 2.8$) line converted to intrinsic colours with the interpolation of the T_{eff} - $(V-I)_0$ scale of Jeffries & Tolley (1998); the continuous line marks the upper envelope for young open clusters (see Martìn 1997) converted into intrinsic colours. All the stars with spectral type later than early-G and falling above, or close to the Li isoabundance line (see text), and showing the correct RV, are classified respectively as PMS and possible PMS members of the Cep OB3 association (red filled triangles); among the possible PMS stars (no. 13, 16, 36, 101), we include also object 101, an F-type star, which has a large extinction and enough Li detected to be classified as a possible PMS member. Kinematic non-members of the association are shown as black open triangles. The objects marked as black asterisks are the doubled-line spectroscopic binaries objects n. 3 and n. 99. The candidate kinematic members (objects no. 10, 56 and 69) which are non-PMS stars (see text) are shown as black filled triangles; the four kinematic non-members (no. 21, 54, 94 and 109) classified as young objects non-members of the association, are shown as red open triangles. Note that the CTTS are not shown, since already classified through their strong Hα emission line.

values for WTTS as a function of the effective temperature, T_{eff}. This Li I-$(V-I)_0$ locus was found by interpolating the T_{eff}-$(V-I)_0$ scale of Jeffries & Tolley (1998). The continuous line marks the upper envelope for young open clusters (see Martìn 1997) converted into intrinsic colours.

In Figure 4.14 there are plotted 47 objects out of 74 with measured RV: the 4 CTTS for which we have RV measurements, are not shown because classified by means of their strong Hα emission line in Section 4.7.1; another 23 objects are not plotted because of their Li non-detection.

For those objects (no. 35, 42, 43, 50, 64, 79, 83, 101) showing a significantly higher extinction with respect to the adopted one, we adopted the intrinsic colours appropriate for their spectral type, i.e., the values expected from Jacoby spectral types, instead of using intrinsic colours derived from measured colours. We assumed subclass 5 for the required Jacoby spectral types and converted the associated effective temperatures (as given in Table 4.5) into intrinsic colours using the T_{eff}-$(V-I)_0$ scale of Jeffries & Tolley (1998). Adopted intrinsic colours, Jacoby spectral types and derived difference in extinction are listed respectively in columns 3, 4, and 8 of Table 4.4.

Note that the uncertainty in the intrinsic colours, due to the uncertainty of the interstellar reddening towards different objects in the association or the uncertainty in having adopted a subclass 5 for those objects which are suffering a significant amount of extinction, would have the effect to shift the datapoints solely along the x axis, therefore this does not change our conclusions about the nature of those objects classified as definite PMS stars.

All the kinematic members with spectral type later than early-G and falling above or close to the dashed line in Figure 4.14, i.e., with EW Li I > 200 mÅ or with 100 < EW Li I < 200 mÅ are classified as WTTS (since we have already classified the possible CTTS by means of their strong Hα emission) and possible PMS (PMS?) objects of the Cep OB3 association respectively. In particular, among the PMS? objects there is also an F type star: this is too hot for the Li test (it may not deplete Li in its PMS phase), but since it has EW Li I > 100 mÅ, it could be a PMS object as well.

Note that three objects (no. 10, 56 and 69) are candidate RV members with Li I EW smaller than 100 mÅ, which we classify as non-PMS, non-member of the association: they are respectively F-G type stars, and expected to show Li even if ZAMS stars; and a K type star expected not to fail the Li test if it were a PMS member (see Section 3.1.7 in Chapter 2). Therefore these are non-PMS non-members of the association happening to have the correct RV by chance. The same classification is valid for objects no. 12, 38, 40, 50, and 76 (F and G type stars) which appear to have the correct RV but for which no Li was detected.

Among the kinematic non-members, there are 4 objects (n. 21, 54, 94, 109), of spectral type K and G, which have a Li I EW larger than 100 mÅ (up to 154 mÅ): they are classified as young stars (Y), since they could be PMS or early-G ZAMS stars which have not totally depleted Li I in their PMS phase (see Section 3.1.7 in Chapter 2). They could have the wrong RV if spectroscopic binaries (SB1; they are not SB2): we classify them as young stars but probably non-members of the association.

Note that there are 18 kinematic non-members with Li non-detections which are classified as non-PMS, non-members of the association.

The classification and kinematic membership or non-membership of all of these objects are given in columns 7 and 9 of Table 4.4 respectively.

Summarising, from this classification we have found 5 WTTS as PMS members of the Cep OB3 association. Their spectra are shown in Figures 4.11 and 4.12, together with those of the 5 CTTS. For the classification of their Hα emission line profiles see Table 4.6. Furthermore, there are 4 objects which are possible PMS members. Among the non-members of the association, there are 4 young objects and 57 non-PMS stars.

4.8 Discussion

In total we found 22 objects as candidate kinematic members, 21 from RV measurements (2σ RV members) plus one plus object without RV but which is a CTTS and therefore a very likely member. Among these, there are 14 association members in total: 10 PMS stars (5 CTTS and 5 WTTS) and 4 possible PMS stars. The other 8 candidate RV members turned out to be non-PMS non-members probably showing the correct RV by chance.

We can then estimate the likely number of contaminants to have the correct RV by chance. Out of 74 objects with measured RV, we found (see Section 4.6.1) 21 candidate kinematic members and 53 kinematic non-members. Of these 45 objects have radial velocities between -88 and 0 km/s, and are pretty evenly spread (with 8 outliers even further out; see Figure 4.10). Assuming for these 45 objects a uniform spread over this velocity range, from Poisson statistics we would expect to see $45 * 12/88 = 6.1 \pm 2.5$ objects to fall by chance in our selection range of ± 6 km/s. Therefore, out of 21 candidate kinematic members, we would expect 6 ± 2 objects to have the correct RV by chance and 15 ± 2 objects to be true association members. Given the fact that from RVs plus Li test we have classified 13 of these candidate RV members as association members and instead 8 as non-members of the association happening to have the correct RV by chance, we can say that the classification results obtained with RV measurements (see Section 4.6.1) coupled with membership criteria (see Section 4.7) are in perfect agreement with statistical expectations.

Therefore we have spectroscopically confirmed the presence of a low-mass stellar association in

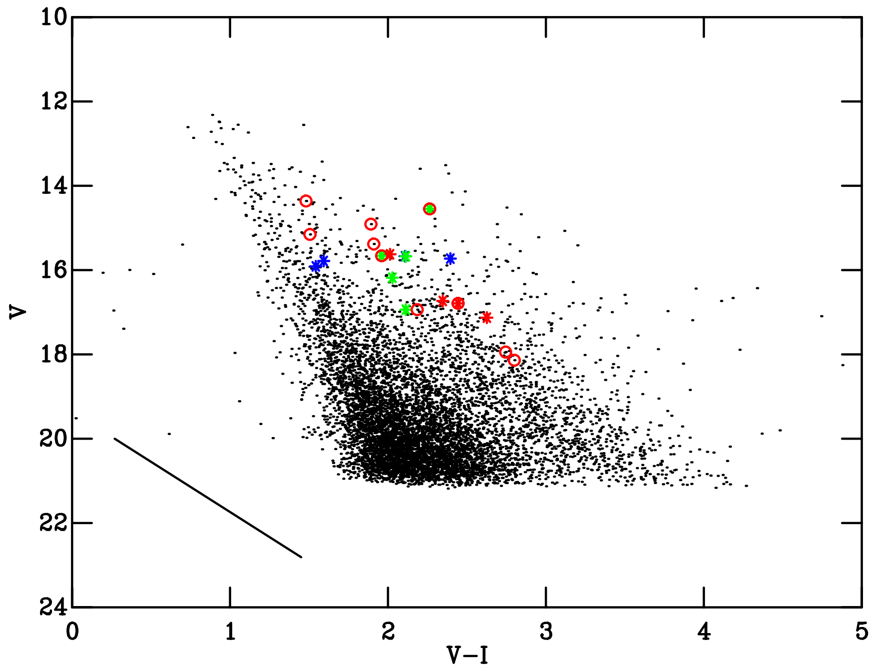

Figure 4.15: The colour-magnitude diagram in V versus (V-I) for the stars in the six fields used for the selection of the PMS sample for the spectroscopic follow-up. CTTS and WTTS are shown respectively as red and green asterisks, whereas the possible PMS members as blue asterisks (note that one of them is hidden behind the WTTS at V= 15.7 mag and (V-I)= 2.1 mag). The CTTS with colour flagged as bad is not shown. Optical counterparts to the X-ray sources of NF99 are circled in red. Also plotted is the reddening vector.

the younger subgroup of the Cep OB3 association.

Out of 14 PMS and possible PMS stars, just 4 (2 WTTS and 2 CTTS) have an X-ray counterpart in NF99. This shows that an X-ray PMS selected sample (instead of our optically selected sample) would have been very incomplete: we would only have seen $\sim 1/3$ of the PMS objects we have identified here.

Figure 4.15 shows the location of the PMS and possible PMS members in the V versus (V-I) colour-magnitude diagram.

There are 14 association members in total, and 61 non-members: this suggests that the contamination in the PMS sample is of order 70%. This large percentage is the consequence of the generous region over which the targets were selected in the CMD, and the fact that no account was taken of reddening variations in different CCD fields (as proposed in Table 3.19 in Chapter 3).

A changing in reddening across the association has the effect of shifting the stars in the colour-magnitude diagrams towards redder colours, and therefore filling the PMS location with non-PMS objects. However, as pointed out in Chapter 3, dereddening the fields by the proposed amount so to match their background sequences with that in field 1a, obviously does not tighten the background sequence and the PMS in the same field, since the dereddening tecnique is applied to all the stars in the field, therefore still giving objects between the 10 and 30 Myr isochrones. This conspires against giving us a cleaned overall picture, with background and PMS well separated as in field 1a, once we deredden the 6 fields used for the spectroscopic PMS selection (see Figure 4.1) of the proposed amount reported in Table 3.19 of Chapter 3. These dereddened fields are plotted in Figure 4.16, together with the spectroscopic objects (dereddened accordingly to the fields they belong to).

Therefore, after taking into account of an extra reddening, there are still a lot of objects in the fields other than in field 1a filling the gap between the 10 and 30 Myr isochrones. Non-members of the association are spread, and do not lie in a narrower sequence. Furthermore, TTS are not confined to a narrower PMS and there are still a lot of objects younger than 1 Myr, suggesting that there is indeed a spread in ages, as suggested in Chapter 3. The global picture in the younger subgroup of this association is therefore quite complex.

If we concentrate, for clarity, on the field 1a only, we have observed spectra for 16 objects, 6 of which are kinematic members and 10 kinematic non-members. Out of 6 candidate RV members we have found 5 PMS association members, plus one F type star with no Li detection classified as non-PMS non-member. Thus, it would seem that we have detected just 5 PMS stars out of 16 spectra, but we must recall that the PMS selection was done considering a very broad region in the CMD, comprising objects well below the 10 Myr isochrone up to until the background sequence. If we had selected just stars younger than the 10 Myr isochrone, we would have ended with the striking result of 5 spectra observed, giving 5 candidate RV members, which are all PMS association members. In fact, both the 10 RV non-members and the F type star all lie in the part of the CMD where we have stars older than 10 Myr (at brighter magnitudes).

If we then consider Figure 4.16, it appears that a better strategy in selecting the PMS sample for the spectroscopic follow-up would have been to create a CMD combining all the required fields, properly dereddened with the proposed amount, and then selecting a narrower region comprising just

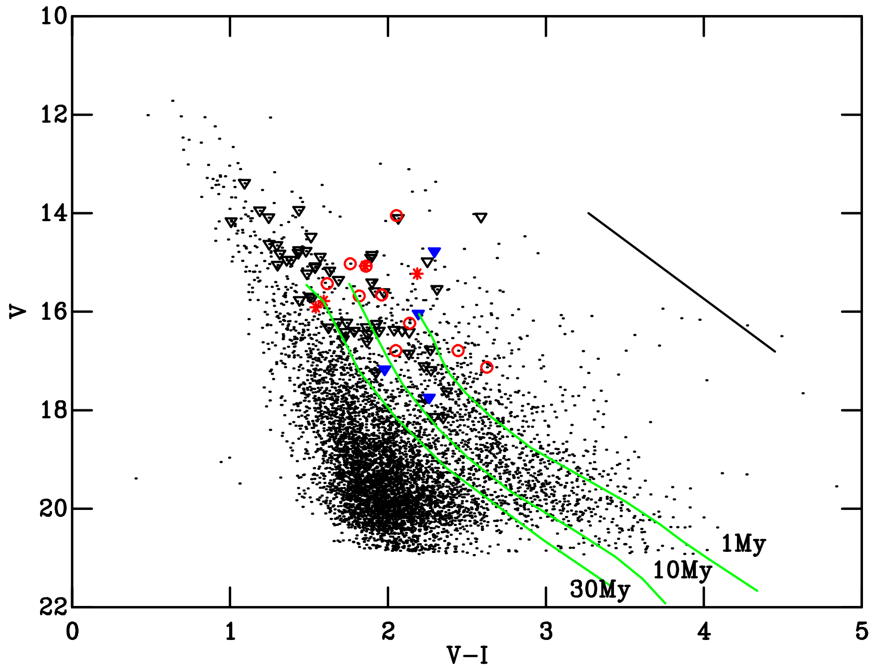

Figure 4.16: The colour-magnitude diagram in V versus (V-I) combining all the stars from the six fields used for the spectroscopic follow-up, together with the spectroscopic objects observed, all properly dereddened (to match the adopted reddening of $A_V = 2.81$ mag, assumed valid for field 1a) of the proposed values in Table 3.19 of Chapter 3, according to the field they belong to. Association members are shown as red circles (CTTS and WTTS) and red stars (possible PMS). Non-members of the association are shown as blue filled triangles (young stars) and open black triangles (non-PMS). Note that there are 6 black triangles which are not centered on a star: these are the only non-stellar objects we retained from the catalogue (all the stars plotted as black dots are just the good ones, i.e., stellar objects with good photometric flags). Also plotted is the reddening vector (according the adopted value of $A_V = 2.81$ mag).

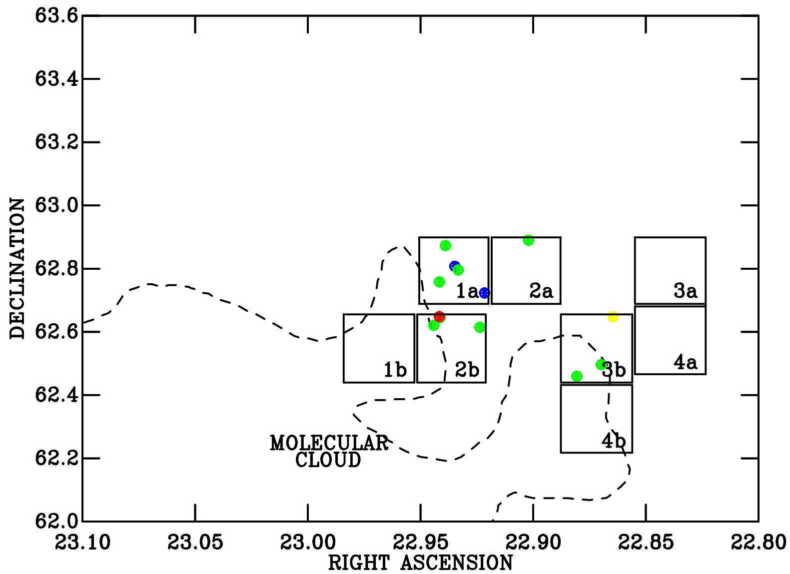

Figure 4.17: Changing in reddening with respect to the adopted value of 2.81 mag for the association members reported in Table 4.4. Objects with a reddening smaller, equal, larger or considerably larger than the adopted one are plotted respectively as blue, green, yellow and red filled circles. Note that one green circle in field 2b is almost entirely hidden behind the red one.

the stars which appear to be about 10 Myr, and younger, and following the direction of the reddening vector. In other words, selecting all the stars above the line passing through the points $(1.0, 14.0)$ and $(3.2, 20.0)$, and with $(V-I) > 1.5$ mag. This would have cleaned the PMS sample from a large fraction of non-members and, conversely, would have taken into account of all the objects which appear to be much younger than 1 Myr, and which were left out, in the original selection, increasing the number of likely PMS objects in the westernmost fields of Cep OB3b. The likely age spread is about 10 Myr.

To have a clearer picture of the interstellar reddening across the association for the Cep OB3 members, we plotted the reddening strength in Figure 4.17.

Association members for which we found a reddening smaller, equal, larger (if the difference in spectral type derived from intrinsic colour and Jacoby is of 1 class) or considerably larger (if the difference in spectral type derived from intrinsic colour and Jacoby is of 2 classes or more) than the adopted one are plotted respectively as blue, green, yellow and red filled circles. Note that object no. 101 (see Table 4.4) has a significantly higher reddening value with respect to the adopted one of

2.81 mag. As can be seen from Figure 4.17, it belongs to field 2b and is close to the CO contour of the molecular cloud. We cannot see a homogeneous trend of increasing reddening going from field 1a towards the westernmost fields (fields 3 and 4), but instead a more patchy distribution. It appears that one star closer to the molecular cloud suffers from a very large reddening, but other stars more on-cloud appear to have the same reddening value of the adopted one.

For fields 1a and 2a, the objects seem to be suffering the same (or even less) extinction than the adopted value. This is in agreement with our previous estimates of a change in reddening in field 2a to be quite small, and confirming field 1a as the best reference field to choose in tackling the problem of a different amount of extinction for the other fields (see Table 3.19).

In field 3b, although there are two stars suffering the same amount of the adopted reddening, there is one object with a larger value (object 36): this is a G-type star according to Jacoby classification, therefore it should have a temperature of about 5600 K (see Table 4.5), which corresponds to an intrinsic colour of about $(V-I)_0 = 0.69$ mag (from Jeffries & Tolley 1998). By comparison with its observed (V-I) colour, we find an extra reddening of about $dA_V = 0.56$ mag. This is in excellent agreement with the value of 0.8 ± 0.2 predicted in Chapter 3 for this field with respect to field 1a (see Table 3.19), and suggests that field 3b may be really suffering a higher extinction than the adopted value, as suspected (see discussion in Section 3.8.2).

Unfortunately we do not have objects in fields 3a and 4a to check if they are suffering a higher extinction, as predicted. Fields 1b and 4b contain no objects, since they were not included in the selection of the PMS candidates.

If we recall the distribution of reddening for already known high-mass members of the Cep OB3b subgroup (see Figure 3.2 in Chapter 3), there is no evidence for a gradient, apart for two stars below field 4b, which are more on-cloud and suffer from a higher extinction. Unfortunately, there are no early-type members in fields 3a and 4a, for which we would predict higher reddening with respect to the other fields.

We can conclude by saying that to support the idea of a reddening gradient across Cep OB3 (see additional extinction values proposed in Table 3.19 for the different CCD fields observed) a larger sample would be required to do a proper statistics. Finally, larger wavelength coverage spectra for a larger sample of objects would be necessary to define exactly the spectral type of the observed objects, and hence to determine the correct amount of extra reddening occurring with respect to the mean adopted value, and to test the possibility of a differential reddening within each CCD field.

Although the statistics are poor, CTTS and WTTS do not seem to occupy distinct locations in the Cep OB3b region. As can be seen from Figure 4.18, they are mixing fairly well one with each other. They are all close to the interface between the molecular cloud and the HII region. Note that the spectroscopic sample was selected from stars in all the fields apart from fields 1b and 4b, which are pointing towards the molecular cloud.

From Figure 4.18 it seems that, apart these two fields, the TTS are spread in all the other fields but are absent from fields 3a and 4a which are the more distant from the CO contour of the molecular cloud. Furthermore, we notice that field 2a has just one WTTS falling in it, whereas fields 1a, 2b and 3b, which are closer to the molecular cloud, have both CTTS and WTTS. Note, however, that we may have biased against the detection of TTS in some fields by the selection procedure used for target stars (in particular, it left out the majority of the objects which seem to be much yonger than the 1 Myr isochrone in the CMD).

From these results, we can derive the WTTS/CTTS ratio (see Section 2.12 in Chapter 2), a very important number in addressing the problem of the dissipation timescales for circumstellar discs. For the younger subgroup of the Cep OB3 association we find a ratio of 1, which can be compared with values found in other star forming regions. For T associations, such as Taurus-Auriga, Chamaleon, Lupus and ρ Ophiuci (see Section 2.12 in Chapter 2 and references therein), where the ratio is in the range 1 to 13, worked out from X-ray selected samples. Recall that it is probably biased towards WTTS, because CTTS are more difficult to detect in soft X-rays, and therefore its value is expected to be even smaller. In OB associations such as λ-Ori and Upp-Sco, the only two OB associations for which the ratio value is known (see Section 2.12 and references therein), this ratio increases up to more than ~ 20, determined from a spectroscopic follow-up of optically selected samples.

The value of 1 we have found for Cep OB3b is closer to the value known for T associations than OB associations, a more striking result, if we compare it with the value of more than 20 found for the PMS stellar association that we have discovered around the Wolf-Rayet star γ^2 Velorum (see Chapter 7). We stress that these numbers are worked out from a spectroscopic follow-up of PMS samples, therefore they are not biased against CTTS. The explanation of such a low WTTS/CTTS value for Cep OB3b could be ascribed to a less effective erosion (through stellar winds and ionizing radiation) of the circumstellar discs around the low-mass PMS members by the high-mass members

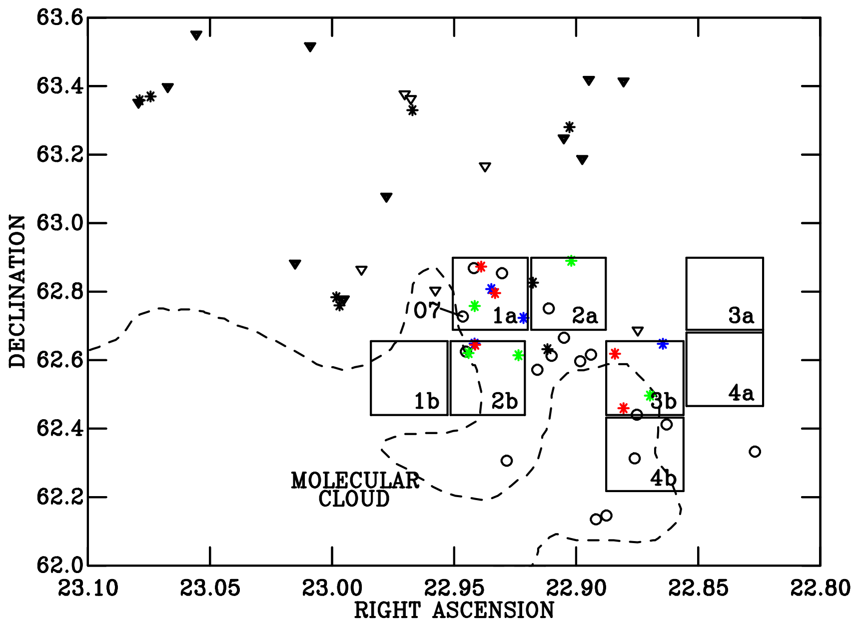

Figure 4.18: The location of the PMS objects found with the spectroscopic observations in the younger subgroup Cep OB3b: CTTS, WTTS and the possible PMS stars are shown as red, green and blue asterisks respectively (note that one possible PMS star is hidden behind the CTTS in field 2b). Boxes are the CCD fields used for the optical photometric investigation, dashes define the lowest CO contour of the molecular cloud (taken from Sargent 1977). Other symbols as in Figure 3.2.

of the association.

Finally, we call attention to Figure 4.19. It shows the colour-colour diagram in (U-V) versus (V-I) for 1241 un-flagged stars in our catalogue, with colour errors less than 0.1 mag. CTTS and WTTS are overplotted as red and green circles respectively (also shown is the veiled CTTS, as red asterisk). This kind of plot allows one to pick up stars undergoing active accretion thanks to their ultraviolet excesses (Rebull et al. 2000, and references therein). The UV excess is defined as the difference between the de-reddened (U-V) colours and the expected values according to their spectral types. All the stars which after dereddening are not likely to intersect the zero-age main-sequence (ZAMS) are the stars with UV excess. If we deredden the T Tauri objects in our plot, following the direction of the reddening vector, it is immediately clear that they are likely to intersect the ZAMS, and that they do not show an UV excess. Therefore it seems to suggest that none of our TTS is accreting mass at an high rate from a circumstellar disc.

Note, however, that besides an optical-ultraviolet continuum excess, mass falling into a central star from an accretion disc can be detected from near-infrared excess too. CTTS are characterized by both excesses (Hartigan et al. 1990), whereas WTTS lack both. According to Rebull et al. (2000), good disc candidate stars selected by means of UV excess should also show IR excess: if they do not, they are likely to have an unfavorable inclination or large holes in the disc (or both).

But the contrary can also happen, i.e., stars which appear to be disc candidates from IR excess may have not been selected as such in the UV, because of low accretion rates.

Therefore, to be sure about the presence or not of circumstellar discs around the T Tauri objects found with spectroscopy, it is necessary to check their IR excesses too. The 2MASS catalogue available on line to the public helped us in the achievement of this purpose. The IR analysis is discussed in detail in the next Chapter.

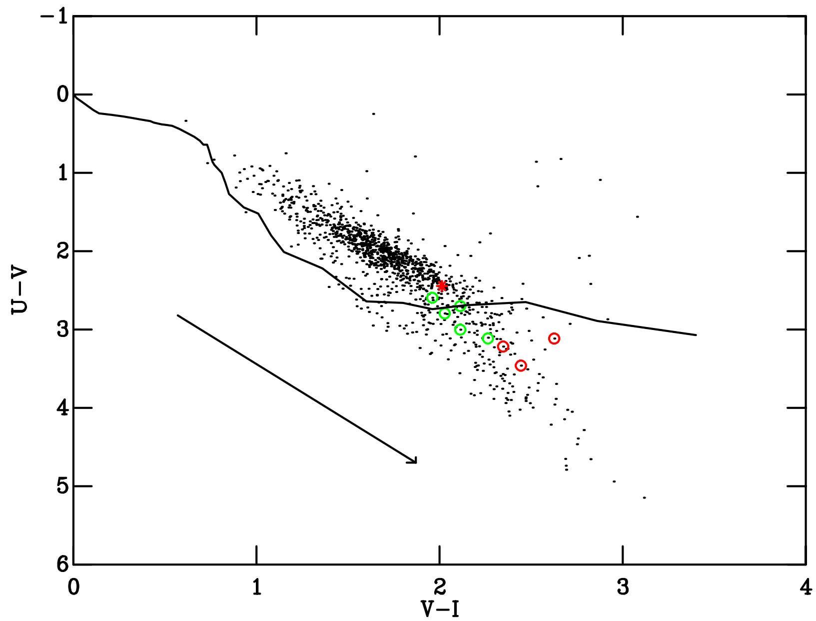

Figure 4.19: The colour-colour plot in (U-V) versus (V-I). CTTS are plotted as red circles, WTTS as green circles, the veiled CTTS as a red asterisk. The CTTS which is on a bad column and for which we cannot trust the photometric colours is not shown. Also plotted the unreddened ZAMS (Kenyon & Hartmann 1995). The direction of the reddening vector is shown, with $E_{V-I} = 1.3E_{B-V}$, and $E_{U-V} = 1.88$ derived from known $E_{U-B} = 0.88$ and $E_{B-V} = 1.00$ for the Cep OB3b region (Moreno-Corral et al. 1993). Note that this is in perfect agreement with the relation $E_{U-V} = 1.45E_{V-I}$ given by Fitzpatrick (1999). It is clear that dereddening the TTS along the direction of the reddening vector does not give stars with UV excess: they are all going to intersect the unreddened ZAMS. However, this is not a striking proof of an absence of circumstellar accretion discs, as explained in the text.

4.9 Conclusions

In this Chapter we have spectroscopically confirmed the presence of low-mass PMS stars in the Cep OB3 association, a result which was previously confined to optical photometric identification.

Out of 110 stars for which we have spectra, we classified 10 PMS and 4 possible PMS objects, all of which are 2σ RV members of the association. There are other 4 objects classified as young stars (for the strength of the Li I line), but which are RV non-members. Just 4 of the PMS objects have a ROSAT X-ray counterpart, suggesting the presence of an X-ray quiet population, and, more important, showing that an X-ray selected sample would have been two thirds incomplete.

Among the PMS members, we found 5 CTTS and 5 WTTS. This gives a WTTS/CTTS ratio equal to 1. This value is more similar to that found in T associations (1-13) than that found in OB associations (up to 20). The lower value we have found for Cep OB3, despite the presence of OB type members, could be the result of less effective stellar winds and ionizing radiation from the high-mass members of the association in eroding and subsequently evaporating the circumstellar discs around the low-mass members. This conclusion is supported by a WTTS/CTTS > 20 found in Chapter 7 for the PMS stellar association discovered around the Wolf-Rayet star γ^2 Velorum, responsible for a massive stellar wind which dissipated the disc from all the PMS stars around it.

5 Infrared observations for Cep OB3b

5.1 The 2MASS catalogue

Infrared wavelengths are useful to detect protostars and young stars still cocooned in gas and dust which prevent them being detected by optical photometric surveys. At these wavelengths, reddening is less of a problem: for the K band $A_K \sim 0.1 A_V$ (see Rieke & Lebofsky 1985). The observed infrared radiation is due to radiation coming from the central star, combined with radiation from a heated circumstellar disc and in part due to intrinsic (viscous) radiation generated by the accretion processes in the disc itself. As a result, young stellar objects still retaining optically thick discs show infrared excesses, since both their optical and ultraviolet radiation, and mass accretion processes in the disc, heat the dust and gas around them.

Near infrared data for Cepheus OB3 are available as part of the 2 Micron All-Sky Survey (2MASS), which aimed to scan 95 % of the entire sky at near-infrared wavelengths, detecting point sources with signal-to noise greater than 10. The 2MASS data tiles are of about $8.5' \times 6^{\circ}$ in size. Each tile is a combination of $\sim$ 273 camera frames, taken in succession at the same RA but at increasing Dec (i.e., each of them at about 1/6 of a frame in Dec from the previous frame; see the Explanatory Supplement to the 2MASS Second Incremental Release[1]). We accessed the 2MASS Second Incremental Release Point Source Catalog (PSC), which contains a list of positions and JHK$_s$ magnitudes (at mid-band wavelengths of 1.25μm, 1.65 μm, and 2.17 μm), plus associated errors and flags indicating the quality of the photometry, for point sources covering about the 47% of the sky. We opened a field centered at 22 53 24.00 in RA, and +62 40 18.0 in declination, and with a search radius of 3600", aiming to cover the optical CCD fields in Cep OB3b (see Figure 3.2). A catalogue of 30666 objects was found with JHK$_s$ colours, hereafter the NIR catalogue, with associated astrometric positions (equinox J2000.0). The approximate magnitude limits in JHK$_s$ for the 2MASS point sources are 15.8, 15.1 and 14.3 mag respectively; the quoted astrometric accuracy is better than 0.2" (from comparison with the positions of stars in the USNO CCD Astrograph Catalogue), but it can be up to 1", for stars in tiles with a small number of reference stars used in computing the astrometry (see the Explanatory

[1] *http://www.ipac.caltech.edu/2mass/releases/second/doc/explsup.html*

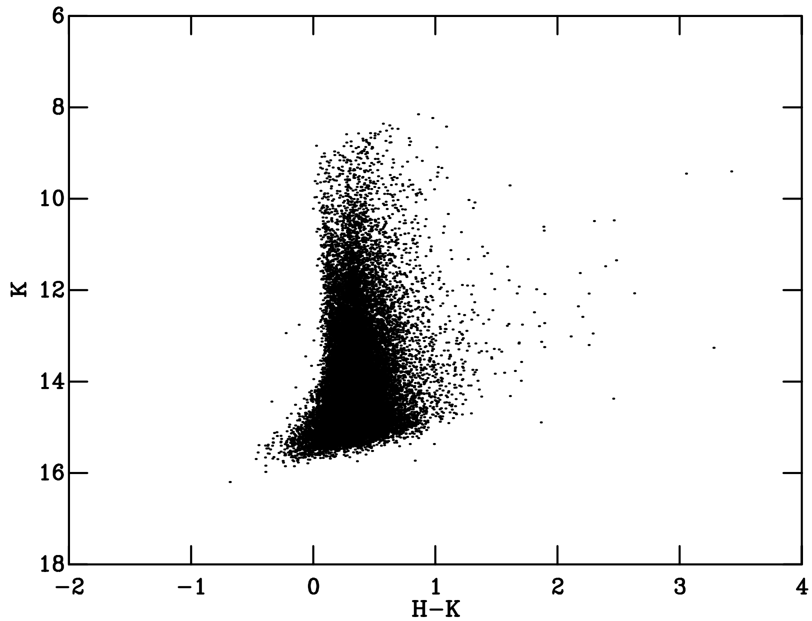

Figure 5.1: Colour-magnitude diagram in K versus (H-K) for the NIR objects found as a result of the search in the 2MASS database (opening a field centered on the Cep OB3b association).

Supplement to the 2MASS Second Incremental Release).

The photometric system in which the magnitudes are given is the natural 2MASS one. Transformation equations to convert 2MASS magnitudes to other photometric systems are not yet available, but the colours for normal stars are very close to the values given by Koornneef (1983) and Bessell & Brett (1988). Therefore, in the following analysis, when plotting a reddened main-sequence in the diagrams, we have used the NIR intrinsic colours for main-sequence stars given by Koornneef (1983), corresponding to the Johnson photometric system (Johnson et al. 1966), without performing any colour transformations.

We have recently discovered that the colour transformation equations to convert colours and magnitudes measured with other photometric systems into the 2MASS system are now available (Carpenter 2001). In particular, transformation equations have been derived indirectly for both the Koornneef (1983) and the Bessell & Brett (1988) photometric systems too, with small colour transformation zero points in the range 0.01-0.05 mag.

In Figures 5.1, 5.2, and 5.3 the colour-magnitude plot in K versus (H-K), the colour-colour plot

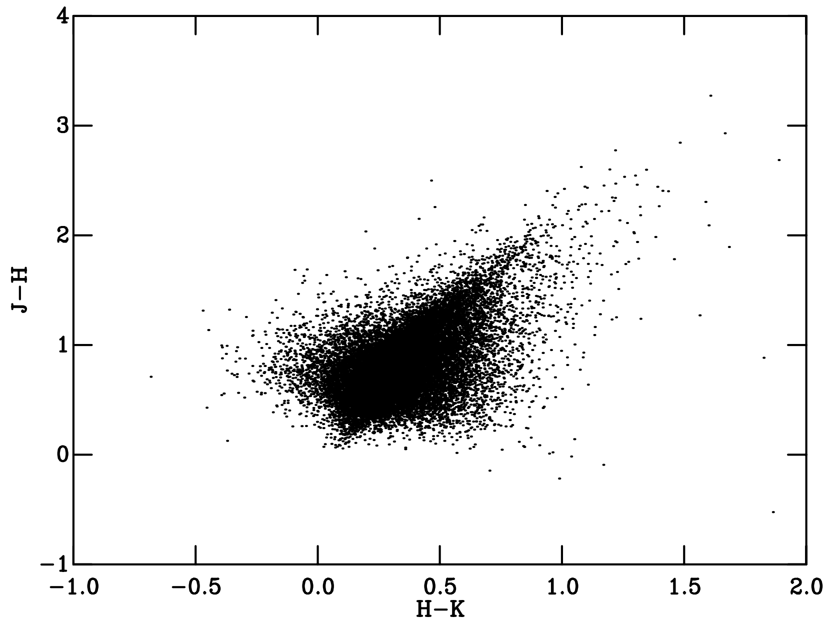

Figure 5.2: Colour-colour diagram in (J-H) versus (H-K) for the NIR objects found as a result of the search in the 2MASS database (opening a field centered on the Cep OB3b association).

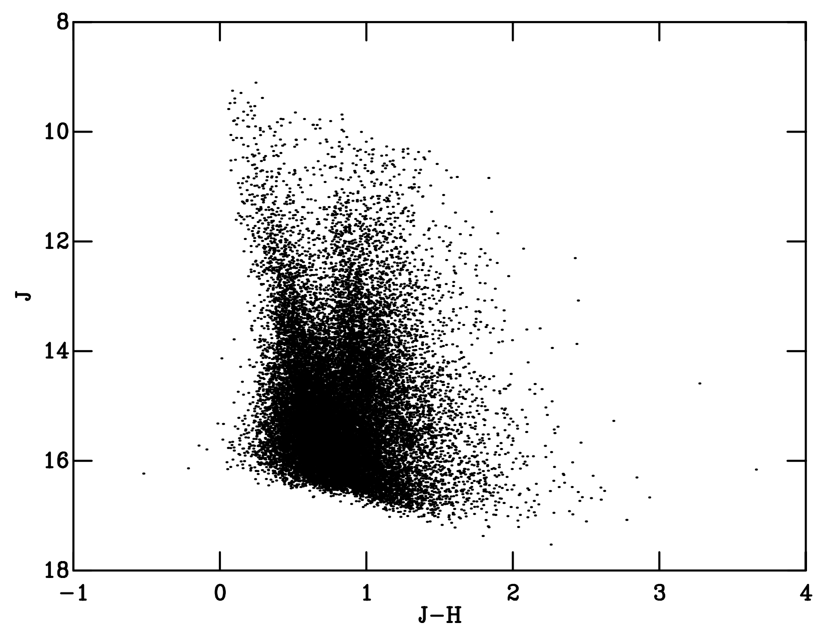

Figure 5.3: Colour-magnitude diagram in J versus (J-H) for the NIR objects found as a result of the search in the 2MASS database (opening a field centered on the Cep OB3b association).

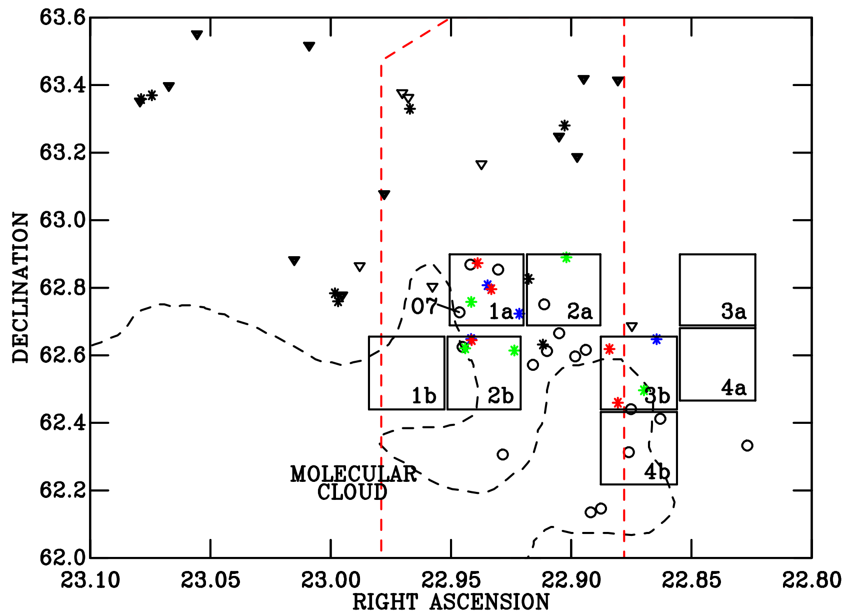

Figure 5.4: The location of the NIR sources (inside the red dashed lines) in the Cep OB3b association (symbols as in Figure 4.18). Apart the fields 1b and 4b which were not included in the spectroscopic sample, it is evident that the NIR sources of the Second Incremental Release did not cover entirely all the other fields. There are three sources (not shown) outside the dashed region, at (22.85h, 61.76d), (22.87h, 63.38d), and (22.88h, 62.66d) respectively (see the footnote).

in (J-H) versus (H-K), and the colour-magnitude plot in J versus (J-H) are shown for objects in the NIR catalogue.

Figure 5.4 shows where these NIR sources are located in Cep OB3b. They are all contained in the region defined by the red dashed lines, apart from three additional sources (not shown).[2]

At the stage where this analysis was performed, only the 2MASS Second Incremental Release was available, which did not cover the entire extent of the optical photometric data.

[2]These sources are very bright star filler entries that were included in the data release to assist in recognising artifacts that might be associated with them. They are denoted with default magnitudes set to −99.999 in J, H and K, and rd_flag values of 888. These and all the other NIR objects flagged as bad were filtered out in creating our working catalogue.

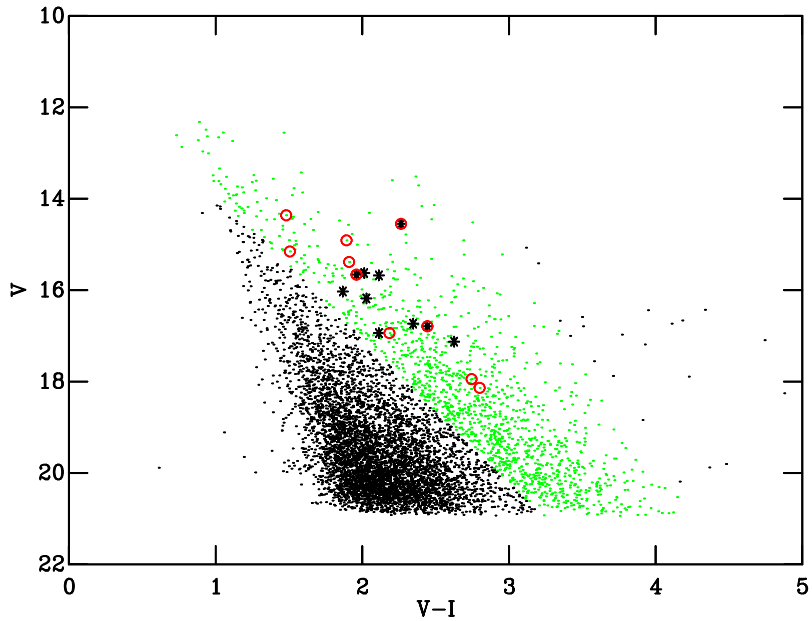

Figure 5.5: The selection of the global PMS strip encompassing the optical counterparts to the X-ray sources of NF99 (red circles) and the spectroscopically confirmed PMS objects (black asterisks). All the stars in our optical photometric catalogue are included for the selection, apart those belonging to the fields 1b and 4b (which are on-cloud), those flagged as bad, and those with photometric errors larger than 0.1 mag.

5.2 Correlation with the optical photometric catalogue

We selected a "global PMS strip" from the objects plotted in the V versus (V-I) colour-magnitude diagram of Figure 4.1, with the restrictions that all these objects must be unflagged at these colours, and have errors less than 0.1 mag, in order to search for PMS objects with possible IR excesses. The selected region is shown in Figure 5.5. We then added by hand the information regarding the CTTS which is on a bad column (and hence flagged as bad). There are 1326 objects in total in the global PMS strip. These objects were correlated with the objects in the NIR catalogue, after filtering out all the 2MASS NIR objects flagged as bad (such as saturated stars, faint stars with a too low S/N, stars on bad or dead pixels, very bright entry fillers, extended sources such as galaxies, and blended sources for which the profile fit photometry failed).

We then searched for positional co-incidences between the two catalogues within a cross-

	Field					
	1a	2a	3a	4a	2b	3b
Ncorr	322	152	0	0	229	60
N_{opt} (PMS)	338	161	147	195	265	220

Table 5.1: The number of correlations NIR catalogue - global PMS strip in the different fields (first raw), followed by the number of optical PMS candidates selected (second raw). Fields 1b and 4b were not included in the selection of the global PMS strip since they are on-cloud.

correlation radius of 1" (the maximum expected error in 2MASS astrometric positions), although we expect the majority of the correlations to be within 0.65" (i.e., the sum of the 2MASS astrometric accuracy and the optical astrometric uncertainty).

We found 763 correlations in total, divided amongst the 4 different fields, as explained in Table 5.1, giving an IR counterpart to just 58% of the objects. However, we must note that the 2MASS data do not cover fields 3a and 4a at all, and only about a third of field 3b. A rough estimate from the data available for the other fields reveals that more than 400 objects are missing due to incomplete coverage, and so $\sim$ 90% of the optically selected PMS candidates have IR counterparts.

The catalogue with all the matches is available in electronic form. In Table 5.2 we give the first 7 entries. Each NIR object in our catalogue has two id numbers, which are a shortened version of the 2MASS astrometric coordinates: in the original 2MASS catalogue, RA and Dec are both given in degrees, and were subsequently converted into RA (hhmmss.ss) and Dec (ddmmss.ss). For simplicity, we therefore adopted ss.s and mmss respectively as the two id numbers associated.

The NIR magnitude ranges in our catalogue are $J = 9.27 - 15.81$ mag, $H = 8.46 - 15.06$ mag, and $K = 8.14 - 14.86$ mag. Table 5.3 lists the confirmed PMS members of Cep OB3b found from spectroscopy (see Chapter 4) for which we have the NIR colours. Table 5.4 list the possible PMS (PMS?) member, plus the possible A-G type kinematic members (see Section 4.7 in Chapter 4), for which we have NIR colours.

Figures 5.6, 5.7 and 5.8 show the NIR objects which are correlated with the objects in the global PMS strip, respectively in a J versus (J-H) and J versus (I-J) colour-magnitude diagram, and (J-H) versus (H-K) colour-colour diagram.

	#1, #2	RA(hms)	Dec(dms)	K	err	flag	H-K	err	flag
J-H	err	flag	sep.(arcsec)	J	err	flag	I-J	err	flag
	field, id	RA(hms)	Dec(dms)	V	err	flag	B-V	err	flag
V-I	err	flag	U-B	err	flag				
	296 5151	22 55 29.66	62 51 51.06	10.826	0.025	00	0.281	0.041	00
0.894	0.043	00	0.5	12.001	0.064	00	1.850	0.065	00
	1a 52	22 55 29.69	62 51 51.53	16.231	0.004	00	2.033	0.010	00
2.380	0.005	00	1.653	0.041	00				
	194 4338	22 56 19.46	62 43 38.30	12.934	0.041	00	0.377	0.058	20
0.892	0.065	22	0.3	14.203	0.096	11	2.236	0.120	11
	1a 1237	22 56 19.49	62 43 38.53	20.158	0.052	00	2.203	0.187	00
3.719	0.050	00	1.098	0.177	90				
	362 4609	22 55 36.28	62 46 9.35	8.685	0.024	00	0.402	0.042	00
1.034	0.043	00	0.4	10.121	0.065	00	2.100	0.065	00
	1a 50	22 55 36.34	62 46 9.48	14.910	0.002	00	2.284	0.006	00
2.689	0.004	00	2.454	0.031	00				
	308 4215	22 56 30.87	62 42 15.75	11.921	0.025	00	0.592	0.039	00
0.931	0.045	00	0.5	13.444	0.065	00	2.620	0.088	00
	1a 1063	22 56 30.88	62 42 16.23	19.974	0.043	00	1.630	0.102	00
3.910	0.042	00	-0.244	0.164	00				
	40 4924	22 56 4.00	62 49 24.59	14.162	0.083	00	0.229	0.103	00
0.876	0.086	00	0.4	15.267	0.158	00	2.006	0.191	00
	1a 1731	22 56 4.05	62 49 24.62	20.607	0.077	00	1.777	0.207	00
3.334	0.075	00	-0.957	0.918	00				
	300 4548	22 55 30.08	62 45 48.37	10.572	0.023	00	0.298	0.040	00
0.831	0.045	00	0.4	11.701	0.064	00	1.675	0.065	00
	1a 68	22 55 30.14	62 45 48.48	15.545	0.003	00	1.929	0.007	00
2.169	0.008	00	1.891	0.026	00				
	152 4322	22 56 15.30	62 43 22.84	13.244	0.036	00	0.393	0.052	00
0.884	0.055	00	0.4	14.521	0.084	00	2.000	0.095	00
	1a 888	22 56 15.33	62 43 23.14	19.501	0.032	00	2.265	0.111	00
2.980	0.031	00	1.937	1.541	00				

Table 5.2: Matchings global PMS stars from the optical photometric catalogue - NIR catalogue in the field 1a. The full catalogue of matchings (in this and the other fields) is available in electronic form. We list here the first 7 entries only as a guidance to its content. For each matching, the first two lines refer to: id no., astrometric positions, K magnitude, (H-K) and (J-H) colours plus associated photometric errors and flags from the NIR catalogue, followed by the separation between the NIR source and its optical counterpart, J magnitude plus photometric error and flag from the NIR catalogue, and derived (I-J) colour with associated error and flag (obtained by combining the corresponding ones from the NIR and the optical photometric catalogues); the last two lines refer to: field and id no., astrometric positions, and UBVI colours plus associated errors and flags from the optical photometric catalogue.

#	Field	sep. (")	class	V	V-I	I	K	H-K	J-H	J	I-J
7	2b	0.7	WTTS	14.548	2.264	12.284	9.448	0.299	0.830	10.577	1.707
8	2b	0.8	CTTS	16.733	2.347	14.386	11.197	0.501	0.931	12.629	1.757
18	1a	0.7	CTTS	16.789	2.444	14.345	11.359	0.315	0.864	12.538	1.807
32	2a	0.5	WTTS	16.939	2.113	14.826	12.427	0.257	0.824	13.508	1.318
49	3b	0.3	CTTS	(a)			11.531	0.553	1.062	13.146	1.017
81	3b		WTTS	15.676	2.113	13.563	(b)				
84	3b	0.5	CTTS	15.626	2.013	13.613	9.792	0.989	1.073	11.854	1.759 (c)
95	1a	0.4	CTTS	17.128	2.626	14.502	11.087	0.543	1.020	12.650	1.852
100	2b	0.3	WTTS	16.180	2.028	14.152	11.678	0.213	0.730	12.621	1.531
106	1a	0.3	WTTS	15.660	1.960	13.700	11.181	0.261	0.806	12.248	1.452

Table 5.3: The confirmed PMS members of Cep OB3b from spectroscopy for which we have JHK colours. (a) this is the CTTS on a bad column, for which we cannot trust the optical photometric colours. (b) this is the WTTS outside the region covered by 2MASS (see Figure 5.4). (c) this is the veiled CTTS.

#	Field	sep. (")	class	V	V-I	I	K	H-K	J-H	J	I-J
10	2a	0.6	non-PMS	15.004	1.962	13.042	10.555	0.196	0.772	11.523	1.519
12	1a	0.0	non-PMS	14.910	1.892	13.018	10.547	0.337	0.712	11.596	1.422
14	1a	0.4	non-PMS	15.545	2.310	13.235	10.305	0.295	0.893	11.493	1.742
15	1a	0.5	non-PMS	14.812	1.432	13.380	11.770	0.186	0.341	12.297	1.083
26	2a	0.5	non-PMS	14.975	1.378	13.597	11.947	0.186	0.472	12.605	0.992
27	2a	0.4	non-PMS	18.305	2.412	15.893	13.460	0.256	0.747	14.463	1.430
29	2a	0.5	non-PMS	14.906	1.499	13.407	11.688	0.138	0.439	12.265	1.142
39	2a	0.6	non-PMS	15.380	1.550	13.830	11.950	0.205	0.493	12.648	1.182
101	2b	0.9	PMS?	15.727	2.395	13.332	10.426	0.332	0.763	11.521	1.811
103	1a	0.6	non-PMS	15.102	1.538	13.564	11.849	0.122	0.515	12.486	1.078
104	1a	0.4	non-PMS	17.189	2.272	14.917	12.586	0.260	0.686	13.532	1.385

Table 5.4: The possible PMS member of Cep OB3b, and the possible A-G type kinematic members (see text), for which we have JHK colours.

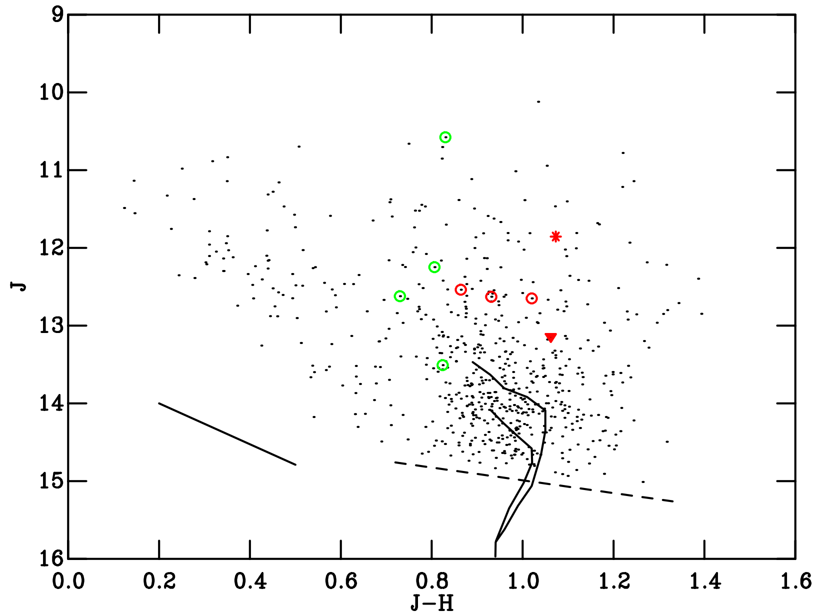

Figure 5.6: Colour-magnitude diagram in J versus (J-H) for the NIR objects which are cross-correlated with the objects in the global PMS strip. The CTTS and WTTS are circled in red and green respectively. The veiled CTTS (red asterisk) and the CTTS for which we do not trust the optical photometric colours (red filled triangle) are also shown. Isochrones at 2 and 5 Myr (respectively the upper and lower one) are from Baraffe et al. (1997). Also plotted the reddening vector. The dashed line represents the mass cut-off at M= 0.5 $M_\odot$ (see text).

All the objects flagged as bad and/or having photometric errors larger than 0.1 mag in the NIR catalogue are rejected; though, we retain the CTTS on the bad column which is flagged as bad in the optical photometric catalogue. Isochrones at 2 Myr and 5 Myr were derived from evolutionary tracks of Baraffe et al. (1997), for stars in the mass range $0.03 < M/M_\odot < 1.0$ (2 Myr is the youngest evolutionary track in their models). The magnitudes are produced self-consistently by the models using realistic atmospheres, and are expected to be good for IJHK colours (see Baraffe et al. 1998).

The isochrones were reddened using the interstellar extinction law $E(\lambda - V)/E(B-V)$ given by Rieke & Lebofsky (1985), for the wavelengths of interest, i.e., respectively, $A_J = 0.27E(B-V) = 0.76$ mag, $E_{H-K} = 0.194E(B-V) = 0.18$ mag, $E_{J-H} = 0.33E(B-V) = 0.3$ mag, and $E_{I-J} = 0.56$ mag, with $A_V = 2.81$ mag, $E(B-V) = 0.91$ mag, and a distance modulus of 9.65 mag adopted for Cep OB3b (see Table 3.7 in Chapter 3), irrespective of possible reddening changes among different CCD

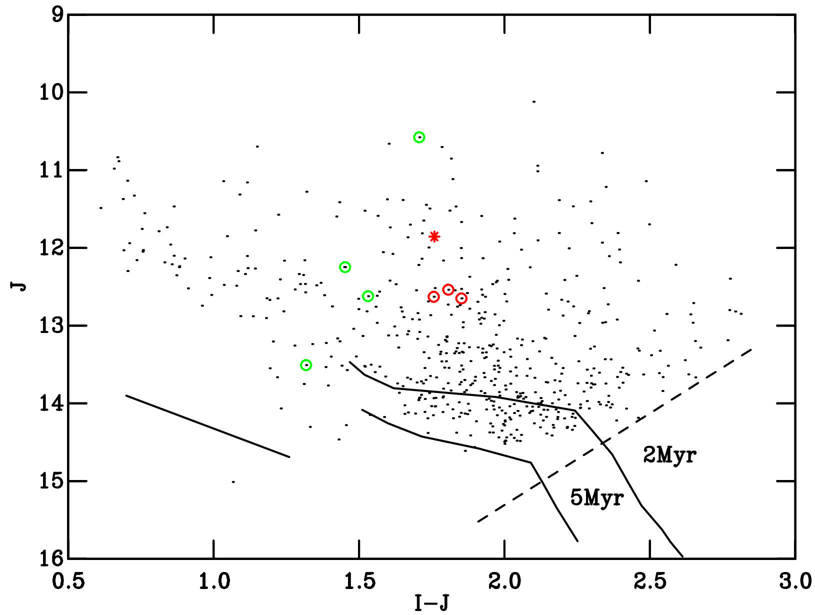

Figure 5.7: Same as Figure 5.6, in J versus (I-J), but without the CTTS for which we do not trust the optical photometric colours (flagged as bad).

fields in order to test them again.

It is clear from Figures 5.6 and 5.7 that we are sensitive to stars down to a certain mass in the association. The mass limit for the plotted objects can be inferred (dashed line) from the isochrones: it corresponds to about M= 0.5 $M_\odot$.

Since we found evidence of a changing in reddening across the subgroup (see Subsection 3.8.2 in Chapter 3), supported by spectroscopic results (see Section 4.6.3 in Chapter 4), we expect this to affect the colour-magnitude diagrams in J versus (J-H) and J versus (I-J) too. In particular, we showed (see Section 4.8 in Chapter 4) that the PMS sample selected in the CMD was contaminated by $\sim$ 70%, because of the generous region selected and of the fact that no correction was applied to take into account of the changing in reddening between the CCD frames according the proposed values (see Table 3.19 in Chapter 3). Therefore the majority of the objects in Figures 5.6 and 5.7 which are spread across the isochrones especially at fainter magnitudes, can be interpreted as this expected contamination, indicative of the reddening spread (see the direction of the reddening vector). On the other hand, it seems that the PMS members do not match the theoretical isochrones, appearing

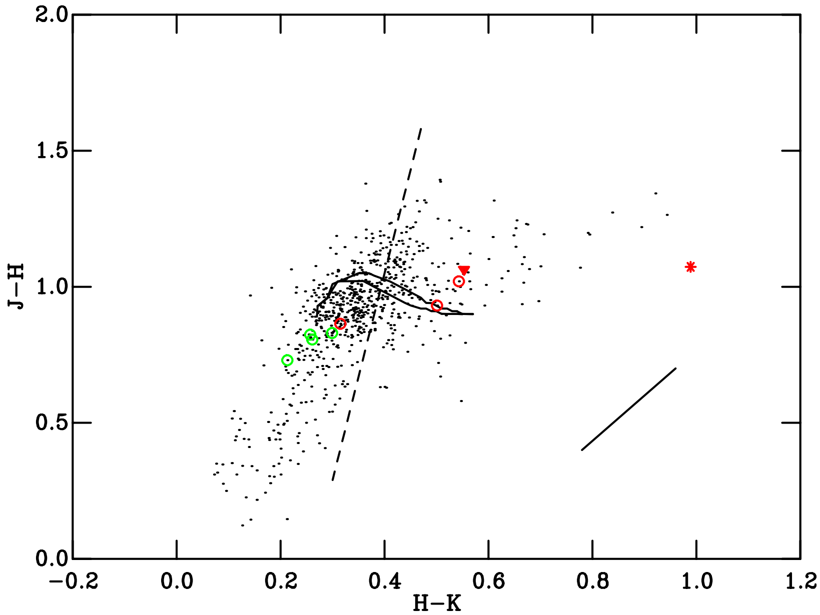

Figure 5.8: Colour-colour diagram in (J-H) versus (H-K). Symbols as in Figure 5.6. The dashed line represents the lower mass limit at 0.5 $M_\odot$ as suggested in Figures 5.6 and 5.7 (see text).

overall younger than 2 Myr and suggesting that there is indeed an age spread among them: the visual extinction found for these objects from spectroscopic results (see Section 4.6.3 in Chapter 4), is in agreement with the adopted value (an exception is the veiled CTTS); therefore, such scattered positions in the CMD can be explained only by a real spread in ages, as proposed in Chapter 3 (see Section 3.8.2).

The presence of a circumstellar accretion disc is more likely to be picked up in a diagram showing the (H-K) colour: Edwards et al. (1993) have in fact shown that the IR colour excess in (H-K) is a good measure of disc accretion and veiling. We plot (H-K) versus (J-H) in Figure 5.8, where we also indicate with a dashed line the mass limit at M= 0.5 $M_\odot$ as suggested by Figures 5.6 and 5.7. Since we are not sensitive to objects at its right, the majority of the objects which indeed fall in such a region are likely to have an (H-K) excess, or be giants (they are not highly reddened background A type stars, since A0 stars would have V= 18.7 mag and (V-I)= 1.9 mag and therefore not in the PMS strip selected).

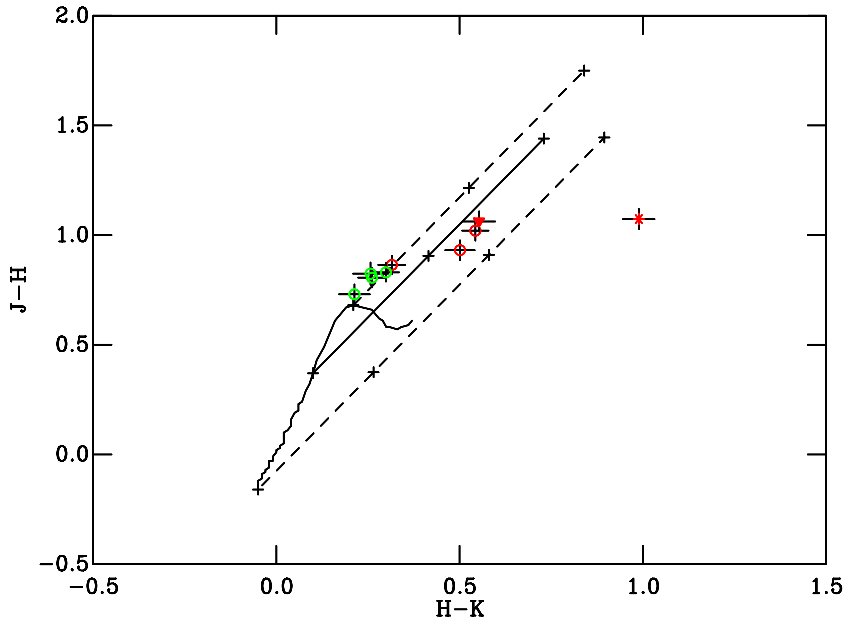

Figure 5.9: Colour-colour diagram in (J-H) versus (H-K) for the PMS association members found with spectroscopy with associated NIR photometric errors. CTTS and WTTS are plotted as red and green circles respectively. The veiled CTTS (red asterisk), and the CTTS for which there is a question about the optical photometric colours (red filled triangle), are also shown. The error bars in both colours are quite small. The continuous line at the bottom is the locus of main sequence stars (Koornneef 1983). The dashed lines represent the reddening law of Rieke & Lebofsky (1985), drawn at intervals (defined by black crosses) of 5 mag in the visual extinction, whereas the continuous line in between them is the reddening line for K0 stars.

5.3 The colour-colour diagram and IR excesses

As anticipated, by plotting (J-H) versus (H-K) we can have an idea of the nature of the objects observed, in particular of the presence of circumstellar discs around them.

In Figure 5.9 we give the colour-colour diagram in (J-H) versus (H-K) for the PMS sources found with spectroscopy. Intrinsic NIR colours for main-sequence stars in the mass range 06-8 to M8 (derived by Koornneef 1983) allow us to plot the "un-reddened" main-sequence. The strip defined by the two parallel dashed lines is the reddening locus, where all reddened stars within the above mass range and with normal stellar photospheres must fall.

The reddening lines (which are parallel to the reddening vector) were derived from the interstellar extinction law of Rieke & Lebofsky (1985), for different amounts of visual extinction ($A_V = 5, 10, 15, 20, 25$ mag), with associated colour excess $E(B-V) = A_V/R$ (R=3.09). We recall that $A_V = 2.81$ mag for Cep OB3b (see Section 3.1.4 in Chapter 3). Although there is the possibility of a changing in reddening across the subgroup (see Subsection 3.8.2 in Chapter 3), all but one (the veiled CTTS) of the TTS which are Cep OB3 members suffer a visual extinction in agreement with the mean adopted value (from spectral type comparisons; see Section 4.6.3 in Chapter 4).

Following the interpretation given by Lada & Adams (1992), data which are spread along the reddening locus of main-sequence stars, are objects suffering different amounts of extinction: moving far from the main-sequence, along the reddening locus, we find objects which are more and more reddened. They are purely reddened objects, with normal stellar photospheres. Note, by the way, that some protostars, with most of the envelope mass transferred to the central object (i.e., in the phase preceding the CTTS phase), have been found inside the reddening locus (see Greene & Meyer 1995). Furthermore, according to the isochrones, very low-mass stars (brown dwarfs) could also occupy this region, but they would have been too faint to be detected. By contrast, if the data are spread to the right of the reddening locus, it means that they must have NIR excesses (and this is typically the region occupied by young stellar objects): i.e., infrared radiation emitted in excess of that normally emitted from a stellar photosphere. Sometimes some of the data fall to the left of the reddening locus, or the main-sequence, which is a forbidden region for young stellar objects, since it cannot be physically explained. These data could be faint stars with large photometric errors (caused by photon noise) or have problems related to cosmetic defects on the images (such as bad pixels). The same problems could shift data-points to the right of the reddening locus, i.e., into the region of NIR excesses. This is not the case for the PMS object in the IR excess region (the veiled CTTS in Figure 5.9), since it has a too small error bar to explain its position outside the reddening locus. However, it could be a problem for other objects, therefore we have to keep this in mind when selecting possible NIR excess candidates (see discussion below).

As can be seen from Figure 5.9, almost all the spectroscopically identified PMS members of the association lie within the reddening locus. The veiled CTTS would seem to be the only one showing a large infrared excess, suggesting the presence of a circumstellar accretion disc, which is supported by the strong Hα emission observed (see Table 4.4 in Chapter 4). Therefore, the broad wings seen in its spectrum (see Figure 4.12), can be attributed to in-falling material from its accretion disc.

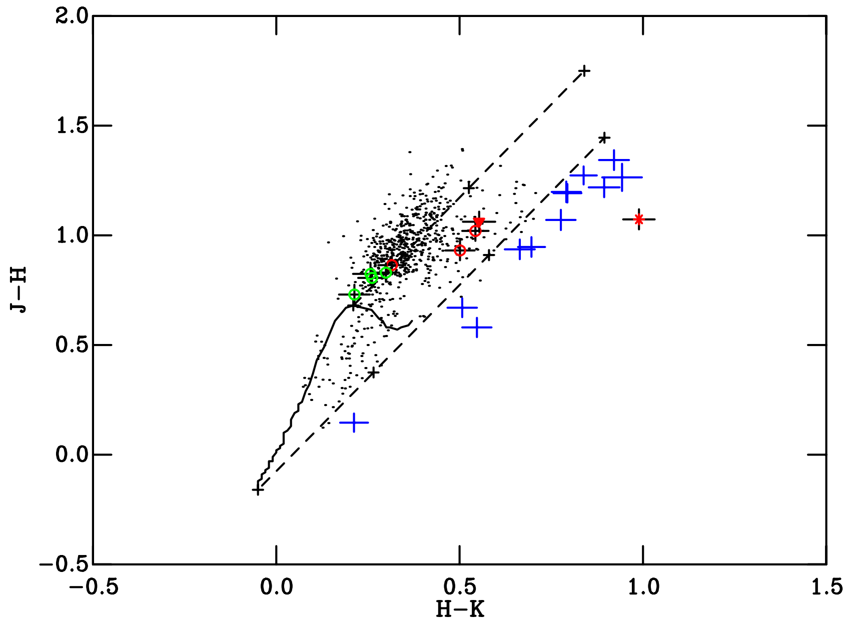

Figure 5.10: Same as Figure 5.9, for all the NIR objects cross-correlated with the stars in the global PMS strip. The m-s stars and the reddening locus are over-plotted. The objects which have NIR excesses are shown as blue dots plus associated 1σ photometric errors. Those objects closer to the boundary of the reddening locus were not included because their positions can be explained by their big photometric errors, and therefore not necessarily showing NIR excesses.

Within the reddening locus we find both WTTS and CTTS. As pointed out by Lada & Adams (1992), the fact that some CTTS are sharing the same position in the colour-colour diagram with the WTTS, does not necessarily mean that such CTTS do not have infrared excesses. If one knows the correct extinction to each single CTTS or the correct spectral type, then a comparison with their position along the reddening locus can confirm or deny it: if from the NIR CMD one finds that the interstellar reddening appears to be higher than the determined one, then this extra reddening could be explained by means of an infrared excess. From the spectral-type classification presented in Chapter 4, we found that our TTS are of K-type, therefore we have drawn the reddening line for increasing extinction expected for stars later than K0 in Figure 5.9. It is then clear that other 3 CTTS are to the right of the reddening line expected for their spectral type, and therefore have a NIR excess too. The total number of members with NIR excess is therefore 4.

If we now do the same with the total number of NIR objects which are cross-correlated with the

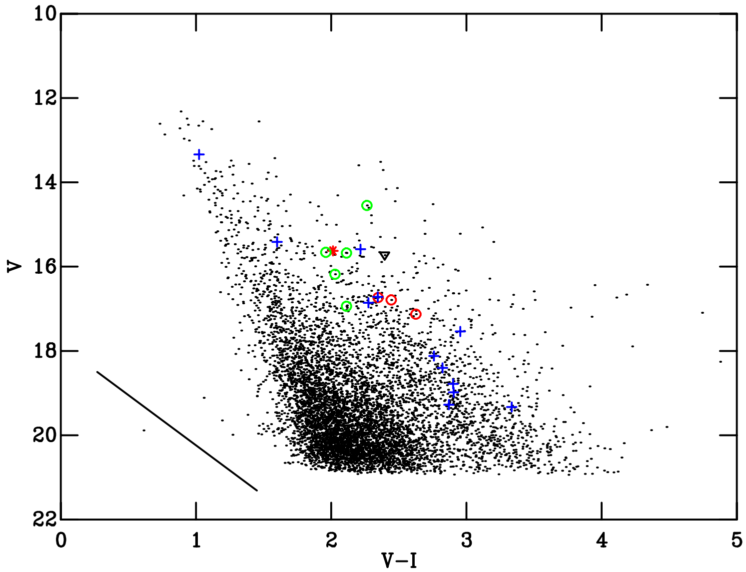

Figure 5.11: Colour-magnitude diagram in V versus (V-I) showing the location of NIR excess candidates (blue crosses) selected in Figure 5.10. They are spread over the entire global PMS strip, and mixed with the confirmed PMS members. CTTS and WTTS are plotted as red and green circles respectively, the veiled CTTS as red asterisk (the CTTS which has optical photometric colours flagged as bad is not shown). Also plotted are the possible PMS member (black open triangle; see text), and the reddening vector (A_V = 2.81 mag, E(V-I)= 1.18 mag).

optical objects in the global PMS strip (see Figure 5.5 and 5.8), we find that there are several objects clearly to the right of the reddening locii, which must have NIR excesses, as shown in Figure 5.10. There are 12 objects (blue dots plus associated error bars) which are selected for further analysis. Note that these would be the lowest mass objects in the association or objects with very large IR excesses. We have not included other objects very close to the boundary of the reddening locus because their 1σ NIR photometric errors could explain their position. Note however that a 2σ error for most of the 12 objects selected would also put them back inside the reddening locii region. These 12 objects belong to four different fields, respectively: 3 objects in field 1a, 6 in field 2b, 2 in field 2a and just 1 in field 3b.

We then plot the selected NIR excess objects on the V versus (V-I) colour-magnitude diagram in Figure 5.11, together with the confirmed PMS members of the association and the possible PMS

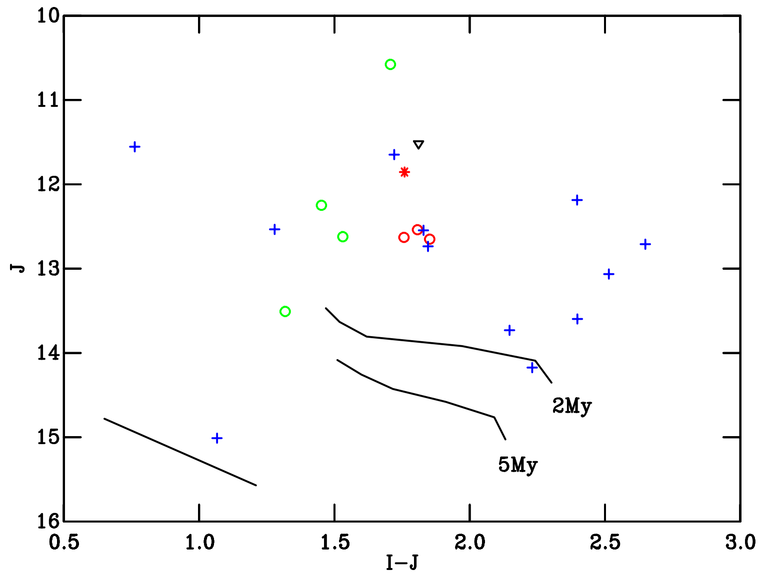

Figure 5.12: Colour-magnitude diagram in J versus (I-J) for the PMS association members found with spectroscopy. CTTS and WTTS are plotted as red and green circles respectively. The veiled CTTS (red asterisk) is also shown, but not the CTTS which has optical photometric colours flagged as bad. Also plotted are the NIR excess candidates selected in Figure 5.10 (blue crosses), and the possible PMS member (black open triangle; see text). NIR isochrones at 2 Myr and 5 Myr of Baraffe et al. (1997) are plotted only for masses $0.5 < M/M_{\odot} < 1.0$ to take into account of the mass cut-off found in Figures 5.6 and 5.7 (see text). Also shown the reddening vector.

member (see Table 5.4). The NIR excess candidates are mixed with the PMS members on the global PMS strip and are scattered from about V= 13 mag to about V= 19 mag. The object at about V= 13.3 mag and (V-I)= 1.0 has (H-K)= 0.21 mag, whereas the object at about V= 19.3 mag and (V-I)= 3.3 has (H-K)= 0.79 mag. Unfortunately, we do not have spectroscopy for these objects to be sure about their spectral type. However, they belong to field 1a and 2b respectively, and therefore they are not expected to suffer a large extinction: if they were members of the association, they would have $M_V = 0.88$, 6.87 mag respectively. On the ZAMS this is equivalent to A0 and K3, for which the intrinsic (H-K) colour is 0.0 and 0.14 mag, giving a (H-K) colour excess of 0.2 and 0.6 mag respectively. We recall that objects with an (H-K) excess larger than 0.2 are good disc candidates (see Section 2.13 and Figure 2.6).

Finally, Figure 5.12 shows the location of the PMS objects listed in Table 5.3 in a J versus (I-J) colour-magnitude diagram. CTTS are shown as red circles, WTTS as green circles; the veiled CTTS as red asterisk. Also plotted are the possible PMS member (black triangle) listed in Table 5.4, and the 12 objects with possible IR excess (blue crosses) selected in Figure 5.10. The object with IR excess in the left lower part of the plot is the object at $(H-K) = 0.2$ mag and $(J-H) = 0.2$ mag in Figure 5.10. As already commented in Figure 5.7, there appears to be a real age spread for the PMS members of the association. We note that the NIR excess candidates seem to be more scattered with respect to the PMS objects: this could be the effect of a change in reddening for objects belonging to different fields.

We must note, however, that these 12 NIR excess candidates represent an underestimated sample, since their selection is clearly biased towards lower mass objects and objects with the higher (H-K) excess. From Figure 5.8 it was instead evident that there is a large number of possible NIR excess candidates (see discussion in Section 5.2).

5.4 Conclusions

The main result achieved with the NIR data from the 2MASS database, is that there appears to be a real spread in ages for the PMS members of the association, strengthening previous suggestions obtained from photometric and spectroscopic data in earlier Chapters.

The cross-correlation of the optical PMS sample with the 2MASS NIR data has confirmed a NIR excess for just 4 objects (CTTS). This seems to suggest that there are just 4 TTS (out of 10 discovered with spectroscopy) which have NIR emission from a circumstellar accretion disc, whereas the remaining TTS have passive discs, i.e., discs which are simply reprocessing the stellar radiation.

There are another 12 objects which seem to be good IR excess candidates too. Unfortunately we do not have spectroscopy for them. It would be interesting to follow up these stars. This is by no means a complete sample, since we have shown that there are several other objects which are likely to have a NIR excess.

A better way of tackling the problem would be to select all the objects at the right of the dashed line in Figure 5.8, disregarding those which would populate the reddening locus expected for giants objects (see intrinsic colours of Koornneef 1983). As a result, we would end up with a larger sample of NIR excess candidates. An optical spectroscopic follow-up for these objects would then be necessary, to test their youthfulness, together with an IR spectroscopic follow-up to look for NIR excesses and test the good disc candidates: this would unable us to distinguish not only objects with active accretion discs but also those with normal passive discs.

6 The discovery of a low-mass PMS association around γ^2 Vel

6.1 Introduction

This chapter is devoted to the serendipitous discovery, by X-ray selection and then the confirmation by optical photometry, of a low-mass pre-main sequence stellar population in the direction of the Wolf-Rayet/O-star binary system γ^2 Vel and the Vela OB2 association (see Pozzo et al. 2000). Yet, the presence of HII and HI regions, possible triggers of star formation (see Chapter 2), around the Wolf Rayet star, were discovered with the Goddard High-Resolution Spectrograph echelle on board of the Hubble Space Telescope (Fitzpatrick & Spitzer 1994). And, in her PhD thesis, Sahu (1992) presented the discovery of the IRAS Vela shell, a ring-like structure around Gamma Velorum, in which low-mass star formation is taking place. The shell has a radius of about 8°, centered around $(l, b) = (26.3°, -7°$, with a kinetic energy compared to the energy output of the Vela OB2 association which is consistent, according to the author, with the former being created by the OB stars of the latter through stellar winds and supernova explosions.

γ^2 Velorum (HD 68273, HIP 39953, WR11) is the nearest example of a Wolf-Rayet (WR) star. Like about half of the $\simeq 200$ galactic WR stars known, it is a binary system (WC8+O8) with an orbital period of 78.5 days and a massive, interacting stellar wind. There is currently some controversy concerning the distance to γ^2 Vel, which impacts upon the deduced luminosities, masses and mass loss rates from the system. It is important to get these parameters right because, as the nearest WR, γ^2 Vel is an extreme test of stellar evolution models and calibrates the absolute magnitudes of WR stars. The Hipparcos parallax yields a distance of 258^{+41}_{-31} pc to γ^2 Vel (Schaerer, Schmutz & Grenon 1997, van der Hucht et al. 1997), in marked contrast to previous distance estimates which place it at 350-450 pc. The larger distance is in better agreement with the mean distance to the Vela OB2 association (410 ± 12 pc), of which γ^2 Vel is the most massive proper-motion member (de Zeeuw et al. 1999). There is some confusion in the literature concerning the naming of OB associations at different distances in the Vela region (see Tovmassian et al. 1993 for an exhaustive review), which does not help the cause.

From our investigation, we argue that γ^2 Vel and the low-mass stars are truly associated, are approximately coeval and that both are at distances between 360-490 pc, disagreeing at the 2σ level with the recent Hipparcos parallax of γ^2 Vel, but consistent with older distance estimates.

Our results clearly have implications for the physical parameters of the γ^2 Vel system, but also offer an exciting opportunity to investigate the influence of a very high-mass star on the mass function and circumstellar disc lifetimes of their lower mass PMS siblings.

6.2 X-ray observations

We suspected the presence of a low mass association around γ^2 Vel from the large surrounding population of X-ray (0.1-2.4 KeV) point sources seen in *ROSAT* images (low-mass PMS stars are usually strong sources of X-ray emission, see Section 2.5 in Chapter 2), taken for a program to investigate its interacting stellar winds (see Willis, Schild & Stevens 1995 and Figure 6.1). Trümper (1983), Pfeffermann et al. (1988), and David, Forman & Jones (1999) give a detailed description of the instrumentation on board the satellite. The X-ray observations of the WR were retrieved from the *ROSAT* public archive and consisted of 10 Position Sensitive Proportional Counter (PSPC) datasets and 2 datasets taken with the High Resolution Imager (HRI). The PSPC is more sensitive and the corresponding images contain the vast majority of the X-ray point sources.

We used the Starlink-distributed ASTERIX data reduction package in our X-ray analysis (Allan & Vallance 1995). The 10 PSPC datasets were sorted into $1^\circ \times 1^\circ$ images, selecting pulse height channels 11 to 240 (approximately 0.1-2.4 keV photons) and excluding times with anomalously high background rates. The images were centered on γ^2 Vel (the brightest source in each dataset) and then summed. The resulting image has dimensions of 720×720 5 arcsecond pixels and an effective on-axis exposure time of 25.3 ks. We used the Point Source Searching (PSS - Allan 1992) algorithm to search for sources by Cash-statistic maximisation. By assuming the background to be zero we obtained a preliminary list of 104 X-ray sources which were masked out of the image. The masked image was then patched and smoothed with a 75 arcsec FWHM gaussian to create a background map. We then executed the PSS algorithm again and found 109 sources above a pseudo-gaussian significance level of 4.5σ, which corresponds roughly to 1 spurious detection in the X-ray image. The positions of the X-ray sources were corrected for errors in the satellite aspect solution by comparing the optical and X-ray positions of γ^2 Vel and four other bright, X-ray detected, stars from the CDS SIMBAD

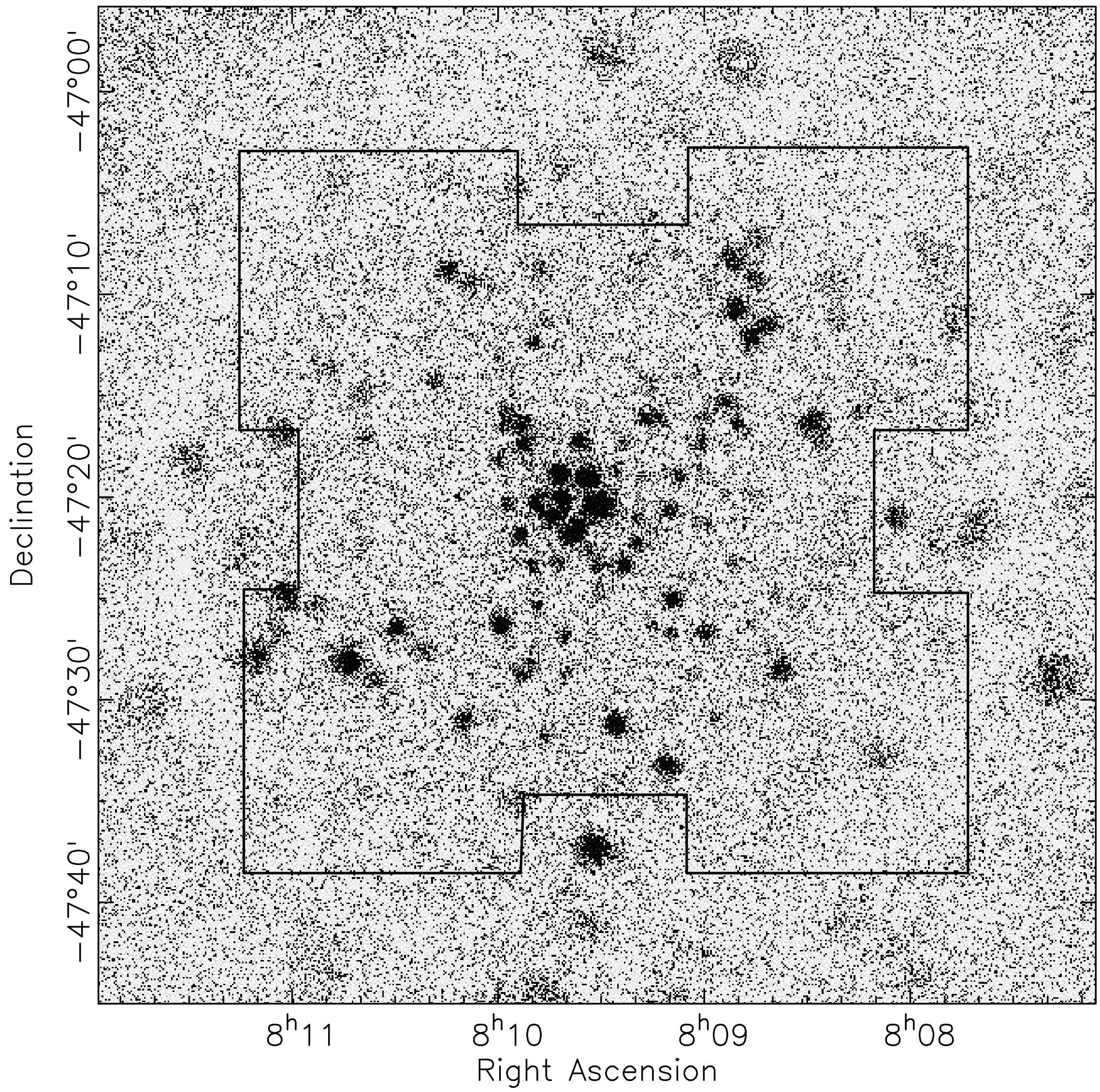

Figure 6.1: *ROSAT* PSPC X-ray image of the region around γ^2 Vel. The greyscale is such that black represents ≥ 1 photon per 5x5 arcsec pixel and the brightest source in the centre of the image is γ^2 Vel. Another 108 significant X-ray sources have been found in this image. The solid outline shows the location of our optical CCD survey.

database. We applied shifts of 4.5 arcsec in RA and 13.8 arcsec in Dec to the X-ray positions. In Table 6.1 we summarise the information about the 109 X-ray sources detected by the PSS algorithm in the summed PSPC image (from Column 1 to 7: the X-ray id, RA and Dec, measured counts and associated 1 σ errors, and significance levels of source detection).

6.3 Optical photometry

CCD photometry of the X-ray field was obtained on 8 February 1999 with the 0.9-m telescope at the Cerro Tololo Inter-American Observatory. A Tek 2048x2048 CCD was used to give a 13.5x13.5 arcmin^2 field of view. Eight overlapping fields around γ^2-Vel were surveyed in BVI with short (20,10,10s) and long (200,100,100s) exposures, together with five fields from Landolt (1992) to determine zeropoints, colour terms and extinction coefficients. Several standards with $V - I_c > 2.5$ were observed. Figure 6.1 illustrates the location of the fields around γ^2 Vel. Photometry of the standard stars and the calibration onto the standard $BVI_{\rm c}$ system were achieved in a similar manner to that described for Cep OB3 in Section 3.2. The external accuracy of our photometry was determined to be around 0.02 mag.

Photometry and astrometry were performed for each of the eight fields using optimal photometry and the program CLUSTER, as previously done for Cep OB3 (see Chapter 3). The results were combined to give an optical catalogue of sources. No attempt was done to normalise the photometric colours for stars belonging to overlapping regions (this will be performed in the future, after implementation of a normalisation routine in the program CLUSTER). However, the catalogue was cleaned of all the stars flagged as bad (see Section 3.3 in Chapter 3, in particular Subsections 3.3.4 and 3.3.5), and from duplicates (i.e., stars with different id number, and belonging to overlapping fields, having positions within 1" of each other). The final catalogue contains 20617 individual objects with their magnitudes, colours and positions. Figure 6.2 (top) shows the V versus $V - I_{\rm c}$ colour-magnitude diagram (CMD). The location of a possible PMS low-mass star association is clearly visible above the bulk of the background contamination. To this optical catalogue, we added the positions of bright ($V < 11$) stars found in this region from the SIMBAD database.

#	RA (hms)	Dec (dms)	Raw Flux (Counts)	Error	Signif (sigma)
1	08 07 22.87	-47 12 19.8	66.5	14.0	5.510
2	08 07 40.09	-47 21 28.9	168.0	17.0	13.685
3	08 07 46.52	-47 11 13.0	112.0	15.0	9.465
4	08 07 52.42	-47 22 09.1	70.4	12.0	6.782
5	08 07 53.51	-47 08 01.0	95.1	15.0	8.020
6	08 07 54.63	-47 02 29.4	96.0	27.0	4.656
7	08 07 54.73	-47 39 42.0	459.0	143.0	5.047
8	08 08 03.79	-47 20 57.4	167.0	15.0	17.877
9	08 08 08.65	-47 32 44.8	128.0	15.0	11.898
10	08 08 14.52	-47 15 50.2	71.3	11.0	8.727
11	08 08 17.70	-47 41 26.0	251.0	51.0	14.271
12	08 08 21.34	-47 11 13.9	63.2	11.0	8.122
13	08 08 22.63	-47 09 26.9	88.7	13.0	9.792
14	08 08 28.42	-47 16 22.0	286.0	19.0	26.421
15	08 08 37.79	-47 28 29.8	301.0	19.0	29.673
16	08 08 38.98	-47 24 50.4	40.6	8.3	6.943
17	08 08 45.73	-47 07 22.7	117.0	14.0	12.446
18	08 08 46.02	-47 09 04.2	154.0	15.0	16.019
19	08 08 46.03	-47 12 03.4	308.0	19.0	29.511
20	08 08 46.50	-47 19 48.0	28.9	7.4	5.293
21	08 08 50.21	-47 16 22.0	92.5	11.0	13.435
22	08 08 50.85	-47 10 42.5	438.0	22.0	39.422
23	08 08 51.42	-47 23 11.3	60.3	9.3	9.953
24	08 08 51.59	-47 08 14.9	242.0	18.0	22.900
25	08 08 53.51	-47 15 19.6	170.0	15.0	20.876
26	08 08 56.49	-47 30 50.0	53.5	9.3	8.455
27	08 08 59.55	-47 26 38.7	151.0	14.0	20.327
28	08 08 59.61	-47 09 17.2	29.2	8.0	4.748
29	08 08 59.64	-47 21 21.0	44.2	8.9	7.109
30	08 08 59.78	-47 16 01.5	52.1	9.3	8.086
31	08 09 01.10	-47 17 21.5	89.9	11.0	12.883
32	08 09 01.14	-47 18 43.7	28.4	7.7	4.894
33	08 09 03.22	-47 28 43.5	33.4	7.7	5.978
34	08 09 06.79	-47 23 59.3	28.9	7.6	5.334
35	08 09 07.22	-47 18 54.6	152.0	14.0	19.521
36	08 09 08.00	-47 07 56.7	25.6	7.3	4.616
37	08 09 09.21	-47 25 02.8	278.0	18.0	31.520
38	08 09 09.49	-47 26 43.1	57.6	9.0	9.835
39	08 09 09.95	-47 20 37.0	149.0	14.0	18.918
40	08 09 10.52	-47 33 11.5	385.0	21.0	34.035
41	08 09 14.74	-47 26 21.6	43.6	8.2	7.818
42	08 09 15.31	-47 14 30.7	45.9	9.0	7.413
43	08 09 15.80	-47 06 10.4	40.8	9.3	5.686

continued ...

... continued

44	08 09 16.38	-47 16 08.3	224.0	17.0	25.095
45	08 09 18.56	-47 08 18.3	37.4	8.8	5.667
46	08 09 19.18	-47 21 04.2	51.9	9.5	7.712
47	08 09 19.29	-47 09 10.7	29.6	8.4	4.557
48	08 09 19.36	-47 22 19.2	110.0	12.0	14.332
49	08 09 23.48	-47 23 20.7	244.0	17.0	27.077
50	08 09 23.64	-47 17 14.5	49.5	9.2	7.654
51	08 09 25.45	-47 31 11.1	584.0	25.0	49.895
52	08 09 25.87	-47 18 40.2	49.3	9.4	7.283
53	08 09 29.19	-47 34 35.5	42.2	10.0	5.162
54	08 09 29.23	-46 58 36.3	195.0	18.0	13.131
55	08 09 30.24	-47 23 14.2	95.4	12.0	11.920
56	08 09 30.32	-47 24 40.0	45.0	8.9	6.998
57	08 09 31.12	-47 20 24.2	3381.0	62.0	150.189
58	08 09 32.09	-47 37 19.0	725.0	29.0	44.058
59	08 09 33.81	-47 19 03.0	596.0	26.0	46.778
60	08 09 33.94	-47 41 06.6	121.0	16.0	9.891
61	08 09 36.03	-47 17 16.3	256.0	17.0	27.213
62	08 09 38.00	-47 21 44.2	969.0	36.0	66.131
63	08 09 39.89	-47 28 39.5	35.7	8.0	6.239
64	08 09 40.83	-47 26 51.3	89.6	11.0	13.264
65	08 09 41.55	-47 20 05.3	638.0	27.0	50.843
66	08 09 41.74	-47 03 46.8	64.4	11.0	7.746
67	08 09 42.21	-47 18 48.1	686.0	27.0	53.570
68	08 09 42.55	-47 23 08.9	81.6	11.0	11.321
69	08 09 43.79	-47 20 53.9	416.0	23.0	36.785
70	08 09 46.32	-47 11 18.6	33.4	7.9	5.785
71	08 09 46.53	-47 31 47.3	68.1	10.0	9.904
72	08 09 47.39	-47 08 46.1	69.1	10.0	9.883
73	08 09 48.71	-47 25 21.6	65.3	9.8	10.167
74	08 09 49.26	-47 12 21.2	92.3	11.0	13.470
75	08 09 49.81	-47 23 23.1	94.4	11.0	12.948
76	08 09 52.11	-47 17 18.0	186.0	16.0	19.709
77	08 09 52.54	-47 28 39.2	107.0	12.0	13.903
78	08 09 53.20	-47 16 23.2	250.0	18.0	25.155
79	08 09 53.67	-47 21 52.4	317.0	19.0	32.496
80	08 09 54.23	-47 34 59.9	125.0	14.0	13.818
81	08 09 54.47	-47 04 46.7	59.1	11.0	6.733
82	08 09 56.98	-47 20 20.6	87.9	11.0	12.037
83	08 09 59.06	-47 26 15.8	511.0	24.0	46.698
84	08 09 59.71	-47 13 09.4	26.3	7.2	4.935
85	08 09 59.93	-47 18 09.2	62.8	10.0	9.132
86	08 10 08.09	-47 09 21.5	106.0	12.0	13.301
87	08 10 09.82	-47 30 58.8	202.0	16.0	23.059
88	08 10 14.27	-47 08 47.3	206.0	16.0	20.954
89	08 10 18.26	-47 14 15.3	81.2	11.0	12.028

continued ...

... continued

90	08 10 21.67	-47 27 30.7	85.1	11.0	11.207
91	08 10 29.76	-47 26 27.9	229.0	17.0	24.620
92	08 10 38.94	-47 17 02.5	65.5	10.0	9.534
93	08 10 39.20	-47 14 51.2	80.7	11.0	11.061
94	08 10 39.57	-47 22 29.7	38.7	8.6	6.090
95	08 10 42.32	-46 59 38.1	74.3	20.0	4.773
96	08 10 43.76	-47 28 04.7	629.0	27.0	44.632
97	08 10 46.34	-47 04 20.3	77.4	14.0	7.049
98	08 10 48.95	-47 13 40.2	79.8	11.0	10.025
99	08 10 53.25	-47 25 19.9	101.0	13.0	11.529
100	08 10 57.50	-47 18 59.7	38.6	9.6	5.031
101	08 11 01.73	-47 24 51.1	380.0	22.0	29.412
102	08 11 02.65	-47 16 46.5	209.0	17.0	18.747
103	08 11 11.05	-47 27 43.9	319.0	21.0	23.880
104	08 11 11.45	-47 01 39.2	590.0	168.0	5.662
105	08 11 13.34	-47 22 23.9	67.3	14.0	5.943
106	08 11 16.37	-47 02 26.7	467.0	154.0	4.747
107	08 11 25.56	-47 06 23.4	67.9	19.0	4.667
108	08 11 29.37	-47 18 05.6	184.0	17.0	15.084
109	08 11 40.26	-47 29 55.7	135.0	21.0	8.481

Table 6.1: Positions of the X-ray sources detected by the PSS algorithm, with associated counts and errors (at the 68% confidence) and significance levels (note that the detection threshold was fixed at 4.5 σ above the background).

To establish an appropriate cross-correlation radius to use between the X-ray and optical source lists we modelled the cumulative number of X-ray sources that were correlated with an optical source with $V < 19$. The cumulative distribution of the closest cross-correlation separations between an optical and an X-ray source, $\Phi(r)$, assuming a uniform spread of optical sources, is given by (see Jeffries, Thurston & Pye 1997)

$$\Phi(r) = T\left[1 - exp\left(\frac{-r^2}{2\sigma^2}\right)\right] + (N-T)\left[1 - exp\left(-\pi r^2 B\right)\right], \tag{6.1}$$

with σ the statistical uncertainty in the X-ray positions, T the number of true correlations, B the number of objects in the optical catalogue per unit area (covered by the CCD survey), N the number of X-ray sources in the same area. The first and second term of the equation are respectively the cumulative distribution of true correlations and spurious sources (which increases for increasing r).

In our case, the number of X-ray sources falling within the CCD fields are N=83, and B= 2.023×10^{-3} arcsec^{-2}. The parameters to be determined are instead A and σ, from which one can derive the number of spurious sources S and then T=N-S. Note that we decided to fix B, instead of leaving it as a parameter to be determined from the fit, because S turned out to be small, causing the fit to be slightly lower than the cumulative distribution of correlations plotted as a function of the correlation radius. We found 77 correlations in total within 10 arcsec of X-ray positions: 66 of these would be true counterparts to X-ray sources, and 11 would be spurious correlations. The average 1σ X-ray error circle was 3.7 arcsecs. Figure 6.2 (bottom) shows 75 sources that have an optical counterpart within 10 arcsecs (another two are bright stars without $V-I$ colours).

Clearly the X-ray emitting population coincides with a possible PMS population in the CMD. Indeed, if we were to consider just a subset of the optical catalogue consisting of a broad strip containing all these PMS sources, we would only expect 1 of these correlations to be spurious.

The cut-off in the PMS X-ray correlations at $V \simeq 18$ is almost certainly due to the X-ray sensitivity. To be detected in X-rays, fainter objects would have to have higher than feasible X-ray to bolometric flux ratios (maximum expected values are $L_x/L_{bol} \sim 10^{-3}$; see Section 2.5 in Chapter 2). However, it is clear that the PMS sequence we have found extends down to the limits of our optical survey at $V \sim 20.5$.

6.4 Discussion

The appearance of Figure 6.2 should leave the reader in no doubt that we have found a young and exceptionally rich population of low mass active stars in the *direction* of γ^2 Vel. The central question to be answered is whether these sources are physically close to γ^2 Vel and/or whether they are background members of the Vela OB2 association. We can tackle this problem in a number of ways.

6.4.1 Are the PMS stars and γ^2 Vel aligned?

Figure 6.3 (top) shows the spatial distribution of PMS stars selected from the CMD in a strip enclosing the bulk of the X-ray sources (marked with a dashed box in Figure 6.2). This box was chosen to avoid background contamination at 1.0< $V-I_{\rm c}$ <1.6. We determined the radial distribution of these stars,

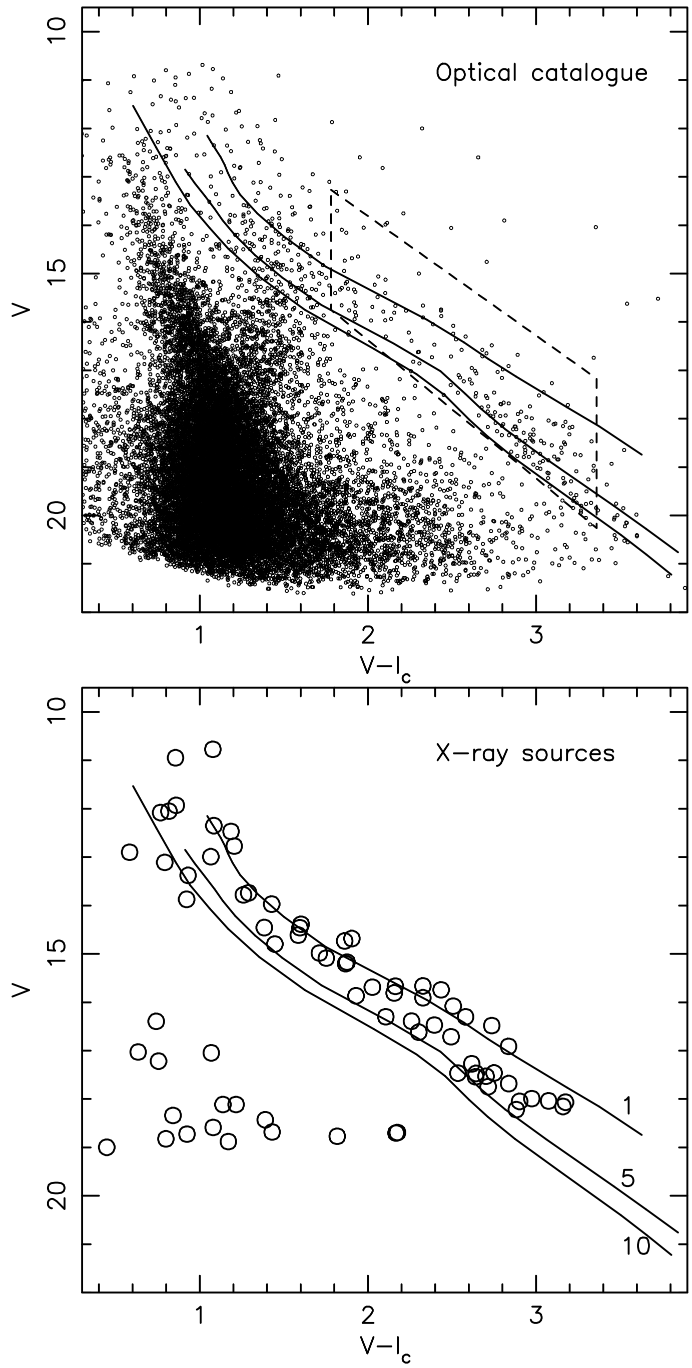

Figure 6.2: (Top) CMD for the region around γ^2 Vel. The solid lines in this and the plot below are isochrones at 1, 5 and 10 Myr calculated from the models of D'Antona & Mazzitelli (1997) at the classical adopted distance of 410 pc. The dashed box indicates the region from which PMS stars were selected for Figure 6.3. (Bottom) The location of the X-ray source correlations in the CMD. Eleven spurious correlations are expected and would most likely lie in the clump of background stars at $V \simeq 19$, $V - I \simeq 1$.

centered on γ^2 Vel. The distribution is normalized using the radial distribution of background stars with a similar V magnitude range, but a colour range of $0.8 < V - I_{\rm c} < 1.7$, under the assumption that the background stars are uniformly distributed. The resulting radial distribution is shown in Figure 6.3 (bottom), which exhibits a small but significant (at the 3σ level) peak within 5 arcmin of the centre of the CCD survey and γ^2 Vel. The point closest to γ^2 Vel is missing because the 30 arcsec region immediately surrounding γ^2 Vel is swamped by its light and no accurate photometry was obtained there. In a similar fashion we can show that the X-ray sources are also marginally concentrated toward the centre of the field even after correction for the PSPC vignetting function. A uniform sensitivity is achieved just in the inner area of the PSPC, $\sim 20'$ (where the PSF is circularly symmetric), whereas outside this region vignetting causes the image to be dimmer at the edges, and the PSF is enlarged.

There is thus some evidence that the PMS stars and γ^2 Vel are spatially correlated, although this does not rule out a chance alignment of γ^2 Vel with a background cluster of low mass stars in Vela OB2. In particular, it is possible that any concentration we see could be associated with γ^1 Vel, a B2III, single lined spectroscopic binary which is a common proper motion companion to γ^2 Vel. γ^1 Vel is also a likely member of the Vela OB2 association, has a spectroscopic parallax of $\simeq 450$ pc and is located only 41 arcsecs at a PA of 220° from γ^2 Vel.

6.4.2 Are the PMS stars and γ^2 Vel at the same distance?

The isochrones plotted in Figure 6.2 come from the D'Antona & Mazzitelli (1997) low mass evolutionary models. We have converted from bolometric luminosity and effective temperature to magnitude and colour using empirical bolometric corrections as a function of colour and a colour-effective temperature relationship derived by forcing the well studied low mass stars in the Pleiades cluster to fit a 120 Myr isochrone (see Jeffries & Tolley 1998). The assumed distance is that appropriate for the Vela OB2 association of 410 pc; as well as the reddening of $E(V - I) \simeq 0.06$ (van der Hucht et al. 1997). It is clear that if the PMS stars are at the mean distance of the Vela OB2 association they appear to be about 4 ± 2 Myr old (taking into account the likely presence of unresolved binary systems). If however, the PMS association were at the Hipparcos distance to γ^2 Vel, the isochrones would have to be shifted upwards by 1 magnitude. In that case we would deduce that the PMS population had an age ~ 20 Myr. The age of γ^2 Vel, based upon the mass of the O star ($\sim 30 M_{\odot}$) at the Hipparcos distance, is less than 5 Myr (Schaerer et al. 1997; de Marco & Schmutz 1999). Thus if the Hipparcos distance is adopted, the PMS stars and γ^2 Vel cannot be at the same distance *and* coeval. However, *if* γ^2 Vel were at the mean distance of the Vela OB2 association, it would be more massive (see below), slightly younger and could easily be coeval with the PMS population. An age range of 2-6 Myr and co-evality of γ^2 Vel and the PMS stars would be compatible with distances between 490 and 360 pc.

6.4.3 How far away is γ^2 Vel?

The evidence that γ^2 Vel is as close as 258 pc from the Hipparcos parallax should be treated with some caution. de Zeeuw et al. (1999) examine the high mass membership of the Vela OB2 association on the basis of both proper motions and parallaxes. The association is well defined by proper motions and has an angular radius of about 6 degrees. The *mean* parallax from 93 members corresponds to 410 ± 12 pc. The parallax dispersion can be quite well modelled as a gaussian with a $\sigma = 0.68$ mas, such that $\sim 95\%$ of the members appear to lie between 260 pc and 900 pc. The dispersion is reasonably consistent with the errors on the individual points and not inconsistent with the idea that all the stars are at nearly *the same* distance. Indeed, if we were to assume that the front to back size of Vela OB2 were similar to its diameter on the sky, then all the stars should be contained within ± 40 pc. We would therefore interpret the parallax to γ^2 Vel simply as a $\sim 2\sigma$ deviation and that its true distance was 410 ± 40 pc.

The companionship of γ^1 Vel is also evidence for a distance closer to the mean Vela OB2 distance. Although these objects have a common proper motion, they were too close together on the sky for Hipparcos to obtain independent parallaxes. The distance to γ^1 Vel from its spectral type and photometry is almost certainly 400-500 pc (e.g. Abt et al. 1976; Hernández & Sahade 1980). The idea that γ^2 Vel is a foreground object randomly placed within 1 arcminute of another bright member of the Vela OB2 association has a probability of only $\sim 10^{-3}$. There is also reasonable evidence that the radial velocities of the two systems are similar. Hernández & Sahade (1980) quote 9.7 ± 1.0 km s^{-1} for γ^1 Vel and Niemelä & Sahade (1980) give 12 ± 1 km s^{-1} for γ^2 Vel, although it is likely that the accuracy of these results is greatly exaggerated (Schmutz et al. 1997).

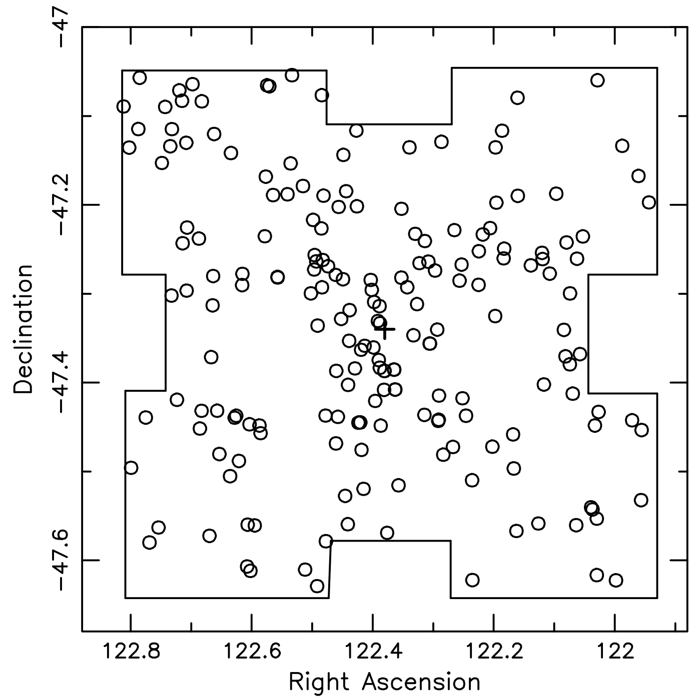

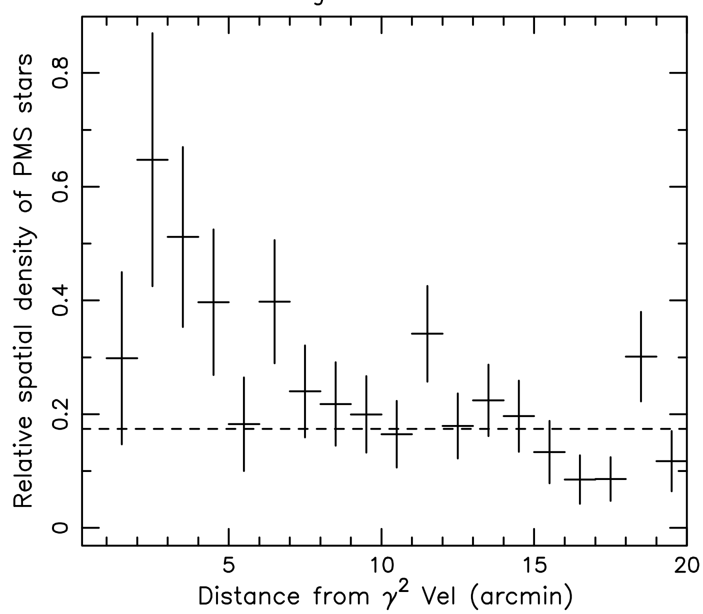

Figure 6.3: (Top) The spatial distribution of PMS stars (from inside the dashed box in Figure 6.2) around γ^2 Vel. A clumping towards γ^2 Vel (marked with a cross) is apparent. (Bottom) The relative spatial density of these PMS sources as a function of distance from γ^2 Vel. This plot is normalized using a background population to account for non-uniform coverage in the CCD survey.

6.4.4 Can the PMS stars be at a range of distances?

Preibisch & Zinnecker (1999) observed a very similar PMS CMD in the Upper Sco OB association, with a similar vertical scatter of about ± 0.6 mag about the isochrones. They showed that if one takes into account unresolved binaries, photometric errors and allowed a $\sim 10\%$ range in distance, the scatter around the PMS isochrones was exactly as expected for a coeval population at ~ 5 Myr. We therefore similarly conclude that the CMD in Figure 6.2 shows no evidence for a large spread in *either* the age or distance of the PMS population we have found. In particular, we can rule out any distance modulus spread in a coeval population that is larger than a few tenths of a magnitude, or any age spread in a co-spatial population of more than a Myr or so (for a mean age of ~ 4 Myr). Thus unless there is a conspiracy to place older stars closer to us, the PMS association seems likely to have a relatively narrow spread around an age and distance that are incompatible with the deduced age for γ^2 Vel *and* its Hipparcos distance.

6.4.5 Is a larger distance to γ^2 Vel consistent with its physical properties?

Our findings challenge the conclusions of several recent papers which use the Hipparcos parallax of γ^2 Vel and its (1σ) error to derive: the absolute magnitude of the system and its components; system masses from the interferometric binary separation of Hanbury Brown (1970); the O star luminosity, mass and age from stellar evolution models and hence the orbital inclination and further mass estimates from radial velocity curves (see van der Hucht et al. 1997; Schaerer et al. 1997, Schmutz et al. 1997, de Marco & Schmutz 1999, de Marco et al. 2000). A distance as large as 410 pc for γ^2 Vel significantly changes the system parameters deduced in these papers. The system luminosity increases by a factor 2.5. The effective temperature and luminosity deduced for the O star would then give it a mass > 40 $M_\odot$ and an age < 3 Myr, compared with the values of 30 $M_\odot$ and 3.6 Myr quoted by de Marco & Schmutz (1999). At this larger distance, an age of 2-3 Myr could be compatible with the low mass PMS stars we have found. The absolute magnitude of the O star would decrease to -6.0 ± 0.3 (van der Hucht et al. 1997), which argues for a supergiant rather than a giant classification. Van der Hucht et al. comment that this would be in better agreement with the published spectra of Conti & Smith (1972) and Niemelä & Sahade (1980). As the mass ratio from the radial velocity curves is fixed, the WR mass increases by a similar fraction. The total system mass, based on a binary separation of

4.3 ± 0.5 mas, increases from 30 ± 10 $M_\odot$ to 120 ± 40 $M_\odot$ (now comfortably exceeding the minimum mass from radial velocity curves – Niemelä & Sahade 1980) and the binary inclination is reduced to around 50° to explain the radial velocity curves.

6.4.6 Conclusions

From our discussion there now seem to be two possible scenarios. (1) That the PMS stars are approximately at the same distance and age as γ^2 Vel, and that this distance places γ^2 Vel within the Vela OB2 association at 360-490 pc. (2) That the PMS stars are part of the Vela OB2 association, possibly surrounding γ^1 Vel, but that γ^2 Vel is an isolated foreground object with no surrounding low mass stars at a similar age. We believe that (1) is *far* more plausible than (2) because of the dispersion in the Vela OB2 Hipparcos parallaxes and the likely association of γ^1 and γ^2 Vel. Recently, the idea that γ^2 Vel could form in isolation without accompanying low mass stars has also been challenged by the near IR detection of a K-type PMS companion only 4.7 arcsec distant (Tokovinin et al. 1999).

If the low mass PMS stars we have found are truly in the vicinity of γ^2 Vel, they represent an exciting opportunity to explore the influence of adjacent high mass loss stars and ionizing UV radiation fields on the mass function and circumstellar disc lifetimes of low mass stars.

It will be interesting to compare the frequencies of T-Tauri discs around these stars with the frequencies found in T associations and OB associations with similar ages. The PMS stars in Figure 6.2 have masses, found from the D'Antona & Mazzitelli (1997) models, down to (an age dependent) mass of about 0.15 $M_\odot$. The mass function can be addressed when we have a better census of the association membership.

To further this work and address some of these issues, a PMS sample of objects was spectroscopically followed-up. A classification was performed in terms of Li I equivalent width measurements, which, together with radial velocity measurements, allowed a clearer definition of the PMS members of the stellar association around γ^2 Vel. This work is discussed in the Chapter 7.

7 Spectroscopic follow-up of the PMS objects around γ^2 Vel

7.1 Selection of PMS candidates

Analogously to the PMS candidate selection in the Cep OB3 association (see Chapter 4), the PMS sample for spectroscopic follow-up of objects around γ^2 Vel was created exclusively by optical selection in the V versus (V-I) colour-magnitude diagram. Here, two regions were selected, avoiding the giant branch contamination, and encompassing the majority of the PSPC X-ray sources found around the Wolf-Rayet star (see Chapter 6). These two regions are defined respectively by: $0.7 < V - I < 1.3$ mag, with $10.4 < V < 12.4$ mag for $V - I = 0.7$ mag, and $12.5 < V < 14.4$ mag for $V - I = 1.3$ mag; and $1.6 < V - I < 2.8$, with $13.4 < V < 15.5$ mag for $V - I = 1.6$ mag, and $16.2 < V < 18.4$ mag for $V - I = 2.8$ mag (see Figure 7.1). There were a total of 180 PMS candidates optically selected for spectroscopic follow-up.

7.2 Spectroscopic observations

High-resolution ($R \sim 25000$) spectra for 83 of the PMS candidates were obtained by Fred Walter in December 1999, with the Hydra fibre spectrograph on the 4-m Blanco telescope (CTIO, Chile). We were supplied directly with reduced data, i.e., with radial velocities (RVs), and Hα and Li I 6707.8 Å equivalent widths (EWs) for the objects observed. These results are shown in Table 7.1. Objects with low signal-to-noise for which EWs and/or RVs values are very uncertain are flagged with a colon. In particular, Hα EWs measurements were difficult because of problems with sky subtraction. Objects for which no clear cross-correlation was found for a reliable RV measurement are flagged with a double colon. For some of the candidates no RV was measured because of their early spectral type, as explained in the Table. For others, it is simply a question of poor signal-to-noise. There are RV measurements for 73 objects and they were estimated to be good to better than 3 km/s.

The radial velocity distribution of the 73 PMS candidates is shown in Figure 7.2. It is clearly clustering in the approximate range $7.5 < RV < 24.5$ km/s. From 36 objects falling in this range, we derive a mean value of 17.0 ± 0.6 km/s. There are 35 objects within 2 standard deviations (=7.2

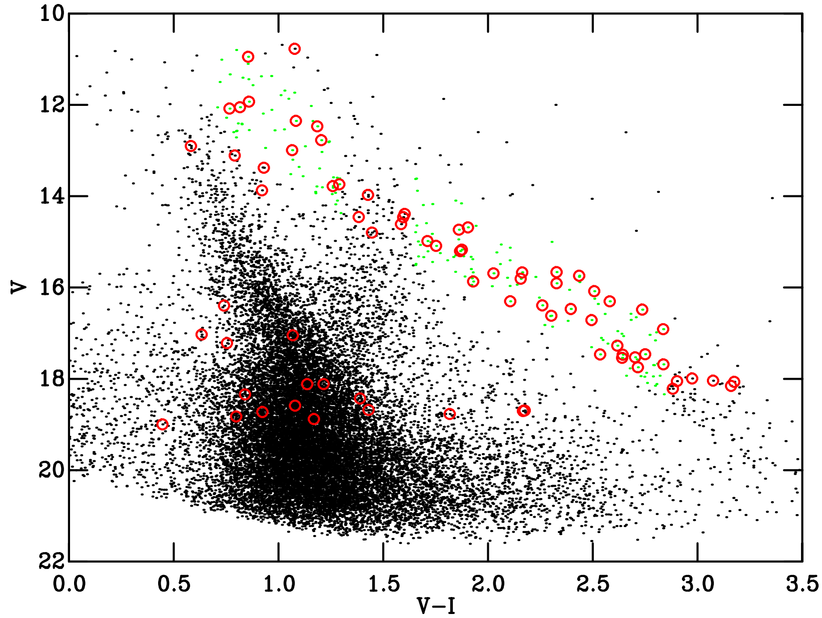

Figure 7.1: The optical selection of the PMS candidates (green dots) in the V versus V-I colour-magnitude diagram for the objects around γ^2 Vel. The 77 PSPC X-ray sources correlated with objects in the optical catalogue (see Chapter 6) are shown as red circles. The majority of the sources clumping at about $V = 19$ and $(V - I) = 1$ are likely to be spurious (we recall that 11 spurious correlations are expected out of 77).

km/s) from the mean, i.e., in the range 9.8-24.2 km/s, which can be considered kinematic members of the same stellar group, and flagged with m in Table 7.1. All the objects which are not 2σ members are flagged as kinematic non-members (nm), although the possibility remains that some of these may be binary association members (see later).

Table 7.2 lists photometric colours, intrinsic $(V - I)_0$, class and correlated X-ray sources for all the objects investigated. Intrinsic colours are determined from measured colour using a colour excess of $E_{V-I} = 0.06$ mag known for the region (van der Hucht et al. 1997). The classification of the PMS candidates was performed on the basis of their RVs and Li I EWs, using a diagram similar to that of Martín (1997), as previously done for the spectroscopic objects in the Cep OB3 association (see Section 4.7; also, Section 2.8.2).

In Figure 7.3 we plot the strength of the Li I line versus the intrinsic colour $(V - I)_0$. The dashed line corresponds to the Li isoabundance line for $logN(Li) = 2.8$ (as a function of T_{eff}; see Martín 1997) expressed as a function of the intrinsic colours by interpolation of the T_{eff} - $(V-I)_0$ scale from Jeffries & Tolley (1998).

All the stars showing a Li I EW larger than, or close to, the Li I isoabundance line (i.e., > 200 mÅ, and less than that but still > 100 mÅ) and a radial velocity consistent at 2σ level of the mean RV value, are classified respectively as PMS and possible PMS (PMS?) stars belonging to the low-mas stellar association clustering around γ^2 Vel (see Table 7.2). Objects with Li I EW smaller than 100 mÅ are considered non-PMS stars. There are two objects, no. 16 and 38, which are non-members according to the measured RV, but with Li I EW smaller than 120 mÅ and equal to 480 mÅ respectively: we classify them as young objects (Y); they could be members of the association (respectively a possible PMS and a PMS object) showing the wrong RV if confirmed as spectroscopic binaries.

We classify 23 stars as PMS stars, 4 as possible PMS, 43 as non-PMS stars and 2 young objects (another 11 objects have no classification since they have uncertain Li I EW measurements). There are 35 kinematic members in total. Of these, 23 are PMS, 4 possible PMS, and 8 non-PMS (with Li I EW < 70 mÅ). Therefore, all the objects classified as PMS and possible PMS are kinematic members of the same stellar cluster. Note that there are another 5 objects (no. 8, 10, 22, 36, 44) which could be PMS stars from their EW(Li), but for which we do not have RV measurements.

We can then estimate the likely number of contaminants to have the correct RV by chance. Out of 73 objects with measured RV, we have found 35 candidate kinematic members and 38 kinematic non-members. There are 29 kinematic non-members with radial velocities in the range -6.0 and 72 km/s (another 9 are outliers), and assuming they are uniformely spread over this velocity range, from Poisson statistics we would expect to find $29 * 7.2/78 = 2.7 \pm 1.6$ objects to fall by chance in our selection range of ± 7.2 km/s. Therefore, out of 35 candidate kinematic members, we would expect 3 ± 2 of them to be field stars having the correct RV by chance.

Out of 23 PMS members just 4 (no. 23, 28, 41 and 63) have Hα line in emission with an EW larger than 5 Å. The spectral types derived from the intrinsic colours would give early M-type stars for no. 23, 28, and 41; whereas late-K for no. 63. The former do not have an Hα EW strong enough for their spectral-type to be classified as CTTS (see Section 2.9 in Chapter 2). The latter is just above the limit of 5 Å for K-type stars.

#	RA (hhmmss)	dec (ddmmss)	RV_{hel} (km/s)	comment	EW(Li I (mÅ)	EW(Hα) (Å)
1	08 10 51.36	-47 14 35.3	112.8	nm	<50	:
2	08 10 39.96	-47 14 43.3	16.1	m	150	:
3	08 09 52.72	-47 14 54.2	79.9	nm	<100	:
4	08 09 59.21	-47 16 21.9	10.8	m	440	-0.4
5	08 10 53.29	-47 17 59.4	35.0	nm,hs		
6	08 10 19.97	-47 18 56.9	124.0	nm	<100	:
7	08 09 42.18	-47 19 53.0	19.3	m,br	390	-0.9
8	08 09 57.84	-47 20 08.9	::		680	:
9	08 09 49.79	-47 20 13.2	15.2	m	480	:
10	08 09 44.75	-47 20 44.4	::		360	-0.9
11	08 10 42.57	-47 21 07.8	70.7	nm	<40	:
12	08 09 39.18	-47 21 39.0	17.3	m	325	:
13	08 09 54.25	-47 21 42.2	21.8	m	250	:
14	08 10 10.81	-47 23 33.6	-14.3	nm	90	2.1
15	08 09 59.65	-47 26 05.0	20.0	m	120	1.1
16	08 09 54.70	-47 26 13.6	92.0	nm	<120	:
17	08 10 30.14	-47 26 14.2	18.1	m	650	-0.5
18	08 10 30.74	-47 26 22.2	16.9	m	600	-0.8
19	08 09 38.23	-47 26 37.4	19.0	m	<75	:
20	08 10 14.79	-47 08 28.1	16.6	m	370	:
21	08 09 45.11	-47 08 48.9	-2.5	nm	<15	:
22	08 10 08.56	-47 09 12.0	::		1100:	:
23	08 09 46.53	-47 11 04.5	14.9:	m:	1160:	-6.8
24	08 09 49.49	-47 12 08.1	16.3	m	980	-3.2
25	08 09 28.22	-47 14 27.6	60.6	nm	<50	:
26	08 09 25.24	-47 14 53.4	51.8	nm	<60	:
27	08 09 00.70	-47 15 45.8	17.4	m	130	:
28	08 09 13.91	-47 15 50.0	15.6	m	400:	-6.0
29	08 09 18.22	-47 15 58.6	131.0	nm	50	:
30	08 09 25.14	-47 16 12.0	66.4	nm	<60	:
31	08 09 36.78	-47 17 04.0	18.1	m	730	-0.5
32	08 09 35.86	-47 18 52.4	18.9	m	360	:
33	08 09 30.81	-47 20 02.1	:	*	:	:
34	08 09 30.04	-47 20 06.5	28.0	nm	<70	:
35	08 08 43.85	-47 14 57.4	38.0	nm	<50	:
36	08 08 53.91	-47 15 07.5	::		1800:	-2.8
37	08 08 51.19	-47 16 07.5	20.1	m	460	-0.9
38	08 08 54.02	-47 17 23.6	29.8	nm	480	:
39	08 08 18.31	-47 19 35.9	41.0	nm	<40	:
40	08 08 57.51	-47 20 22.4	18.6	m	70	2.3
41	08 09 10.39	-47 20 25.0	12.8	m	600	-7.2
42	08 08 13.79	-47 22 04.4	102.0	nm	<80	:
43	08 09 15.98	-47 24 11.1	125.0	nm	<80	:

continue ...

... continued

44	08 09 09.70	-47 24 52.6	:	SB	290, 250	-2.6
45	08 08 29.57	-47 25 48.3	35.0	nm	<20	:
46	08 08 17.35	-47 26 09.8	20.0	m	<70	:
47	08 09 31.29	-47 23 12.6	16.0	m	400	:
48	08 10 10.91	-47 27 15.9	71.4	nm	<100	:
49	08 09 55.91	-47 27 23.9	63.2	nm	55:	1.8
50	08 09 02.11	-47 28 24.4	54.5	nm	<30	:
51	08 09 54.19	-47 28 31.8	18.1	m	130	:
52	08 10 10.36	-47 30 46.5	19.4	m	540	:
53	08 09 26.25	-47 31 00.2	20.1	m	350	:
54	08 10 01.20	-47 31 21.5	10.6	m	<20	:
55	08 09 11.02	-47 33 00.6	19.3	m	390	:
56	08 10 47.25	-47 04 25.1	36.5	nm	<20	:
57	08 11 14.29	-47 05 30.4	-5.0	nm	<50	:
58	08 10 27.11	-47 07 21.1	-37.2	nm	40	:
59	08 11 03.47	-47 12 01.1	28.1	nm	<20	:
60	08 08 16.82	-47 03 50.6	-5.9	nm	55:	:
61	08 08 49.71	-47 04 28.8	21.5	m	<25	:
62	08 08 44.69	-47 06 59.4	14.0:	m:	500:	-3.9
63	08 07 55.44	-47 07 46.4	17.9	m	440	-5.4
64	08 08 46.97	-47 11 50.9	:		:	:
65	08 08 46.08	-47 12 32.7	60.0	nm	<60	:
66	08 08 25.62	-47 13 33.7	42.0	nm	<50	:
67	08 08 00.35	-47 26 26.0	33.5	nm	<70	:
68	08 08 37.06	-47 27 37.2	:	hs		
69	08 08 38.36	-47 28 18.8	21.4	m	250	-0.4
70	08 08 17.32	-47 28 56.1	40.0	nm	<100	:
71	08 08 40.64	-47 29 21.4	3.5	nm	60	:
72	08 08 12.45	-47 30 10.1	:	hs		
73	08 08 45.94	-47 31 04.6	1.1	nm	45:	:
74	08 08 49.70	-47 32 11.4	17.2	m	<70	:
75	08 10 48.80	-47 27 22.7	11.7	m	30	:
76	08 11 11.43	-47 27 38.1	16.0	m	310	0.7
77	08 10 44.28	-47 27 56.2	4.4	nm	50	-0.4
78	08 10 58.12	-47 29 14.0	:	hs		
79	08 10 29.03	-47 29 17.1	26.0	nm	<100	:
80	08 10 38.17	-47 29 19.6	17.0:	m:	<50	:
81	08 10 24.04	-47 29 55.1	31.6	nm	<40	:
82	08 09 54.46	-47 36 28.8	8.9	nm	<25	:
83	08 10 06.07	-47 37 02.6	24.7	nm,fr	<30	:

Table 7.1: Astrometric positions, heliocentric radial velocities, membership, Li I and Hα equivalent widths for the 83 objects of the spectroscopic sample. In column 5: m and nm stand for kinematic member and kinematic non member; hs for hot star (early spectral-type); SB for spectroscopic binary; br for broad lines in the spectrum; fr for fast rotator. (*) this object has a broad Hα line in emission, and a very strange spectrum. In the last two columns, positive values are for line in absorption, negative values for line in emission. Objects with low signal-to-noise for which EWs and/or RVs values are very uncertain are flagged with a colon, whereas those for which no clear cross-correlation was found for a reliable RV measurement are flagged with a double colon.

#	V	(V-I)	$(V\text{-}I)_0$	class	comment
1	14.157	1.871	1.811	non-PMS	nm
2	12.080	0.766	0.706	PMS?	m, X93
3	14.641	1.658	1.598	non-PMS	nm
4	15.316	1.882	1.822	PMS	m
5	11.100	0.853	0.793		nm
6	14.825	1.732	1.672	non-PMS	nm
7	12.470	1.185	1.125	PMS	m, X65
8	15.202	1.867	1.807		X82
9	13.596	1.278	1.218	PMS	m
10	14.173	1.734	1.674		
11	12.423	0.824	0.764	non-PMS	nm
12	12.190	0.925	0.865	PMS	m
13	11.929	0.859	0.799	PMS	m, X79
14	12.576	0.797	0.737	non-PMS	nm
15	12.108	0.966	0.906	PMS?	m
16	14.946	1.858	1.798	Y	nm
17	14.683	1.904	1.844	PMS	m, X91
18	15.231	2.040	1.980	PMS	m
19	14.194	1.689	1.629	non-PMS	m
20	12.991	1.065	1.005	PMS	m, X88
21	11.568	0.876	0.816	non-PMS	nm
22	15.669	2.163	2.103		X86
23	17.461	2.750	2.690	PMS	m:, X70
24	15.170	1.875	1.815	PMS	m, X74
25	13.202	1.066	1.006	non-PMS	nm
26	13.622	1.652	1.592	non-PMS	nm
27	10.946	0.855	0.795	PMS?	m, X30
28	17.035	2.771	2.711	PMS	m
29	12.413	0.823	0.763	non-PMS	nm
30	13.806	1.207	1.147	non-PMS	nm
31	14.733	1.861	1.801	PMS	m, X61
32	12.799	1.241	1.181	PMS	m
33	12.558	0.981	0.921		
34	13.881	1.661	1.601	non-PMS	nm
35	14.095	1.844	1.784	non-PMS	nm
36	15.689	2.026	1.966		X25
37	14.982	1.711	1.651	PMS	m, X21
38	15.329	1.917	1.857	Y	nm
39	13.814	1.259	1.199	non-PMS	nm
40	12.406	0.806	0.746	non-PMS	m
41	15.663	2.327	2.267	PMS	m, X39
42	14.649	1.941	1.881	non-PMS	nm
43	15.208	1.711	1.651	non-PMS	nm

continue ...

... continued

44	15.001	2.303	2.243		
45	11.866	1.047	0.987	non-PMS	nm
46	12.711	0.797	0.737	non-PMS	m
47	15.296	1.844	1.784	PMS	m
48	13.905	1.175	1.115	non-PMS	nm
49	12.566	0.800	0.740	non-PMS	nm
50	11.686	1.028	0.968	non-PMS	nm
51	11.367	0.965	0.905	PMS?	m
52	13.739	1.290	1.230	PMS	m, X87
53	12.538	1.026	0.966	PMS	m
54	12.025	1.154	1.094	non-PMS	m
55	12.772	1.204	1.144	PMS	m, X40
56	12.053	0.707	0.647	non-PMS	nm
57	12.354	1.162	1.102	non-PMS	nm
58	11.406	0.828	0.768	non-PMS	nm
59	11.732	1.075	1.015	non-PMS	nm
60	13.586	1.260	1.200	non-PMS	nm
61	11.787	1.010	0.950	non-PMS	m
62	16.624	2.297	2.237	PMS	m:
63	13.561	1.115	1.055	PMS	m
64	15.808	2.156	2.096		X19
65	14.095	1.279	1.219	non-PMS	nm
66	13.360	1.096	1.036	non-PMS	nm
67	13.611	1.290	1.230	non-PMS	nm
68	11.333	0.767	0.707		
69	13.779	1.259	1.199	PMS	m, X15
70	14.177	1.271	1.211	non-PMS	nm
71	11.499	0.719	0.659	non-PMS	nm
72	11.374	0.916	0.856		
73	12.944	0.936	0.876	non-PMS	nm
74	14.369	1.296	1.236	non-PMS	m
75	11.438	0.856	0.796	non-PMS	m
76	12.051	0.816	0.756	PMS	m, X103
77	12.350	1.083	1.023	non-PMS	nm, X96
78	10.797	0.798	0.738		
79	15.127	2.104	2.044	non-PMS	nm
80	13.393	1.194	1.134	non-PMS	m:
81	13.926	1.270	1.210	non-PMS	nm
82	12.552	0.858	0.798	non-PMS	nm
83	11.009	0.727	0.667	non-PMS	nm

Table 7.2: Visual magnitude, (V-I) colour and associated intrinsic colour and classification for the 83 stars spectroscopically observed. Y= young object; it could be a PMS member with the wrong radial velocity if spectroscopic binary. In the last column we recall the membership of the objects; X-ray counterparts are also given (the number refers to the X-ray id of objects listed in Table 6.1, see Chapter 6, preceded by an X). The classification is omitted for those objects with not measured values of Li I EW or RV. Membership or non-membership of objects with uncertain values of RV is flagged with a colon. Intrinsic colours are determined from measured colour using a colour excess of $E_{V-I} = 0.06$ mag known for the region (van der Hucht et al. 1997).

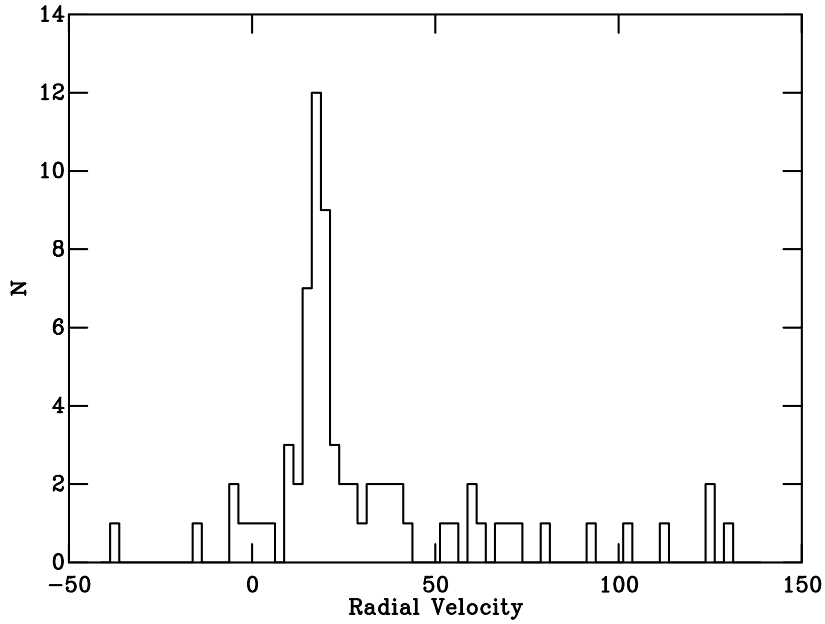

Figure 7.2: Radial velocity distribution of the PMS candidates for which we have a RV measurement.

In conclusion, we can say that none, or perhaps one, of the PMS members has an Hα EW large enough to be explained by means of physical processes other than stellar chromospheric activity associated with their youth, and which would classify them as CTTS. Therefore all 23, or perhaps 22 out of 23, of the PMS members are WTTS.

Figure 7.4 shows the V versus (V-I) colour-magnitude diagram for the PMS and possible PMS kinematic members (red crosses), together with non-PMS kinematic members (green crosses), and the non-PMS kinematic non-members (black crosses). It is clear that the PMS population is contaminated by non-members objects until about $V = 15$ mag, whereas the non-PMS kinematic members are confined to $V < 15$ mag. Note that we have PMS-members spread around the 1 Myr isochrone (with the 5 Myr isochrone as an upper limit) until lower masses: the faintest object is at $V = 17.5$ mag and has an X-ray counterpart associated.

Note that not all of the PMS and possible PMS members of the association have an X-ray counterpart. Out of 27 of them, just 15 are X-ray emitting (13 PMS and 2 possible PMS). Furthermore, there are 3 objects (no. 8, 22 and 36) for which we do not have the RV measurement but which have

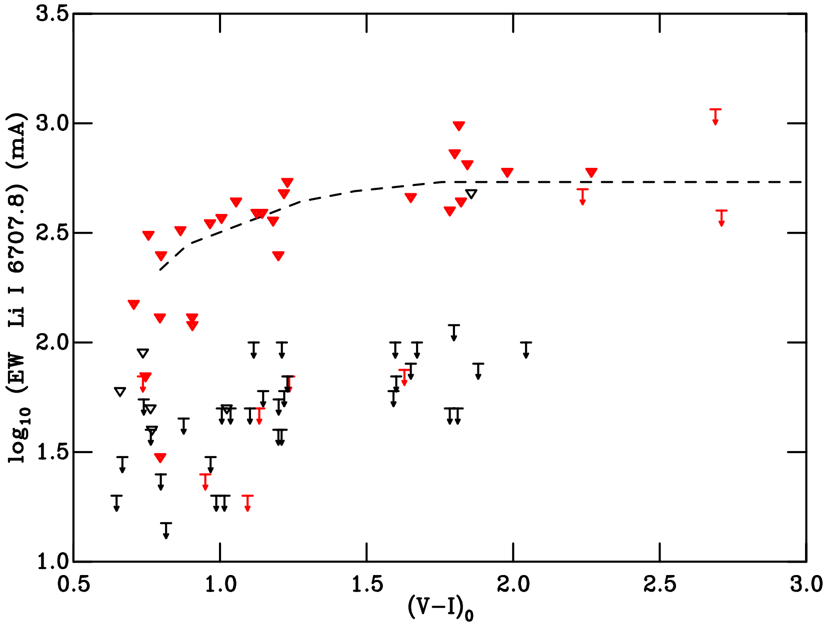

Figure 7.3: The Li I EW versus intrinsic (V-I) colour for the kinematic members (red filled triangles) and kinematic non-members (black open triangles). Objects with just upper limits or uncertain EW measurement are represented by an arrow in the corresponding colour (i.e., red for kinematic members and black for kinematic non-members). The dashed line is the Li isoabundance line converted to intrinsic colours thanks to the interpolation of the T_{eff} - $(V-I)_0$ scale of Jeffries & Tolley (1998). All the stars falling above, or close to (see text) this line, and showing the correct RV are classified as PMS members of the stellar association clustering around the Wolf-Rayet star. Note that the non-member at $(V-I)_0 = 1.857$ is object no. 38, a suspected spectroscopic binary PMS member with the “wrong” RV.

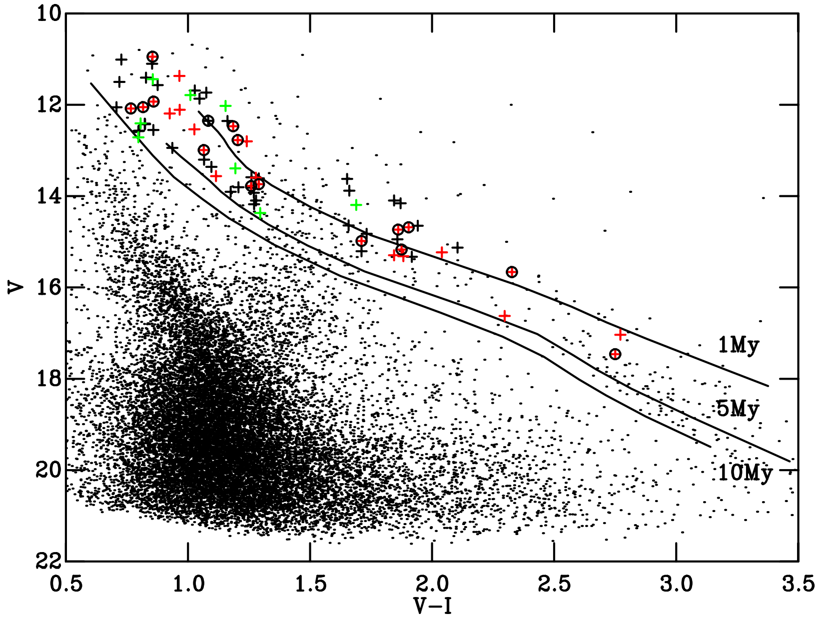

Figure 7.4: The V versus (V-I) colour-magnitude diagram with PMS kinematic members and non-PMS kinematic members overplotted (respectively red and green crosses), together with kinematic non-members (black crosses). Objects with an X-ray counterpart are circled. The non-PMS members have intrinsic colours suggesting G and K-type stars. Isochrones are from D'Antona & Mazzitelli (1997), for an assumed distance of 410 pc.

Li EW larger than 600 mÅ and have an X-ray counterpart associated; and just one object (a non-member) of the 43 non-PMS objects with an X-ray counterpart. This simultaneously demonstrates the power of X-ray selection, but also that an X-ray selected PMS sample can be seriously incomplete. It is evident from our results that an X-ray selection would have revealed only half of the PMS members.

Note that the presence of undepleted Li in the coolest PMS stars shows that they are very young. The faintest PMS object no. 38, at $V = 17.5$ mag and $(V - I) = 2.8$ mag, has spectral type M and a very large Li EW. At the adopted distance of 410 pc, it is likely to be 1-5 Myr old. Since for M5 to K0-type stars Li is depleted by no more than a factor of 2 by 10 Myr (D'Antona & Mazzitelli 1994; see also Section 3.1.7), this suggests, independently of the assumed distance, that the object is really very young. This upper limit to the possible age of the association leads to a minimum distance of about 360 pc based on the isochrones. This value is just 50 pc less than the adopted distance, but surely rules out the smaller distance of 258 pc proposed by Hipparcos (see also the discussion in Chapter 6), if γ^2 Vel and the PMS stars are physically associated. Brandt et al. (1971) found a small group of 9 stars (possibly a B association) around γ^2 Vel, which are at an average distance of 460 pc. From SIMBAD database, it appears that these stars have radial velocities in the range 8-27 km/s, whereas γ^2 Vel has RV of 35 km/s. Straka (1973) obtained radial velocities for the same stars, finding 4 objects plus γ^2 Vel with RV in the range 20-26 km/s, and the remaining 5 objects with RV in the range 8-14 km/s. If these RVs are heliocentric, the RV range of our kinematic members (9.8-24.2 km/s) is within the RV range given by Straka (1973), including γ^2 Vel.

7.3 Final remarks

Out of 83 stars for which we have spectra, we classified 23 PMS and 4 possible PMS objects, which are all kinematic members of the stellar association clustering around γ^2 Vel. Another 5 objects could be PMS stars, but we do not have RV measurements to confirm their membership. There are two Li-rich objects which are kinematic non-members, but these could be PMS members showing the "wrong" RV if they can be confirmed as spectroscopic binaries.

Not all of the PMS objects are detected ROSAT X-ray sources, suggesting the presence of X-ray quiet objects and confirming the incompleteness of X-ray selected samples.

The most important result of this study is that almost all of the 23 low-mass PMS stars members around the Wolf-Rayet star γ^2 Vel are WTTS: only one could have an $H\alpha$ EW large enough to signify ongoing accretion for it to be classified as a CTTS. Therefore, the number of CTTS is at most a few per cent of the PMS population, and may be zero. It is interesting to compare the WTTS/CTTS ratio around γ^2 Vel with that in other star forming regions, which have mainly been surveyed in X-ray. The problem with X-ray selected samples is that they are probably biased towards WTTS, with CTTS being more difficult to detect in soft X-rays (possibly because they are absorbed in circumstellar envelopes, or because they are intrinsically fainter; see also Section 2.5). This is not the case for an optically selected sample such as our own, but the selection bias towards WTTS in X-ray selected samples make our extreme WTTS/CTTS ratio of > 20 even more significant. For example, we find that the ratio of WTTS/CTTS is in the range 1 to 13 in T associations such as Taurus-Auriga, Chamaleon, Lupus and ρ Ophiuci (Neuhäuser et al. 1995b; Hartmann et al. 1991; Feigelson et al.

1993; Alcalá et al. 1995; Krautter et al. 1997; Martín et al. 1998); and increases up to more than 20 in OB associations such as λ-Ori and Upper-Scorpius (Dolan & Mathieu 1999, 2001; Preibisch & Zinnecker 1999; Preibisch et al. 2001; see Section 2.12 in Chapter 2 for more details).

The presence of 22 (if not 23) WTTS out of 23 PMS objects is striking. This seems to suggest that γ^2 Vel could be responsible for dispersing the discs around the low-mass PMS objects through its stellar winds and UV radiation. This is supported by the model of photoevaporation of circumstellar discs by an external source of UV radiation produced by nearby massive stars, which was applied to stars (at less than 1 pc from the brightest member θ^1 Ori C) in the Orion nebula by Johnstone et al. (1998); disc destruction timescales derived from theoretical models of Störzer & Hollenbach (1999), give values of about 1 Myr (see Section 2.14 in Chapter 2). The low-mass PMS objects we have found are within a 0.2° radius from γ^2 Vel: at a distance of 450 pc, this corresponds to 1.6 pc $\times$ 1.6 pc. Therefore, in the past they must have been closer than they are now, in order to have their circumstellar discs evaporated. Perhaps they formed in a bound cluster which broke up when γ^2 Vel blew all the gas/dust out.

Finally, note that the stars which were spectroscopically followed-up account for about 50% of the PMS candidates of the optically selected sample: they have visual magnitudes in the range $11 < V < 17$ mag, and are located in a $0.2° \times 0.2°$ region around the Wolf-Rayet star. It would be interesting to have spectroscopic results for the other PMS candidates as well, and to compare the X-ray sources detected in the HRI summed image with those found from the summed PSPC, to separate multiple sources.

8 Conclusions

8.1 Discussion and conclusions

In the past it was believed that star formation was a bimodal process (Larson 1986), with high-mass stars forming in OB associations and low-mass stars in T associations, considering the formation of both high and low-mass stars altogether a very rare event. The discovery of low-mass stars in OB associations questioned this assumption, and, moreover, it showed that, by assuming a Miller-Scalo IMF (Miller & Scalo 1979), low-mass stars mainly form in OB association, and just a small fraction in T associations (see Walter et al. 2000). OB associations are therefore considered the key to understand star formation processes and test the universality of the IMF. From recent studies, the number of low-mass stars formed seem to follow the Miller-Scalo IMF of the field stars (see for example Walter & Boyd 1991; Walter et al. 1994; Preibisch & Zinnecker 1999; Preibisch et al. 2001; Dolan & Mathieu 2001).

The effect that high-mass stars may have on the formation of their lower-mass siblings is crucial. The difficulty in finding faint low-mass stars in very large regions on the sky such as those covered by OB associations, can be overcome with joint optical, X-ray and spectroscopic surveys. This investigation method was proven to be extremely successful for the targets observed and discussed in this thesis, i.e., the younger subgroup of the Cep OB3 association, Cep OB3b, and the region surrounding the Wolf-Rayet star γ^2 Velorum.

The investigation of Cep OB3b lead us to the discovery of a low-mass stellar population co-existing with the high-mass members of the association. The spectroscopic follow-up of the optically selected PMS candidates (thanks to the location of the known X-ray sources present in the region) confirmed 10 PMS members, respectively 5 CTTS and 5 WTTS. From a cross-correlation with 2MASS IR data, 4 CTTS showed IR excess indicative of the presence of a circumstellar accretion disc. We found the ratio of WTTS/CTTS to be 1, more in agreement with values typical of T associations than OB associations, at the same age.

The X-ray investigation of the region around the ultra-massive Wolf-Rayet star γ^2 Velorum lead us instead to the serendipitous discovery of a very rich low-mass stellar association which was able to form in such an apparently hostile environment. The subsequent optical follow-up confirmed the presence of a PMS population, whose location in the colour-magnitude diagram coincides with that of the X-ray sources. Spectroscopic results confirmed 23 PMS members, all of which are WTTS and of about the same age of γ^2 Velorum. Furthermore, the ratio of WTTS/CTTS is at least 20, a value which is similar to that found in OB associations. This suggests that the stellar winds and UV radiation from the 0-star in the binary system γ^2 Vel did not halt the low-mass star formation process in the region, but that they were responsible for the circumstellar disc erosion and their subsequent evaporation, determining their PMS nature.

This has important implications for protoplanetary formation: if planets form around low-mass PMS stars, their formation timescales must be shorter than that for the evaporation of the circumstellar discs (see Section 2.14 in Chapter 2, and references therein). In a star-forming region such as the Cep OB3b subgroup, they may have had more time to build up, whereas, in one such as that around the Wolf-Rayet star they must have (if they have) formed in a time shorter than the age of the WTTS. In both cases, planetary formation may have formed in a few Myr. This of course would need to be tested with proper disc diagnostics (see Section 2.13 in Chapter 2), in order to exclude the presence of (passive) circumstellar discs.

8.2 Final remarks and future work to do

There is plenty of possible future work to do, both with respect to the low-mass stellar association around the younger subgroup of the Cep OB3 association, and to that around the Wolf-Rayet star γ^2 Velorum.

In particular, for Cep OB3b, Gemini North time should be asked for a spectroscopic follow-up of the lower mass PMS objects. This will allow us to make a better census of the PMS population and to determine the IMF. At present, the IMF in Cep OB3 seems to be consistent with that of field stars (Naylor & Fabian 1999) for masses in the range $0.3M_\odot < M < 3M_\odot$ (from the ratio low-mass stars to high-mass stars).

Regarding γ^2 Velorum, first of all a normalisation of the photometric catalogue for stars falling in the overlapping regions is demanded. Furthermore, with the launch of the XMM satellite, deep imaging will be available for the region around the Wolf-Rayet star. This would allow us to explore the brown-dwarf population (M< 0.08 M$_\odot$). Finally, Hydra spectroscopic follow-up of the remaining

PMS objects not previously observed is necessary for the IMF to be properly defined. We have used Figure 7.4 (see Chapter 7) to estimate the IMF for low-mass stars around γ^2 Velorum, assuming that the ratio of PMS to non-PMS stars is constant as we go to lower masses. We find good agreement with a Miller-Scalo type law, with a possible turnover at around 0.2-0.3 $M_\odot$, but with evidence for stars forming down to at least 0.15 $M_\odot$. 2MASS NIR data could be used to look for NIR excess signatures, indicatitive of active accretion discs. Other disc diagnostics, such as mid-IR imaging would be useful in searching for the presence of circumstellar discs.

The surveys of Cep OB3b and γ^2 Velorum could be extended to lower masses and wider areas, with an IR photometric study and a larger optical spectroscopic follow-up (with WYFFOS and 2dF respectively).

We could also test for the presence of discs around γ^2 Velorum using 2MASS data for the region, mid-IR imaging or imagining in the sub-millimetre (with the Submillimeter Common-User Bolometer Array).

A more ambitious project would be the demography of circumstellar discs. The SUPERCOSMOS Hα survey may offer the excellent opportunity to detect Hα emitting objects in already known, as well as yet unknown, star-forming regions, and together with a spectroscopic follow-up of the circumstellar disc candidates it would be possible to confirm their kinematic membership and infrared excesses.

Finally, more accurate kinematic surveys could be used to study the expansion of the associations, by checking how close the stars were in the past with radial velocity measurements and proper motions (by comparing the astrometric positions of our samples with those found with SUPERCOSMOS scans of old photographic plates).

A Cross-correlation with the J95 catalogue

The optical catalogue for the Cep OB3b region was cross-correlated with the catalogue of J95 (see Chapter 3 for details). As a result, we found 326 matches in total, for stars in fields 1a, 2a, 2b, and 4b (see Fig. 3.2).

In the following Tables A.1, A.2, A.3, and A.4 just few entries are shown for stars belonging to the four different fields, since there are 55 matches in total in field 1a; 138 in field 2a; 110 in field 2b; and 23 in field 4b.

The matching star from the J95 catalogue and its information is reported in the first two lines of each entry, immediately followed by the star in our catalogue and its information, for a total of four lines for each match. Starting from the first line, it contains the J95 id number, followed by RA, Dec, V, error in V, (B-V) colour and its error; additional information continues in the second line, giving respectively the (V-I) colour and error, and (U-B) colour and error. The third and fourth lines contain the information regarding the star matched in our catalogue, following the same criteria, apart from the id number which is preceded by the field number the star belongs to, and the flags for the different colours (denoted with the F). The value 9.99 is given to a colour and associated error when their information is missing in the J95 catalogue.

	J95 id	RA	Dec	V	errV		(B-V)	errBV	
(V-I)	errVI		(U-B)	errUB					
	field id	RA	Dec	V	errV	F(V)	(B-V)	errBV	F(BV)
(V-I)	errVI	F(VI)	(U-B)	errUB	F(UB)				
	BHJ28-116	22 55 25.2	62 42 52	21.07	0.19		9.99	9.99	
2.23	0.16		9.99	9.99					
	1a 1750	22 55 25.36	62 42 51.47	20.747	0.085	00	1.375	0.173	00
2.133	0.090	00	-0.028	0.628	00				
	BHJ28-118	22 55 25.9	62 42 49	20.38	0.11		9.99	9.99	
2.01	0.11		9.99	9.99					
	1a 1235	22 55 26.00	62 42 48.92	20.250	0.054	00	1.574	0.127	00
1.988	0.060	00	1.102	0.574	00				
	BHJ28-119	22 55 26.3	62 42 28	20.06	0.09		9.99	9.99	
2.08	0.09		9.99	9.99					
	1a 1087	22 55 26.44	62 42 28.37	19.576	0.530	00	1.880	0.562	00
1.675	0.502	00	0.250	0.262	00				
	BHJ28-120	22 55 27.1	62 41 44	18.55	0.04		1.51	0.09	
1.77	0.05		9.99	9.99					
	1a 626	22 55 27.27	62 41 43.76	18.365	0.176	88	1.586	0.305	88
1.645	0.180	88	3.543	0.239	88				
	BHJ28-125	22 55 28.0	62 41 31	18.88	0.04		9.99	9.99	
2.43	0.04		9.99	9.99					
	1a 585	22 55 28.10	62 41 31.63	18.769	0.019	00	1.982	0.050	00
2.558	0.020	00	1.589	0.305	00				
	BHJ34-002	22 55 31.9	62 51 21	18.81	0.06		9.99	9.99	
1.62	0.11		9.99	9.99					
	1a 514	22 55 32.06	62 51 20.70	18.889	0.290	11	1.069	0.393	11
1.522	0.298	11	0.051	0.616	11				
	BHJ34-003	22 55 32.3	62 50 52	15.93	0.02		1.27	0.04	
1.59	0.03		0.48	0.12					
	1a 102	22 55 32.45	62 50 52.95	15.896	0.004	00	1.258	0.006	00
1.556	0.005	00	0.504	0.011	00				
	BHJ34-004	22 55 33.1	62 50 32	18.56	0.06		9.99	9.99	
2.33	0.06		9.99	9.99					
	1a 432	22 55 33.22	62 50 33.16	18.737	0.019	00	1.938	0.048	00
2.473	0.020	00	1.199	0.217	00				
	BHJ34-006	22 55 35.6	62 50 59	18.64	0.06		9.99	9.99	
2.70	0.06		9.99	9.99					
	1a 181	22 55 35.67	62 50 59.53	18.574	0.017	00	2.119	0.047	00
2.584	0.017	00	1.853	0.378	00				

Table A.1: Matches our optical catalogue - J95 catalogue in the field 1a (few entries).

	J95 id	RA	Dec	V	errV		(B-V)	errBV	
(V-I)	errVI		(U-B)	errUB					
	field id	RA	Dec	V	errV	F(V)	(B-V)	errBV	F(BV)
(V-I)	errVI	F(VI)	(U-B)	errUB	F(UB)				
	BHJ25-001	22 54 10.8	62 45 37	18.47	0.05		9.99	9.99	
1.71	0.06		9.99	9.99					
	2a 295	22 54 10.94	62 45 35.93	18.570	0.019	00	1.295	0.033	00
1.656	0.022	00	0.704	0.102	00				
	BHJ25-003	22 54 12.6	62 44 48	19.00	0.07		9.99	9.99	
1.75	0.08		9.99	9.99					
	2a 263	22 54 12.70	62 44 47.83	19.022	0.026	00	1.354	0.046	00
1.664	0.031	00	0.728	0.158	00				
	BHJ25-004	22 54 12.7	62 43 22	19.16	0.07		9.99	9.99	
1.76	0.08		9.99	9.99					
	2a 768	22 54 12.83	62 43 23.07	19.321	0.033	00	1.729	0.073	00
1.835	0.037	00	0.581	0.253	00				
	BHJ25-005	22 54 13.3	62 45 3	19.21	0.07		9.99	9.99	
1.85	0.08		9.99	9.99					
	2a 837	22 54 13.43	62 45 3.12	19.305	0.032	00	1.404	0.060	00
1.837	0.036	00	0.400	0.175	00				
	BHJ25-006	22 54 13.5	62 45 43	19.02	0.06		9.99	9.99	
1.90	0.07		9.99	9.99					
	2a 651	22 54 13.65	62 45 42.60	19.009	0.025	00	1.511	0.050	00
1.806	0.029	00	0.437	0.144	00				
	BHJ25-007	22 54 13.9	62 44 4	17.63	0.03		1.64	0.10	
1.91	0.03		9.99	9.99					
	2a 302	22 54 14.05	62 44 3.83	17.686	0.010	00	1.518	0.020	00
1.903	0.012	00	0.738	0.059	00				
	BHJ25-008	22 54 14.6	62 44 34	18.55	0.05		9.99	9.99	
1.79	0.06		9.99	9.99					
	2a 566	22 54 14.74	62 44 34.11	18.592	0.019	00	1.377	0.034	00
1.760	0.022	00	0.506	0.095	00				
	BHJ25-009	22 54 14.8	62 44 44	18.07	0.04		9.99	9.99	
2.54	0.03		9.99	9.99					
	2a 381	22 54 14.94	62 44 43.69	18.123	0.014	00	2.114	0.036	00
2.596	0.014	00	1.821	0.358	00				
	BHJ25-010	22 54 15.9	62 44 16	17.83	0.04		1.59	0.12	
1.79	0.03		9.99	9.99					
	2a 334	22 54 15.96	62 44 16.36	17.894	0.012	00	1.464	0.022	00
1.788	0.014	00	0.847	0.073	00				

Table A.2: Matches this optical catalogue - J95 catalogue in the field 2a (few entries).

	J95 id	RA	Dec	V	errV		(B-V)	errBV	
(V-I)	errVI		(U-B)	errUB					
	field id	RA	Dec	V	errV	F(V)	(B-V)	errBV	F(BV)
(V-I)	errVI	F(VI)	(U-B)	errUB	F(UB)				
	BHJ40-015	22 56 12.8	62 37 9	18.94	0.04		1.78	0.16	
1.87	0.05		9.99	9.99					
	2b 379	22 56 12.95	62 37 9.46	19.751	0.265	88	1.494	0.658	88
1.514	0.322	88	-0.582	1.286	88				
	BHJ40-016	22 56 12.9	62 37 52	19.57	0.06		9.99	9.99	
1.88	0.06		9.99	9.99					
	2b 499	22 56 12.97	62 37 52.85	19.831	0.288	88	1.267	0.622	88
2.374	0.291	88	2.350	0.529	88				
	BHJ40-017	22 56 13.1	62 35 32	16.06	0.02		1.94	0.03	
2.18	0.02		0.71	0.09					
	2b 33	22 56 13.24	62 35 33.21	16.227	0.004	00	1.865	0.009	00
2.385	0.004	00	0.929	0.026	00				
	BHJ40-018	22 56 13.4	62 36 45	18.94	0.04		9.99	9.99	
2.74	0.03		9.99	9.99					
	2b 389	22 56 13.49	62 36 45.52	19.215	0.024	00	2.283	0.087	00
3.223	0.024	00	1.434	0.835	00				
	BHJ40-019	22 56 13.5	62 35 54	20.19	0.09		9.99	9.99	
1.85	0.09		9.99	9.99					
	2b 777	22 56 13.56	62 35 55.57	20.267	0.056	00	1.658	0.148	00
1.923	0.063	00	0.026	0.342	00				
	BHJ40-020	22 56 13.6	62 35 38	19.60	0.06		9.99	9.99	
2.77	0.05		9.99	9.99					
	2b 496	22 56 13.66	62 35 39.02	19.717	0.036	00	2.126	0.129	00
3.359	0.035	00	1.060	0.815	00				
	BHJ40-021	22 56 13.6	62 36 58	19.00	0.04		1.64	0.15	
1.85	0.05		9.99	9.99					
	2b 378	22 56 13.66	62 36 58.83	19.083	0.022	00	1.465	0.048	00
1.926	0.025	00	1.080	0.237	00				
	BHJ40-022	22 56 13.6	62 36 35	17.30	0.02		2.41	0.07	
2.43	0.02		9.99	9.99					
	2b 142	22 56 13.68	62 36 36.31	17.424	0.008	00	2.232	0.022	00
2.730	0.008	00	1.899	0.209	00				
	BHJ40-023	22 56 13.7	62 37 22	18.32	0.03		1.38	0.09	
1.59	0.05		9.99	9.99					
	2b 224	22 56 13.78	62 37 22.83	18.380	0.013	00	1.327	0.026	00
1.632	0.017	00	0.682	0.082	00				

Table A.3: Matches this optical catalogue - J95 catalogue in the field 2b (few entries).

	J95 id	RA	Dec	V	errV		(B-V)	errBV	
(V-I)	errVI		(U-B)	errUB					
	field id	RA	Dec	V	errV	F(V)	(B-V)	errBV	F(BV)
(V-I)	errVI	F(VI)	(U-B)	errUB	F(UB)				
	BHJ11-015	22 52 31.8	62 20 11	19.42	0.08		9.99	9.99	
3.28	0.07		9.99	9.99					
	4b 163	22 52 31.84	62 20 11.17	19.446	0.028	00	2.654	0.134	00
3.464	0.028	00	0.642	0.686	00				
	BHJ11-016	22 52 32.8	62 19 30	20.34	0.17		9.99	9.99	
2.81	0.14		9.99	9.99					
	4b 266	22 52 32.82	62 19 30.40	20.194	0.050	00	2.310	0.200	00
2.674	0.050	00	-1.879	0.865	00				
	BHJ11-017	22 52 33.7	62 18 47	9.84	0.02		1.19	0.01	
1.54	0.02		0.01	0.04					
	4b 1	22 52 33.73	62 18 47.52	10.589	0.001	44	1.314	0.002	44
0.559	0.002	44	-0.643	0.002	44				
	BHJ11-019	22 52 34.3	62 19 51	18.61	0.05		9.99	9.99	
2.52	0.05		9.99	9.99					
	4b 117	22 52 34.34	62 19 51.14	18.703	0.017	00	1.967	0.044	00
2.613	0.017	00	0.969	0.417	00				
	BHJ11-021	22 52 34.6	62 20 4	18.91	0.06		9.99	9.99	
2.32	0.05		9.99	9.99					
	4b 120	22 52 34.58	62 20 4.10	18.897	0.019	00	1.772	0.046	00
2.338	0.020	00	0.733	0.214	00				
	BHJ11-022	22 52 37.3	62 18 7	18.34	0.04		9.99	9.99	
3.20	0.04		9.99	9.99					
	4b 89	22 52 37.26	62 18 8.23	18.361	0.013	00	2.646	0.054	00
3.381	0.013	00	2.577	0.051	90				
	BHJ11-023	22 52 37.3	62 17 19	18.05	0.04		1.68	0.11	
2.29	0.04		9.99	9.99					
	4b 41	22 52 37.30	62 17 20.39	18.148	0.012	00	1.763	0.027	00
2.313	0.013	00	1.105	0.134	00				
	BHJ11-024	22 52 38.4	62 19 29	14.76	0.02		1.48	0.03	
1.88	0.02		0.92	0.05					
	4b 15	22 52 38.43	62 19 29.68	14.815	0.010	00	1.509	0.011	00
1.888	0.011	00	0.978	0.009	00				
	BHJ11-025	22 52 40.3	62 20 5	18.53	0.05		9.99	9.99	
4.10	0.04		9.99	9.99					
	4b 96	22 52 40.29	62 20 4.78	18.504	0.014	00	3.283	0.100	00
4.440	0.016	00	1.782	0.096	90				

Table A.4: Matches this optical catalogue - J95 catalogue in the field 4b (few entries).

Bibliography

Abt H.A., Landolt A.U., Levy S.G., Mochnacki S., 1976, AJ, 81, 541

Adams F.C., Shu F.H., 1986, ApJ, 308, 836

Adams F.C., Lada C.J., Shu F.H., 1987, ApJ, 312, 788

Adams F.C., Lada C.J., Shu F.H., 1987, ApJ, 326, 865

Alcalá J.M., Krautter J., Schmitt J.H.M.M., Covino E., Wichmann R., Mundt R., 1995, A&AS, 114, 109

Alcalá et al., 1996, A&AS, 119, 7

Alcalá J.M., Krautter J., Covino E., Neuhäuser R., Schmitt J.H.M.M., Wichmann R., 1997, A&A, 319, 184

Alcalá J.M., Covino E., Torres G., Sterzik M.F., Pfeiffer M.J., Neuhäuser R., 2000, A&A, 353, 186

Allan D.J., 1992, ASTERIX User note number 004, Starlink, Rutherford Appleton Laboratory, UK

Allan D.J., Vallance R.J., 1995, STARLINK User note number 98.6, Rutherford Appleton Laboratory, UK

Ambartsumian V.A., 1947, Stellar evolution and Astrophysics (Armenian Acad. of Sci.)

Ambartsumian V.A., 1949, Astron. J. USRR, 26, 3

Anders E., Grevesse N., 1989, Geochim. Cosmochim. Acta, 53, 197

Andrè P., Montmerle T., 1994, ApJ, 420, 837

Appenzeller I., Mundt R., 1989, A&AR, 1, 291

Appenzeller I., Jankovics I., Östreicher R., 1984, A&A, 141, 108

Assousa G.E., Herbst W., Turner K.C., 1977, ApJ, 218, L13

Baade W., 1963, Evolutions of Stars and Galaxies, C. Payne-Gaposchkin ed., Harward University Press, Cambridge (Massachusetts), p. 224

Baker N., 1967, unpublished report, Goddard Space Flight Center

Balachandran S., Lambert D.L., Stauffer J.R., 1988, ApJ, 333, 267

Bally J., Sutherland R.S., Devine D., Johnstone D., 1998, AJ, 116, 293

Baraffe I., Chabrier G., Allard F., Hauschildt P.H., 1997, A&A, 327, 1054

Baraffe I., Chabrier G., Allard F., Hauschildt P.H., 1998, A&A, 337, 403

Barrado y Navascuúes D., Stauffer J.R., 1996, A&A, 310, 879

Barsella B., Panagia N., Perinotto M., 1982, A&A, 111, 130

Basri G., Bertout C., 1989, ApJ, 341, 340

Basri G., Martín E.L., Bertout C., 1991, A&A, 252, 625

Bastian U., Finkenzeller U., Jaschek C., Jaschek M., 1983, A&A, 126, 438

Beckwith S.V.W., Sargent A.I., Chini R.S., Güsten R., 1990, AJ, 99, 924

Beckwith S.V.W., Sargent A.I., Koresko C.D., Weinstraub D.A., 1989, ApJ, 343, 393

Bertelli G., Bressan A., Chiosi C., Fagotto F., Nasi E., 1994, A&AS, 106, 275

Bertout C., 1987, Circumstellar matter, IAU Symposium, D. Reidel Publishing Co., Dordrecht, p. 23

Bertout C., 1989, ARA&A, 27, 351

Bertout C., Basri G., Bouvier J., 1988, ApJ, 330, 350

Bessell M.S., 1979, PASP, 91, 589

Bessell M.S., 1991, AJ, 101, 662

Bessell M.S., Brett J.M., 1988, PASP, 100, 1134

Beuther H., Kramer C., Deiss B., Stutzki J., 2000, A&A, 362, 1109

Blaauw A., 1964, ARA&A, 2, 213

Blaauw A., Irish Astron. J., 1983, 16, 141

Blaauw A., 1991, The Physics of Star Formation and Early Stellar Evolution. Kluwer Academic Publishers, Dordrecht, p. 125

Blaauw A., Hiltner W.A., Johnson H.L., 1959, ApJ, 130, 69 (BHJ). *Erratum*: 1960, ApJ, 131, 527

Bodenheimer P., 1965, ApJ, 142, 451

Boesgaard A., M., 1990, in Cool Stars, Stellar Systems, and the Sun, 6th Cambridge Workshop, ASP Conference Series, G. Wallerstein ed., p. 317

Boesgaard A.M., Steigman G., 1985, ARA&A, 23, 319

Bok B.J., 1934, Harvard Circ. No. 384

Bonsack W.K., 1961, ApJ, 133, 340

Bouvier J., 1986, PhD thesis, Paris VII University, Paris, France

Bouvier J., 1994, in Cool Stars, Stellar Systems, and the Sun, 8th Cambridge Workshop, ASP Conference Series, Caillault J.P. ed., Vol. 64, p. 151

Bouvier J., Appenzeller I., 1992, A&AS, 92, 481

Bouvier J., Bertout C., Benz W., Mayor M., 1986, A&A, 165, 110

Bouvier J., Cabrit S., Fernández M., Martín E.L., Matthews J.M., 1993, A&A, 272, 176

Bouvier J., Covino E., Kovo O., Martín E.L., Matthews J.M., Terranegra L., Beck S.C., 1995, A&A, 299, 89

Bouvier J., Forestini M., Allain S., 1997, A&A, 326, 1023

Bouvier J., Wichmann R., Grankin K., Allain S., Covino E., Fernandez M., Martín E.L., Terranegra L., Catalano S., Marilli E., 1997, A&A, 318, 495

Brandner W., et al. 2000, AJ, 120, 950

Brandt J.C., Stecher T.P., Crawford D.L., Maran S.P., ApJ, 163, L99

Braz M.A., Lépine J.R.D., Sivagnanam P., Le Squeren A.M., 1990, A&A, 236, 479

Briceño C., Hartmann L.W., Stauffer J.R., Gagne M., Stern R.A., 1997, AJ, 113, 740

Brodskaja E.S., 1955, Izvest. Krim. Ap. Obs., 14, 3

Brown A.G.A., Dekker G., de Zeeuw P.T., 1997, MNRAS, 285, 479

Burrows A., Hubbard W.B., Lunine J.I., 1989, ApJ, 345, 939

Burrows C.J., et al. 1996, ApJ, 473, 437

Calvet N., Gullbring E., 1998, ApJ, 509, 802

Calvet N., Basri G., Kuhi L.V., 1984, ApJ, 277, 725

Cameron A.G.W., Truran J.W., 1977, Icarus, 30, 447

Canuto V.M., Goldman I., Mazzitelli I., 1996, ApJ, 473, 550

Cardelli J.A., Clayton G.C., Mathis J.S., 1989, ApJ, 345, 245

Carpenter J.M., 2001, AJ, in press

Carr J.S., 1987, ApJ, 323, 170

Casanova S., Montmerle T., Feigelson E.D., Andre P., 1995, ApJ, 439, 752

Choi P.I., Herbst W., 1996, AJ, 111, 283

Claret A., Giménez A., 1989, A&AS, 81, 1

Clausen J.V., Giménez A., 1991, A&A, 241, 98

Codella C., Felli M., Natale V., Palagi F., Palla F., 1994, A&A, 291, 261

Cohen R.S., Cong H., Dame T.M., Thaddeus P., 1980, ApJ, 239, L53

Cohen M., Kuhi L.V., 1979, ApJS, 41, 743

Conti P.S., Leep E.M., 1974, ApJ, 193, 113

Conti P.S., Smith L.F., 1972, ApJ, 172, 623

Covino E., Alcalá J.M., Allain S., Bouvier J., Terranegra L., Krautter J., 1997, A&A, 328, 187

Crawford D.L., 1970, Stellar Rotation, IAU Colloquium No. 4, A. Slettebak ed., (D. Reidel Publishing Co, Dordrecht, Holland), p. 114

Crawford D.L., Barnes J.V., 1970, AJ, 75, 952

D'Antona F., Mazzitelli I., 1994, ApJS, 90, 467

D'Antona F., Mazzitelli I., 1997, Mem. Soc. Astron. Ital., Vol. 68, p. 807

David L.P., Forman W., Jones C., 1999, ApJ, 519, 533

de la Fuente Marcos R., 1995, A&A, 301, 407

de Jager C., Nieuwenhuijzen H., 1987, A&A, 177, 217

De Marco O., Schmutz W., 1999, A&A, 345, 163

De Marco O., Schmutz W., Crowther P.A., Hillier D.J., Dessart L, de Koter A., Schweickhardt J., 2000, A&A, 358, 187

De Vegt C., 1966, Z. Astrophys., 64, 268

de Zeeuw P.T., Brand J., 1985, in Birth and Evolution of Massive Stars and Stellar Groups, W. Boland and H. van Woerden ed., (Dordrecht: Reidel), p. 95

de Zeeuw P.T., Hoogerwerf R., de Bruijne J.H.J., Brown A.G.A., Blaauw A., 1999, AJ, 117, 354

Dolan C.J., Mathieu R.D., 1999, AJ, 118, 2409

Dolan C.J., Mathieu R.D., 1999, AJ, 121, 2124

Doremus C., 1970 (private communication)

Duncan D.K., 1981, ApJ, 248, 651

Dutrey A., Guilloteau S., Simon M., 1994, A&A, 286, 149

Edwards S., Cabrit S., Strom S.E., Heyer I., Strom K.M., Anderson E., 1987, ApJ, 321, 473

Edwards S. et al., 1993, AJ, 106, 372

Elmegreen B.G., 1985, in Protostars and Planets II, D.C. Black and M.S. Matthews eds., Univ. of Arizona Press, Tucson, p. 33

Elmegreen B.G., Elmegreen D.M., 1986, ApJ 311, 554

Elmegreen B.G., Lada C.J., 1977, ApJ, 214, 725

Elsasser H., Staude H.J., 1978, A&A, 70, L3

Evans N.J. et al., 1981, ApJ, 244, 115

Fabian A.C., Stewart G.C., 1983, MNRAS, 202, 697

Favata F., Micela G., Sciortino S., 1996, A&A, 311, 951

Feigelson E.D., 1996, ApJ, 468, 306

Feigelson E.D., DeCampli W.M., 1981, ApJ, 243, L89

Feigelson E.D., Kriss G.A., 1989, ApJ, 338, 262

Feigelson E.D., Lawson W.A., 1997, AJ, 113, 2130

Feigelson E.D., Montmerle T., ARA&A, 1999, 363

Feigelson E.D., Casanova S., Montmerle T., Guibert J., 1993, ApJ, 416, 623

Felli M., Tofani G., Harten R.H., Panagia N., 1978, A&A, 69, 199

Fitzgerald M.P., 1970, A&A, 4, 234

Fitzpatrick E.L., 1999, PASP, 111, 63

Fitzpatrick E.L., Spitzer L., 1994, ApJ, 427, 232

Flower P.J., 1996, ApJ, 469, 355

Frink S., Röser S., Neuhäuser R., Sterzik M.F., 1997, A&A, 325, 613

Gahm G., 1981, The Universe at Ultraviolet Wavelegths (NASA Conf. Pub. 2171), p. 105

Gaposhkin G., 1949, Variable Stars, 7, 34

García López R.J., Rebolo R., Martín E.L., 1994, A&A, 282, 518

Garmany C.D., 1972, AJ, 77, 38

Garmany C.D., 1973, AJ, 78, 185

Garmany C.D., 1994, PASP, 106, 25

Garmany C.D., Stencel R.E., 1992, A&AS, 94, 211

Garrison R.F., 1970, AJ, 75, 1001

Georgelin Y.M., Georgelin Y.P., 1976, A&A, 49, 57

Ghez A.M., Neugebauer G., Matthews K., 1993, AJ, 106, 2005

Gorti U., Bhatt H.C., 1996, MNRAS, 278, 611

Gómez de Castro A., Fernández M., 1996, MNRAS, 283, 55

Gomez M., Hartmann L., Kenyon S.J., Hewett R., 1993, AJ, 105, 1295

Gordon M.A., 1990, ApJ, 352, 636

Grasdalen G., Strom S., Strom K., Capps R., Thompson D., Castalez M., 1984, ApJ, 283, L57

Greene T.P., Meyer M.R., 1995, ApJ, 450, 233

Grevesse N., 1968, Solar Phys., 5, 159

Grevesse N., Sauval A.J., 1998, Space Sci. Rev., 85, 161

Haisch K.E., Lada E.A., Lada C.J., 2001, AJ, 121, 2065

Haisch K.E., Lada E.A., Lada C.J., 2001b, ApJ, 553, L153

Haisch K.E., Lada E.A., Piña R.K., Telesco C.M., Lada C.J., 2001, AJ, 121, 1512

Habing H.J. et al., 1999, Nature, 401, 456

Hanbury Brown R., Davis J., Herbison-Evans D., Allen L.R., 1970, MNRAS, 148, 103

Harper C.L., 1996, ApJ, 466, 1026

Harten R.H., Thum C., Felli M., 1981, A&A, 94, 231

Hartigan P., Hartmann L., Kenyon S.J., Strom S.E., Skrutskie M.F., 1990, ApJ, 354, L25

Hartmann L., Raymond J., 1989, ApJ, 337, 903

Hartmann L., Stauffer J.R., 1989, AJ, 97, 873

Hartmann L., Hewett R., Stahler S., Mathieu R.D., 1986, ApJ, 309, 275

Hartmann L., Hewett R., Calvet N., 1994, ApJ, 426, 669

Hartmann L., Cassen P., Kenyon S., 1997, ApJ, 475, 770

Hartmann L., Jones B.F., Stauffer J.R., Kenyon S.J., 1991, AJ, 101, 1050

Hayashi M., 1965, Pub. Astr. Soc. Japan, 17, 177

Hayashi C., Nakazawa K., Nakagawa Y., 1985, in Protostars and Planets II, D.C. Black and M.S. Matthews eds., Univ. of Arizona Press, Tucson, p. 1100

Heard J.F., 1967, Determination of Radial Velocities and Their Application, IAU Symposium, A.H. Batten and J.F. Heards eds., Vol. 30, p. 219

Herbig G.H., 1960, ApJS, 4, 337

Herbig G.H., 1962, Adv. Astr. Astrophys., 1, 47

Herbig G.H., 1965, ApJ, 141, 588

Herbig G.H., 1977, ApJ, 214, 747

Herbig G.H., 1978, in *Problems of Physics and Evolution of the Universe*, p. 171, Yerevan: Acad. Sci. Armen. SSR

Herbig G.H., Bell K.R., 1988, Lick Obs. Bull. No. 1111

Herbig G.H., Goodrich R.W., 1986, ApJ, 309, 294

Herbig G.H., Rao N.K., 1972, ApJ, 174, 401

Herbig G.H., Soderblom D.R., 1980, ApJ, 242, 628

Herbst W., Miller D.P., 1982, AJ, 87, 1478

Herbst W., Herbst D.K., Grossman E.J., Weinstein D., 1994, AJ, 108, 1906

Hernández C.A., Sahade J., 1980, PASP, 92, 819

Heyer M.H., Carpenter J.M., Ladd E.F., 1996, ApJ, 463, 630

Hill G., 1967, ApJS, 14, 301

Hillenbrand L.A., 1997, AJ, 113, 1733

Hillenbrand L.A., Meyer M.R., 1999, American Astronomical Society Meeting 195

Hillenbrand L.A., Strom S.E., Vrba F.J., Keene J., 1992, ApJ, 397, 613

Hiltner W.A., 1956, ApJS, 2, 389

Hobbs L.M., Pilachowski C., 1988, ApJ, 334, 734

Hodgkin S.T., Pinfield D.J., Jameson R.F., Steele I.A., Cossburn M.R., Hambly N.C., 1999, MNRAS, 310, 87

Houdebine E.R., Stempels H.C., 1997, A&A, 326, 1143

Hurley J., Tout C.A., 1998, MNRAS, 300, 977

Iben I., Talbot R.J., 1966, ApJ, 144, 968

Jacoby G.H., Hunter D.A., Christian C.A., 1984, ApJS, 56, 257

Jeffries R.D., Tolley A.J., 1998, MNRAS, 300, 331

Jeffries R.D., Thurston M.R., Pye J.P., 1997, MNRAS, 287, 350

Johnson H.L., 1957, ApJ, 126, 121

Johnson H.L., Mitchell R.I., Iriarte B., Wisniewski W.Z., 1966, Commun. Lunar and Planetary Lab. 4, 99

Johnson H.L., Morgan W.W., 1953, ApJ, 117, 313

Johnstone D., Hollenbach D., Bally J., 1998, ApJ, 499, 758

Jones B.F., Herbig G.H., 1979, AJ, 84, 1872

Jordi C., Trullols E., Rosselló G., Lahulla F., 1992, A&AS, 94, 519

Jordi C., Galadì-Enrìquez D., Trullols E., Lahulla F., 1995, A&AS, 114, 489 (J95)

Jordi C., Trullols E., Galadì-Enrìquez D., 1996, A&A, 312, 499 (J96)

Joy A.H., 1945, ApJ, 102, 168

Joy A.H., 1949, ApJ, 110, 424

Kenyon S.J., Hartmann L., 1987, ApJ, 323, 714

Kenyon S.J., Hartmann L., 1995, ApJS, 101, 117

Kenyon S.J., Yi I., Hartmann L., 1996, ApJ, 462, 439

Kimeswenger S., Weinberger R., 1989, A&A, 209, 51

Koornneef J., 1983, A&A, 128, 84

Kraft R.P., 1967, ApJ, 150, 551

Krautter J., Bastian U., 1980, A&A, 88, L6

Krautter J., 1996 in Cool Star, Stellar Systems, and the Sun, 9th Cambridge Workshop, ASP Conference Series, R. Pallavicini and A.K. Dupree eds., Vol. 109, p. 395

Krautter J., Wichmann R., Schmitt J.H.M.M., Alcalá J.M., Neuhäuser R., Terranegra L., 1997, A&AS, 123, 329

Kroupa P., 1998, MNRAS, 298, 231

Kuhi L.V., 1964, ApJ, 140, 1409

Lada C.J., 1985, ARA&A, 23, 267

Lada C.J., 1987, in Star Forming Regions, M. Peimbert and J. Jugaku eds., (Reidel, Dordrecht), p. 1

Lada C.J., Adams F.C., 1992, ApJ, 393, 278

Lada C.J, Elmegreen B.G., Blitz L., 1978, in Protostars and planets: Studies of Star Formation and of the Origin of the Solar System, Tucson, Ariz., University of Arizona Press, p. 341-367

Lada E.A., Bally J., Stark A.A., 1991, ApJ, 368, 432

Lada C.J., Muench A.A., Haisch K.E., Lada E.A., Alves J.F., Tollestrup E.V., Willner S.P., 2000, AJ, 120, 3162

Ladd E.F., Hodapp K.-W., 1997, ApJ, 474, 749

Landolt A.U., 1992, AJ, 104, 340

Larson R.B. 1986, MNRAS, 218, 409

Lasker B.M., Sturch C.R., McLean B.J., Russell J.L., Jenkner H., Shara M.M., 1990, AJ, 99, 2019

Lawson W.A., Feigelson E.D., Huenemoerder D.P., 1996, MNRAS, 280, 1071

Lee T., Papanastassiou D.A., Wasserburg G.J., 1977, ApJ, 211, 107

Leisawitz D., Bash F.N., Thaddeus P., 1989, ApJS, 70, 731

Leitherer C., Wolf B., 1984, A&A, 132, 151

Lesh J.R., 1968, ApJ, 152, 905

Lesh J.R., 1969, AJ, 74, 891

Henyey L.G., Lelevier R., Levée R.D., 1955, PASP, 67, 154

Lin D.N.C., Papaloizou J.C.B., 1985, in Protostars and Planets II, D.C. Black and M.S. Matthews eds., Univ. of Arizona Press, Tucson, p. 981

Lynden-Bell D., Pringle J.E., 1974, MNRAS, 168, 603

McCaughrean M.J., O'Dell R.C., 1996, AJ, 111, 1977

McCray R., Kafatos M., 1987, ApJ, 317, 190

Maeder A., Meynet G., 1991, A&AS, 89, 451

Maeder A., Meynet G., 2000, A&A, 361, 101

Magazzú A., Rebolo R., Pavlenko Y., 1992, ApJ, 392, 159

Magazzú A., Martín E.L., Rebolo R., 1993, ApJ, 404, L17

Magazzú A., Martín E.L., Sterzik M.F., Neuhäuser R., Covino E., Alcalá J.M., 1997, A&AS, 124, 449

Mamajek E.E., Lawson W.A., Feigelson E.D., 1999, ApJ, 516, L77

Martín E.L., 1997, A&A, 321, 492

Martín E.L., 1998, AJ, 115, 351

Martín E.L., Claret A., 1996, A&A, 306, 408

Martín E.L., Magazzù A., 1999, A&A, 342, 173

Martín E.L., Montes D., 1997, A&A, 318, 805

Martín E.L., Magazzú A., Rebolo R., 1992, A&A, 257, 186

Martín E.L., Rebolo R., Magazzú A., Pavlenko Ya.V., 1994, A&A, 282, 503

Martín E.L., Montmerle T., Gregorio-Hetem J., Casanova S., 1998, MNRAS, 300, 733

Massa D., Savage B.D., 1984, ApJ, 279, 310

Mezger P.G., Schraml J., Terzian Y., 1967, ApJ, 150, 807

Mendoza E.E.V., 1968, ApJ, 151, 977

Michaud G., Charbonneau P., 1991, SSRv, 57, 1

Miller G.E., Scalo J.M., 1979, ApJS, 41, 513

Minchin N.R., Ward-Thompson D., White G.J., 1992, A&A, 265, 733

Mineur H., 1939, Ann. Astrophys., 2, 1

Mizuno et al., 1998, ApJ, 507, L83

Monet D.G., 1998, A&AS, 193, 12003

Montes D., Martín E.L., Fernández-Figueroa M.J., Cornide M., De Castro E., 1997, A&AS, 123, 473

Montmerle, T., 1996, Cool Stars, Stellar Systems, and the Sun, 9th Cambridge Workshop, ASP Conference Series, R. Pallavicini and A.K. Dupree eds., Vol. 109, p. 405

Montmerle, T., 1999, in Proceedings of "Astronomy with radioactivities", Schloss Ringberg, 1999, Vol. 274, p. 225 (Ed. R. Diehl)

Montmerle T., Koch-Miramond L., Falgarone E., Grindlay J.E., 1983, ApJ, 269, 182

Moreno-Corral M.A., Chavarrìa K.C., De Lara E., Wagner S., 1993, A&A, 273, 619

Morgan W.W., Whitford A.E., Code A.D., 1953, ApJ, 118, 318

Münch L., 1954a, Bol. Obs. Ton. y Tac., No. 10, p. 40

Münch L., 1954b, Bol. Obs. Ton. y Tac., No. 11, p. 34

Mundt R., 1984, ApJ, 280, 749

Mundt R., Giampapa M.S., 1982, ApJ, 256, 156

Muzerolle J., Calvet N., Hartmann L., 1998, ApJ, 492, 743

Muzerolle J., Hartmann L., Calvet N., 1998, AJ, 116, 455

Muzerolle J., Calvet N., Hartmann L., 2001, ApJ, 550, 944

Naylor T., 1998, MNRAS, 296, 339

Naylor T., Fabian A.C., 1999, MNRAS, 302, 714 (NF99)

Neuhäuser R., Sterzik M.F., Schmitt J.H.M.M., Wichmann R., Krautter J., 1995a, A&A, 297, 391

Neuhäuser R., Sterzik M.F., Schmitt J.H.M.M., Wichmann R., Krautter J., 1995b, A&A, 295, L5

Neuhäuser R., Sterzik M.F., Torres G., Martín E.L., 1995c, A&A, 299, L13

Neuhäuser R., Torres G., Sterzik M.F., Randich S., 1997, A&A, 325, 647

Neuhäuser R. et al., 2000, A&AS, 146, 323

Nichiporuk W., Moore C.B., 1974, Geochim. Cosmochim. Acta, 38, 1691

Niemelä V.S., Sahade J., 1980, ApJ, 238, 244

O'Dell C.R., Wen Z., 1994, ApJ, 436, 194

O'Dell C.R., Wong K., 1996, AJ, 111, 846

O'Dell C.R., Wen Z., Hu X., 1993, ApJ, 410, 696

Olmi L., Felli M., 1998, A&A, 339, 872

Palla F., Galli D., 1997, ApJ, 476, L35

Palla F., Stahler S.W., 1990, ApJ, 360, L47

Palla F., Stahler S.W., 1993, ApJ, 418, 414

Palla F., Stahler S.W., 1999, ApJ 525, 772

Pallavicini R., 1989, A&A Rev., 1, 177

Pallavicini R., Pasquini L., Randich S., 1992, A&A, 261, 245

Panagia N., Thum C., 1981, A&A, 98, 295

Pasquini L., Liu Q., Pallavicini R., 1994, A&A, 287, 191

Pavlenko Y.V., Rebolo R., Martín E.L., García López R.J., 1995, A&A, 303, 807

Pfeffermann E., et al., 1988, The focal plane instrumentation of the ROSAT telescope. In: Proc. SPIE 733, p. 519

Pinsonneault M.H., Kawaler S.D., Sofia S., Demarque P., 1989, ApJ, 338, 424

Pinsonneault M.H., Kawaler S.D., Demarque P., 1990, ApJS, 74, 501

Pinsonneault M.H., Deliyannis C.P., Demarque P., 1992, ApJS, 78, 179

Pozzo M., Jeffries R.D., Naylor T., Totten E.J., Harmer S., Kenyon M., 2000, MNRAS, 313, L23

Preibisch T., Zinnecker H., 1999, AJ, 117, 2381

Preibisch T., Zinnecker H., Herbig G.H., 1996, A&A, 310, 456

Preibisch T., Guenther E., Zinnecker H., Sterzik M., Frink S., Röser S., 1998, A&A, 333, 619

Preibisch T., Guenther E., Zinnecker H., 2001, AJ, 121, 1040

Price S.D., Walker R.G., 1976, AFGL Report AFGL-TR-76-0208

Profitt C.R., Michaud G., 1989, ApJ, 346, 976

Randich S., Aharpour N., Pallavicini R., Prosser C.F., Stauffer J.R., 1997, A&A, 323, 286

Rebolo R., Martín E.L., Magazzú A., 1992, ApJ, 389, L83

Rebull L.M., Hillenbrand L.A., Strom S.E., Duncan D.K., Patten B.M., Pavlovsky C.M., Makidon R., Adamds M.T., 2000, AJ, 119, 3026

Reipurth B., Bertout C., 1997, Herbig-Haro Flows and the Birth of Stars, IAU Symp. 182, B. Reipurth and C. Bertout eds., (Dordrecht: Kluwer)

Reipurth B, Pedrosa, Lago M.T.V.T., 1996, A&AS, 120, 229

Rieke G.H., Lebofsky M.J., 1985, ApJ, 288, 618

Robberto M., Beckwith S.V.W., Herbst T.M., 1999, in Nakamoto T., ed., Proceedings of Star Formation 1999, Star Formation 1999, Nagoya, Japan, p. 231

Rogers F.J., Swenson F.J., Iglesias C.A., 1996, ApJ, 456, 902

Rucinski S.M., 1985, AJ, 90, 2321

Rucinski S.M., Krautter J., 1983, A&A, 121, 217

Ruprecht J., 1966, Bull. Inst. Czech., 17, 34. *Erratum*: 1966, Bull. Inst. Czech., 17, 98

Rydgren A.E., Zak D., 1987, AJ, 274, 677

Rydgren A.E., Strom S.E., Strom K.M., 1976, ApJS, 30, 307

Rydgren A.E., Schmelz J.T., Vrba F.J., 1982, ApJ, 256, 168

Rydgren A.E., Zak D.S., Vrba F.J., Chugainov P.F., Zajtseva G.V., 1984, AJ, 89, 1015

Sahu M.S., 1992, PhD thesis, University of Groningen

Sanctos Mendes L.T., D'Antona F., Mazzitelli I., 1997, Mem. Soc. Astron. Ital., Vol. 68, p. 823

Sandford M.T. II, Whitaker R.W., Klein R.I., 1982, ApJ, 260, 183

Särg K., Wramdemark S., 1970, A&AS, 2, 251

Sargent A.I., 1977, ApJ, 218, 736

Sargent A.I., 1979, ApJ, 233, 163

Sargent A.I., Beckwith S., 1987, ApJ, 323, 294

Sargent A.I., van Duinen R.J., Nordh H.L., Fridlund C.V.M., Aalders J.W.G., Beintema D., 1983, AJ, 88, 1236

Sellgren K., Allamandola L.J., Bregman J.D., Werner M.W., Wooden D., 1985, ApJ, 299, 416

Schaerer D., Schmutz W., Grenon M., 1997, ApJ, 484, L153

Schaller G., Schaerer D., Meynet G., Maeder A., 1992, A&AS, 96, 269

Sharpless S., 1959, ApJS, 4, 257

Schatzman E., 1962, Ann. d'Ap., 25, 18

Schmutz W. et al., 1997, A&A, 328, 219

Shu F.H., Adams F.C., Lizano S., 1987, ARA&A, 25, 23

Siess L. Forestini M., Bertout C., 1997, A&A, 326, 101

Silk J., 1995, ApJ, 438. L41

Simon M., Chen W.P., Howell R.R., Benson J.A., Slowik D., 1992, ApJ, 384, 212

Simonson S.C. III, van Someren Greve H.W., 1976, A&A, 49, 343

Skrutskie M.F., Dutkevitch D., Strom S., Edwards S., Strom K.M., 1990, AJ, 99, 1187

Skumanich A., 1972, ApJ, 171, 565

Soderblom D.R., Jones B.F., Balachandran S., Stauffer J.R., Duncan D.K., Fedele S.B., Hudon J.D., 1993, AJ, 106, 1059

Soderblom D.R., Jones B.F., Stauffer J.R., Chaboyer B., 1995, AJ, 110, 729

Stahler S.W., 1983, ApJ, 274, 822

Stapelfeldt K.R., Krist J.E., Ménard F., Bouvier J., Padgett D.L., Burows C.J., 1998, ApJ, 502, L65

Stassun K.G., Mathieu R.D., Mazeh T., Vrba F.J., 1999, AJ, 117, 2941

Stauffer J.R., Hartmann L.W., 1986, ApJS, 61, 531

Stauffer J.R., Hartmann L.W., Barrado y Navascues D., 1995, ApJ., 454, 910

Stelzer B., Neuhäuser R., 2000, A&A, 361, 581

Sterzik M.F., Durisen R.H., 1995, A&A, 304, L9

Sterzik M.F., Alcalá J.M., Neuhäuser R., Schmitt J.H.M.M., 1995, A&A, 297, 418

Sterzik M.F., Alcalá J.M., Covino E., Petr M.G., 1999, A&A, 346, L41

Stetson P.B., 1987, PASP, 99, 191

Stocke J.T., Liebert J., Gioia I.M., Maccararo T., Griffiths R.E., Danziger I.J., Kunth D., Lub J., 1983, ApJ, 273, 458

Störzer H., Hollenbach D., 1999, ApJ, 515, 669

Straka W.C., 1973, ApJ, 180, 907

Strom K.M., Strom S.E., 1994, ApJ, 424, 237

Strom K.M., Strom S.E., Edwards S., Cabrit S., Skrutskie M.F., 1989a, AJ, 97, 1451

Strom K.M., Wilkin F., Strom S.E., Seaman R.L., 1989b, AJ, 98, 1444

Strom K.M. et al., 1990, ApJ, 362, 168

Strom K.M., Strom S.E., Merrill K.M., 1993, ApJ, 412, 233

Testi L., Olmi L., Hunt L., Tofani G., Felli M., Goldsmith P., 1995, A&A, 303, 881

Thé P.S., de Winter D., Pérez M.R., 1994, A&AS, 104, 315

Thorburn J.A., Hobbs L.M., Deliyannis C.P., Pinsonneault M.H., 1993, ApJ, 415, 150

Tokovinin A.A., Chalabaev A., Shatsky N.I., Beuzit J.L., 1999, A&A, 346, 481

Topka K.P., 1980, PhD thesis, University of Harvard (Cambridge, MA)

Torres C.A.O., da Silva L., Quast G.R., de la Reza R., Jilinski E., 2000, AJ, 120, 1410

Tout C.A, Livio M., Bonnell I.A., 1999, MNRAS, 310, 360

Tovmassian H.M., Hovhannessian R.Kh., Epremian R.A., Huguenin D., 1993, A&AS, 100, 501

Trullols E., Jordi C., Galadì-Enrìquez D., 1997, in Proceedings of the ESA Symposium 'Hipparcos-Venice '97', Vol. 402, p. 299

Trümper J., 1983, Adv. Space Res., 2, 241

Vaiana G.S. et al. 1981, ApJ, 244, 163

Vallée J.P., 1995, ApJ, 454, 119

van der Hucht K.A. et al., 1997, New Astronomy, 2, 245

Vauclair S., Vauclair G., Schatzman E., Michaud G., 1978, ApJ, 223, 567

Ventura P., Zeppieri A., Mazzitelli I., D'Antona F., 1998, A&A, 331, 1011

Verschuur G.L., 1973, A&A, 24, 193

Vogel S.N., Kuhi L.V., 1981, ApJ, 245, 960

Walborn N.R., 1971, ApJS, 23, 257

Walker M.F., 1972, ApJ, 175, 89

Walker A.R., 1985, MNRAS, 213, 889

Wallace P.T., 1998, ASTROM, Basic astrometry program, v3.6 User's Guide, Starlink User Note 5.17

Wallerstein G., Herbig G.H., Conti P.S., 1965, ApJ, 141, 610

Walter F.M., 1986, ApJ 306, 573

Walter F.M., Boyd W.T., 1991, ApJ, 370, 318

Walter F.M., Kuhi L.V., 1981, ApJ, 250, 254

Walter F.M., Brown A., Mathieu R.D., Myers P.C., Vrba F.J., 1988, AJ, 96, 297

Walter F.M., Vrba F.J., Mathieu R.D., Brown A., Myers P.C., 1994, AJ, 107, 692

Walter F.M., Wolk S.J., Sherry W., 1998, in Cool Stars, Stellar Systems and the Sun, 10th Cambridge Workshop, ASP Conference series, Donahue R.A. and Bookbinder J.A. eds, Vol. 154, p. 1793

Walter F.M., Alcalá J.M., Neuhäuser R., Sterzik M., Wolk S.J., 2000, in Protostars and Planets IV, University of Arizona Press, Mannings V., Boss A.P. and Russell S.S. eds., p. 273

Ward-Thompson D., André P., Lay O.P., 2000, in Planetary Systems in the Universe, IAU Symposium no. 202, p. 101

Wesselius P.R., van Duinen R.J., de Jonge A.R.W., Aalders J.W.G., Luinge W., Wildeman K.J., 1982, A&AS, 49, 427

Wichmann R. et al., 1996, A&A, 312, 439

Wichmann R., Krautter J., Covino E., Alcalá J.M., Neuhäuser R., Schmitt J.H.M.M., 1997, A&A, 320, 185

Wichmann R., Bouvier J., Allain S., Krautter J., 1998, A&A, 330, 521

Wielen R., 1974, PASP, 86, 341

Willis A.J., Schild H., Stevens I.R., 1995, A&A, 298, 549

Willson L.A., 1975, ApJ, 197, 365

Winkler H., 1997, MNRAS, 287, 481

Wolk S., 1996, PhD Thesis, State University of New York

Wolk S.J., Walter F.M., 1996, AJ, 111, 2066

Woodward P.R., 1976, ApJ, 207, 484

Wouterloot J.G.A., Walmsley C.M., 1986, A&A, 168, 237

Wouterloot J.G.A., Walmsley C.M., Henkel C., 1988, A&A, 203, 367

Zapatero-Osorio M.R., Rebolo R., Martín E.L., García López R.J., 1996, A&A, 305, 519

Zappala R.R., 1972, ApJ, 172, 57

Zickgraf F.-J., Alcalá J.M., Krautter J., Sterzik M.F., Appenzeller I., Motch C., Pakull M.W., 1998, A&A, 339, 457

Zuckerman B., Palmer P., 1974, ARA&A, 12, 279

Zuckerman B., Webb R.A., Schwartz M., Becklin E.E., 2001, ApJ, 549, L233